



**Joana Marcelino
Pinheiro**

**Desenvolvimento de um permutador de calor
zeolítico para aplicações de aquecimento**



**Joana Marcelino
Pinheiro**

Desenvolvimento de um permutador de calor zeolítico para aplicações de aquecimento

Tese apresentada à Universidade de Aveiro para cumprimento dos requisitos necessários à obtenção do grau de Doutor em Engenharia da Refinação, Petroquímica e Química, realizada sob a orientação científica do Doutor Carlos Manuel Santos Silva, Professor Associado do Departamento de Química da Universidade de Aveiro, coorientação científica da Doutora Anabela Tavares Valente, Investigadora Principal do Departamento de Química da Universidade de Aveiro, e coorientação empresarial do Engenheiro Sérgio Varo de Oliveira Loureiro Salústio, Vice-Presidente Sénior de Engenharia de Produto da Bosch Termotecnologia, S.A., Aveiro.

Apoio financeiro do POCTI no âmbito do III Quadro Comunitário de Apoio.

Apoio financeiro da FCT e da Bosch (PD/BDE/113538/2015), e do POPH/FSE no âmbito do III Quadro Comunitário de Apoio.



BOSCH
Invented for life

"If we want to decarbonize society, we must decarbonize the heating sector"
(European Heat Pump Association)

o júri

presidente

Prof. Doutor Fernando Manuel Bico Marques

Professor Catedrático do Departamento de Engenharia de Materiais e Cerâmica da Universidade de Aveiro

Prof.^a Doutora Rosa Maria de Oliveira Quinta-Ferreira

Professora Catedrática do Departamento de Engenharia Química da Faculdade de Ciências e Tecnologia da Universidade de Coimbra

Prof.^a Doutora Maria Filipa Gomes Ribeiro

Professora Associada com Agregação do Instituto Superior Técnico da Universidade de Lisboa

Prof. Doutor João Paulo Serejo Goulão Crespo

Professor Catedrático da Faculdade de Ciências e Tecnologia da Universidade Nova de Lisboa

Prof. Doutor José Paulo Barbosa Mota

Professor Catedrático da Faculdade de Ciências e Tecnologia da Universidade Nova de Lisboa

Prof. Doutor João Carlos Matias Celestino Gomes da Rocha

Professor Catedrático do Departamento de Química da Universidade de Aveiro

Prof. Doutor Carlos Manuel Santos Silva

Professor Associado do Departamento de Química da Universidade de Aveiro

Eng. Sérgio Varo de Oliveira Loureiro Salústio

Coordenador Empresarial e Vice-Presidente Sénior de Engenharia de Produto da Bosch Termotecnologia, S.A., Aveiro

agradecimentos

Primeiramente, agradeço à minha família pelo incondicional amor, carinho e apoio que me deram ao longo desta caminhada. Dirijo o agradecimento mais especial aos meus pais. Sem eles não teria sido possível chegar até aqui.

Em segundo lugar, um agradecimento sincero ao meu orientador, Professor Doutor Carlos Manuel Silva, e aos meus coorientadores, Doutora Anabela Valente e Engenheiro Sérgio Salústio, por tudo o que me ensinaram, pela orientação, por todas as reuniões e discussões frutíferas, pelo incansável apoio e amizade que sempre demonstraram.

Uma palavra de apreço a todos os meus amigos, colegas do grupo EgiChem e colegas da Bosch, pelas sugestões e suporte que foram dando ao longo do trabalho, e pela constante boa disposição, sorrisos e espírito de entreatajuda.

Um agradecimento a todos aqueles que, pontualmente e de variadas formas, também contribuíram para a concretização deste trabalho, nomeadamente, o Professor Doutor Vítor Geraldês, o Professor Doutor Vítor Amaral, o Professor Doutor João Pires da Silva, o Professor Doutor João Rocha, o Professor Doutor Francisco Avelino da Silva, a Professora Doutora Inês Portugal, o Engenheiro Nelson Ferreira, o Doutor Zhi Lin, etc.

Agradeço ainda ao Programa Doutoral do EngIQ, especialmente ao Professor Doutor Fernando Martins, pelo excelente suporte em diversas questões burocráticas relativas ao doutoramento.

Quero ainda agradecer à FCT e à Bosch Termotecnologia pelo apoio financeiro prestado, que tornou possível a concretização desta tese.

Por fim, agradeço à Universidade de Aveiro, em particular ao Laboratório Associado CICECO-Instituto de Materiais de Aveiro, e à Bosch Termotecnologia, S.A., Aveiro, pela disponibilização dos meios necessários à realização deste trabalho.

palavras-chave

Aquecimento de água doméstica, *benchmarking*, bombas de calor por adsorção, cinética, desenho fatorial de experiências, equilíbrio, modelação, otimização, pares adsorvente/água, protótipo, simulação

resumo

As alterações climáticas e a escassez de recursos naturais têm motivado a criação de medidas para reinventar o sistema energético, rumo a uma economia mais sustentável. As bombas de calor por adsorção (AHP) fazem parte das alternativas investigadas para a criação de edifícios com necessidades energéticas quase nulas. Este trabalho abrange vários domínios com relevância para a investigação e desenvolvimento das AHP, nomeadamente, caracterização de adsorventes, modelação e simulação de unidades de aquecimento por adsorção, otimização do *design* e operação de AHP, prototipagem e comparação com tecnologias convencionais.

Foram investigados os desempenhos de diversos adsorventes em AHP, considerando a água como adsorvato e diferentes condições de operação e de geometria. Os adsorventes selecionados foram o titanossilicato número 10 (ETS-10), três zeólitos (13X, 4A e NaY), a rede metalo-orgânica cristalina (MOF) CPO-27(Ni) e o fosfato de sílica-alumina AQSOA™ FAM-Z02.

No tocante ao par ETS-10/água, foram medidas isotérmicas de adsorção e propriedades cinéticas, assim como condutividades térmicas e capacidades caloríficas específicas do adsorvente. Estes resultados foram utilizados para modelar e simular um permutador de calor tubular contendo ETS-10. O modelo desenvolvido contemplou balanços de massa e energia, equilíbrio de adsorção, resistência externa à transferência de calor e transporte intraparticular de massa. Para espessuras de leito (δ) de ETS-10 entre 2 e 6 mm, obtiveram-se valores de coeficiente de performance (*COP*) e de potência específica de aquecimento (*SHP*) nos intervalos 1.36-1.39 e 249-934 W kg⁻¹, respetivamente. Estudos de sensibilidade mostraram que parâmetros como o δ e a temperatura de regeneração do adsorvente podem influenciar consideravelmente o tempo de ciclo (t_{ciclo}) e a capacidade cíclica de adsorção (ΔW_{ciclo}) do sistema.

O ETS-10 foi comparado com adsorventes bastante conhecidos, tais como, sílica gel e os zeólitos 4A e 13X, tendo-se concluído que o seu desempenho para fins de aquecimento é ultrapassado pelo do zeólito 13X, para regeneração de leito realizada a 473 K, e condensação e evaporação do refrigerante a 333 K e 278 K, respetivamente. Estes resultados foram, em parte, atribuídos a uma maior libertação de calor por ciclo, quando se usa o par 13X/água. Para tamanhos de partícula entre 0.2 e 0.6 mm, este par apresentou *COP* = 1.48 e *SHP* no intervalo 1141-1254 W kg⁻¹.

Com o objetivo de reduzir o esforço numérico e computacional em simulações, foi estudado o impacto de se introduzirem algumas simplificações no modelo, sem deixar de garantir as previsões razoáveis de desempenho das AHP. Por exemplo, a utilização de um valor médio fixo para o coeficiente intraparticular de transferência de massa é razoável na avaliação dos desempenhos nos ciclos de aquecimento.

Uma vez que a presença de agentes ligantes na formulação de adsorventes pode diminuir a capacidade de adsorção e afetar a cinética, foram estudados os desempenhos de aquecimento de adsorventes zeolíticos comerciais (13X e NaY) com e sem ligantes. Os resultados, considerando água como adsorvato, indicaram que a existência de um ligante na formulação do zeólito 13X não afetava consideravelmente o seu desempenho. No âmbito deste estudo, verificou-se ainda que o zeólito NaY sem ligante é o adsorvente mais promissor para temperaturas de regeneração do leite, condensação e evaporação de 398.15-448.15 K, 308.15-328.15 K e 278.15 K, respetivamente, atingindo $COP \leq 1.53$ e $SHP \leq 430 \text{ W kg}^{-1}$, essencialmente devido a ΔW_{ciclo} mais elevado do que o dos zeólitos 13X.

Dado que a otimização das AHP é importante para aumentar a sua competitividade, o potencial de combinar modelação fenomenológica com ferramentas estatísticas, tais como o desenho fatorial de experiências e a metodologia da superfície de resposta (DoE/RSM), foi estudado na otimização de AHP com o par zeólito NaY/água. Para tal, foi considerado o desenho de experiências de Box-Behnken com quatro fatores – tempo de adsorção e dessorção, temperatura de condensação, temperatura da fonte de aquecimento e espessura de leite – e três níveis, sendo COP e SHP as variáveis de resposta. Deste estudo obtiveram-se gráficos de Pareto, mostrando a importância dos diversos fatores no COP e no SHP , e equações polinomiais para estimar de forma expedita o COP e o SHP em função dos fatores e *vice-versa*. Estas equações permitiram mapear o desempenho da AHP numa ampla gama de condições com um número pequeno de simulações, e ainda identificar combinações ótimas de parâmetros geométricos e de operação para cumprir pré-requisitos de desempenho. Em suma, este estudo mostrou o grande potencial de DoE/RSM para desenvolver componentes mais otimizados e estratégias de controlo avançadas de AHP.

Tendo em conta a miríade de potenciais aplicações que tem sido reivindicada para redes metalo-orgânicas cristalinas (MOFs), sobre os quais existe um grande foco da investigação científica, o potencial do MOF CPO-27(Ni) para aplicações de aquecimento por adsorção de água foi investigado usando ferramentas de modelação e simulação computacional. Para este efeito, foi desenvolvido em OpenFOAM um *solver* customizado e uma metodologia para simular ciclos de aquecimento por adsorção, que foram validados com dados da literatura. Neste estudo, considerou-se uma geometria de leite de adsorvente mais avançada, consistindo num tubo metálico revestido com um filme de um compósito de CPO-27(Ni)/espuma de cobre. Os COP e SHP foram, respetivamente, 1.16-1.39 e 1922-5130 W kg^{-1} , para temperatura de evaporação, condensação e regeneração de leite de 278.15 K, 308.15 K e 368.15 K. Uma comparação deste MOF com o adsorvente de referência para AHP, nomeadamente AQSOA™ FAM-Z02, permitiu concluir que o desempenho do CPO-27(Ni) é ultrapassado pelo do segundo, essencialmente devido ao ΔW_{ciclo} inferior e à transferência intraparticular de massa mais lenta do CPO-27(Ni).

No contexto desta dissertação, foi ainda desenhada uma instalação experimental combinando uma AHP com um esquentador, que poderá ser montada proximamente para testar o desempenho de diversos adsorventes, tendo sido elaborado o respetivo protocolo. As especificações técnicas de diversos componentes para o protótipo foram definidas e foram analisadas propostas de vários fornecedores, a partir das quais se estimou o custo da instalação.

Finalmente, foi desenhado um possível conceito de uma AHP para aquecimento de água doméstica, o qual foi comparado com a atual bomba de calor da Bosch para este fim (*Supraeco W*). Apesar dos benefícios ambientais das AHP, concluiu-se que estes sistemas suscitam ainda grandes desafios técnico-económicos, uma vez que exigem dimensões significativas, bem como complexidade e preço elevados. No cômputo geral, conclui-se que a competitividade da tecnologia de aquecimento de água doméstica por adsorção depende largamente do desenvolvimento de adsorventes de água com melhor rácio desempenho/preço e da aposta em formulações mais eficientes como, por exemplo, na preparação de filmes ao invés de enchimentos aleatórios de partículas de adsorvente.

keywords

Adsorbent/water pairs, adsorption heat pumps, benchmarking, design of experiments, domestic water heating, equilibrium, kinetics, modeling, optimization, prototype, simulation

abstract

The worldwide climate changes and the scarcity of natural resources have been driving measures to reinvent the energy system towards a low-carbon and sustainable model. Adsorption heat pumps (AHPs) are among the alternatives investigated for the creation of nearly zero energy buildings, as they may help to globally decarbonize the society. This work addresses various domains which are important for the research and development of AHPs, namely, experimental characterization of adsorbents, modeling and simulation of adsorption heating units, optimization of the AHPs design and operation, prototype design and benchmarking against more conventional solutions.

The overall heating performance of several adsorbents - ETS-10, zeolites (13X, 4A and NaY), silica-gel, MOF CPO-27(Ni), and AQSOA™ FAM-Z02 - for water AHPs was investigated under distinct geometric and operating conditions. Regarding ETS-10/water pair, adsorption equilibrium and kinetic properties were measured, along with the effective thermal conductivity and specific heat capacity of ETS-10. These results were used to model and simulate a tubular adsorbent heat exchanger (AHEx). The developed model contemplated material and energy balances, adsorption equilibrium, external heat transfer limitations, and intraparticle mass transport. Values of coefficient of performance (*COP*) and specific heating power (*SHP*) in the range 1.36-1.39 and 249-934 W kg⁻¹ were obtained, respectively, for adsorbent bed thicknesses (δ) of 2-6 mm. Sensitivity studies showed that parameters δ and adsorbent regeneration temperature may influence considerably the cycle time (t_{cycle}) and the cyclic adsorption loading swing (ΔW_{cycle}).

The ETS-10 was compared against well-known adsorbents like silica gel, zeolite 4A and zeolite 13X, for water AHPs, showing that it is outperformed by zeolite 13X, for bed regeneration, condensation and evaporation at 473 K, 333 K and 278 K, respectively. This was partly attributed to the higher amount of heat generated per cycle when using the pair zeolite 13X/water. For zeolite 13X particle diameters between 0.2 and 0.6 mm, values of *COP* = 1.48 and *SHP* = 1141–1254 W kg⁻¹ were obtained. Aiming to reduce computational and numerical efforts in the simulations, the impact of considering some model simplifications while ensuring comparable predictions of the AHP performance for zeolite 13X/water pair was investigated. It was concluded that, e.g., the use of an average and fixed value of the intraparticle mass transfer coefficient is sufficient to predict reliable cycle performances.

Since the presence of a binder in the formulation of the adsorbents may harm the adsorption loading and kinetics, the heating performance of commercial 13X and NaY zeolites, with and without binder, was compared for water AHPs, through modeling and simulations. The results unveiled that the performance of zeolite 13X is not significantly penalized by the presence of the binder. The binderless NaY surpassed zeolites 13X for regeneration, condensation, and

evaporation temperatures of 398.15-448.15 K, 308.15-328.15 K and 278.15 K, respectively, achieving $COP \leq 1.53$ and $SHP \leq 430 \text{ W kg}^{-1}$, essentially due to its higher ΔW_{cycle} .

As boosting the market competitiveness of AHPs implies the development of optimized appliances, the potential of combining phenomenological modeling and statistical tools like design of experiments and response surface methodology (DoE/RSM) to aid efficient optimization of AHPs was demonstrated for the pair binderless zeolite NaY/water. A Box-Behnken design with four factors - time of adsorption and desorption, condensation temperature, heat source temperature, bed thickness - and three levels was considered, taking COP and SHP as response variables. The statistical outcomes from DoE/RSM included: (i) Pareto charts displaying the impact ranking of the factors upon COP and SHP , and (ii) polynomial equations to efficiently estimate both performance indicators as function of the factors and *vice-versa*. These models allowed to map the system performances in a broad range of conditions with a low number of simulations, and to select optimal combinations of geometric and operating parameters to meet pre-established performance requisites. Overall, these results provided insights into the great potential of DoE/RSM for building up optimized AHExs and advanced control strategies of AHPs.

Given the myriad of potential applications claimed for metal-organic frameworks (MOFs), for which massive scientific investigation is ongoing, the potential of MOF CPO-27(Ni) for water adsorption heating was investigated in this work, with the aid of modeling and computational simulations. A customized solver and methodology for simulating adsorption heating cycles was developed in OpenFOAM, and validated using data from the literature. An improved AHEx design was considered, consisting of a tube surrounded by a coating composite of CPO-27(Ni)/copper foam. The obtained $COPs$ and $SHPs$ were, respectively, in the interval 1.16-1.39 and 1922-5130 W kg^{-1} , for evaporation, condensation and bed regeneration temperatures of 278.15 K, 308.15 K and 368.15 K, respectively. Under these working conditions, the CPO-27(Ni) was surpassed by the benchmark adsorbent AQSOA™ FAM-Z02, which was essentially attributed to lower ΔW_{cycle} and slower intraparticle mass transfer kinetics of the MOF.

An experimental installation combining an AHP and a gas water heater (GWH) that may be assembled to test the performance of several adsorbents was designed, and an experimental protocol prepared. Technical specifications of assorted components were defined and suppliers' proposals analyzed, in order to estimate the budget for such prototype.

Finally, a potential concept of an adsorption appliance for domestic hot water production (DHW) was presented and compared against the current Bosch heat pump water heater (HPWH *Supraeco W*). Despite the eco-friendliness of AHPs, these systems still raise considerable techno-economic challenges, since they require significant dimensions, as well as high complexity and price. In the whole, one concludes that the competitiveness of adsorption technology for DHW production strongly depends on the development of water adsorbents with better performance/price ratio, and on improved formulations like coatings, instead of beds with random particles of adsorbent.

Thesis Outline

List of Figures.....	vi
List of Tables.....	xiv
<i>Chapter 1: Motivation and thesis plan.....</i>	<i>1</i>
1.1. Motivation.....	1
1.2. Thesis plan.....	3
References.....	7
<i>Chapter 2: Introduction.....</i>	<i>9</i>
2.1. Contextualization.....	10
2.2. Working principles and performance indicators of adsorption heat pumps...	12
2.2.1. Working principles.....	12
2.2.2. Performance indicators	14
2.2.3. Impact of the operating conditions on the performance of AHPs.....	15
2.3. Design and operation of AHPs.....	19
2.3.1. Heating performances based on <i>COP</i> and <i>SHP</i>	19
2.3.2. The working adsorbent/adsorbate pairs.....	23
2.3.3. Adsorbates and temperature heat sources for the evaporator.....	29
2.3.4. Temperature operation levels and cycle features.....	32
2.3.5. Adsorbent bed configurations.....	34
2.3.6. Adsorbent heat exchanger (AHEx) geometries.....	39
2.3.7. Patents and applications.....	42
2.4. Commercial AHPs <i>versus</i> conventional technologies.....	51
2.4.1. Vaillant and Viessmann heating appliances.....	51
2.4.2. AHPs <i>versus</i> conventional heating technologies.....	55
2.5. Outlook.....	57

Nomenclature.....	58
References.....	60
Annex A2.....	71
<i>Chapter 3: Adsorption heat pump based on ETS-10/water pair.....</i>	<i>89</i>
3.1. Introduction.....	90
3.2. Materials and methods.....	92
3.3. Mathematical modeling of the adsorption unit.....	93
3.3.1. Model description.....	93
3.3.2. Numerical approach.....	99
3.4. Results and discussion.....	99
3.4.1. Synthesis, properties and isotherms of ETS-10.....	99
3.4.2. Simulation of the ETS-10/water heating system, and sensitivity studies...	103
3.4.2.1. Simulation of the ETS-10/water heating system.....	103
3.4.2.2. Sensitivity studies.....	111
3.4.2.2.1. Effect of the adsorbent bed thickness.....	111
3.4.2.2.2. Effect of final regeneration temperature and heating fluid temperature	112
3.5. Conclusions.....	114
Nomenclature.....	115
References.....	117
Annex A3.....	119
<i>Chapter 4: Comparison of different porous metal/metalloid oxides...</i>	<i>127</i>
4.1. Introduction.....	128
4.2. Mathematical modeling of the adsorption unit.....	131
4.2.1. Model description and estimations of heating performance	131
4.2.2. Estimation of the heating performance.....	132
4.2.3. Numerical approach.....	135
4.3. Results and discussion.....	136
4.3.1. Equilibrium and kinetic properties of the working pairs.....	136

4.3.1.1. Adsorption isotherms.....	136
4.3.1.2. Estimation of $Q_{\text{ads}} = Q_{\text{ads}}(W)$ for zeolites 13X, 4A and ETS-10.....	139
4.3.1.3. Estimation of $D_{\text{eff}} = D_{\text{eff}}(T, W)$ of water on zeolites 13X, 4A and silica gel.....	140
4.3.2. Simulation of the heating performance of the working pairs.....	142
4.3.2.1. Effect of using constant or variable thermal conductivity.....	148
4.3.2.2. Effect of using constant or variable Q_{ads}	149
4.3.2.3. Modeling the intraparticle mass transfer kinetics.....	149
4.3.2.3.1. Effect of assuming $D_{\text{eff}} = D_{\text{eff}}(T, W)$ in the simulations.....	149
4.3.2.3.2. Effect of using a constant K_{LDF} in the simulations.....	151
4.3.3. Sensitivity study - effect of the particle size on the performance of the AHS.....	152
4.4. Conclusions.....	154
Nomenclature.....	155
References.....	157
Annex A4.....	161

Chapter 5: Phenomenological modeling and statistical optimization 167

5.1. Introduction.....	168
5.2. Materials and methods.....	171
5.3. System description and mathematical modeling.....	171
5.3.1. Adsorbent Heat Exchanger (AHEx) geometry.....	171
5.3.2. Modeling and performance indicators.....	172
5.3.3. Design of experiments and response surface methodology (DoE/RSM)...	174
5.4. Results and discussion.....	176
5.4.1. Measurement and determination of properties of NaYBfK and 13XB.....	176
5.4.1.1. Morphology, equilibrium isotherms, heats of adsorption and adsorption kinetics.....	176
5.4.1.2. Solid densities (ρ_s) and thermal conductivities ($\lambda_{\text{eff},s}$).....	179
5.4.2. Simulation studies and optimization through DoE/RSM.....	180
5.4.2.1. Comparison of NaYBKF, 13XBfK and 13XB beds.....	181

5.4.2.2. Statistical outcomes from DoE/RSM for NaYBKF and insights into AHPs optimization.....	182
5.4.2.2.1. Impact of operating/geometric factors on <i>COP</i> and <i>SHP</i>	182
5.4.2.2.2. RSM models for <i>COP</i> and <i>SHP</i>	184
5.5. Conclusions.....	190
Nomenclature.....	191
References.....	194
Annex A5.....	199
<i>Chapter 6: Computer simulation using OpenFOAM.....</i>	<i>221</i>
6.1. Introduction.....	222
6.2. System description and mathematical modeling.....	224
6.2.1. Adsorbent heat exchanger (AHEX) geometry and mesh.....	224
6.2.2. Modeling and performance indicators.....	226
6.3. Computational simulations.....	231
6.3.1. OpenFOAM.....	231
6.3.2. Numerical methodology.....	231
6.4. Results and discussion.....	235
6.4.1. Validation of OpenFOAM solver and methodology using literature data...	235
6.4.2. Performance of CPO-27(Ni) coated copper foam for AHPs.....	240
6.4.3. Comparison of copper foams coated with CPO-27(Ni) or AQSOA™ FAM-Z02.....	247
6.5. Conclusions.....	250
Nomenclature.....	251
References.....	254
Annex A6.....	257
<i>Chapter 7: Prototype design.....</i>	<i>261</i>
7.1. Prototype.....	262

Development of a zeolitic heat exchanger for heating applications

7.1.1. Experimental setup.....	262
7.1.2. Experimental procedure.....	264
7.1.3. Specification of components, suppliers' proposals and costs.....	267
7.2. Product concept, comparison with conventional technology, and challenges	267
7.2.1. Product concept.....	267
7.2.2. Adsorption system <i>versus</i> Bosch heat pump water heater (HPWH).....	270
7.3. Final outlook.....	273
Nomenclature.....	274
References.....	276
Annex A7.....	277
<i>Chapter 8: Final outlook and future work.....</i>	<i>293</i>
Suggestions of future work.....	298
Nomenclature.....	301
References.....	302

List of Figures

Chapter 1: Motivation and thesis plan

- Fig. 1.1 Components of a basic AHP, main working stages, and operating temperature levels..... 2

Chapter 2: Introduction

- Fig. 2.1 (a) Final energy consumption in the EU-28 residential sector by type of end use in 2015. (b) Share of fuels in the final energy consumption for space heating and DHW production in the EU-28 residential sector in 2015 (values in %). (c) Evolution of electricity and natural gas prices for household consumers in EU-28 from the second semester (S2) of 2007 (2007-S2) to the second semester of 2016 (2016-S2) (all taxes and levies included)..... 11
- Fig. 2.2 (a)-(d) Simplified representation of a basic AHP involving four stages of an adsorption heating cycle ((a) isobaric adsorption, (b) isosteric heating, (c) isobaric desorption, and (d) isosteric cooling). (e) An ideal adsorption cycle (P vs. T). (f)-(h) Profiles of bed pressure (P), temperature (T) and adsorbent loading (W) for four consecutive heating cycles..... 12
- Fig. 2.3 Impact of increasing: (a, d) $T_{\text{cond}} (= T_2)$ from $T_{\text{cond},1} (= T_{2,1})$ to $T_{\text{cond},3} (= T_{2,3})$; (b, e) P_{evap} from $P_{\text{evap},1}$ to $P_{\text{evap},3}$; and (c, f) T_4 from $T_{4,1}$ to $T_{4,3}$, using (a, b, c) type I isotherms and (d, e, f) ideal P vs. T plots. The equilibrium adsorption cycles are represented by colored rectangles..... 17
- Fig. 2.4 Scheme of an AHP combined with a domestic hot water (DHW) tank, operating during (a) isobaric adsorption (ADS) and (b) isobaric desorption (DES). Impact of increasing the condensation and minimum bed temperatures (T_{cond} , T_2) along three consecutive adsorption heating cycles: (c) P , (d) T , and (e) W along time in the adsorbent bed... 18
- Fig. 2.5 Literature data for $COPs$ of AHPs (1985 - 2017)..... 20
- Fig. 2.6 Literature data for SHP values of AHPs along the years (1985 - 2017)... 21

Fig. 2.7	(a) Types of adsorbents for AHPs grouped by theoretical, technical and economic potentials. (b) S-curve showing the level of industrial production maturity of the adsorbents included in the technical potential subset.....	25
Fig. 2.8	(a) ΔW_{eq} vs. T_{cond} at $T_{\text{evap}} = 278$ K and $T_4 = 368$ K for zeolite Köstrolith® 13XBFK, microporous silica gel type RD, MOF CPO-27(Ni), SAPO-34 and AQSOA® FAM-Z02 using water as adsorbate. T_{cond} and corresponding ΔW_{eq} for zeolite Köstrolith® 13XBFK at $T_4 = 473$ K are plotted for comparison. (b) Water ΔW_{eq} vs. T_{cond} at $T_{\text{evap}} = 288$ K and $T_4 = 368$ K for Köstrolith® 13XBFK, microporous silica gel type RD, MOFs CPO-27(Ni) and aluminum fumarate, and AQSOA® FAM-Z02. (c) Qualitative comparison of aluminosilicate zeolites, AQSOA® FAM-Z02, SAPO-34, microporous silica gel and MOFs regarding: ΔW_{eq} (based on (a) and (b), for $T_4 = 368$ K), ability to be regenerated at low T ($T \leq 373$ K), hydrothermal stability, commercial availability and cost.....	27
Fig. 2.9	Data for the refrigerants studied for AHPs, namely water, ammonia, methanol and ethanol: (a) general view regarding the use of the adsorbates in AHPs over the years; (b) enthalpies of vaporization (ΔH_v) at 313 K; (c) toxicity and/or flammability issues, global warming potential (GWP; for 100 years), ozone depletion potential (ODP), stability concerns and compatibility with metals; (d) P^σ vs. T in the range 278 – 313 K; (e) Applicable T_{evap} ranges (considering 253 – 303 K as reasonable interval in heat pumps).....	30
Fig. 2.10	Typical low (T_{evap} and/or $T_{\text{heat source}}^{\text{low}}$), medium (T_{cond} and/or T_2), and high (T_4 and/or $T_{\text{heat source}}^{\text{high}}$) temperature levels for basic and advanced AHPs using water, methanol, ethanol or ammonia with different adsorbents (zeolites, silica gel, AQSOA® FAM-Z02, SAPO-34, MOFs, CSPMs and activated carbons).....	33
Fig. 2.11	Comparison of the adsorbent configurations for AHPs (loose grains, consolidated beds, binder-based coatings, and directly synthesized coatings) in terms of λ_{ads} , h_{ads} , δ , bed permeability, stability issues and industrial application features. Quantitative data for the figure was essentially based on literature for zeolites, zeotypes (e.g., AQSOA® FAM-Z02, SAPO-34) and silica gels, using water as adsorbate.....	36

Fig. 2.12	AHEX geometries which have been investigated for AHPs (tubular with and without fins, extended surface and plate-type) and percentage of works that adopted each geometry, along with information of the respective investigated adsorbent/adsorbate pairs.....	39
Fig. 2.13	Schematic representation of the AHEX geometries mostly adopted in AHPs using adsorbent/water (tubular with fins and extended surface heat exchangers). (b) Values of U , m_{ads}/V_{AHEX} and m_{ads}/m_{metal} for both geometries, using loose grains or coatings.....	41
Fig. 2.14	Scope of the patents from Vaillant and Viessmann listed in Table 2.1 displayed by priority year. The years in which their first AHPs were launched in the market are also marked.....	50
Fig. 2.15	Simplified representation of the gas-fired AHP from Vaillant (ZeoTHERM VAS) during (a) desorption and (b) adsorption stages.....	52
Fig. 2.16	Simplified representation of the gas-fired AHP from Viessmann (Vitosorp 200-F) during (a) desorption and (b) adsorption stages.....	54
Fig. 2.17	Potential of gas-fired AHPs for a typical 150 m ² German house over gas non-condensing and condensing boilers, in terms of primary energy consumption, renewable energy share and reduction in the CO ₂ emissions.....	55

Chapter 3: Adsorption heat pump based on ETS-10/water pair

Fig. 3.1	Simplified representation of an adsorption heating system and (b) corresponding Clapeyron diagram.....	90
Fig. 3.2	Schematic representation of the adsorption unit modeled in this work...	93
Fig. 3.3	Powder X-ray diffraction pattern of ETS-10 sample.....	100
Fig. 3.4	Water adsorption isotherms for ETS-10 at 298 K, 323 K and 348 K. The surface is the Dubinin-Astakhov model (Eq. (3.5)).....	100
Fig. 3.5	Kinetics of water adsorption on ETS-10 at 298 K, which contributed to the determination of K_{LDF} using Eq. (3.2).....	101
Fig. 3.6	Effective thermal conductivity and specific heat capacity of ETS-10 as a function of T	102

Fig. 3.7	Operational cycles for bed thicknesses of 2, 4 and 6 mm, and ideal cycle.....	104
Fig. 3.8	Evolution of (a) temperatures of adsorbent and vapor, (b) pressure and (c) adsorbate loading against time, for different bed positions during the adsorption stage.....	106
Fig. 3.9	Curves of (a) adsorbent and vapor temperatures, (b) pressure and (c) adsorbate loading against time, for different bed positions, during isosteric heating stage.....	107
Fig. 3.10	Evolution of (a) temperatures of adsorbent and vapor, (b) pressure and (c) adsorbate loading against time, for different bed positions, during desorption stage.....	108
Fig. 3.11	Curves of (a) temperature of adsorbent and vapor, (b) pressure and (c) adsorbate loading against time, for different bed positions, during the isosteric cooling stage.....	109
Fig. 3.12	Evolution of the (a) average temperatures of adsorbent and vapor, (b) average pressure and (c) average adsorbate loading, for the first 4 cycles.....	110
Fig. 3.13	Variation of (a) $\Delta\bar{W}_{\text{cycle}}$, (b) <i>COP</i> and (c) <i>SHP</i> with the final bed regeneration temperature, for different heating fluid temperatures.....	113

Chapter 4: Comparison of different porous metal/metalloid oxides

Fig. 4.1	Clapeyron diagram of an adsorption heating system (AHS).....	129
Fig. 4.2	Schematic representation of the AHS modeled in this work.....	131
Fig. 4.3	Adsorption isotherms of water on zeolite 13X: Experimental data at 294, 314, 333 and 355 K; lines are Dubinin-Astakhov model (Eq. (4.18)).....	139
Fig. 4.4	Isosteric heat of adsorption of ETS-10/water pair as function of <i>W</i>	140

Fig. 4.5	$D_{\text{eff}} = D_{\text{eff}}(T, W)$ of water on: (a) zeolite 13X; (b) zeolite 4A; (c) silica gel type RD.....	141
Fig. 4.6	Operational cycles for different particle sizes of zeolite 13X: $d_p = 2.0 \times 10^{-4}$, 3.5×10^{-4} and 6.0×10^{-4} m, and ideal cycle. Pie charts indicating the time spent on each stage of the heating cycle for each particle size.....	144
Fig. 4.7	(a) Heats generated or supplied to the AHS during each stage of the cycle (isobaric desorption; isosteric heating; isosteric cooling; condenser; isobaric adsorption), for each adsorbent. (b) Contribution of different cycle stages to the <i>COP</i>	146
Fig. 4.8	(a) Water adsorption isotherms of zeolite 13X, zeolite 4A, ETS-10 and silica gel at 333 K. (b) Water adsorption isotherms of zeolite 13X, zeolite 4A and ETS-10 at 473 K and of silica gel at 423 K.....	148
Fig. 4.9	(a) D_{eff} vs. time curves and (b) variation of K_{LDF} along time for each stage of the heating cycle (isobaric adsorption, isosteric heating, isobaric desorption, isosteric cooling), for zeolite 13X/water pair.....	150
Fig. 4.10	D_{eff} versus time curve for each stage of the cycle (isobaric adsorption, isosteric heating, isobaric desorption, isosteric cooling), for zeolite 4A/water pair.....	151
Fig. 4.11	Evolution of the average water loading (\bar{W}) in zeolite 13X, during the first four cycles, for three distinct particle sizes ($d_p = 2.0 \times 10^{-4}$ m, $d_p = 3.5 \times 10^{-4}$ m, $d_p = 6.0 \times 10^{-4}$ m).	153

Chapter 5: Phenomenological modeling and statistical optimization

Fig. 5.1	Schematic representation of the cylindrical adsorbent heat exchanger (AHEX) studied in this work.....	172
Fig. 5.2	SEM images of (a) NaYBFK and (b) 13XB (crushed particle).....	176
Fig. 5.3	Adsorption isotherms of water vapor on zeolite NaYBFK: experimental data at 298.15, 333.15 and 353.15 K provided by Chemiewerk Bad Köstritz GmbH (CWK); lines are the Dubinin-Astakhov model fitting.....	178

Fig. 5.4	Adsorption isotherms of water vapor on zeolite 13XB: experimental data at 298.15, 313.15, 338.15 K, 368.15 K and 423.15 K provided by Grace; lines are the Dubinin-Astakhov model fitting	178
Fig. 5.5	Variation of $\lambda_{\text{eff},s}$ of 13XB and NaYBFK with temperature. Squares are experimental results (using the Gustafsson probe method), and lines are the corresponding linear fittings.....	179
Fig. 5.6	Pareto charts of (a) <i>COP</i> and (b) <i>SHP</i> for NaYBFK considering the Box-Behnken design of Table 5.4 with confidence interval of 95 %.....	183
Fig. 5.7	Surface plots of (a) <i>COP</i> (Eq. (5.15)) and (b) <i>SHP</i> (Eq. (5.16)) as function of $T_{\text{HTF,hot}}$ and δ obtained for NaYBFK with $T_{\text{cond}} = 318.15$ K and $t_{\text{ADS+DES}} = 2250$ s.....	185
Fig. 5.8	Contour plots of (a) <i>COP</i> (Eq. (5.15)) and (b) <i>SHP</i> (Eq. (5.16)) obtained for NaYBFK as function of T_{cond} and $t_{\text{ADS+DES}}$, for fixed $T_{\text{HTF,hot}} = 448.15$ K and $\delta = 5 \times 10^{-3}$ m. Filled black circles to the specification requiring $COP \geq 1.40$ and the simultaneous maximization of <i>SHP</i> in all cycles; open white circles concern the requisite of $SHP \geq 400 \text{ W kg}^{-1}$ and the concomitant maximization of <i>COP</i> in all cycles.....	186
Fig. 5.9	Pairs of <i>SHP</i> and <i>COP</i> estimated using Eqs. (5.15)-(5.16) for $T_{\text{HTF,hot}} = 448.15$ K, δ and $t_{\text{ADS+DES}}$ in the range $5 \times 10^{-3} - 10 \times 10^{-3}$ m and 900 - 3600 s, respectively, and T_{cond} of (a) 308.15 K, (b) 318.15 K and (c) 328.15 K. Exemplified requisites of $COP \geq 1.40$ and $SHP \geq 400 \text{ W kg}^{-1}$ are marked. The $(\delta, t_{\text{ADS+DES}})$ pairs considered for the performance estimations at each T_{cond} are also shown, where the combinations that allow meeting the <i>COP</i> and <i>SHP</i> requisites are highlighted.....	189

Chapter 6: Computer simulation using OpenFOAM

Fig. 6.1	Schematic representation of the cylindrical AHEx studied in this work, along with the computational domain (2D) and mesh considered in the CFD simulations.....	225
----------	---	-----

Fig. 6.2	Directory structure for an OpenFOAM application: (a) generically denoted by <i>newApp</i> ; and (b) developed in this work, designated by <i>customizedSolver</i> . (c) Simplified flowchart of the <i>customizedSolver</i> application.....	233
Fig. 6.3	Directory structure of OpenFOAM cases: (a) general; (b) adopted in this work to simulate the four stages of an adsorption heating cycle. The methodology followed to construct the cases and perform the simulations is outlined, along with the stopping criteria considered for each stage.	234
Fig. 6.4	Evolution of (a) T , (b) P and (c) W along time during the isobaric adsorption stage, for different positions in the cylindrical adsorbent bed reported by J. Pinheiro <i>et al.</i> . Dotted lines are the results obtained in OpenFOAM, and solid lines are those reported J. Pinheiro <i>et al.</i>	236
Fig. 6.5 -	Evolution of (a) T , (b) P and (c) W along the isosteric heating stage, for different positions in the adsorbent bed reported by J. Pinheiro <i>et al.</i> . Dotted lines are the results obtained in OpenFOAM, and solid lines are those reported in J. Pinheiro <i>et al.</i>	237
Fig. 6.6 -	Evolution of (a) T , (b) P and (c) W along time during the isobaric desorption stage, for different positions of the adsorbent reported by J. Pinheiro <i>et al.</i> . Dotted lines are the results obtained in OpenFOAM, and solid lines are those reported by J. Pinheiro <i>et al.</i>	238
Fig. 6.7	Evolution of (a) T , (b) P and (c) W along the isosteric cooling stage for different positions in the cylindrical adsorbent bed of J. Pinheiro <i>et al.</i> . Dotted lines are the results obtained in OpenFOAM, and solid lines are those reported by J. Pinheiro <i>et al.</i>	239
Fig. 6.8	Evolution of P , T and W along the isosteric heating stage in the CPO-27(Ni) coated copper foam, for $t_{\text{cycle}} \approx 600$ s.....	241
Fig. 6.9	Evolution of P , T and W fields along the isobaric desorption stage in the composite CPO-27(Ni) coating/copper foam, for $t_{\text{cycle}} \approx 600$ s.....	242
Fig. 6.10	Evolution of P , T and W in the CPO-27(Ni) coated copper foam along the isosteric cooling stage, for a cycle time of <i>ca.</i> 600 s.....	243
Fig. 6.11	Evolution of P , T and W along the isobaric adsorption stage in CPO-27(Ni) coated copper foam, for $t_{\text{cycle}} \approx 600$ s.....	244

Fig. 6.12	Average pressure (a), temperature (b) and adsorbate loading (c) along time in a bed of copper foam coated with CPO-27(Ni) and AQSOA™ FAM-Z02: t_{cycle} of 600 s (double lines) and 180 s (dashed lines); equilibrium values (ΔW_{eq}) (dotted lines).....	248
-----------	--	-----

Chapter 7: Prototype design

Fig. 7.1	Experimental setup of a hybrid system combining a heat pump module with a GWH.....	263
Fig. 7.2	Hybrid system for DHW production combining an AHP, a GWH, a water tank and a solar panel, and illustration of its three distinct operation modes.....	268
Fig. 7.3	(a) Mechanical vapor compression heat pump water heater (HPWH) from Bosch, and (b) adsorption-based system combining a heat pump module, a gas water heater (GWH), a tank for domestic hot water (DHW) production and a solar panel, and overall qualitative assessment of the two systems. Main challenges of the adsorbents for DHW production shown in a triangle: affordable, widely available and high performance adsorbents as key enablers for the development of efficient AHPs.....	271

Chapter 8: Final outlook and future work

Fig. 8.1	Infographic with general information regarding AHPs design, performance, optimization and challenges discussed along the thesis...	297
Fig. 8.2	(a) Draft of water adsorption isotherms at 333 K and 368 K of an adsorbent for AHPs intended to heat domestic water, and values of relative pressure (P/P^σ) of interest for the considered application; (b) Estimates of COP and SHP for $\Delta W_{\text{eq}} = 0.2 \text{ kg kg}^{-1}$ and $t_{\text{cycle}} = 600 \text{ s}$	299
Fig. 8.3	(a) Volumes required by sensible, latent and thermo-chemical storage systems to store the annual energy for an energy efficient house (6480 MJ). Adsorption thermal energy storage (TES): (b) closed-cycle, (c) open-cycle.....	300

List of Tables

Chapter 1: Motivation and thesis plan

Table 1.1	Titles of Chapters 2-7, and tags connected to the topics covered in each chapter.....	6
-----------	---	---

Chapter 2: Introduction

Table 2.1	Published patents regarding AHPs, where the patent number and the priority year are indicated, along with the patent scope and observations.....	43
-----------	--	----

Chapter 3: Adsorption heat pump based on ETS-10/water pair

Table 3.1	Mathematical model of the adsorption heating system investigated in this work.....	95
Table 3.2	Initial and boundary conditions of the model of the adsorption heating system investigated in this work.....	98
Table 3.3	Main features and properties necessary for the simulations.....	103
Table 3.4	Influence of the bed thickness (δ) on the performance of the adsorption heating system. The $\Delta\bar{W}_{\text{cycle}}$ and COP of the ideal cycle are also listed for comparison.....	112

Chapter 4: Comparison of different porous metal/metalloid oxides

Table 4.1	Mathematical model of the adsorption systems investigated in this work.....	133
Table 4.2	Initial and boundary conditions of the model of the adsorption heating systems investigated in this work.....	134

Table 4.3	Mathematical expressions of the water adsorption isotherms of ETS-10, zeolite 13X (obtained in this work), zeolite 4A and silica gel considered in the simulations, equations for the calculation of $Q_{\text{ads}} = Q_{\text{ads}}(W)$, and equations obtained in this work for the determination of D_{eff} of water on zeolite 13X, zeolite 4A and silica gel as a function of temperature and adsorbate loading. Clausius-Clapeyron model is also given.....	137
Table 4.4	Main properties of the adsorbents, operating conditions and adsorbent bed dimensions considered in the simulations.....	143
Table 4.5	Results obtained from the simulations for the different adsorbents. Performance values for ideal cycles are given for comparison.....	145
Table 4.6	Average value of K_{LDF} considered in the simulations for the operating conditions under study and corresponding results obtained from the simulations of zeolite 13X/water and zeolite 4A/water pairs.....	152

Chapter 5: Phenomenological modeling and statistical optimization

Table 5.1	Factors, levels and codification considered for the Box-Behnken design	175
Table 5.2	Dubinin-Astakhov (DA) isotherms of water vapor on 13XBFK, NaYBFK and 13XB, and expressions for the linear driving force (LDF) global mass transfer coefficient (K_{LDF}).....	177
Table 5.3	Main properties of the adsorbents, bed dimensions and operating conditions considered in the simulations.....	180
Table 5.4	Box-Behnken design matrix of four factors ($t_{\text{ADS+DES}}$, T_{cond} , $T_{\text{HTF,hot}}$, δ) and three levels, and results of <i>COP</i> and <i>SHP</i> for NaYBFK, 13XBFK and 13XB beds.....	182

Chapter 6: Computer simulation using OpenFOAM

Table 6.1	Mathematical model of the AHEx unit investigated in this work.....	227
Table 6.2	Boundary conditions (BCs) of the 2D model of the adsorption unit investigated in this work.....	228
Table 6.3	Equations to compute the heats involved in the four stages of the adsorption heating cycle, and those to calculate the mass of adsorbent (m_s), copper foam (m_{foam}) and copper tube (m_{tube}).....	230
Table 6.4	Main properties of CPO-27(Ni) and AQSOA™ FAM-Z02 coated copper foams, and operating parameters considered in the simulations of the adsorption heating cycle.....	240
Table 6.5	Values of cycle time (t_{cycle}), adsorbent-to-metal mass ratio (m_s/m_{copper}), $\Delta\bar{W}$, ΔW_{eq} , COP , SHP , $VSHP$, number of necessary AHEx tubes to achieve a power of 2000 W (N_{tubes}) and volume occupied by N_{tubes} ($V_{N_{\text{tubes}}}$), obtained for the copper foam composite bed using CPO-27(Ni) or AQSOA™ FAM-Z02.....	245

Chapter 1: Motivation and thesis plan

1.1. Motivation

Climate changes and scarcity of resources have been identified as global shifts that will reshape the world and influence the way that society lives and does business [1]. To mitigate these problems, the European Commission has been outlining strategies to decarbonize the energy system, aiming to reduce, until 2050, the greenhouse gas emissions by 80-95 % in relation to 1990, which implies far more energy efficiency and alternatives [2].

Regarding energy demands in Europe, almost 50 % of the final consumption is used for heating and cooling, and the building sector accounts for more than 35 % of the overall consumption, of which 75 % is for domestic hot water (DHW) production and space heating [3]. The study of technologies allying efficiency and cost effectiveness is pertinent in order to meet the market needs, and face the energy and environmental challenges of the society [4, 5].

Bosch Thermotechnology develops solutions for residential heating and DHW production, namely, electric and gas water heaters, gas boilers, and vapor compression heat pumps. Aligned with the need for mitigating the climate changes and the scarcity of natural resources (*e.g.*, fossil fuels as coal, crude oil and natural gas), and the mission of improving the thermal comfort and well-being of the customers, the company intends to develop clean and efficient technologies, which require less energy, have enhanced efficiency and reduced emissions of pollutant gases, and better acoustic features. R&D in fields such as renewable energies, energy efficiency, intelligent materials, and connectivity has been focused by the organization, in order to develop innovative and sustainable solutions for the domestic water heating sector.

Adsorption heat pumps (AHPs) have been increasingly investigated for heating/cooling purposes due to its eco-friendly features over vapor compression heat pumps (VCHPs). They are essentially composed by an evaporator (*evap*), a condenser (*cond*) an adsorbent heat exchanger (AHEx), and a set of valves (see Fig. 1.1, top), and their working principle

is schematically shown in Fig. 1.1. An initially dry adsorbent is connected to an evaporator filled with a refrigerant fluid (Fig. 1.1, left). During this process, heat at a low temperature (Q_{low}) is received from the environment (e.g., from air) enabling evaporation of the working fluid, which is then adsorbed by the adsorbent material of the bed. As adsorption is exothermic, heat is released to the surroundings at an intermediate temperature ($Q_{intermediate}$), which can be used for heating purposes like DHW production. When the refrigerant/adsorbent system approaches equilibrium, the solid regeneration is required (Fig. 1.1, right). Accordingly, heat is transferred to the adsorbent bed at relatively high temperature (Q_{high}) (for instance, waste heat) to desorb the working fluid, which is subsequently condensed, releasing heat at an intermediate temperature (useful heat, $Q_{intermediate}$) [6]. Basically, an AHP works at three temperature levels (Fig. 1.1, bottom): the heat released at an intermediate temperature ($Q_{intermediate}$) corresponds to the sum of the heats that are supplied at low and high temperature ($Q_{low} + Q_{high}$) [7]. A more detailed description of the adsorption cycles is given in Chapter 2.

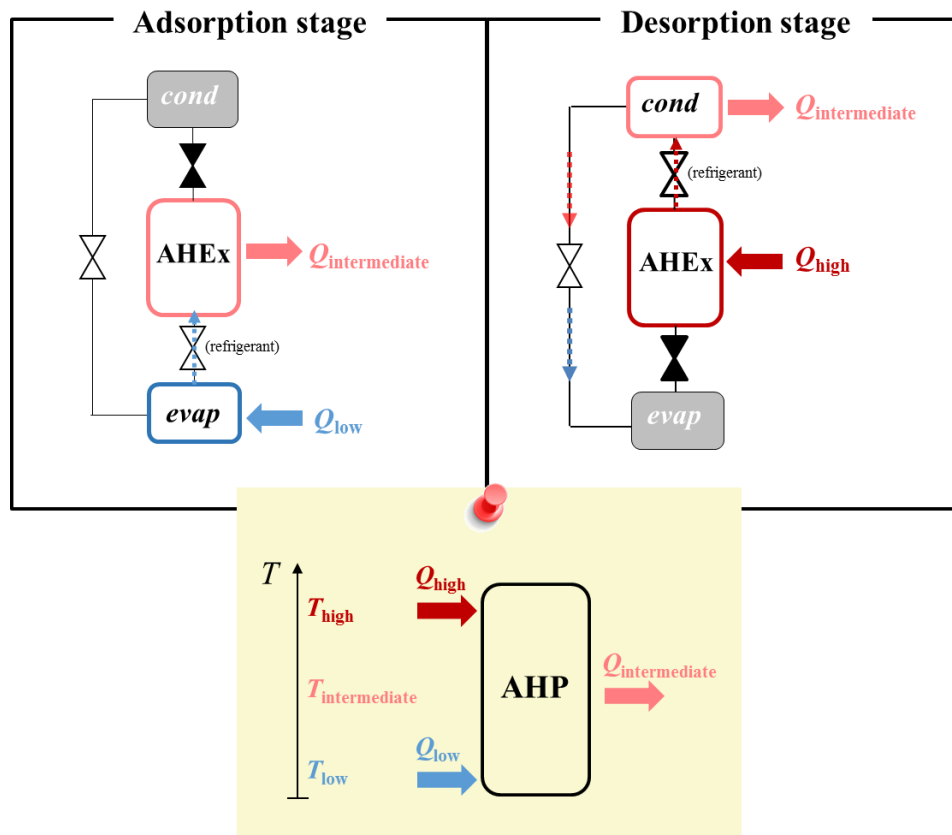


Fig. 1.1 – Components of a basic AHP, main working stages, and operating temperature levels (bottom).

Comparing with VCHPs, AHPs may use natural refrigerants (*e.g.*, water) instead of the nefarious fluorocarbon-based ones, may be powered by sources as solar energy or waste heat instead of electricity, and have neither noise nor vibration issues [5, 8-10]. The correct choice of the adsorbent for a given AHP application is a key factor for the efficiency and cost-effectiveness of the system [11, 12]. Activated carbons, silica gels, zeolites and zeotypes are among the materials employed so far. On the other hand, due to the complexity of the phenomena occurring simultaneously in AHPs, the use of modeling and simulation tools to determine key parameters of the process, predict dynamic and equilibrium performances, optimize operating conditions, and size the appliances, is essential.

CICECO-Aveiro Institute of Materials is an Associate Laboratory of recognized scientific merit, with internal competences in several fields, such as energy and industrial applications, sustainability and health, modeling and computational simulation, synthesis and characterization of materials for energy and environmental applications, etc. [13].

As a leading supplier of heating appliances and water heaters in Europe, and manufacturer of a diversified set of products for the entire world, Bosch Thermotechnology is uniquely positioned to meet the market needs and the emerging energetic and environmental challenges. On the other hand, CICECO-Aveiro Institute of Materials was identified as a strong partner to carry out this work, due to the set of reputed internal competences, and the proximity to the facilities of Bosch Thermotechnology. In the whole, this partnership reflects the commitment of the two organizations in walking together towards the development of cleaner and efficient solutions for the future, with special focus on DHW production.

1.2. Thesis plan

The thesis is divided in eight chapters. A brief description of the remaining seven chapters follows, and a reader-friendly guide to chapters 2-7, showing tags for each one, is furnished in Table 1.1.

Chapter 2 presents a review of the state-of-the-art in AHPs for heating purposes, and corresponds to the manuscript entitled *Adsorption heat pumps for heating applications*

[14]. Following a lead-in to fundamental aspects of operation, design and performance, the AHPs of small capacity available in the market are presented, and comparisons with conventional heating technologies are provided. Important achievements, trends and gaps of the R&D in this field are identified.

Chapter 3 regards the study of ETS-10 (Engelhard Titanosilicate number 10) as water adsorbent for AHPs, and includes the measurement of equilibrium and kinetic properties of the ETS-10/water pair, along with modeling and simulation, aiming the prediction of the AHPs heating performance. It is based on the article entitled *Application of the novel ETS-10/water pair in cyclic adsorption heating processes: Measurement of equilibrium and kinetics properties and simulation studies* [15].

Chapter 4 covers a comparison of performances of well-known porous metal/metalloid oxide adsorbents and the less explored ETS-10 for water AHPs, aided by phenomenological modeling and simulation. Sensitivity studies are presented, and the impact of several model simplifications while ensuring comparable performance results is discussed. This chapter corresponds to the article entitled *Analysis of equilibrium and kinetic parameters of water adsorption heating systems for different porous metal/metalloid oxide adsorbents* [16].

Chapter 5 contemplates two distinct parts. Firstly, a comparison of the performance of several commercial zeolites, with and without binder in its formulation, for water AHPs is presented. Secondly, the huge potential of statistical tools, such as design of experiments (DoE) and response surface methodology (RSM), to efficiently optimize operating and geometric parameters of AHPs is demonstrated. This chapter is based on the article entitled *Adsorption heat pump optimization by experimental design and response surface methodology* [17].

In **Chapter 6**, the potential of emergent adsorbents such as metal-organic framework (MOF) CPO-27(Ni) over benchmark materials for AHPs is investigated through phenomenological modeling and CFD simulations, considering metal foams coated with the adsorbents. A customized solver and methodology to simulate adsorption cycles developed in OpenFOAM is reported. This work corresponds to the manuscript entitled *Copper foam coated with CPO-27(Ni) metal-organic framework for adsorption heat pump: simulation study using OpenFOAM* [18].







Chapter 1: Motivation and thesis plan

A setup of a hybrid system combining an AHP and a gas water heater (GWH) that may be assembled in Bosch Thermotechnology to perform functional tests and measure the performances of several adsorbents was designed, being presented in **Chapter 7**, along with the derived experimental procedure. Technical specifications of main components and cost estimations of the prototype are provided. This chapter ends with a draft of an adsorption appliance for domestic water heating, which is compared to the actual Bosch heat pump water heater (HPWH), and general techno-economic challenges are discussed.

Finally, **Chapter 8** collects major conclusions of the thesis, along with some suggestions of future work.

Chapter 1: Motivation and thesis plan

Table 1.1 – Titles of Chapters 2-7, and tags connected to the topics covered in each chapter.

	Chapter	Title	Tags
<p>Literature overview</p> 	2	Introduction	#adsorption heat pump (AHP); #state-of-the-art; #technology progress; #AHP performance; #working pair; #operating conditions; #cycle features; #adsorbent form; #heat exchanger; #articles; #patents; #commercial AHPs
<p>Experiments, modeling, and simulation</p> 	3	Adsorption heat pump based on ETS-10/water pair	#ETS-10 characterization; #experiment; #isotherm; #adsorption kinetics; #thermophysical data; #modeling; #simulation; #dedicated programming; #AHP performance; #sensitivity analysis
<p>Modeling and simulation</p> 	4	Comparison of different porous metal/metalloid oxides	#zeolite 13X; #zeolite 4A; #silica gel; #ETS-10; #modeling; #simulation; #computational efforts; #model approximations; #AHP performance; #sensitivity analysis
<p>AHP optimization</p> 	5	Phenomenological modeling and statistical optimization	#zeolite 13X; #zeolite NaY; #binder effect; # modeling; #simulation; #AHP performance; #DoE/RSM; #efficient optimization; #optimal operation/design; #gaining R&D insights; #advanced control strategies
<p>OpenFOAM simulation</p> 	6	Computer simulation using OpenFOAM	#MOF CPO-27(Ni); #benchmark; #copper foam; #adsorbent coating; #modeling; #OpenFOAM simulation; #solver development; #AHP performance
<p>Prototyping</p> 	7	Prototype design	#experimental setup; #protocol; #hybrid concept; #AHP-GWH; #technical specifications; #suppliers proposals; #cost estimation; #AHP product concept; #Bosch HPWH; #benchmark; #challenges

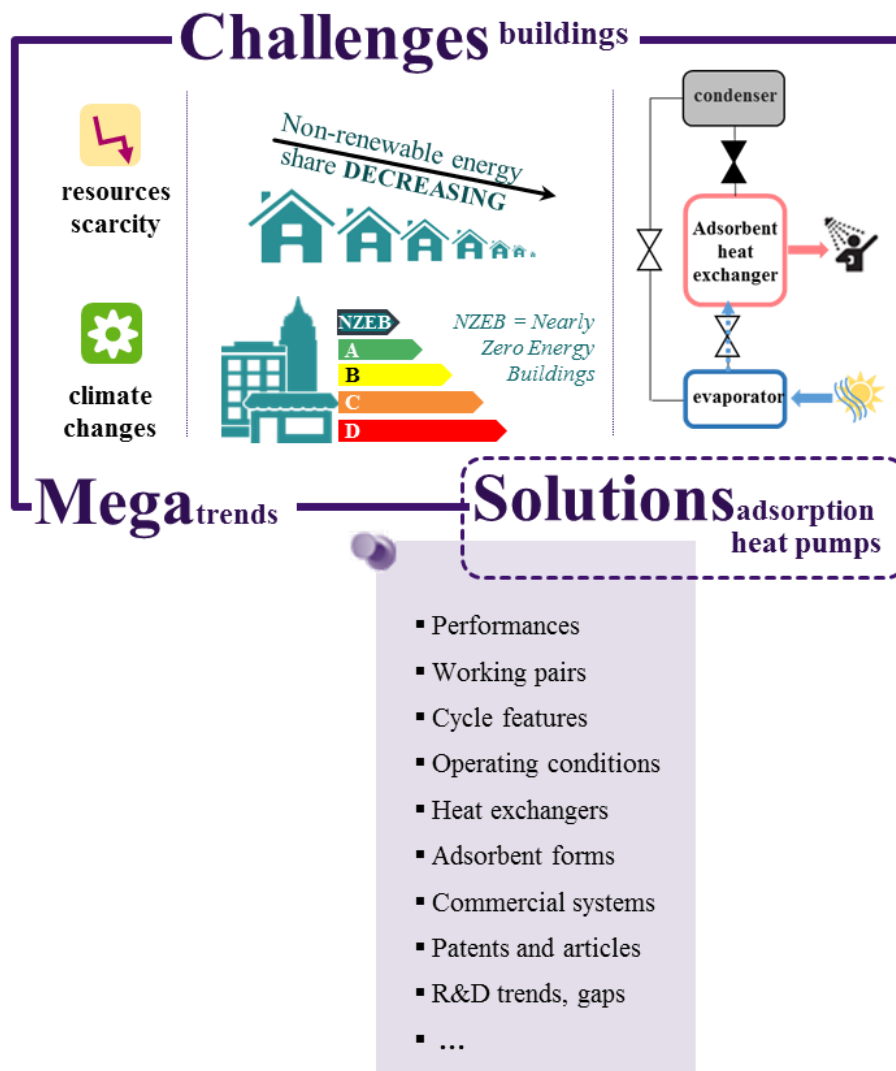
References

- [1] PricewaterhouseCoopers (PwC) UK - Megatrends, <https://www.pwc.co.uk/issues/megatrends.html>, (accessed in 12.09.2017).
- [2] European Commission - Energy roadmap 2050, https://ec.europa.eu/energy/sites/ener/files/documents/2012_energy_roadmap_2050_en_0.pdf, (accessed in 12.09.2017).
- [3] B. Mette, H. Kerskes, H. Drück, H. Müller-Steinhagen, Experimental and numerical investigations on the water vapor adsorption isotherms and kinetics of binderless zeolite 13X, *International Journal of Heat and Mass Transfer*, 71 (2014) 555-561.
- [4] S. Narayanan, S. Yang, H. Kim, E.N. Wang, Optimization of adsorption processes for climate control and thermal energy storage, *International Journal of Heat and Mass Transfer*, 77 (2014) 288-300.
- [5] B. Dawoud, On the development of an innovative gas-fired heating appliance based on a zeolite-water adsorption heat pump; system description and seasonal gas utilization efficiency, *Applied Thermal Engineering*, 72 (2014) 323-330.
- [6] M.F. de Lange, K.J.F.M. Verouden, T.J.H. Vlucht, J. Gascon, F. Kapteijn, Adsorption-Driven Heat Pumps: The Potential of Metal–Organic Frameworks, *Chemical Reviews*, 115 (2015) 12205-12250.
- [7] A. Kühn, F. Ziegler, Cycle basics of thermally driven heat pumps in: A. Kühn (ed.) *Thermally driven heat pumps for heating and cooling*, Universitätsverlag der TU Berlin, Berlin, 2013.
- [8] F. Ziegler, State of the art in sorption heat pumping and cooling technologies, *International Journal of Refrigeration*, 25 (2002) 450-459.
- [9] F. Meunier, Adsorption heat powered heat pumps, *Applied Thermal Engineering*, 61 (2013) 830-836.
- [10] H. Demir, M. Mobedi, S. Ülkü, A review on adsorption heat pump: Problems and solutions, *Renewable and Sustainable Energy Reviews*, 12 (2008) 2381-2403.
- [11] Y.I. Aristov, Challenging offers of material science for adsorption heat transformation: A review, *Applied Thermal Engineering*, 50 (2013) 1610-1618.
- [12] S.K. Henninger, S.-J. Ernst, L. Gordeeva, P. Bendix, D. Fröhlich, A.D. Grekova, L. Bonaccorsi, Y. Aristov, J. Jaenchen, New materials for adsorption heat transformation and storage, *Renewable Energy*, 110 (2017) 59-68.
- [13] CICECO - Aveiro Institute of Materials: research structure, <http://www.ciceco.ua.pt/index.php?menu=204&language=eng&tabela=geral> (accessed in 13.06.2018).
- [14] J.M. Pinheiro, S. Salústio, A.A. Valente, C.M. Silva, Adsorption heat pumps for heating applications, *Renewable and Sustainable Energy Reviews*, *Submitted* (2018).
- [15] J.M. Pinheiro, A.A. Valente, S. Salústio, N. Ferreira, J. Rocha, C.M. Silva, Application of the novel ETS-10/water pair in cyclic adsorption heating processes: Measurement of equilibrium and kinetics properties and simulation studies, *Applied Thermal Engineering*, 87 (2015) 412-423.
- [16] J.M. Pinheiro, S. Salústio, J. Rocha, A.A. Valente, C.M. Silva, Analysis of equilibrium and kinetic parameters of water adsorption heating systems for different porous metal/metalloid oxide adsorbents, *Applied Thermal Engineering*, 100 (2016) 215-226.

- [17] J.M. Pinheiro, S. Salústio, A.A. Valente, C.M. Silva, Adsorption heat pump optimization by experimental design and response surface methodology, *Applied Thermal Engineering*, 138 (2018) 849-860.
- [18] J.M. Pinheiro, S. Salústio, V. Geraldes, A.A. Valente, C.M. Silva, Copper foam coated with CPO-27(Ni) metal-organic framework for adsorption heat pump: simulation study using OpenFOAM, *Applied Thermal Engineering*, *Submitted* (2018).

Chapter 2: Introduction[†]

The state-of-the-art in adsorption heat pumps (AHPs) for heating applications is presented in the following. Crucial aspects like operating conditions, working pairs, performances, adsorbent bed forms, adsorbent heat exchanger geometries and cycle features are discussed. A comparison of AHPs with conventional heating technologies is provided, and commercial small capacity adsorption heating appliances are presented. Important achievements, gaps and trends of the R&D in this field are discussed.



[†] Based on:

Joana M. Pinheiro, Sérgio Salústio, João Rocha, Anabela A. Valente, Carlos M. Silva, Adsorption heat pumps for heating applications (*submitted*).

2.1. Contextualization

Rapid urbanization, shifts in the global economic power, demographic and social changes, technological breakthroughs, climate changes and scarcity of resources have been identified as global driving forces that will reshape the world and influence the way that society lives and does business [1]. To mitigate the climate alterations and resources shortage, governmental institutions have been developing and implementing policies aligned with energetic and environmental issues. The European Commission has been outlining a strategy to decarbonize the energy system, aiming at the reduction of greenhouse gas emissions by 80-95 % from 1990 until 2050, which implies far more energy efficiency: for instance, *ca.* two thirds of the energy should come from renewable sources, and electricity production needs to be almost emission-free, regardless of the higher energy demand [2]. In the particular case of the energy demands in the EU-28 residential sector, heating applications such as space heating and domestic hot water (DHW) production accounted for almost 80 % of the final energy consumption in 2015 [3] (Fig. 2.1(a)), where the energy sources were mainly gas and renewables for space heating, and gas and electricity for DHW (Fig. 2.1(b)) [4]. Given the increasing prices of electricity and natural gas for household consumers (Fig. 2.1(c)) [5, 6], it is important to develop technologies able to convert inexpensive environmental energy into useful heat, lowering the thermal comfort expenses, while simultaneously mitigating the worldwide environmental and energy impacts.

Among the heating technologies meeting the market requirements are vapor-compression systems (VCS). However, VCS are powered by electricity (which is still produced to a great extent from non-renewable sources such as coal and oil (*ca.* 48 % of the net electricity generated in the EU-28 in 2015 [7]), use nefarious fluorocarbon type refrigerants (with global warming potential (GWP) and/or ozone depletion potential (ODP)), and present noise and vibration drawbacks [8, 9]. Adsorption-based technology has been receiving increasing attention due to its eco-friendly characteristics over VCS [10-12]. Adsorption heat pumps (AHPs) may be powered by thermal energy sources like solar energy or waste heat instead of electricity, may use benign refrigerants such as water, and have no noise or vibration problems. In addition, adsorption-based thermal compressors require low maintenance in relation to conventional mechanical compressors due to the absence of moving parts for the circulation of the working fluid [9, 13, 14].

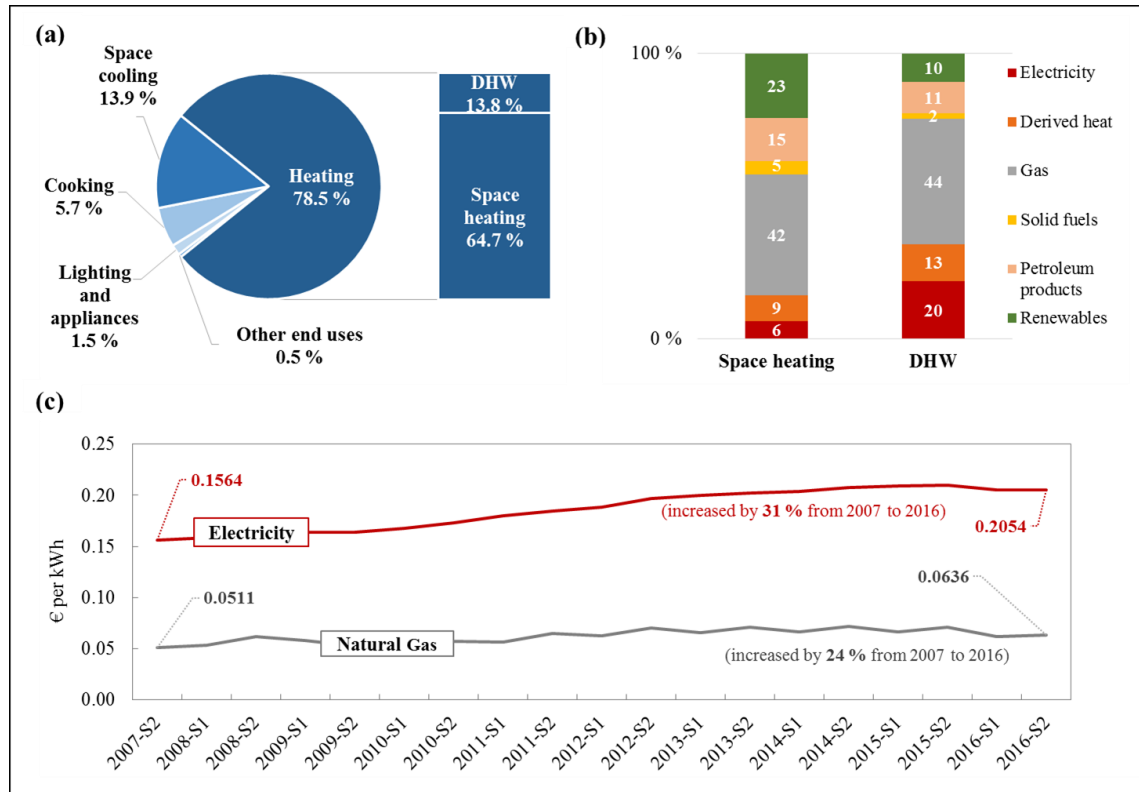


Fig. 2.1 – (a) Final energy consumption in the EU-28 residential sector by type of end use in 2015 (adapted from [3]). (b) Share of fuels in the final energy consumption for space heating and DHW production in the EU-28 residential sector in 2015 (values in %) (adapted from [4]). (c) Evolution of electricity and natural gas prices for household consumers in EU-28 from the second semester (S2) of 2007 (2007-S2) to the second semester of 2016 (2016-S2) (all taxes and levies included) (adapted from [5, 6]).

Despite the potential of AHPs to ally energetic and environmental sustainability with the heating market needs, there are few literature reviews regarding adsorption-based heating [9, 12, 15, 16]. Instead, several reviews focused on cooling applications [17-27]. This literature review presents the state-of-the-art in AHPs for heating purposes. Following a lead-in to fundamental aspects of operation and performance (*e.g.*, adopted working pairs, operating conditions, cycle features, adsorbent bed configurations and heat exchanger geometries), key cases (*e.g.*, AHPs available in the market) and comparisons of AHPs vs. conventional heating technologies are presented. The literature data of these complex systems is systemized in different perspectives (employing tables and graphical means to integrate different studies), aiming to identify important achievements, trends and gaps of the R&D in this field.

2.2. Working principles and performance indicators of adsorption heat pumps (AHPs)

2.2.1. Working principles

The working principles of AHPs may be understood using a relatively simple case of a single-bed unit, which encompasses an adsorbent heat exchanger (AHEx), a condenser, an evaporator and a set of valves, including an expansion device (V). As shown in Fig. 2.2(a)-(d), the adsorption heating cycle comprehends four stages, namely the isobaric adsorption (1→2), isosteric heating (2→3), isobaric desorption (3→4), and isosteric cooling (4→1) [9, 13, 28]. Fig. 2.2(e) shows an ideal cycle, and Figs. 2.2(f)-(h) exemplify how pressure (P), temperature (T) and adsorbate loading (W) may vary with time (t) throughout four consecutive cycles [13, 29].

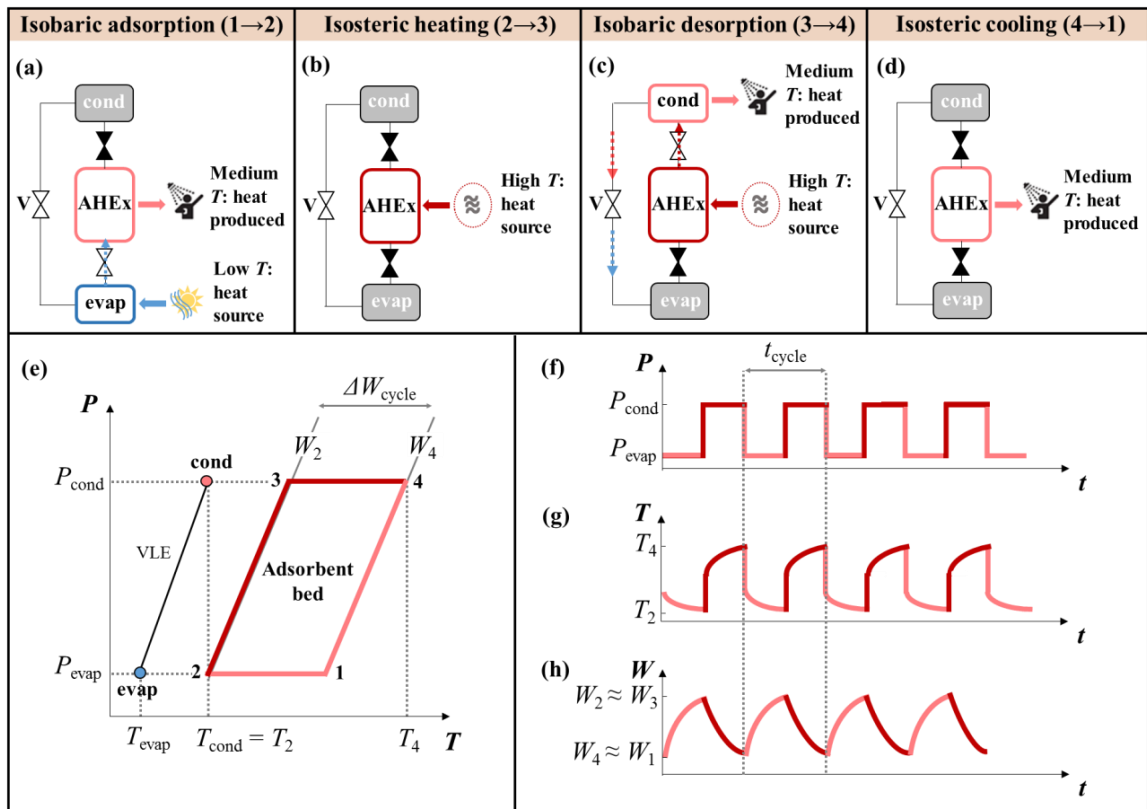


Fig. 2.2 – (a)-(d) Simplified representation of a basic AHP involving four stages of an adsorption heating cycle ((a) isobaric adsorption (1→2), (b) isosteric heating (2→3), (c) isobaric desorption (3→4), and (d) isosteric cooling (4→1)), where *evap*, *cond*, *AHEx*, *V* and *T* denote, respectively, the evaporator, condenser, adsorbent heat exchanger containing the adsorbent bed, expansion valve and temperature. (e) An ideal adsorption cycle (P vs. T), where VLE is vapor-liquid equilibrium. (f)-(h) Profiles of bed pressure (P), temperature (T) and adsorbate loading (W) for four consecutive heating cycles.

Each cycle operates as follows. In the isobaric adsorption (1→2, Fig. 2.2(a) and (e)), the bed is connected to the evaporator, that receives heat from the environment. As the bed temperature decreases, vapor is adsorbed on the porous adsorbent (increasing W from W_1 to W_2 (Fig. 2.2(h)), and heat is released from the system, which can be used for heating applications. This stage may last until the maximum (equilibrium) concentration in the adsorbent is reached at pressure P_{evap} . However, in practice, this is likely not the case, and the stage may be interrupted when the temperature difference between the adsorbent bed and the heat transfer fluid (HTF) are no longer satisfactory [30]. Subsequently, the bed is isolated and heated during the isosteric heating stage (2→3, Fig. 2.2(b)), and the pressure of the bed increases (from P_{evap} to P_{cond} , Fig. 2.2(e)) because part of adsorbate is desorbed. When P_{cond} is reached, the adsorbent bed is opened to the condenser and the isobaric desorption (3→4) begins (Fig. 2.2(c)). Heat supply is required for this stage in order to promote the regeneration of the adsorbent. As the bed temperature increases (from T_3 to T_4), the adsorbate is desorbed (W decreases from W_3 to W_4) and subsequently condenses inside the condenser, releasing latent heat that may be used for heating purposes. Finally, the bed is isolated and cooled in the isosteric cooling stage (4→1, Fig. 2.2(d)), which is accompanied by pressure decrease (from P_{cond} to P_{evap}) because a fraction of the vapor is adsorbed; mainly sensible heat is released which may be recovered for heating purposes. When the bed pressure reaches P_{evap} , a new cycle is initialized by reopening the adsorbent bed to the evaporator [9, 13, 31]. The evaporator and condenser work under vapor-liquid equilibrium (VLE) conditions, in which pressure and temperature are influenced by the inlet temperature and flow rate of the HTFs used in these heat exchangers.

In a practical perspective, each cycle of an AHP may be considered as a two-stage process where heat is supplied to the bed (stage involving isosteric heating and isobaric desorption), or heat is released from the bed (stage involving isosteric cooling and isobaric adsorption). The startup of AHP units commonly coincides with the beginning of the isosteric heating step (point 2 in Fig. 2.2(e)) [10].

In each cycle, heat is pumped in and out of the AHP unit, as represented in Fig. 2.2(a)-(d) using arrows of three different colors, which represent the three distinct temperature levels of operation of AHPs. While the heat for evaporation is supplied at a low temperature level, the regeneration of the adsorbent bed requires a high temperature heating source, and, on the other hand, the useful heat is released at an intermediate temperature level. The sum

of the heats supplied at low and high temperatures (for the evaporation, and bed heating and regeneration, respectively) corresponds to the released heat at an intermediate T level (by the condenser, and by the bed during the isosteric cooling and isobaric adsorption) [32]. The broader the temperature range of the cycle ($\Delta T_{\text{cycle}} = T_4 - T_2$), the greater the ΔW_{cycle} , and hence the more significant the heat transfer effect is (more heat is transferred from the evaporator to the condenser) [33].

2.2.2. Performance indicators

The performance of a basic AHP is commonly evaluated by means of the coefficient of performance (COP) and the specific heating power (SHP), which may be calculated as follows:

$$COP = \frac{|Q_{1 \rightarrow 2} + Q_{\text{cond}} + Q_{4 \rightarrow 1}|}{Q_{2 \rightarrow 3} + Q_{3 \rightarrow 4}} \quad (2.1)$$

$$SHP = \frac{|Q_{1 \rightarrow 2} + Q_{\text{cond}} + Q_{4 \rightarrow 1}|}{m_{\text{ads}} t_{\text{cycle}}} \quad (2.2)$$

where $Q_{1 \rightarrow 2}$, $Q_{4 \rightarrow 1}$ and Q_{cond} are, respectively, the heats released by the adsorbent bed during the adsorption and isosteric cooling stages, and by the condenser during the desorption stage; $Q_{2 \rightarrow 3}$ and $Q_{3 \rightarrow 4}$ are, respectively, the heats supplied to the adsorbent bed during the isosteric heating and desorption stages; m_{ads} and t_{cycle} are, respectively, the mass of adsorbent and the cycle time. The coefficient of performance for heating may be estimated knowing the coefficient of performance for cooling mode (COP_{cool}) as $COP \approx 1 + COP_{\text{cool}}$ [32]. The main contribution for $COP > 1$ is provided by the heat generated in the condenser (Q_{cond}), which is favored by enhancing ΔW_{cycle} (theoretically, $|Q_{1 \rightarrow 2} + Q_{4 \rightarrow 1}| \approx (Q_{2 \rightarrow 3} + Q_{3 \rightarrow 4})$) [8].

The SHP has a direct impact on the dimensions of the appliances and its enhancement is very important for the miniaturization of AHPs. Wittstadt *et al.* [34] adopted the definition

of volume specific heating power (*VSHP*) that is calculated by dividing the heating power by the total volume of the AHEx module instead of m_{ads} .

As recently reported by Cabeza and Schossig [35], the careful evaluation of the performance of AHPs for real applications requires the clear definition of key performance indicators (KPIs). For example, the primary energy ratio (*PER*) is the ratio of the total useful energy (Q_{useful}) to the total primary energy inputs, and allows the comparison of efficiencies of systems that use different energy sources (like electricity, gas) [36]. *PER* may be calculated as follows:

$$PER = \frac{Q_{useful}}{Ff_{p,fuel} + Ef_{p,elect}} \quad (2.3)$$

where F is the fuel energy input (gross calorific value), E is the electrical energy input and $f_{p,fuel}$ and $f_{p,elect}$ are the primary energy conversion factors for fuel and electricity, respectively (e.g., according to Italian regulations, $f_{p,fuel} = 1$ and $f_{p,elect} = 2.18$ [36]). Since the electrical energy required by AHPs may be neglected, a thermal *COP* is usually calculated discarding this contribution (Eq. (2.1)) [32].

2.2.3. Impact of the operating conditions on the performance of AHPs

The operating conditions, such as the minimum bed temperature (T_2 in Fig. 2.2(e)), the temperatures of condensation (T_{cond}), evaporation (T_{evap}), and bed regeneration (T_4), impact strongly on the performance of AHPs [37-39]. The T_{cond} and T_2 are dependent on the temperature of the useful heat required, and should be preferably similar in order to deliver the heat (from the condenser and the bed during the adsorption stage) to the user at a similar T level [16, 40, 41]. The T_{evap} depends on the environmental heat source (for instance, air, solar, geothermal) temperature ($T_{heat\ source}^{low}$), and is constrained by the vapor-liquid equilibrium of the refrigerant used (see discussion regarding water in Section 2.3.3). On the other hand, T_4 partly depends on the thermal stability of the working pairs, and the heat source temperature available for regeneration of the adsorbent ($T_{heat\ source}^{high}$). The $T_{heat\ source}^{high}$

may be constrained by the maximum allowable pressure in heating circuits for domestic applications (in Europe, it is 3×10^5 Pa [42]), the type and cost of the HTF (water, thermal oils, etc.), and durability issues (*e.g.*, using DHW as HTF may require T_4 below certain limits in order to minimize limescale formation).

Fig. 2.3 exemplifies how $T_{\text{cond}} (\cong T_2)$, T_{evap} , and T_4 may affect the adsorption heating cycle (considering type I adsorption isotherm, which is characteristic of water vapor and microporous adsorbents such as zeolites X and Y, and has been widely used for studying AHPs since the 1980s [43, 44]).

Influence of condenser and minimum bed temperatures (T_{cond}, T_2). Increasing the condenser and minimum bed temperatures (T_{cond}, T_2) constrains both adsorption and desorption stages. Specifically, from Fig. 2.3(a), increasing T_{cond} from $T_{\text{cond},1} (= T_{2,1})$ to $T_{\text{cond},3} (= T_{2,3})$, at constant T_{evap} and T_4 , leads to decrease in ΔW_{eq} from $\Delta W_{\text{eq},1}$ to $\Delta W_{\text{eq},3}$ ($W_{\text{eq}}(T_{2,1}, P_{\text{evap}}) > W_{\text{eq}}(T_{2,3}, P_{\text{evap}})$ and $W_{\text{eq}}(T_4, P_{\text{cond},1}) < W_{\text{eq}}(T_4, P_{\text{cond},3})$). The adsorption cycles become progressively narrower as $T_{\text{cond}} (= T_2)$ increases from $T_{\text{cond},1} (= T_{2,1})$ to $T_{\text{cond},3} (= T_{2,3})$ (Fig. 2.3(d)), leading to gradual drop in AHP performance. This effect occurs when performing successive cycles for producing domestic hot water (DHW), for example, from ambient temperature up to a set point value defined by the user. Fig. 2.4(a)–(b) schematically shows an AHP combined with a DHW tank, operating during the isobaric adsorption and isobaric desorption stages, respectively, and Fig. 2.4(c)–(e) shows the bed P , T and W vs. time profiles for three consecutive heating cycles in which T_2 gradually increases from $T_{2,1}$ to $T_{2,3}$ and P_{cond} from $P_{\text{cond},1}$ to $P_{\text{cond},3}$. In the isobaric adsorption stage of the first cycle, while the adsorbent is retaining the vapor coming from the evaporator, the cold domestic water circulates through the bed and promotes the adsorbent cooling up to $T_{2,1}$ (Fig. 2.4(a), (d)). During the isobaric desorption stage (Fig. 2.4(b)), the condensation pressure is imposed by the temperature of the DHW at the condenser inlet, which is heated by removing the heat of condenser. While the adsorbent at pressure $P_{\text{cond},1}$ is heated up to T_4 and regenerated (Fig. 2.4(c)–(e)), the condensation of the (desorbed) adsorbate inside condenser releases latent heat.

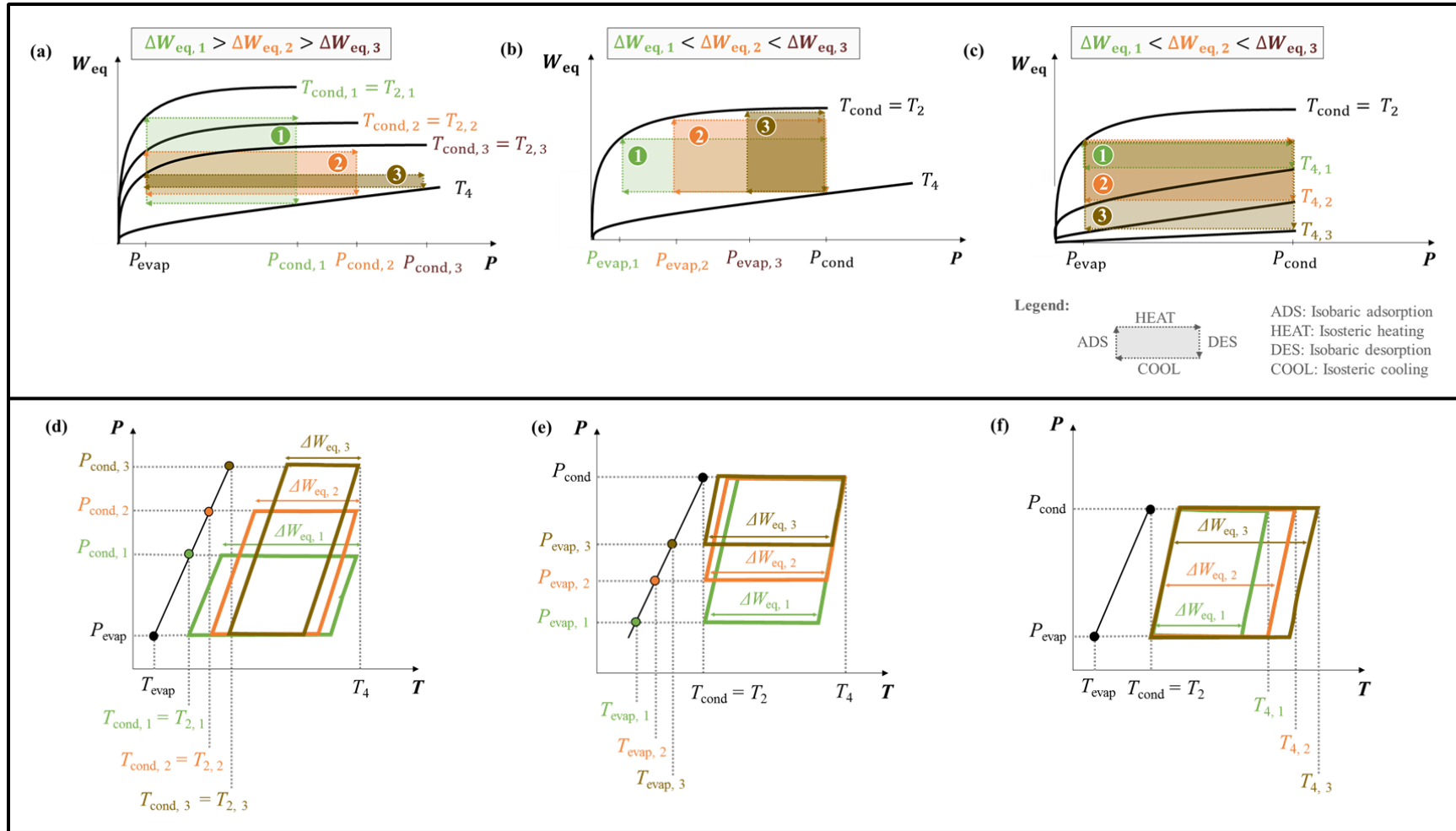


Fig. 2.3 – Impact of increasing: (a, d) T_{cond} ($= T_2$) from $T_{cond,1}$ ($= T_{2,1}$) to $T_{cond,3}$ ($= T_{2,3}$); (b, e) P_{evap} (directly related to T_{evap}) from $P_{evap,1}$ to $P_{evap,3}$; and (c, f) T_4 from $T_{4,1}$ to $T_{4,3}$, using (a, b, c) type I isotherms and (d, e, f) ideal P vs. T plots. ΔW_{eq} is the cyclic adsorption capacity in equilibrium conditions. The equilibrium adsorption cycles are represented by colored rectangles (case 1: green; case 2: orange; case 3: brown). Nomenclature in accordance with Fig. 2.2(e).

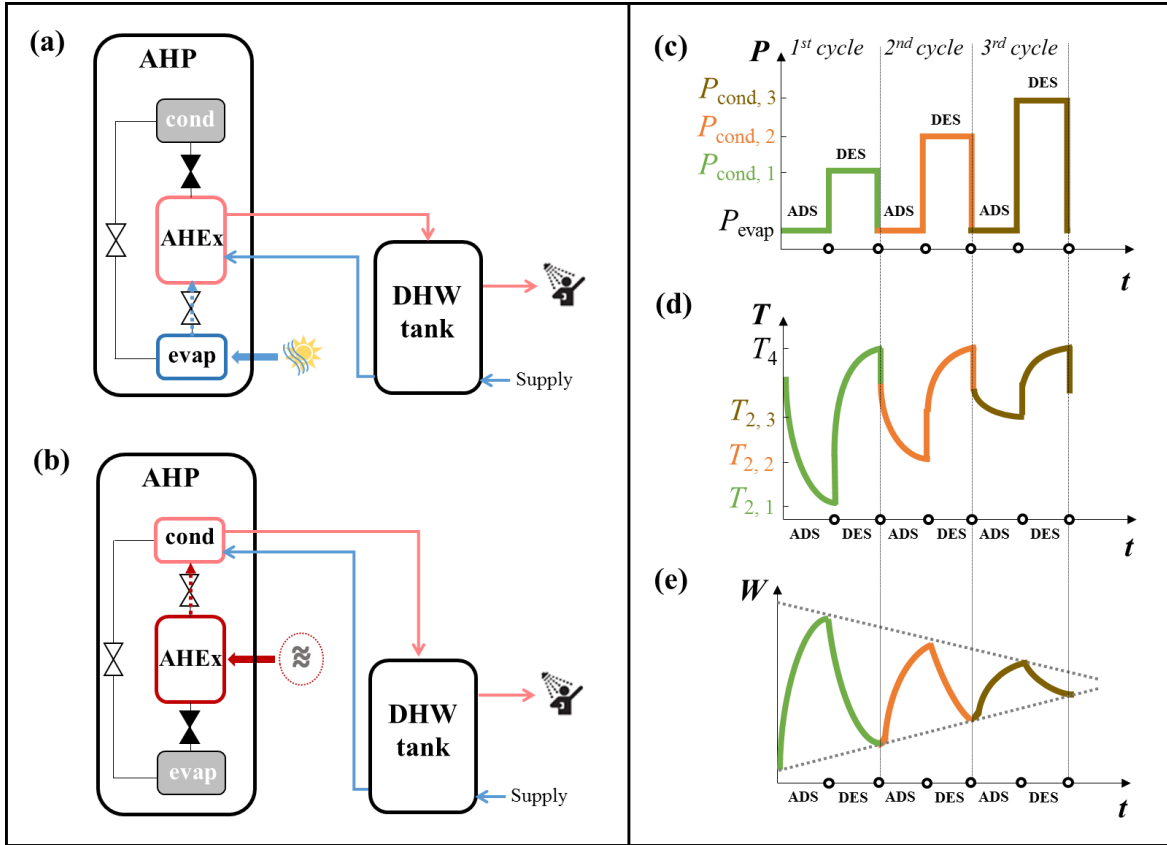


Fig. 2.4 – Scheme of an AHP combined with a domestic hot water (DHW) tank, operating during (a) isobaric adsorption (ADS) and (b) isobaric desorption (DES). Impact of increasing the condensation and minimum bed temperatures (T_{cond} , T_2) along three consecutive adsorption heating cycles: (c) P , (d) T , and (e) W along time in the adsorbent bed. Nomenclature in accordance with Fig. 2.3.

At the end of the first cycle, the water in the tank is hotter than in the beginning. Accordingly, in the isobaric adsorption stage of the second cycle, the bed is cooled to a smaller extent than in the first cycle (only up to $T_{2,2}$), causing lower adsorbate loading. In the isobaric desorption of the second cycle, the domestic water circulating through the condenser is hotter than in the first cycle, and consequently, this stage occurs at higher pressure $P_{\text{cond},2}$, which constrains the adsorbent regeneration. Overall, as the water in the tank becomes hotter, P_{cond} and T_2 increase, which is accompanied by decreasing ΔW along the cycles. Consequently, the heat pumping efficiency gradually degrades.

Influence of evaporation and bed regeneration temperatures (T_{evap} , T_4). The evaporation temperature (T_{evap}) is associated with P_{evap} . From Fig. 2.3(b), increasing P_{evap} from $P_{\text{evap},1}$ to $P_{\text{evap},3}$, at constant $T_{\text{cond}} (= T_2)$ and T_4 , enhances ΔW_{eq} as a result of a higher W_{eq}

achieved at the end of the adsorption stage (Fig. 2.3(b) and (e)). Increasing T_4 improves the adsorbent regeneration and increases ΔW_{eq} (from $\Delta W_{eq,1}$ at $T_{4,1}$ to $\Delta W_{eq,3}$ at $T_{4,3}$ (Fig. 2.3(c) and (f)).

2.3. Design and operation of AHPs

Several studies regarding the design and operation of AHPs have been reported in the literature. Details regarding the work domain, adsorbent/refrigerant fluid pairs, operating conditions, cycle features, adsorbent configurations, adsorbent heat exchanger (AHEx) geometries, and performance indicators are given in Table A2.1 (Annex A2). Nearly 50 % of the research studies are theoretical, *i.e.*, AHP performance is evaluated *via* modeling and simulation. Some studies are based on experimental work, *i.e.*, involving AHP setups/prototypes, and others combine theoretical and experimental approaches (*ca.* 22 % and 28 % of the total reports, respectively).

2.3.1. Heating performances based on COP and SHP

It is interesting to analyze the range of *COP* and *SHP* values reported in the literature for adsorption heating applications over the past decades. Figs. 2.5 and 2.6 show this evolution, distinguishing (with different colors/symbols) the working pairs, cycle features and work domain for the various case studies (the highest performance values from Table A2.1 have been selected). The *COPs* for commercial AHPs are in the range 1.40-1.60 using silica gel/water, or 1.30-1.50 using zeolite/water [33]. A minimum *COP* of 1.50 was recommended for competitiveness of gas-driven AHPs in the space heating market [45]. Consistently, Freni *et al.* [46] reported recently that $COP > 1.55$ is reasonable for heat pumping. The referred *COP* values serve as references in Fig. 2.5. On the other hand, the minimum *SHP* for cost competitiveness of AHPs is *ca.* 1000 W kg⁻¹ [47], and an interesting benchmark case is the adsorbent coating technology from Viessmann AHP, for which $SHP = 1600$ W kg⁻¹ [10]. These *SHP* values serve as references in Fig. 2.6.

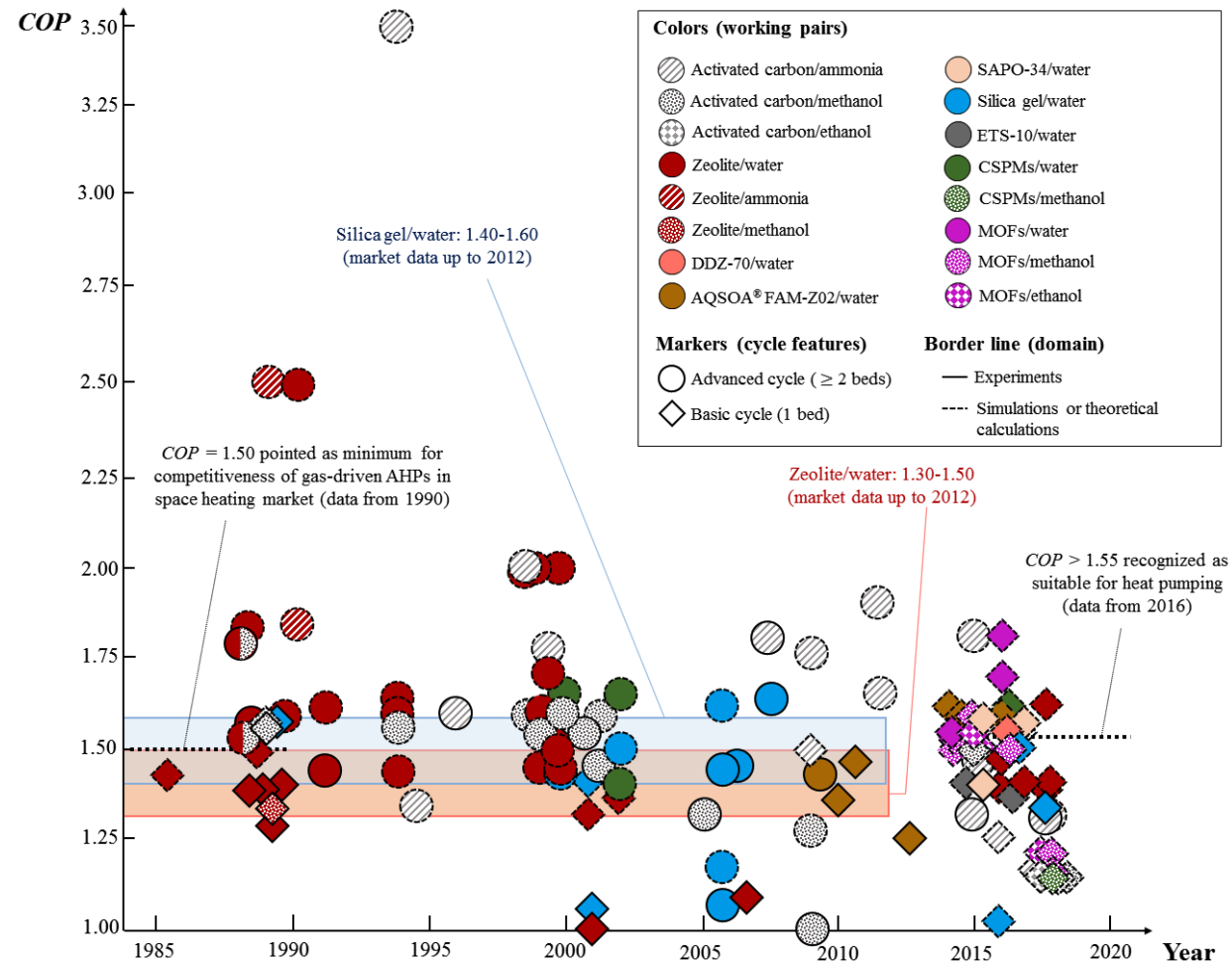


Fig. 2.5 – Literature data for $COPs$ of AHPs (1985 - 2017; maximum values from Table A2.1). The working pairs are distinguished by colors/patterns; cycle features are distinguished by marker type (basic (diamonds) or advanced (circles)); the work domain is indicated by the markers border line (theoretical (dashed) or experimental (solid line)). The COP ranges for commercial AHPs using silica gel/water (1.40-1.60) or zeolite/water (1.30-1.50) are indicated for comparisons (blue and orange rectangles, respectively) [33], as well as the reasonable minimum COP values (horizontal black dotted lines) [45, 46].

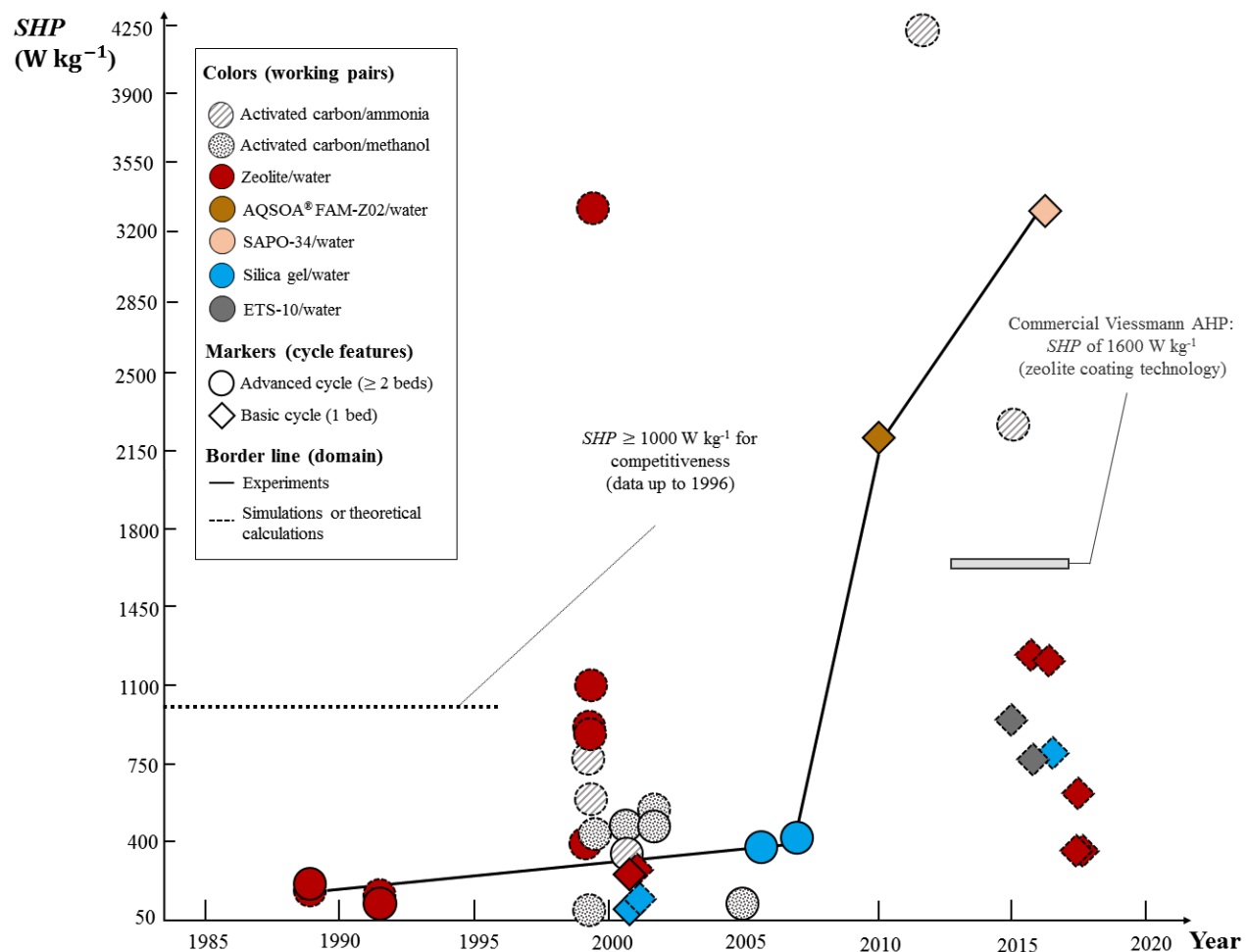


Fig. 2.6 – Literature data for SHP s of AHPs along the years (1985 - 2017; maximum values from Table A2.1). The working pairs are distinguished by colors/patterns; cycle features are distinguished by marker type (basic (diamonds) or advanced (circles)); the work domain is indicated by the markers border line (theoretical (dashed) or experimental (solid line)). The minimum SHP of 1000 W kg^{-1} for competitiveness of AHPs [47] is indicated (black dotted line), and SHP of 1600 W kg^{-1} for the benchmark adsorbent coating technology of Viessmann AHP [10]. The black solid lines are a visual guide of the trends of experimental SHP s reported along the years.

The theoretical *COP* values reported in the literature were in average 18 % higher than those obtained experimentally (calculated relative deviations from *ca.* 1 to 40 %; based on the data from Table A2.1). The highest *COPs* reported in experimental works are, in general, within the market range of values, 1.30-1.60 [33] (Fig. 2.5). For example, *COP* of 1.47 was reported for a single-bed prototype using AQSOA[®] FAM-Z02/water (2011) [48], and *COPs* up to 1.40 were reported for a single-bed AHP, using the working pair silicoaluminophosphate SAPO-34/water (2016) [34]. In 2007, Critoph [49] reported an experimental *COP* = 1.80 for a double-bed, forced convection AHP prototype using activated carbon (AC)/ammonia, and later *COP* = 1.31 was reported for a prototype based on a heat recovery cycle with four beds, using the same working pair (2015) [50]. In comparison to the AHP market data until 2012, no significant improvements in experimental *COPs* were reported since then. This may be partly associated with the limited adsorption capacities of the studied adsorbents. Research efforts are ongoing to develop new materials with high adsorption capacities, aiming at improved AHPs performances [51]. Theoretical *COPs* above 1.55 were recently reported for single-bed AHPs using novel metal organic frameworks (MOFs) and water as adsorbate [41].

The evaluation of AHPs based on *SHP* (Fig. 2.6, Table A2.1) seems to be less addressed in the literature than that based on *COP*. The *SHP* values were in average 35 % higher in theoretical than practical scenarios (relative deviations range from 2 to 60 %). Until 2007, experimental *SHPs* up to *ca.* 500 W kg⁻¹ were reported for AC/methanol and silica gel/water pairs in advanced cycles, in which the adsorbents were essentially in a configuration of loose grains [52-54]. In 2010, coatings were introduced, and a high *SHP* of 2200 W kg⁻¹ was reported for a single-bed AHP using AQSOA[®] FAM-Z02 binder-based coating and water as adsorbate [55]. In 2016, *SHP* exceeding 3200 W kg⁻¹ was reported using a coating of SAPO-34 prepared *via* direct crystallization, with water as adsorbate [34]. A comparison of single-bed AHPs using (zeolite or zeotype)/water working pairs shows the influence of the adsorbent configuration on experimental *SHP*: loose grains (240 W kg⁻¹ (zeolite/water in 2001)) < binder-based coatings (2200 W kg⁻¹) < directly synthesized coatings (3200 W kg⁻¹). A ten-fold increase in *SHP* was verified for coatings in relation to loose grains. Indeed, Dawoud *et al.* [10] reported that zeolite coating technology allows achieving *SHPs* in the order of magnitude of thousands, *i.e.*, ten times higher than for zeolite random pellets

between finned tubes. Accordingly, moving from conventional pellets/grains to novel adsorbent configurations is crucial to enhance *SHP* and the cost-competitiveness of AHPs.

Overall, the development of materials with enhanced adsorption capacities, and improved adsorbent configurations for efficient heat transfer is essential to improve the performance of AHPs.

2.3.2. The working adsorbent/adsorbate pairs

The heart of the AHP is the adsorbent/adsorbate working pair. Water is by far the most eco-friendly adsorbate, without toxicity and flammability concerns. The types of adsorbents studied for heating applications using water as adsorbate include zeolites (crystalline microporous aluminosilicates of the type 13X, 4A, NaY, and clinoptilolite) [8, 56-58], amorphous silica gel [54, 59], AQSOA[®] FAM-Z02 (silicoaluminophosphate SAPO-34 specially developed by Mitsubishi Plastics for AHP applications [60, 61]) [48, 55, 62, 63], zeotype SAPO-34 [34, 46, 64], composites “Salt in Porous Matrix” (CSPMs) (such as SWS-1S, SWS-2L) [46, 65], and porous coordination polymers such as MOFs (like CPO-27(Ni) and aluminum fumarate) [16, 41] (Table A2.1). In particular, zeolite/water pairs were thoroughly investigated until *ca.* 2000 (Fig. 2.5). Activated carbons (ACs) have been combined with adsorbates such as methanol [52, 66], ammonia [67-69], and, more recently, ethanol [70] (Table A2.1). MOFs have also been explored using alcohols (methanol, ethanol) as adsorbates (Fig. 2.5) [40, 71].

Aluminosilicates such as zeolite 13X and 4A possess relatively high water adsorption capacity at low pressures. However, $T_{\text{heat source}}^{\text{high}} > 473 \text{ K}$ is required for efficient regeneration of zeolites [46], which may imply the use of, for example, thermal oils as HTFs instead of water (to avoid excessive pressure inside the circuits), and decrease the cost competitiveness of the appliances. Possibly, this was one of the reasons why adsorbents implying less demanding regeneration were investigated since the beginning of this century, like silica gel, AQSOA[®] FAM-Z02 (emerged around 2010) and MOFs (since *ca.* 2014). In the case of silica gel, most of the water adsorption occurs at too high relative pressures, and hence the achieved ΔW_{cycle} is only a small part of the total capacity [72]. The adsorbent AQSOA[®]

FAM-Z02 represents an important advancement for AHPs [33], and was tested in prototypes using water vapor [55, 62, 63]. AQSOA[®] FAM-Z02 advantageously exhibits S-shaped water isotherms in a reasonable range of relative pressure (P/P^σ) [60]. The adsorbents for AHPs should preferably exhibit enhanced water uptake in the P/P^σ range 0.05-0.3 of the equilibrium isotherm [51] (*e.g.*, for a heat pumping process with $T_{\text{evap}} = 278$ K ($P^\sigma = 870$ Pa), $T_{\text{cond}} = T_2 = 318$ K ($P^\sigma = 9536$ Pa), and $T_4 = 398$ K ($P^\sigma = 2.3291 \times 10^5$ Pa), for the adsorption stage one has $P/P^\sigma = P_{\text{evap}}/P^\sigma(T_2) = 0.09$, and for the desorption stage $P/P^\sigma = P_{\text{cond}}/P^\sigma(T_4) = 0.04$). Focus has been put on SAPO-34/water pair in recent years [34, 64], albeit SAPOs are expensive due to the templated syntheses, and still possess limited capacities [72].

MOFs/(water or alcohol) working pairs are receiving increasing attention for AHP applications (Fig. 2.5). This is partly due to the fact that MOFs possess high specific surface area (S_{BET} typically in the range 1000 - 4000 m² g⁻¹, compared to *ca.* 500 - 800 m² g⁻¹ for zeolites), high porosity, narrow pore size distribution, favorable S-shaped isotherms, and may be prepared with a plethora of combinations of types of metals and organic linkers and different structure dimensionality, which allows tuning the materials properties for adsorption applications [51, 72, 73].

Studies using AC/(ammonia or methanol) have been reported over the years [74-77], and since *ca.* 2010 ammonia seems the preferred adsorbate. These working pairs are effective at $T_{\text{evap}} < 273$ K, contrarily to water-based pairs (Section 2.3.3). Recently, AC composites were investigated to improve the performance of AHPs using ammonia as adsorbate, and *COPs* in the range *ca.* 1.10 -1.30 were reported for a consolidated bed of lignin-carbon composite material in a finned tube heat exchanger [69].

The types of adsorbents studied for AHPs may be grouped considering theoretical, technical and economic potentials (see Fig. 2.7). All the materials (or families) reported in Table A2.1 are indicated in the subset of theoretical potential (*i.e.*, which were studied at least theoretically with calculations/modelling), and the subset of technical potential contemplates the adsorbents tested in prototypes, experimental setups or used in final products. The subset of economic potential encompasses the materials employed in commercial systems, where minor and major potentials are distinguished taking into account commercial availability and costs criteria. Fig. 2.7(b) shows the level of maturity for industrial production of the adsorbents included in the technical potential subset

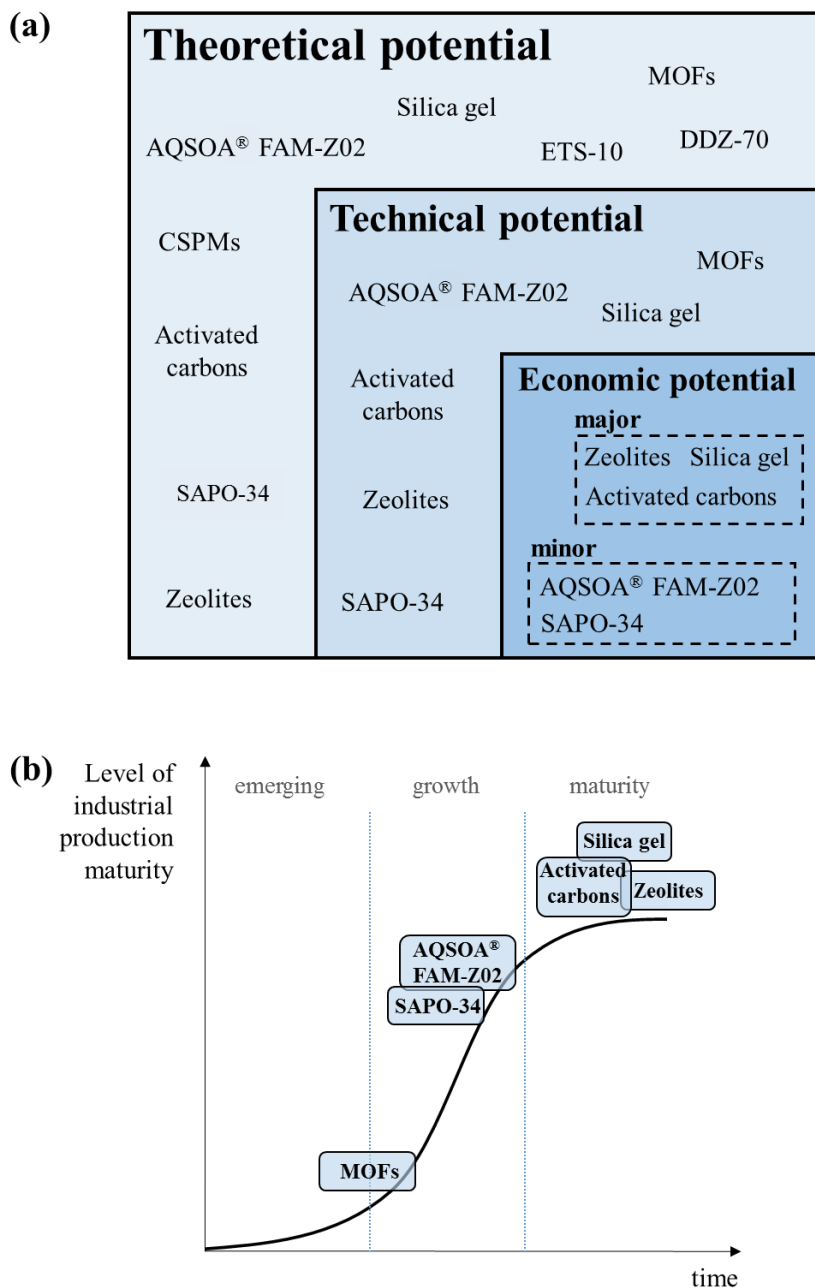


Fig. 2.7 – (a) Types of adsorbents for AHPs grouped by theoretical, technical and economic potentials. (b) S-curve showing the level of industrial production maturity of the adsorbents included in the technical potential subset.

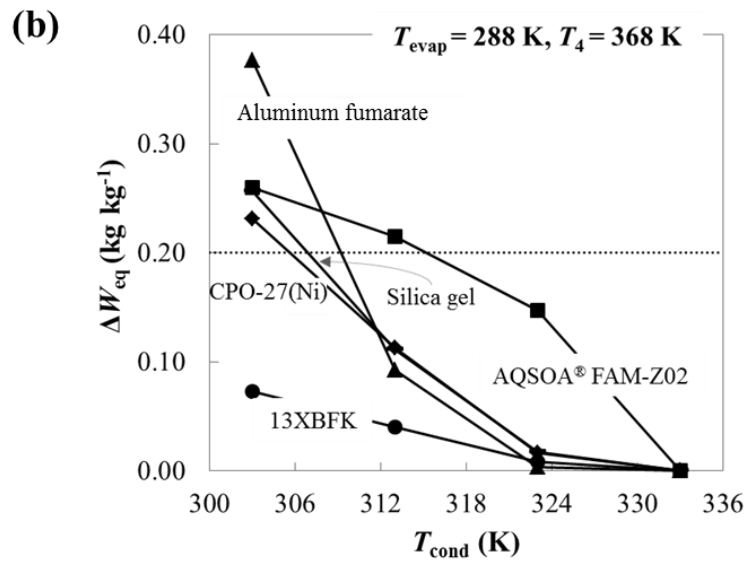
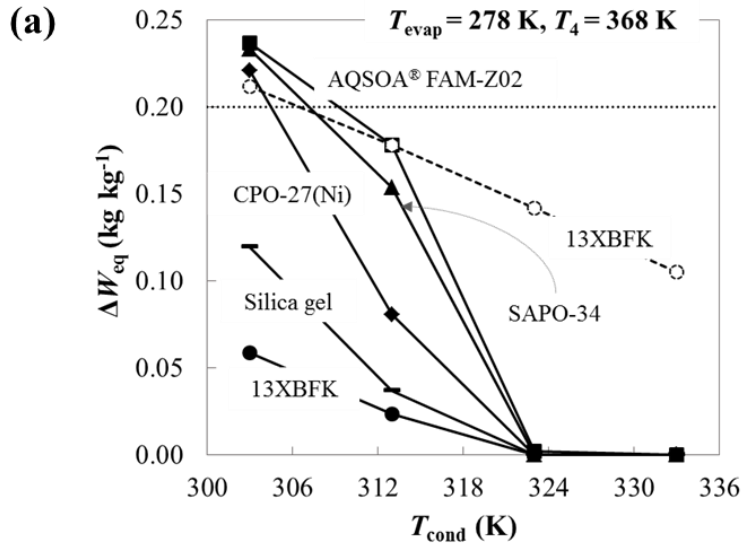
of Fig. 2.7(a). Zeolites and microporous silica gel have been applied in commercial AHPs and chillers [33, 73]. Zeolites, silica gel and activated carbons are most attractive in terms of price (*ca.* < 5 – 20 € kg⁻¹) and are readily available in the market [78]. Zeotypes such as SAPO-34 and AQSOA[®] FAM-Z02 are more expensive (*ca.* 50-100 € kg⁻¹ for SAPOs [78]) and poorly available (industrial scale production has not been reached, to the best of our

knowledge), albeit they are employed nowadays [46, 51, 73, 78]. MOFs are not included in the economic potential subset, due to the present high production costs preventing them from the market [51]. Restuccia [79] indicated high prices of *ca.* 8500-9500 € kg⁻¹ for Basolite[®] C300 (HKUST-1) and Basolite[®] F300 (Fe-BTC). Nevertheless, a proof-of-concept prototype on a pre-industrial scale using MOFs has been recently demonstrated [51].

Fig. 2.8(a)-(b) shows a comparison of the adsorbents with technical potential for AHPs using water as adsorbate in terms of cycle equilibrium loadings (ΔW_{eq}), for T_{cond} (coincident with T_2) in the range 303-333 K, $T_4 = 368$ K (mild regeneration conditions), and T_{evap} of 278 K (Fig. 2.8(a)) and 288 K (Fig. 2.8(b)). The ΔW_{eq} vs. T_{cond} values for Köstrolith[®] 13XBFK at $T_4 = 473$ K (very high regeneration temperature) are given for comparison in Fig. 2.8(a) (dashed line with markers). Fröhlich *et al.* [84] recently reported that the adsorption capacity should be higher than 0.2 kg kg⁻¹ for good AHP performance, and this value serves as reference in Fig. 2.8(a)-(b). The isotherms used to compute ΔW_{eq} for each pair were those from refs. [41, 80-83].

SAPOs and MOFs fulfill the desirable requirement of $\Delta W_{\text{eq}} \geq 0.20$ kg kg⁻¹ only for $T_{\text{cond}} < 313$ K. For higher T_{cond} values, ΔW_{eq} drops considerably: *e.g.*, in the case of AQSOA[®] FAM-Z02, from *ca.* 0.24 to 0 kg kg⁻¹, as T_{cond} increases from 303 to 333 K ($T_{\text{evap}} = 278$ K, Fig. 2.8(a)). The adsorbents regenerated under mild conditions ($T_4 = 368$ K) are not efficient over a broad range of T_{cond} (303-333 K), leading the AHP to operate in a narrow window of T_{cond} , outside of which its performance drops significantly, as reported by Corberan *et al.* [33]. As demonstrated in Fig. 2.8(a) for Köstrolith[®] 13XBFK, when zeolites are regenerated at $T_4 = 368$ K, they perform inferiorly to other adsorbents, but at $T_4 = 473$ K (dashed line with markers), they outperform the remaining ones at high T_{cond} (> 313 K), reaching $\Delta W_{\text{eq}} \geq 0.10$ kg kg⁻¹.

Fig. 2.8(c) shows a qualitative comparison of the different adsorbents with respect to ΔW_{eq} (based on Fig. 2.8(a)-(b), and $T_4 = 368$ K), the ability to be regenerated at low temperature, hydrothermal stability, commercial availability and cost, which are among the most important factors influencing techno-economic viability of AHPs. The ΔW_{eq} for the adsorbents regenerated under mild conditions may be roughly ordered as follows:



(c)

	Zeolites	AQSOA® FAM-Z02	SAPO-34	Silica gel	MOFs
Equilibrium performance (ΔW_{eq})	●	●	●	●	●
Ability to be regenerated at low T	●	●	●	●	●
Hydrothermal stability	●	●	●	●	●
Commercial availability	●	●	●	●	●
Cost	●	●	●	●	●

● Favorable ● Medium ● Poor

Fig. 2.8 – (a) ΔW_{eq} vs. T_{cond} (coincident with T_2) at $T_{\text{evap}} = 278 \text{ K}$ and $T_4 = 368 \text{ K}$ for zeolite Köstrolith® 13XBFK, microporous silica gel type RD, MOF CPO-27(Ni), SAPO-34 and AQSOA® FAM-Z02 using water as adsorbate (solid

Chapter 2: Introduction

lines). T_{cond} and corresponding ΔW_{eq} for zeolite Köstrolith® 13XBFK at $T_4 = 473$ K are plotted for comparison (dashed line with markers). (b) Water ΔW_{eq} vs. T_{cond} , at $T_{\text{evap}} = 288$ K and $T_4 = 368$ K for Köstrolith® 13XBFK, microporous silica gel type RD, MOFs CPO-27(Ni) and aluminum fumarate, and AQSOA® FAM-Z02 (solid lines). Lines are visual guides. Desirable minimum $\Delta W_{\text{eq}} = 0.20$ kg kg⁻¹ for good performance of AHPs is marked as reference in (a) and (b) (horizontal dashed line) [84]. The isotherms are available from references [41, 80-83]. (c) Qualitative comparison of aluminosilicate zeolites, AQSOA® FAM-Z02, SAPO-34, microporous silica gel and MOFs regarding: ΔW_{eq} (based on (a) and (b), for $T_4 = 368$ K), ability to be regenerated at low T ($T \leq 373$ K), hydrothermal stability, commercial availability and cost.

AQSOA® FAM-Z02 and SAPO-34 > MOFs > silica gel > zeolites (aluminosilicates). Zeolites need heat sources at 473 – 573 K for efficient regeneration [46], whereas the remaining adsorbents are more easily regenerated: *e.g.*, for SAPOs and microporous silica gel, $T_4 \leq 373$ K [60, 85]; for MOFs CPO-27 (Ni) and aluminum fumarate, $T_4 < 383$ K [41].

Prototypes for space heating and DHW production showed the need to perform 10000 cycles/year, which for 12-15 years of service life corresponds to a required stability of the adsorbents over 120000-150000 cycles [86]. High hydrothermal stability of the working pairs in ranges of T and P of operation of the AHPs is therefore crucial. Hydrothermal aging upon successive cycles may lead to irreversible changes in the adsorbent material properties, with detrimental effects on the loading capacities and kinetics of adsorption [73]. The hydrothermal and mechanical stabilities of the materials may be influenced by factors such as the adsorbent form (pellets, granules, consolidated layers), the formulation process, binder type and amount. When developing an AHP, it is recommendable to assess stable operation and the system lifetime using a similar adsorbent form and operating conditions to those expected for the final product [73].

Restuccia [79] classified favorably NaY zeolites and silica gels (Fuji Davison and Siogel) in terms of hydrothermal stability for adsorption heating/cooling applications. Freni *et al.* [73] highlighted the structure stability of zeolites (13X, 4A, NaY) over a high number of operating cycles due to the hydrophilic (polar) surface and affinity for water. Silica gel tends to be less stable than crystalline zeolites (Fig. 2.8(c)) due to its amorphous nature [46] (thermal decomposition may have an onset at *ca.* 373 K [73]). For AQSOA® FAM-Z02, almost no changes in the water adsorption capacity occurred for 100000 cycles, suggesting that it is stable enough for practical use in AHPs [61, 73, 79]. The hydrothermal stability of the related material SAPO-34 was ranked poor [79] or intermediate [78], which depends partly on the synthesis conditions and templates used [51]. The poor hydrothermal stability of various MOFs is a drawback for practical application in AHPs [72, 73, 79] (Fig. 2.8(c)).

Stability issues, adsorption properties and applications of MOFs [16, 40, 72, 87-97], SAPOs [43, 98-103] and Composites “Salt in Porous Matrix” (CSPMs) [46, 104-108] in adsorption heat transformation processes have been addressed in various studies.

In the whole, R&D in the field of materials science is essential for the development of efficient and cost effective AHPs. Novel adsorbents should ensure a good compromise between performance, stability and cost.

2.3.3. Adsorbates and temperature heat sources for the evaporator

The adsorbate (sometimes called refrigerant) should have low or no global warming potential (GWP) neither ozone depletion potential (ODP), high latent heat of vaporization (ΔH_v), good thermal stability and high stability with respect to materials and sealings, be non-flammable and non-toxic, and its saturation pressure (P^s) should be near atmospheric level in the temperature range between 263 and 353 K [109, 110]. The adsorbates used in AHPs over the years are given in Fig. 2.9(a) (based on Table A2.1 (Annex A2)). Experimental and theoretical studies of AHPs using water, methanol and ammonia were reported since the 1980s, and more recently theoretical studies using ethanol. Increasing attention is being given to ethanol, which is less toxic than methanol, and is produced from renewable biomass (Table A2.1 and Figs. 2.5-2.6).

Fig. 2.9(b) compares the latent heat of vaporization (ΔH_v at $T = 313$ K) of the various adsorbates. High ΔH_v is desirable since the greater the amount of heat released from the condenser, at constant m_{ads} and ΔW_{cycle} ($Q_{cond} \approx m_{ads} \Delta W_{cycle} \Delta H_v$), the better is the heating performance (Eqs. (2.1)-(2.2)). In this sense, water stands on a higher footing than ammonia and alcohols (*e.g.*, for ethanol, ΔH_v is *ca.* a third of that of water).

Fig. 2.9(c) indicates the characteristics of the refrigerants in terms of toxicity and/or flammability issues, GWP (for 100 years), ODP, stability concerns and compatibility with metals. For example, water and ammonia have zero GWP and ODP, and methanol has GWP = 2.8, which is much lower than for hydrofluorocarbon R134a (GWP = 1300) presently used in VCS [111-113]. Nevertheless, ammonia poses concerns for indoor use in occupied spaces (except small machines) due to its high toxicity [72, 114]. One of the main drawbacks of methanol is the lack of thermal stability above 393 K [109]. Freni *et al.*

reported that activated carbon (AC) is active for the condensation of methanol to dimethyl ether, at $T > 398$ K [73]. Hence, if high regeneration temperature is desired for taking advantage of higher $COPs$ in AHPs, the working pair AC/alcohol may present stability issues [115]. Although ammonia is more stable (up to at least 473 K [115]), it is incompatible with copper, and the same applies for methanol at high temperatures [109].

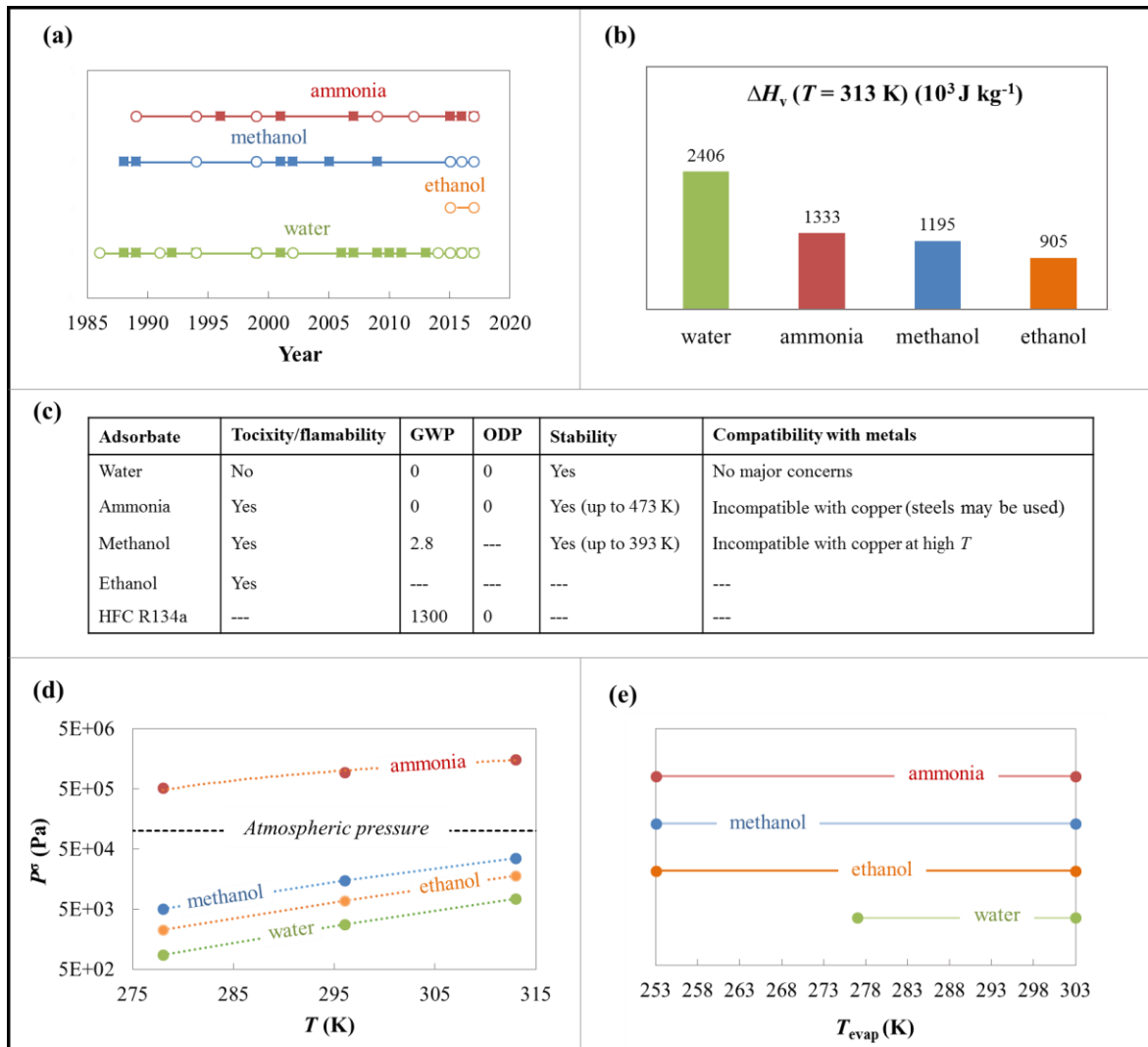


Fig. 2.9 – Data for the refrigerants studied for AHPs, namely, water, ammonia, methanol and ethanol: (a) general view regarding the use of the adsorbates in AHPs over the years (data from Table A2.1: theoretical studies (○), experimental or simultaneously experimental and theoretical studies (■)); (b) enthalpies of vaporization (ΔH_v) at 313 K [120, 121]; (c) toxicity and/or flammability issues, global warming potential (GWP; for 100 years; value for hydrofluorocarbon (HFC) R134a is given for comparisons), ozone depletion potential (ODP), stability concerns and compatibility with metals [109, 111, 115, 122]; (d) P^s vs. T in the range 278 – 313 K [120]; (e) Applicable T_{evap} ranges (considering 253 – 303 K as reasonable interval in heat pumps).

Fig. 2.9(d) shows (T, P^σ) for water, ammonia, methanol and ethanol in the temperature range 278-313 K. The operation with ammonia requires working above atmospheric pressure (e.g., at $T = 313$ K, $P^\sigma = 15.46 \times 10^5$ Pa), whereas with the remaining fluids it involves vacuum. The use of water as adsorbate implies more demanding vacuum conditions: for instance, at 278 K, $P_{\text{water}}^\sigma = 870$ Pa and $P_{\text{methanol}}^\sigma = 5000$ Pa, which are *ca.* 115 and 20 times below atmospheric pressure, respectively.

The range of applicable T_{evap} (within the reasonable range 253-303 K for heat pumps) for the different adsorbates is given in Fig. 2.9(e). Ammonia and methanol allow operation in a broader range of T_{evap} than water, and are suitable adsorbates for a variety of porous carbons (which are attractive adsorbents for AHPs using $T_{\text{heat source}}^{\text{high}} > 373$ K – 423 K), despite the stricter demands of safety in ammonia-based appliances [85, 115]. The eco-friendliest adsorbate water is the only studied refrigerant that requires minimum T_{evap} of 273 K [116] (triple point is around 273 K), in order to avoid freezing inside the evaporator. On the other hand, water as adsorbate presents some limitations to the use of air as a low temperature heat source due to the wide ambient temperature variations during the year. Tajima *et al.* [59] reported that the AHP operation with water as adsorbate is only feasible if the outside air temperature is greater than 280 K. However, according to the European Heat Pump Association, air is and will remain the dominant energy source for heat pumps [117]. To use water as adsorbate in air-source AHPs, one may adopt an integrated concept such as the one proposed by Tajima *et al.* [59], which combines a gas water heater with an AHP, in which the first one operates when the air temperature is below 283 K, and the AHP operates when the exterior $T \geq 283$ K. Alternatively, other low temperature heat sources may be used such as geothermal and/or solar (e.g., operating temperature range for solar thermal collectors is $\sim 276 - 403$ K [118]), as already applied in Vaillant and Viessmann commercial AHPs [118, 119]. However, these approaches generally lead to more expensive appliances than air-source heat pumps.

The evaluation of the suitability of alternative refrigerants for AHPs, such as carbon dioxide, diethyl ether, n-butane, propane, 1-propanol, 2-propanol, nitrogen, hydrogen, and even binary mixtures of adsorbates requires further investigation, considering technical and safety issues [17, 123, 124].

2.3.4. Temperature operation levels and cycle features

Fig. 2.10 shows operating temperature ranges reported in the literature for advanced and basic AHPs when using water, methanol, ethanol or ammonia as adsorbates and different adsorbents (zeolites, silica gel, AQSOA[®] FAM-Z02, SAPO-34, MOFs, CSPMs and activated carbons). Three temperature levels are considered: the low level corresponds to T_{evap} and/or $T_{\text{heat source}}^{\text{low}}$; the medium level corresponds to T_{cond} and/or T_2 ; the high level regards T_4 and/or $T_{\text{heat source}}^{\text{high}}$ (data from Table A2.1). The maximum recommended T_4 for AHPs is 393 K [84], which served as reference in Fig. 2.10.

When using water as refrigerant, average values of low (T_{evap} and/or $T_{\text{heat source}}^{\text{low}}$) and medium (T_{cond} and/or T_2) temperature levels range from 280 to 286 K, and from 309 to 326 K, respectively. The operation with zeolites allows broadening the range of T_{cond} and/or T_2 to higher values in relation to the remaining adsorbents, at the expense of generally higher T_4 and/or $T_{\text{heat source}}^{\text{high}}$, as discussed in Section 2.3.2. $T_{\text{heat source}}^{\text{high}}$ as high as 473 K may be achieved using, for example, special solar thermal collectors or gas burning units [116]. The remaining adsorbents using water as adsorbate were mostly studied under milder regeneration conditions: for instance, *ca.* 345 – 393 K for MOFs, and below *ca.* 425 and 445 K for AQSOA[®] FAM-Z02 and CSPMs, respectively. For the pairs AC/(ammonia or alcohols), the average temperature values studied in the literature were: T_{evap} and/or $T_{\text{heat source}}^{\text{low}}$ in the range 250 – 274 K; T_{cond} and/or T_2 of 315 – 323 K (somewhat similar to that for water-based pairs); T_4 and/or $T_{\text{heat source}}^{\text{high}}$ of 382 - 468 K. For MOFs/alcohol pairs, average T_4 and/or $T_{\text{heat source}}^{\text{high}}$ of 399 and 420 K were calculated from literature data for methanol and ethanol, respectively, and are higher than those for MOFs/water (Table A2.1).

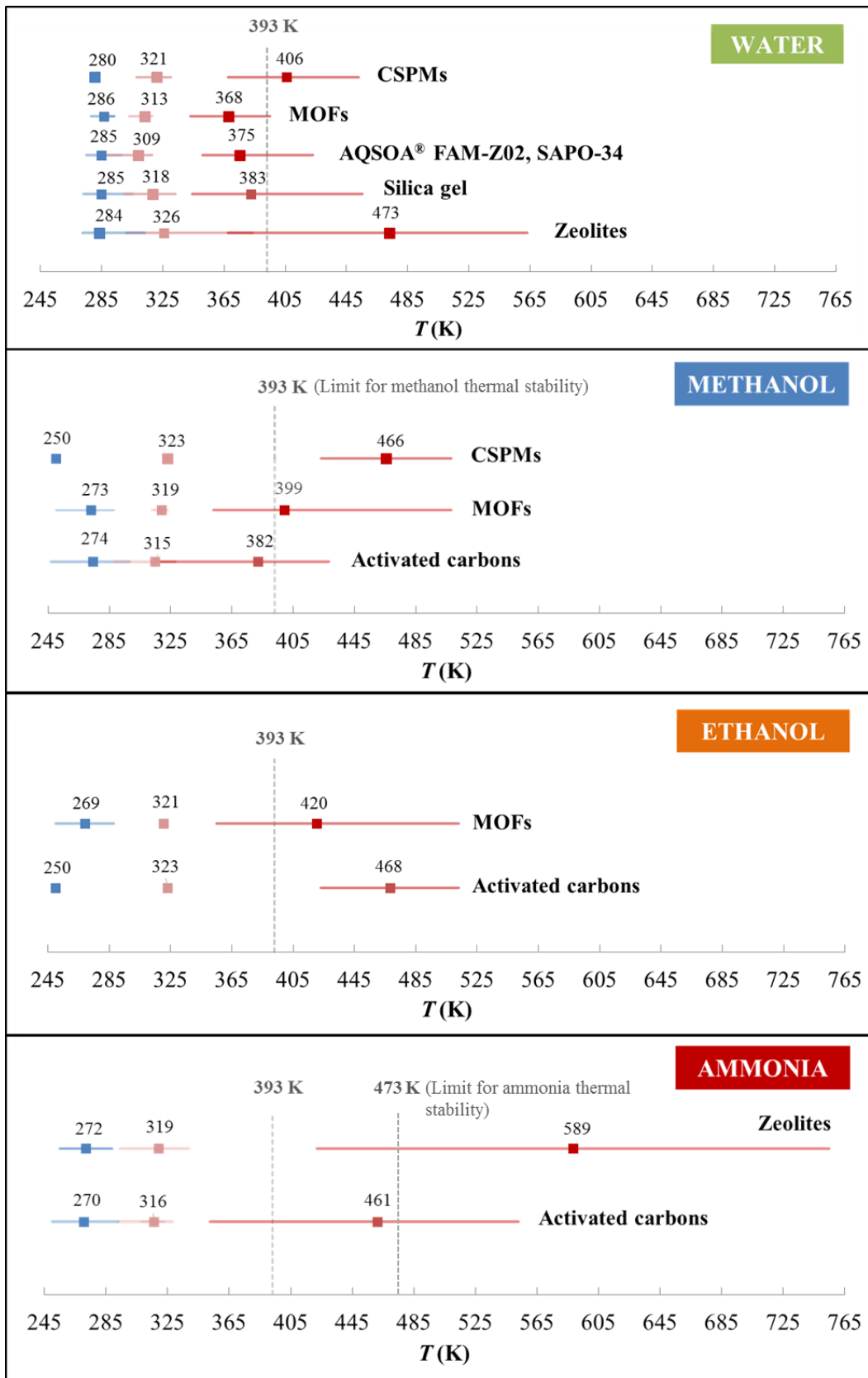


Fig. 2.10 - Typical low (T_{evap} and/or $T_{\text{heat source}}^{\text{low}}$ (blue lines)), medium (T_{cond} and/or T_2 (pink lines)), and high (T_4 and/or $T_{\text{heat source}}^{\text{high}}$) temperature levels for basic and advanced AHPs using water, methanol,

ethanol or ammonia with different adsorbents (zeolites, silica gel, AQSOA[®] FAM-Z02, SAPO-34, MOFs, CSPMs and activated carbons) (literature data given in Table A2.1). Squares are average values. The recommended maximum T_4 of 393 K for AHPs is a reference (gray dashed line) [84]. Methanol and ammonia thermal stability limits are vertically marked (Section 2.3.3).

Regarding the cycle features, the literature covers basic and advanced AHPs (*i.e.*, systems with one or more beds, respectively) (Table A2.1). The advanced AHPs encompass heat recovery, heat and mass recovery, thermal wave, forced convection and cascading cycles. Advanced cycles allow enhanced *COP* in relation to basic ones. For example, Meunier *et al.* [125] reported experimental *COPs* of 1.39 and 1.57 for operation with one and two beds, respectively.

Fig. 2.5 indicates that until *ca.* 2010, advanced cycles were predominantly investigated for heating purposes, and since then a higher focus has been put on basic cycles. This may be because advanced systems present a very high complexity to efficiency enhancement ratio when compared to basic ones, as reported by Dawoud *et al.* [55]. In recent years (2015-2017), only advanced AHPs using AC/ammonia have been investigated.

The cycle time (t_{cycle}) of basic systems (with a single adsorbent bed) studied are commonly in the range *ca.* 300-3600 s (Table A2.1). A recent experimental study on basic AHPs, with *SHP* up to 3200 W kg⁻¹, indicated t_{cycle} around 600 s using the SAPO-34/water working pair [34]. Possibly, $t_{\text{cycle}} < 900$ s is interesting for improved performance of basic AHPs [126]. Half t_{cycle} values of *ca.* 720 - 10800 s were reported for heat recovery cycles consisting of two beds in alternate operation (Table A2.1). In the patent literature, the time switch between the adsorption-evaporation and desorption-condensation phases has been pointed as preferably between 300 and 1800 s [30], which results in total t_{cycle} ranging from 600 to 3600 s.

2.3.5. Adsorbent bed configurations

The adsorbent bed configurations used for AHPs may be grouped into four types (Table A2.1) [73]: loose grains, consolidated beds, binder-based coatings, and directly synthesized coatings. In the first case, adsorbent grains, pellets, powder or fibers are embedded in the heat exchanger without any binder, while, in the second case, a binder and eventually a pore-

forming additive are compressed with the adsorbent to form a relatively thick consolidated layer on the surface of the walls of the heat exchanger. Binder-based coatings are prepared using the adsorbent and a binder, and the composite material may be supported on the heat exchangers *via* spray or dip coating techniques. Directly synthesized coatings are obtained through synthesis of very thin layers of adsorbent directly on the walls of the heat exchangers [73]. The loose grains configuration is the mostly investigated (*ca.* 80 % of the reported studies (Table A2.1)), likely due to its simplicity and low cost. Each of the remaining configurations represents less than 10 % of the studies.

Fig. 2.11 shows a quantitative comparison of the four bed configurations regarding the thermal conductivity of the adsorbent bed (λ_{ads}), the heat transfer coefficient on the adsorbent side (h_{ads}), and the bed thickness (δ) (essentially based on literature for zeolites, zeotypes (for instance, AQSOA[®] FAM-Z02, SAPO-34) and silica gels, using water as adsorbate), as well as qualitative information on the bed permeability, stability issues (pore structure stability, mechanical resistance) and industrialization features (*e.g.* restrictions to the use of complex AHEx geometries, production process complexity and costs).

The heating power is favored by improvements of the AHEx overall heat transfer coefficient (U), for which enhanced λ_{ads} and h_{ads} , and smaller δ are beneficial according to the following equation [127], which simply serves to analyze the relative importance of the physical components of the heating unit, where resistances to heat transfer may exist:

$$\frac{1}{UA_{\text{fluid}}} = \frac{1}{h_{\text{fluid}}A_{\text{fluid}}} + \frac{1}{h_{\text{ads}}A_{\text{ads}}} + \frac{\delta}{\lambda_{\text{ads}}A_{\text{ads}}} \quad (2.4)$$

where A_{fluid} and A_{ads} are the heat exchanger areas on the fluid and adsorbent sides, respectively, and h_{fluid} is the convective heat transfer coefficient on the fluid side.

Values of λ_{ads} in the order of tenths of $\text{W m}^{-1} \text{K}^{-1}$ have been reported for beds composed of loose grains/pellets or binder-based coatings (Fig. 2.11): *e.g.*, λ_{ads} in the range 0.10 – 0.20 $\text{W m}^{-1} \text{K}^{-1}$ for zeolites, zeotypes and silica gel [28, 128, 129]; $\lambda_{\text{ads}} = 0.36 \text{ W m}^{-1} \text{K}^{-1}$ for AQSOA binder-based coating, and $\lambda_{\text{ads}} = 0.11 \text{ W m}^{-1} \text{K}^{-1}$ for the corresponding powdered bed [73]. Restuccia *et al.* [28] reported $\lambda_{\text{ads}} = 0.30 \text{ W m}^{-1} \text{K}^{-1}$ for a binder-based coating. Values of λ_{ads} were roughly two orders of magnitude higher for consolidated beds and directly synthesized coatings in relation to loose grains/pellets and binder-based coatings:

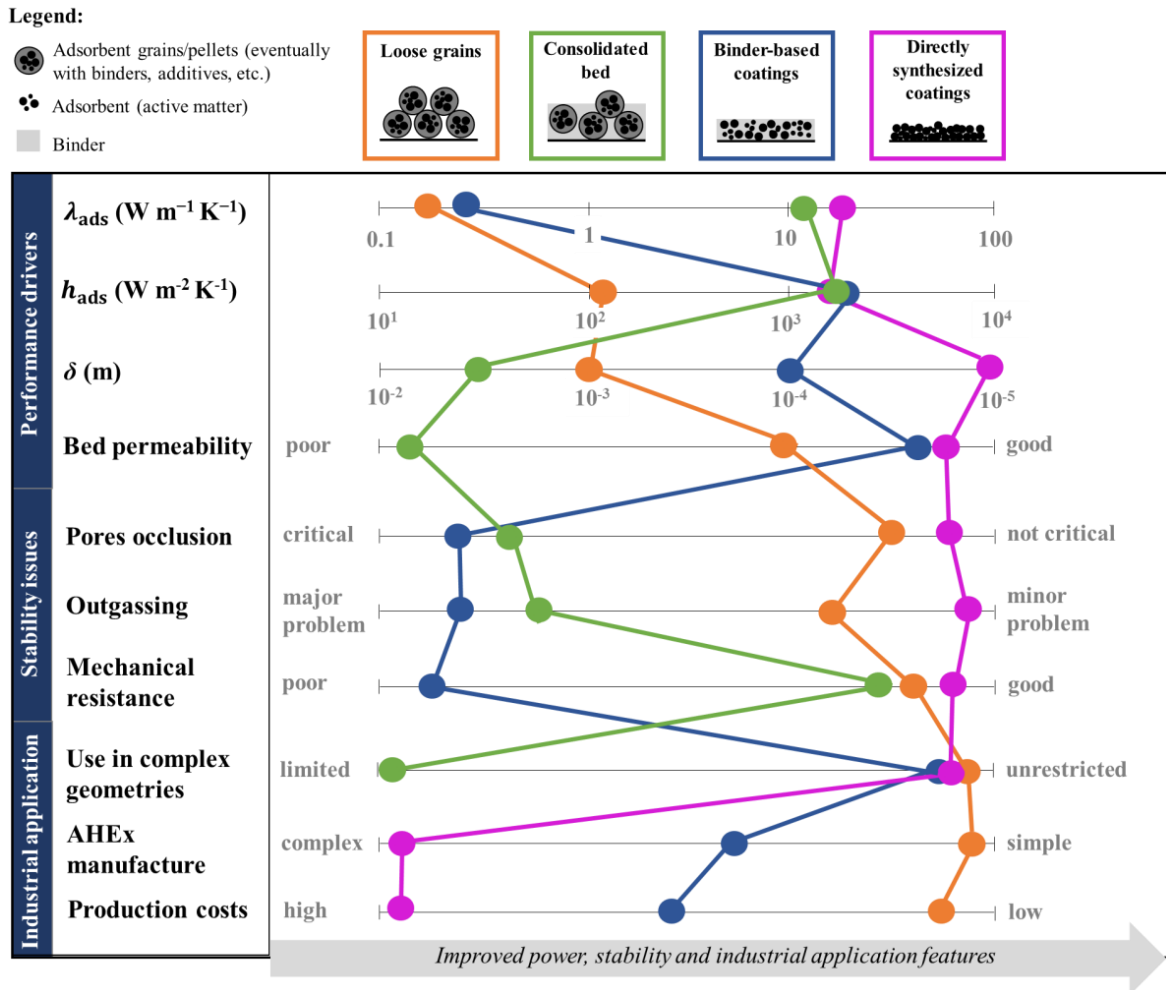


Fig. 2.11 – Comparison of the adsorbent configurations for AHPs (loose grains, consolidated beds, binder-based coatings, and directly synthesized coatings) in terms of λ_{ads} , h_{ads} , δ , bed permeability, stability issues and industrial application features. The marked λ_{ads} and h_{ads} refer to the highest reported values in the literature, and δ regards the most typical orders of magnitude. The heating power, bed permeability, stability and industrial application features improve from the left to the right hand side of the figure. Quantitative data for the figure were essentially based on literature for zeolites, zeotypes (e.g., AQSOA[®] FAM-Z02, SAPO-34) and silica gels, using water as adsorbate.

for instance, λ_{ads} in the range 4-17 W m⁻¹ K⁻¹ and $\lambda_{ads} = 27$ W m⁻¹ K⁻¹ for consolidated zeolite 13X (powder in expanded natural graphite), and a bed of copper foam coated with zeolite NaA, respectively (the adsorbate was water) [73].

The convective heat transfer coefficients (h_{ads}) for loose grains (water as adsorbate) are often considered in the range 10-50 W m⁻² K⁻¹ [130]; values between 70 and 120 W m⁻² K⁻¹ were also reported [130]. For the remaining configurations, $h_{ads} > 1000$ W m⁻² K⁻¹: for example, for a binder-based coating of silica gel, h_{ads} up to ca. 3000 W m⁻² K⁻¹ [131]; for consolidated 13X zeolite (powder in expanded natural graphite),

h_{ads} up to $3000 \text{ W m}^{-2} \text{ K}^{-1}$ [73]; for directly synthesized SAPO-34 coatings on aluminum fibers, $h_{\text{ads}} > 1000 \text{ W m}^{-2} \text{ K}^{-1}$ [73]. These results are due to more efficient contact between the adsorbent and the AHEx metal surface when using coatings or consolidated beds instead of loose grains.

The bed thicknesses (δ) studied for loose grains and consolidated beds are in the order of 10^{-2} - 10^{-3} m. Lang *et al.* [128] designed an AHEx possessing a layer of zeolite pellets with $\delta = (1-1.6) \times 10^{-3}$ m. Frazzica *et al.* [132] reported $\delta \sim 1 \times 10^{-3}$ m for multilayers of loose grains of SAPO-34. The range $2 \times 10^{-3} < \delta \text{ (m)} < 10 \times 10^{-3}$ is typical for consolidated beds [73]. In the case of coatings, δ is relatively low (*ca.* 10^{-4} - 10^{-5} m): *e.g.*, $1 \times 10^{-4} < \delta \text{ (m)} < 8 \times 10^{-4}$ was reported for binder-based coatings [73, 133, 134], and δ in the range $(1-5) \times 10^{-5}$ m for directly synthesized coatings [133]. However, $\delta = 1 \times 10^{-4}$ m was pointed as minimum acceptable for directly synthesized coatings (using zeolites), suggesting the need for multiple depositions [135].

The substitution of loose grains by directly synthesized coatings (the most recent configuration) enables an increment in λ_{ads} and h_{ads} of 1 to 2 orders of magnitude, and a significant decrease of δ by a factor of *ca.* 100. However, this leads to lower $m_{\text{ads}}/m_{\text{metal}}$ ratio, impairing COP [73].

Poor bed permeability is a major drawback for consolidated beds [73, 102]. Recent studies of this configuration for AHPs seem mostly focused on AC/ammonia working pairs [69].

Excessive pressure drops may occur in beds of grains, depending on the particle size, albeit this issue is generally not as significant as the heat transfer limitations (low λ_{ads} and h_{ads}) [73, 102]. Due to insufficient literature data, qualitative comparisons of bed permeability are presented in Fig. 2.11. Nonetheless, values in the range $10^{-14} - 10^{-8} \text{ m}^2$ for the permeability of adsorbent beds (using water, ammonia or methanol as adsorbates) were reported [73], and values greater than 10^{-12} m^2 are preferred [136].

The loose grains configuration and coatings obtained through direct synthesis usually do not present major concerns in terms of stability. Freni *et al.* [73] reported that direct zeolite crystallization offers high coating stability. For binder-based coatings, the limited mechanical resistance [137], possible occlusion of pores due to the binder and the risk of outgassing of volatile compounds from organic binders (which influences the system pressure and may cause complete failure [134]) are drawbacks which still need to be overcome in order to obtain reliable products [73]. The high amount of binder/additives in

the formulation of consolidated beds may also lead to the occlusion of pores, and consequent loss of adsorption capacity, which negatively impacts on the AHP performance [73].

Industrialization features are of primary importance in order to make the products marketable. Loose grains beds are undoubtedly the simplest configuration, allowing lower production costs. The adsorbent particles are packed in the heat exchanger and covered with a grid to support the material [135]. For consolidated layers, the shaping of the adsorbent is restricted to simple geometries (planar, cylindrical), which limits their practical use in real and complex heat exchangers [73]. Directly synthesized coatings may imply demanding and expensive production processes (*e.g.*, for SAPOs, drastic conditions of 20 bar and 200 °C in autoclaves are required). Hence, the development of simpler and cheaper preparation procedures are desirable for industrialization [73]. Binder-based coatings lie between loose grains and directly synthesized coatings in terms of AHEx manufacture complexity and costs, since they may be produced under mild reaction conditions, and are easy to scale-up and implement in serial production lines [73]. Schicktanz *et al.* [135] reported that binder-based coatings may be prepared *via* dip coating (which consist of immersing the metal substrate into a liquid solution containing the active powder and an organic (*e.g.*, resins) or inorganic (for instance, aluminum hydroxide clays) binder, with subsequent thermal treatment to remove the excess solvent), which allow to easily vary the coating thickness in the range $(1-10)\times 10^{-4}$ m by controlling the viscosity of the liquid solution and the dipping velocity.

From the literature survey, binder-based coatings seem to allow a good trade-off between performance drivers (λ_{ads} , h_{ads} , δ , bed permeability) and industrialization features, and improvements in terms of stability may strengthen their marketability. Patent literature dealing with this configuration has been arising: Sauer *et al.* [134] claimed the preparation of coatings that do not release any gases during the desired lifetime of 15 years of AHPs, and that are composed of an inorganic colloidal binder (*e.g.*, colloidal silicon oxides or colloidal aluminum oxides/hydroxides) for binding the adsorbent particles, and thermally conductive inorganic fibers (for instance, carbon fibers, glass fibers, carbon nanotubes), which impart elasticity and mechanical stability. Nonetheless, the experimental work on beds of loose grains have shown that this configuration may provide acceptable performances if particles with sizes smaller than 5×10^{-4} m and heat exchangers with areas per volume greater than $1000\text{ m}^2\text{ m}^{-3}$ are employed [135].

The development of coated AHExs permitting compact designs, and the scale-up of coating techniques remain well-recognized R&D priorities in the field of AHPs [33].

2.3.6. Adsorbent heat exchanger (AHEx) geometries

The adsorbent beds geometries of AHPs were grouped into four categories (Table A2.1): tubular (*e.g.*, hairpin, spiral) with or without fins (annular or longitudinal), extended surface (includes finned plate and fiber plate geometries) and plate-type (*e.g.*, lamella heat exchangers). This categorization of the geometries was partly based on the general classification of heat exchangers according to construction features reported by Shah *et al.* [138]; exceptionally, finned tubes are included in the single category of tubular with fins. Fig. 2.12 shows the literature studies in a systemized fashion regarding AHEx geometries and investigated pairs (Table A2.1), where only works whose domain is experimental or both theoretical and experimental were considered for calculating the percentages shown.

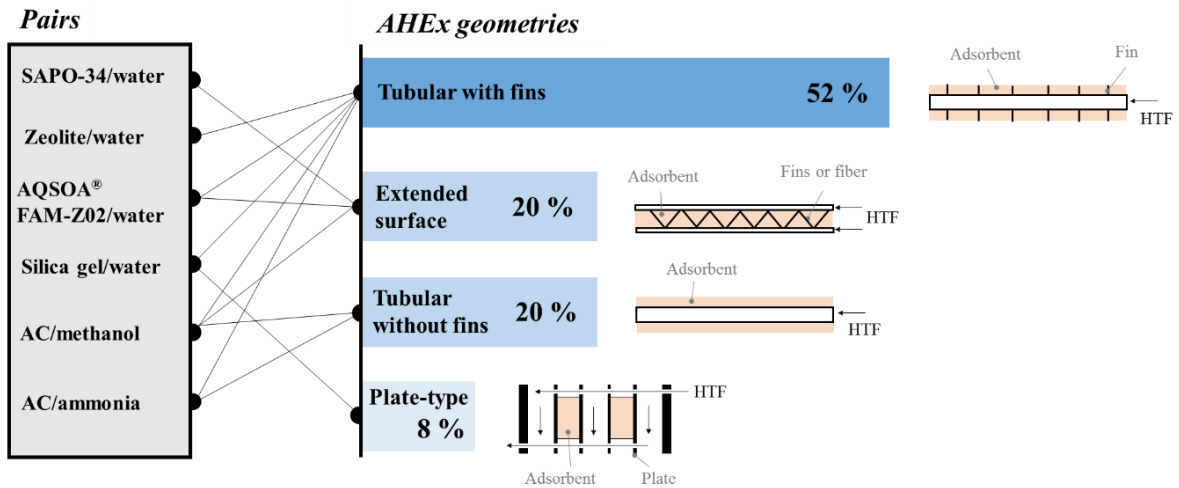


Fig. 2.12 – AHEx geometries investigated for AHPs (tubular with and without fins, extended surface (*e.g.*, finned plate and fiber plate) and plate-type (*e.g.*, lamella heat exchangers)) and percentage of works that adopted each geometry, along with information of the respective investigated adsorbent/adsorbate pairs. Only essays focusing experimental or both theoretical and experimental work were considered for calculating the percentages (data from Table A2.1).

The tubular geometry with fins is attractive for vacuum operation [23], and applied in commercial AHPs [139]. More than 50 % of the studies involving some experimental work

on AHPs deal with this geometry (with almost all the working pairs, from zeolite/water to AC/ammonia). Tubular AHExs without fins were essentially used with AC/(ammonia or methanol) (20 % of the studies), which may be partly due to the higher λ_{ads} of ACs (up to *ca.* $0.5 \text{ W m}^{-1} \text{ K}^{-1}$ [93]) in relation to zeolites, zeotypes and silica gel (Section 2.3.5). Nonetheless, most of the theoretical works listed in Table A2.1 (*ca.* 70 %) adopted tubular geometry without fins, since it is simple and well-studied in the literature for AHPs, facilitating comparative studies of different working pairs and the analysis of general trends. Extended surface type AHExs, such as finned plate and fiber plate were focused by 20 % of the experimental works reported in the literature, mainly for operation under vacuum (using water or methanol as refrigerants), and are among the most promising geometries [34, 140].

The overall heat transfer coefficient (U) (Eq. (2.4), Section 2.3.5), heat exchanger area, and the ratio $m_{\text{ads}}/m_{\text{metal}}$ are factors with significant impact on the performance of an AHEx [133, 140, 141]. Fig. 2.13(a) is a simplified representation of the most adopted AHEx geometries for adsorbent/water pairs, which are tubular with fins and extended surface heat exchangers (Fig. 2.12). For finned tubes, values of heat transfer area per overall volume of heat exchanger (or surface area density) up to $3300 \text{ m}^2 \text{ m}^{-3}$ have been reported, while finned plate heat exchangers (extended surface type) may reach *ca.* $5900 \text{ m}^2 \text{ m}^{-3}$ [138], allowing more compact designs.

Fig. 2.13(b) shows typical values of U , $m_{\text{ads}}/V_{\text{AHEx}}$ (indicator of compactability) and $m_{\text{ads}}/m_{\text{metal}}$, for the two geometries, using loose grains or coating configurations: finned tubes/loose grains [56, 110, 125, 142-144], finned tubes/coatings [55, 63, 131, 142, 144], extended surface/loose grains [133, 140, 145-147], or extended surface/coatings [63, 83, 148]. Using coated finned tubes instead of loose grains increased U by a factor of *ca.* 4.5, approaching $106 \text{ W m}^{-2} \text{ K}^{-1}$, due to enhanced h_{ads} and λ_{ads} , and decreased δ (Eq. (2.4) and Fig. 2.11). Somewhat consistently, Dawoud *et al.* [55] reported that for loose pellets in a finned tube AHEx, the *SHPs* were less than a quarter of those measured using coatings.

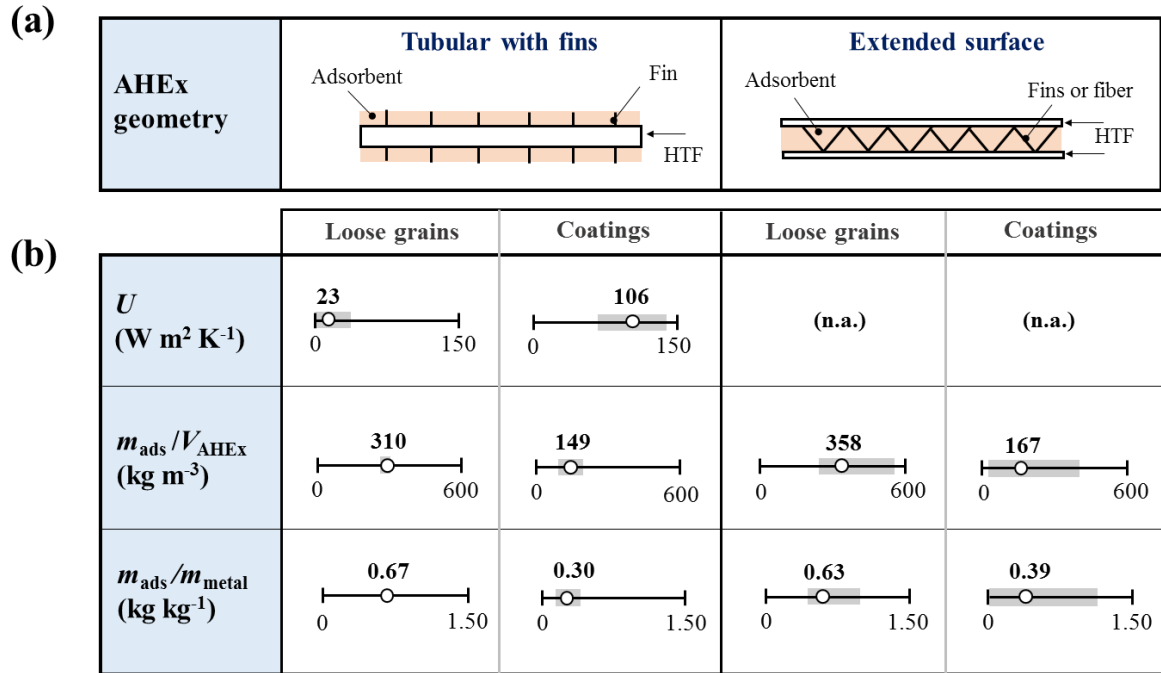


Fig. 2.13 – (a) Schematic representation of the AHEX geometries mostly adopted in AHPs using adsorbent/water pairs (tubular with fins and extended surface heat exchangers). (b) Values of U , m_{ads}/V_{AHEX} and m_{ads}/m_{metal} for both geometries, using loose grains or coatings, where the gray rectangles refer to the typical intervals found in the literature for adsorbent/water pairs, and the marked dots are averages (finned tubes/loose grains [56, 110, 125, 142-144], finned tubes/coatings [55, 63, 131, 142, 144], extended surface/loose grains [133, 140, 145-147], or extended surface/coatings [63, 83, 148]). When literature studies reported transient U values, the highest ones were used for comparison.

Independently of the geometry, a higher quantity of adsorbent may be embedded per unit volume of heat exchanger (m_{ads}/V_{AHEX}) when using loose grains instead of coatings (Fig. 2.13(b)). For coatings in finned tubes and extended surface AHEXs, the ratio m_{ads}/V_{AHEX} is in the range of 100 – 200 $kg m^{-3}$ [63, 142] and 40 – 390 $kg m^{-3}$ [63, 83, 133, 148], respectively (the respective average values are 149 and 167 $kg m^{-3}$). In general, the highest m_{ads}/V_{AHEX} values were reported for extended surface heat exchangers (567 $kg m^{-3}$ [145] for loose grains, and 388 $kg m^{-3}$ [148] for coatings); for finned tubes, values of 315 $kg m^{-3}$ [110] and 203 $kg m^{-3}$ [142] were reported for loose grains and coatings, respectively. These results suggest that more compact AHEXs may be constructed using an extended surface geometry.

The inert metal mass of the AHEX has a strong influence on the AHP thermodynamic performance (COP). This may be levelled off by the selection of a working pair that allows enhanced ΔW_{cycle} [46]. Higher maximum values of m_{ads}/m_{metal} have been published for extended surface heat exchangers (which are usually made of aluminum): with loose grains,

$m_{\text{ads}}/m_{\text{metal}}$ was in the range $0.5 - 1 \text{ kg kg}^{-1}$ [133, 140, 145-147] (0.63 kg kg^{-1} in average), whereas for coatings, $m_{\text{ads}}/m_{\text{metal}}$ of up to *ca.* 1.2 kg kg^{-1} was reported [148]. On the other hand, for finned tubes/(loose grains or coatings) $m_{\text{ads}}/m_{\text{metal}} < 0.7 \text{ kg kg}^{-1}$ [55, 63, 142, 143]. Freni *et al.* [46] reported that $m_{\text{ads}}/m_{\text{metal}}$ is typically in the interval $0.67 - 1.43 \text{ kg kg}^{-1}$ for extended surface AHExs consisting of finned flat-tube aluminum heat exchangers, and that traditional copper/aluminum finned tubes present $0.45 < m_{\text{ads}}/m_{\text{metal}} (\text{kg kg}^{-1}) < 0.63$. Hence, extended surface AHExs may lead to enhanced $m_{\text{ads}}/m_{\text{metal}}$, which is beneficial for *COP*. Girnik *et al.* [149] reported $m_{\text{ads}}/m_{\text{metal}}$ in the range $0.29 - 0.67 \text{ kg kg}^{-1}$ for prototypes; the average values indicated in Fig. 2.13(b) lie in this range.

Overall, a good compromise between the various factors is important to develop efficient, compact, lightweight and high surface area AHExs, which is a R&D priority in the field of components for AHPs [33].

2.3.7. Patents and applications

Commercial AHPs using water as refrigerant include those from Vaillant and Viessmann (described below in Section 2.4.1), which are amongst play leaders in the field of AHPs for heating purposes in the building sector, particularly when using water as refrigerant. Table 2.1 lists several filed and granted patents by Vaillant and Viessmann.

Chapter 2: Introduction

Table 2.1 – Published patents regarding AHPs, where the patent number and the priority year are indicated, along with scope and observations.

Patent number	Priority year	Patent scope	Observations	Ref.
DE19902695B4	1998	Concepts of an AHP system and components (radiation shielding)	<ul style="list-style-type: none"> ▪ AHP with low structural complexity and simple construction is proposed, with a single vacuum container (less design effort comparing to prior art, in which separate containers were used for the AHEx, condenser and evaporator); ▪ Use of radiation shielding with perforations between the AHEx and evaporator/condenser, facilitating the refrigerant circulation and avoids heat transfer by radiation between the components (since it decreases the efficiency). 	[150]
EP1178269B1	2000	Concept of AHP components (evaporator/condenser)	<ul style="list-style-type: none"> ▪ Improvement of heat transfer in the evaporator/condenser by means of a spiral shape concept using corrugated tube. 	[151]
EP1180650B1	2000	Concept of AHP components (AHEx)	<ul style="list-style-type: none"> ▪ Fast and efficient adsorption-desorption process is achieved by means of an AHEx with increased surface area, with a single layer of grains between ribs. 	[152]
EP1184629B1	2000	Concept of an AHP	<ul style="list-style-type: none"> ▪ An AHEx (1) and a high T heat exchanger (connected to a burner) (2) are included in an adsorption heating circuit (closed water loop), and the water for the adsorbent regeneration is heated in (2); ▪ For improved efficiency, a higher water flow rate in (2) than in (1) is provided, by means of a bifurcation of the water circuit at the outlet of (2), which allows part of the water to be joined to the inlet of (2) (an injector pump is used), while the remaining enters in the AHEx. 	[153]

(continuation in the next page)

Chapter 2: Introduction

EP1239240B1	2001	Concept of AHP components (AHEX) and production method	<ul style="list-style-type: none"> AHEX in which the zeolite pellets are held securely around a pipe through lamellas and flanged rims, which ensures good heat transfer with the HTF. A simple production method of the adsorbent heat exchanger is proposed (prior art systems involved expensive and unsafe filling processes) 	[154]
EP1245910B1	2001	Concept of an AHP and operation method	<ul style="list-style-type: none"> AHP of simple construction is claimed, and a method to avoid heat losses when switching the stages (time switch between adsorption-evaporation and desorption-condensation preferably between 5 and 30 min). 	[30]
EP1278028B1	2001	Concept of AHP components (radiation shielding)	<ul style="list-style-type: none"> Several variants for radiation shielding in AHPs are described (the heat transfer by radiation from the AHEX to the condenser leads to reduced condensation capability (in desorption stage), and between the AHEX and the evaporator decreases the quantity of heat extracted from the environment (in adsorption stage)). 	[155]
EP1279910B1	2001	Operation method and control strategy of an AHP	<ul style="list-style-type: none"> Method for optimal release of heat and efficient heat use in AHPs (<i>e.g.</i>, abrupt shutdown of the system would lead to overheating and heat losses). 	[156]
EP1279909B1	2001	Concept of an AHP and operation method	<ul style="list-style-type: none"> An AHP combined with a burner. For utmost exploitation of the heat in the exhaust gases, they may be used to: (i) preheat the air entering the burner; (ii) heat the evaporator (mainly when the air temperature is low); (iii) heat the fluid in the customer heating circuit. 	[157]
DE10235737A1	2001	Concept of an AHP and operation method	<ul style="list-style-type: none"> AHP combined with a burner, in which the heating is ensured by a conventional heater when the AHP module cannot operate (<i>e.g.</i>, when the environmental heat source T is very low, the fluid in the heating circuit is by-passed directly to the alternative heater). 	[158]

(continuation in the next page)

Chapter 2: Introduction

EP1288596B1	2001	Control strategy of an AHP	<ul style="list-style-type: none"> ▪ The control of AHPs (which is difficult) is managed by a continuous-action cascade control system. ▪ The controlled variables include the temperature of the consumer circuit, and the manipulated variables include the mass flow rates of the HTF in the AHEx circuit, and fuel and air fed to the burner. 	[159]
DE10242820A1	2001	Operation method and control strategy of an AHP	<ul style="list-style-type: none"> ▪ Exhaust gas + air are used to heat the AHEx. ▪ ΔT between the inlet and outlet of the AHEx is monitored by a controller that reverses the operation (from adsorption to desorption and <i>vice-versa</i>) when the differences achieve set point values. 	[160]
DE10310748B3	2003	Operation method of an AHP (in the presence of disturbing gases)	<ul style="list-style-type: none"> ▪ The invention regards a foreign gas removal method, carried out between the adsorption and desorption stages in regular intervals (<i>e.g.</i>, every 500 h) or when disturbing gases (such as CO₂, N₂) are detected. It consists on heating the AHEx while simultaneously promoting an overpressure on the condenser, where the discharge of the vapor and the foreign gases <i>via</i> a discharge device occurs. 	[161]
DE 102004049411B4	2004	Concept of an AHP	<ul style="list-style-type: none"> ▪ A vacuum AHP in which the evaporator and condenser are in different compartments and construction costs are kept as low as possible. ▪ The concept of this system encompasses an annular jacket enclosing the evaporator, condenser and AHEx, where exhaust gases circulate and release heat to the AHP system, for enhancing the efficiency. 	[162]
DE102004049408 B4	2004	Concept of AHP components (element for separation between evaporator and condenser)	<ul style="list-style-type: none"> ▪ A technical solution is provided to ensure proper separation between the evaporator and the condenser of a vacuum AHP, to avoid condensation of the desorbed vapor in the evaporator instead of condenser (P is lower in the evaporator than in the condenser). 	[163]

Chapter 2: Introduction

DE202004015674 U1 (utility model)	2004	Concept of an AHP	<ul style="list-style-type: none"> ▪ Wall-mounted AHP combined with a heat generator (burner for liquid or gaseous fuel) is provided (prior art systems are floor-standing units). 	[164]
EP1653168B1	2004	Hydraulics	<ul style="list-style-type: none"> ▪ The absence of hydraulic separation between the AHEx and the costumer heating circuits leads to losses of efficiency, since that the HTF needs to periodically heat or cool the AHEx; ▪ The invention aims at the design of separated hydraulic circuits, for instance, including an additional heat exchanger between the AHEx and the costumer heating circuits, in which the AHEx circuit can by-pass this heat exchanger. 	[165]
EP1645820B1	2005	Operation method and control strategy of a burner in an AHP system	<ul style="list-style-type: none"> ▪ A burner heats a HTF for adsorbent regeneration in an AHP. The desorption stage lasts $t_{DES} = t_1 + t_2 + t_3$, during which the burner operates at two distinct power levels: during t_1 at a high power level until a temperature of 5-10 °C below the maximum desorption temperature is reached; during t_2 at a lower power level until reaching the maximum desorption temperature; during t_3 the burner is turned off; ▪ Modulating burners are discarded. 	[166]
EP2058608A2	2007	Concept of AHP components (AHEx)	<ul style="list-style-type: none"> ▪ An AHEx allowing effective adsorption and desorption, by means of increasing the surface area of the AHEx and providing channels for the circulation of the refrigerant. 	[167]
EP1985948B1	2007	Hydraulics and operation method of an AHP	<ul style="list-style-type: none"> ▪ A vacuum AHP in which the AHEx and the costumer heating circuits are decoupled in the desorption stage and coupled in the adsorption stage. A safe operation, without excessive pressure in the AHEx circuit during the desorption stage, is ensured. 	[42]

(continuation in the next page)

Chapter 2: Introduction

EP2045547B1	2007	Concept of AHP components (element for separation between evaporator and condenser)	<ul style="list-style-type: none"> Proper separation between the evaporator and condenser of a vacuum AHP (“ball closure element”). 	[168]
EP2083231B1	2008	Concepts of an AHP and components (evaporator and displacement body between evaporator and AHEx chambers)	<ul style="list-style-type: none"> Improved evaporation process in a vacuum AHP is achieved, by means of pumping the refrigerant to the evaporator (helical tube), which results in wetting or spraying the evaporator with refrigerant. A displacement body between the AHEx and evaporator chambers is used. 	[169]
US20110183835 A1	2008	Adsorbents and production methods	<ul style="list-style-type: none"> Adsorbent coatings are prepared with 80-85 % of adsorbent, inorganic binders and fibers, in order to avoid prior art drawbacks (degradation of organic substances, <i>P</i> increase in the AHP, incompatibility of binders with adsorbents). Possible coating methods for metals are spraying, painting and application by immersion, followed by a drying stage. 	[134]
EP2309211B1	2009	Concept of an AHP and operation method	<ul style="list-style-type: none"> The invention aims at the optimisation of hydraulic interconnections and operation during the adsorption stage of a vacuum AHP, to achieve higher efficiency comparing with the prior art; A buffer tank is included in the system, which temporarily receives and stores cold HTF that is used to cool the AHEx prior to the adsorption stage. 	[170]

(continuation in the next page)

Chapter 2: Introduction

US8544293B2	2009	Concept of AHP components (element for separation between evaporator and AHEx chambers)	<ul style="list-style-type: none"> ▪ An optimal separation between the AHEx and the evaporator chambers during desorption stage is ensured by a separating body. 	[171]
EP2447623A3	2010	Concept of an AHP	<ul style="list-style-type: none"> ▪ AHP system with a modular design, that can be easily manufactured and assembled, and is favorable for mass production. 	[172]
US20120055194 A1	2010	Concept of AHP components (condenser)	<ul style="list-style-type: none"> ▪ An improved vacuum sorption device containing an AHEx enclosed by a condenser. Details on the condenser characteristics are given, which ensure high pressure stability and high heat transfer, with a simple production process. 	[173]

Pertinent aspects may be summarized from the patent literature as follows:

- (i) reducing efforts of design, manufacture and assembling, and costs of AHP components seem a major concern (for instance, modular system designs are favorable [172]) [30, 150, 154, 162];
- (ii) overall performance improvements depend on the optimization of control strategies [30, 156, 159, 160, 166], and components (*e.g.*, using condenser-jacket designs or spiral shape concepts [151, 173], coated and high surface area AHExs [134, 152, 167], radiation shieldings (to avoid unfavorable heat transfer by radiation between the AHP components) [150, 155], adequate separation elements between the AHP compartments working at different pressures (to avoid condensation of the desorbed vapor inside the evaporator) [163, 168, 171]);
- (iii) hybrid appliances combining AHPs with conventional heaters are a solution to assure the system operation when a low $T_{\text{heat source}}^{\text{low}}$ prohibits the evaporation process [158];
- (iv) safe operation without excessive pressure in circuits implies proper hydraulics (*e.g.*, use of overflow valves) [42];
- (v) AHPs working under vacuum may be susceptible to pressure perturbations by foreign gases (CO_2 , N_2), which should be properly removed from the system [161];
- (vi) in systems combining AHPs and gas burners, various alternatives exist for utmost exploitation of the heat of exhaust gases (for example, preheating of the air entering the burner, heating the evaporator and/or the consumer heating circuit) [157].

Fig. 2.14 displays the scope of the patents from Vaillant and Viessmann listed in Table 2.1 by priority year (*i.e.*, the filing year of the very first patent application for each invention), along with the year in which their first AHPs were launched in the market. Based on this information, *ca.* 10 years of R&D are likely to be necessary for developing such complex systems.

In the whole, the analyzed patents address R&D priorities for improving AHPs, which include the development of compact, efficient and low cost components, and the implementation of advanced strategies for optimal control of the operation of AHPs [33].

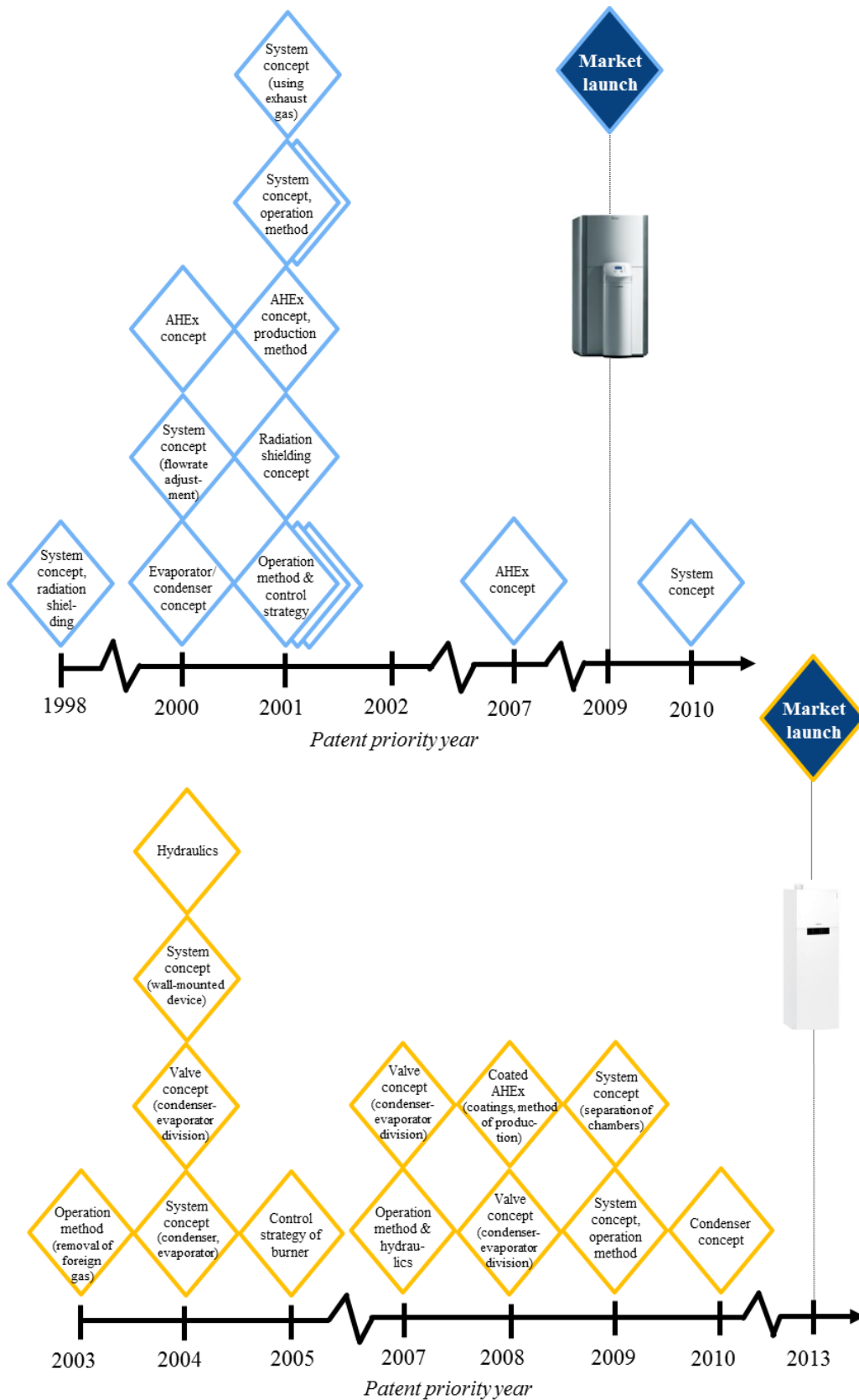


Fig. 2.14 – Scope of the patents listed in Table 2.1 displayed by priority year (*i.e.*, the filing year of the very first patent application for each invention): (top) Vaillant; (bottom) Viessmann. The years in which their first AHPs were launched in the market are also marked.

2.4. Commercial AHPs *versus* conventional technologies

In this chapter, the concepts of Vaillant and Viessmann AHPs available in the market are presented, along with comparisons of adsorption-based systems with conventional heating technologies regarding primary energy consumption, CO₂ emissions, dimensions and costs.

2.4.1. Vaillant and Viessmann heating appliances

Vaillant and Viessmann commercialize small capacity (up to 15 kW) gas-fired hybrid AHPs, which comprise a gas condensing boiler to intermittently drive a zeolite/water AHEx, and to meet the peak load if the required heat demand exceeds the heating capacity of the AHP module. These products may be used for space heating and DHW production and present $COP \cong 1.35$ (for water delivered at 308-313 K), and, when in heat pumping mode, they cannot produce water above 328 K [12, 119, 174].

Fig. 2.15 is a simplified representation of a gas-fired AHP from Vaillant (ZeoTHERM VAS) (launched in the market in 2009) during desorption and adsorption stages [12, 175]. It includes a gas heating system, one AHEx (composed of a finned tube heat exchanger with zeolite pellets between the fins), one heat exchanger that works either as condenser or evaporator, a solar thermal collector acting as the low temperature heat source for the evaporator (in the summer, the solar collector can provide DHW), two additional heat exchangers (identified with 1 and 2 in Fig. 2.15) used to transfer the heat from the AHP module to the space heating system, and a DHW tank [119].

During isobaric desorption stage (Fig. 2.15(a)), the zeolite is heated by hot water at *ca.* 383 K, which circulates in a loop connecting the AHEx with the gas burner heat exchanger. As regeneration proceeds, the adsorbed water vapor is released and condenses in the condenser, delivering useful heat to the heating system through the heat exchanger 2. During isobaric adsorption stage (Fig. 2.15(b)), the burner is switched off, and the dried zeolite adsorbs water vapor from the evaporator, which in turn is feeding environmental heat into the process through the solar thermal collector. As adsorption continues, latent heat of adsorption is supplied to the heating system through the heat exchanger 1 [118, 119].

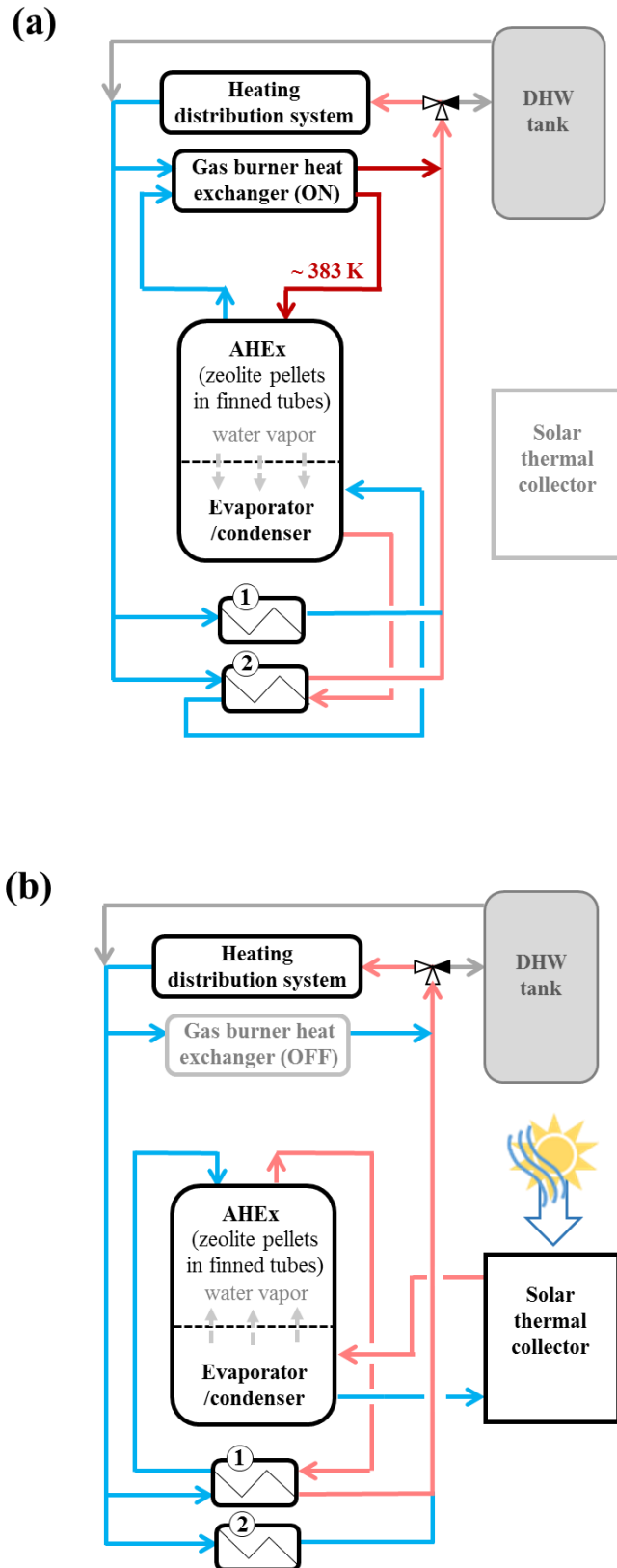


Fig. 2.15 – Simplified representation of the gas-fired AHP from Vaillant (ZeoTHERM VAS) during (a) desorption and (b) adsorption stages (adapted from [119]). (1) and (2) are heat exchangers used to transfer the heat from the AHP module to the space heating system. Blue, pink and red lines represent low, intermediate and high temperature fluids, respectively.

Fig. 2.16 shows the Vitosorp 200-F gas-fired AHP from Viessmann (launched in the market in 2013-2014) during desorption and adsorption stages, which presents some improvements in relation to the Vaillant technology [10, 86, 119, 139]. The Vitosorp technology can use either geothermal energy (geothermal collectors, cages or probes), solar energy, or a combination of both as thermal sources for the evaporator; the condenser and the evaporator are independent, eliminating the internal heat losses emerging from heating up and cooling down the same heat exchanger working periodically as an evaporator or condenser; a falling film evaporator is used, which offers much higher evaporator capacity; coatings are adopted instead of loose pellets (Vaillant), allowing improvements in the *SHPs* by a factor of ten (*ca.* 1600 W kg^{-1}). There is always direct heat transfer between water from the heating distribution system and the condenser or AHEx, due to the integration of the AHP module into the hydraulic scheme of the heating appliance, offering quasi continuous heat delivery. The Viessmann appliance has three distinct operating modes [10]: (i) a heat pump mode for low heat demand, in which the AHP module covers the base load; (ii) a mixed mode, performed when the demand is higher than the heating capacity of the adsorption module, in which both the AHP and the condensing boiler work in series to cover the demand; (iii) a direct heating mode, carried out if the demand is higher than the heating capacity of the mixed operating mode, and in which the heating appliance is operated as a traditional condensing boiler.

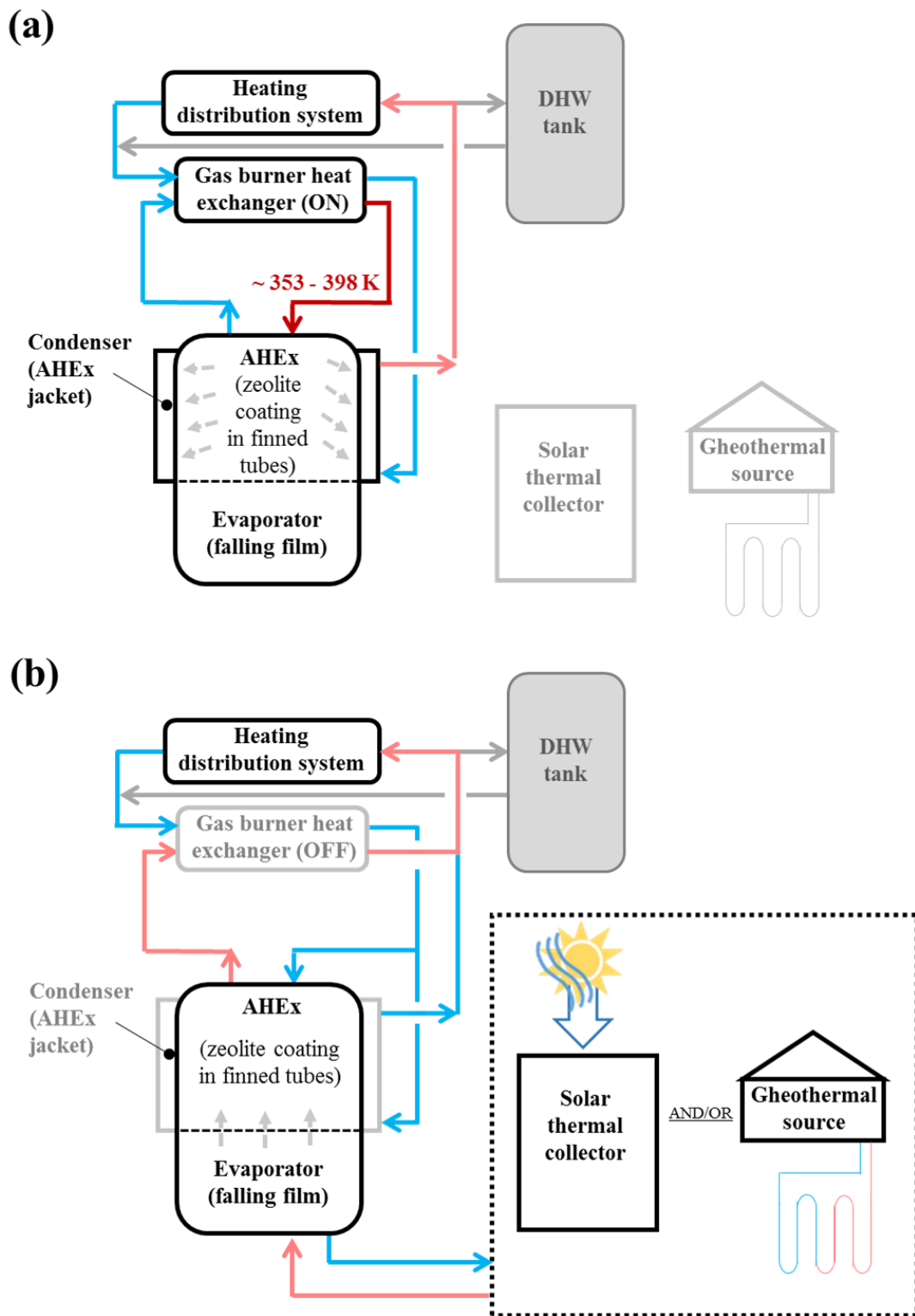


Fig. 2.16 - Simplified representation of the gas-fired AHP from Viessmann (Vitosorp 200-F) during (a) desorption and (b) adsorption stages (adapted from [10, 119]). Blue, pink and red lines regard low, intermediate and high temperature fluids, respectively.

2.4.2. AHPs versus conventional heating technologies

The advantages of a gas-fired AHP over more conventional gas heating technologies (non-condensing and condensing boilers) in terms of primary energy consumption, renewable energy share, and reduction of CO₂ emissions are exemplified in Fig. 2.17 for a 150 m² house [119].

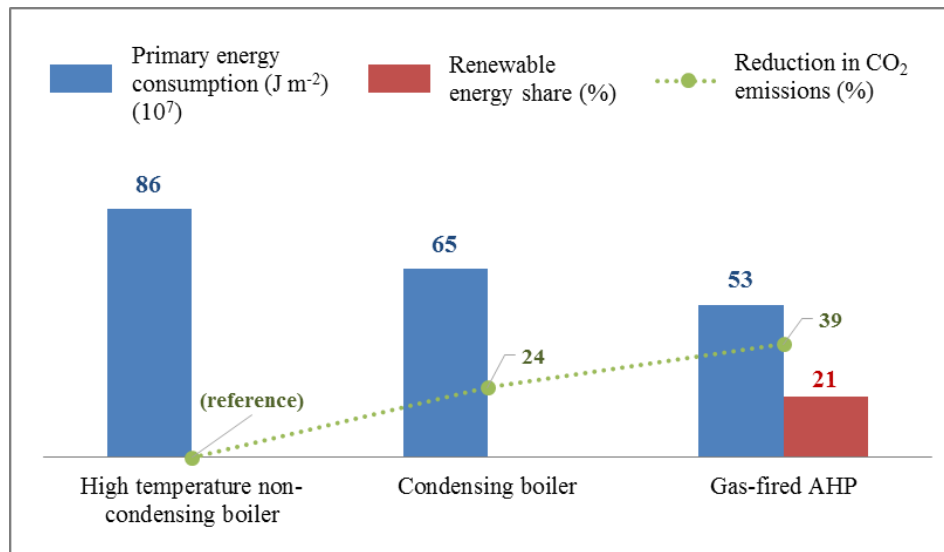


Fig. 2.17 – Potential of gas-fired AHPs for a typical 150 m² German house over gas non-condensing and condensing boilers, in terms of primary energy consumption, renewable energy share and reduction in the CO₂ emissions [119].

Comparing with non-condensing boilers (main house heating technology in Germany), gas-fired AHPs allow a decrease in primary energy consumption from 86×10⁷ to 53×10⁷ J m⁻² (ca. 38 %) due to the pumping of environmental energy into the process (21 % of renewable energy share), along with a reduction in CO₂ emissions of 39 %.

Comparing gas-fired AHPs with vapor compression heat pumps (powered by electricity), the first technology has been leading to bigger and more costly products. Vitosorp 200-F appliance from Viessmann has the dimensions 0.600×0.595×1.875 m³, which includes the gas condensing boiler and the AHP module, albeit the DHW tank is located outside the appliance, and costs ca. 13000 € (without VAT [176]; September 2017). On the other hand,

for instance, the IVT GEO 312C electrically driven heat pump, which is a ground source heat pump with equivalent power range, and intended for space heating and DHW production, has similar dimensions ($0.600 \times 0.660 \times 1.800 \text{ m}^3$), but includes the heat pump module and also a DHW storage tank of 190 L inside the appliance, and costs *ca.* 7500 € (without VAT; September 2017) [175, 177]. In terms of primary energy ratio (*PER*), electrically driven heat pumps, which are highly efficient to provide space heating and DHW in buildings, lead to values of 1.60 and 1.40 (ground-coupled and air-source appliances, respectively), and thermally driven heat pumps lead to similar *PER* (in the range of 1.20 – 1.60) [33].

Overall, gas-fired AHPs are an interesting technology to reduce primary energy consumption and CO₂ emission in the heating sector [12]. Although primary energy ratios of thermally driven appliances have already approached those of vapor compression technology, efforts need to be put on the development of smaller and cheaper systems in order to increase their market share. Presently, AHPs are expensive, too big and heavy to compete with conventional systems, and hence poorly present in the market in comparison to electrically driven heat pumps [33, 35]. Although sanitary hot water heat pumps have been the fastest growing heat pump segment in Europe, with double digit growth [117], AHPs exclusively intended for DHW production are absent from the market, to the best of our knowledge. Few prototypes aiming at this application have been reported. Dong *et al.* [62] studied an hybrid system combining a gas boiler, a water storage tank and an AHP with two adsorbent beds of AQSOA[®] FAM-Z02/water pair. The gas boiler supplies hot water for bed regeneration (at 358 K) and promotes additional heating (up to 343 K) of the water that exits the AHP. Tajima *et al.* [59] combined a gas water heater with an AHP with two and four adsorbent beds using silica gel/water, and concluded that using two beds is more practical. Ally [178] reported the modeling and testing of a residential gas-fired adsorption heat pump water heater using AC/ammonia, for which the obtained performances were below the target, although a competitive cost premium for market introduction was pointed out.

2.5. Final outlook

The climate changes and scarcity of resources have been forcing the adoption of policies for driving a more sustainable development of the society. In the building heating sector, increasing attention has been put on adsorption heat pumps (AHPs) due to their eco-friendly characteristics over conventional technologies, as vapor compression systems. Several adsorbents have been investigated over the years for AHPs, from conventional zeolites and activated carbon to SAPOs, CSPMs and MOFs, using mainly water, methanol and ammonia as adsorbates. Nevertheless, only very few adsorbents are applied today, due to their generally limited loading capacities, operation in a relatively narrow window of conditions, stability issues, cost, and complex bed configurations, which, in the whole, are constraining the expansion of this technology. Along with the necessary R&D in the field of materials and scale-up techniques, efforts should focus on the development of optimized components and control strategies, such as: (i) coated extended surface heat exchangers (*e.g.*, finned plate and fiber plate geometries) to develop compact and lightweight AHExs, providing high efficiency and thermal power; (ii) advanced control strategies allowing adaption to changes in operating conditions and user requirements, while ensuring optimal duration of the cycle stages. With respect to the market of small capacity adsorption appliances (up to 15 kW), gas-fired AHPs using water as refrigerant for space heating and DHW production have been commercialized, which comprise a gas condensing boiler and a zeolitic module. AHPs exclusively for DHW production seem absent from the market so far.

Nomenclature

A	Heat exchanger area (m^2)
AC	Activated carbon
AHE _x	Adsorbent heat exchanger
AHP	Adsorption heat pump
COP	Coefficient of performance
CSPM	Composite “Salt in Porous Matrix”
DHW	Domestic hot water
E	Electrical energy input (J)
EU-28	European Union which is composed by 28 countries
$f_{p,elect}$	Primary energy conversion factor for electricity
$f_{p,fuel}$	Primary energy conversion factor for fuel
F	Fuel energy input (gross calorific value) (J)
GWP	Global warming potential
h	Heat transfer coefficient ($\text{W m}^{-2} \text{K}^{-1}$)
HTF	Heat transfer fluid
KPI	Key performance indicator
m	Mass (kg)
MOFs	Metal organic frameworks
ODP	Ozone depletion potential
P	Pressure (Pa)
P^{σ}	Saturation pressure (Pa)
PER	Primary energy ratio
Q	Heat (J)
SAPO	Silicoaluminophosphate
SHP	Specific heating power (W kg^{-1})
t	Time (s)
t_{cycle}	Cycle time (s)
T	Temperature (K)
T_1	Temperature at the beginning of isobaric adsorption (K)

Chapter 2: Introduction

T_2	Temperature at the beginning of isosteric heating (K)
T_3	Temperature at the beginning of isobaric desorption (K)
T_4	Temperature at the beginning of isosteric cooling (K)
$T_{\text{heat source}}^{\text{low}}$	Temperature of the energy source for evaporator (K)
$T_{\text{heat source}}^{\text{high}}$	Temperature of the energy source for bed regeneration (K)
U	Overall heat transfer coefficient of the AHEx ($\text{W m}^{-2} \text{K}^{-1}$)
V_{AHEx}	Volume of the AHEx (m^3)
VCS	Vapor-compression systems
$VSHP$	Volume specific heating power (W m^{-3})
VLE	Vapor-liquid equilibrium
W	Adsorbent loading (adsorbate concentrated in the solid) (kg kg^{-1})

Greek symbols

δ	Adsorbent bed thickness (m)
ΔH_v	Latent heat of vaporization (J kg^{-1})
ΔT_{cycle}	Maximum bed temperature difference in the adsorption cycle (K)
ΔW_{cycle}	Solid loading swing (kg kg^{-1})
λ_{ads}	Thermal conductivity of the adsorbent bed ($\text{W m}^{-1} \text{K}^{-1}$)

Subscripts

ads	Adsorbent; adsorbent side
cond	Condenser
eq	Equilibrium
evap	Evaporator
fluid	Fluid side
metal	Metal components of the adsorbent heat exchanger
1 → 2	Isobaric adsorption stage
2 → 3	Isosteric heating stage
3 → 4	Isobaric desorption stage
4 → 1	Isosteric cooling stage

References

- [1] PricewaterhouseCoopers (PwC) UK - Megatrends, <https://www.pwc.co.uk/issues/megatrends.html>, (accessed in 12.09.2017).
- [2] European Commission - Energy roadmap 2050, https://ec.europa.eu/energy/sites/ener/files/documents/2012_energy_roadmap_2050_en_0.pdf, (accessed in 12.09.2017).
- [3] Eurostat - Final energy consumption in the EU-28 residential sector by type of end-use (2015), http://ec.europa.eu/eurostat/statistics-explained/index.php/File:Final_energy_consumption_in_the_residential_sector_by_type_of_end-use,_EU-28,_2015.png, (accessed in 20.09.2017).
- [4] Eurostat - Share of fuels in the final energy consumption in the EU-28 residential sector by type of end-use in 2015, [http://ec.europa.eu/eurostat/statistics-explained/index.php/File:Share_of_fuels_in_the_final_energy_consumption_in_the_residential_sector_by_type_of_end-use,_2015_\(%25\).png](http://ec.europa.eu/eurostat/statistics-explained/index.php/File:Share_of_fuels_in_the_final_energy_consumption_in_the_residential_sector_by_type_of_end-use,_2015_(%25).png), (accessed in 20.09.2017).
- [5] Eurostat - Evolution of electricity prices for household consumers in EU-28 (2007-2016), http://ec.europa.eu/eurostat/statistics-explained/index.php/Electricity_price_statistics#Electricity_prices_for_household_consumers, (accessed in 18.09.2017).
- [6] Eurostat - Evolution of natural gas prices for EU-28 household consumers (2007-2016), http://ec.europa.eu/eurostat/statistics-explained/index.php/Natural_gas_price_statistics#Natural_gas_prices_for_household_consumers, (accessed in 20.09.2017).
- [7] Eurostat - Electricity production, consumption and market overview, http://ec.europa.eu/eurostat/statistics-explained/index.php/Electricity_production,_consumption_and_market_overview, (accessed in 11.09.2017).
- [8] J.M. Pinheiro, S. Salústio, J. Rocha, A.A. Valente, C.M. Silva, Analysis of equilibrium and kinetic parameters of water adsorption heating systems for different porous metal/metalloid oxide adsorbents, *Applied Thermal Engineering*, 100 (2016) 215-226.
- [9] H. Demir, M. Mobedi, S. Ülkü, A review on adsorption heat pump: Problems and solutions, *Renewable and Sustainable Energy Reviews*, 12 (2008) 2381-2403.
- [10] B. Dawoud, On the development of an innovative gas-fired heating appliance based on a zeolite-water adsorption heat pump; system description and seasonal gas utilization efficiency, *Applied Thermal Engineering*, 72 (2014) 323-330.
- [11] F. Ziegler, State of the art in sorption heat pumping and cooling technologies, *International Journal of Refrigeration*, 25 (2002) 450-459.
- [12] F. Meunier, Adsorption heat powered heat pumps, *Applied Thermal Engineering*, 61 (2013) 830-836.
- [13] J.M. Pinheiro, A.A. Valente, S. Salústio, N. Ferreira, J. Rocha, C.M. Silva, Application of the novel ETS-10/water pair in cyclic adsorption heating processes: Measurement of equilibrium and kinetics properties and simulation studies, *Applied Thermal Engineering*, 87 (2015) 412-423.
- [14] N.D. Banker, P. Dutta, M. Prasad, K. Srinivasan, Performance studies on mechanical+adsorption hybrid compression refrigeration cycles with HFC 134a, *International Journal of Refrigeration*, 31 (2008) 1398-1406.

- [15] L.F. Cabeza, A. Solé, C. Barreneche, Review on sorption materials and technologies for heat pumps and thermal energy storage, *Renewable Energy*, 110 (2017) 3-39.
- [16] M.F. de Lange, K.J.F.M. Verouden, T.J.H. Vlugt, J. Gascon, F. Kapteijn, Adsorption-Driven Heat Pumps: The Potential of Metal–Organic Frameworks, *Chemical Reviews*, 115 (2015) 12205-12250.
- [17] A.A. Askalany, M. Salem, I.M. Ismael, A.H.H. Ali, M.G. Morsy, B.B. Saha, An overview on adsorption pairs for cooling, *Renewable and Sustainable Energy Reviews*, 19 (2013) 565-572.
- [18] A.A. Askalany, B.B. Saha, K. Kariya, I.M. Ismail, M. Salem, A.H.H. Ali, M.G. Morsy, Hybrid adsorption cooling systems—An overview, *Renewable and Sustainable Energy Reviews*, 16 (2012) 5787-5801.
- [19] B. Choudhury, B.B. Saha, P.K. Chatterjee, J.P. Sarkar, An overview of developments in adsorption refrigeration systems towards a sustainable way of cooling, *Applied Energy*, 104 (2013) 554-567.
- [20] A.N. Shmroukh, A.H.H. Ali, S. Ookawara, Adsorption working pairs for adsorption cooling chillers: A review based on adsorption capacity and environmental impact, *Renewable and Sustainable Energy Reviews*, 50 (2015) 445-456.
- [21] D.C. Wang, Y.H. Li, D. Li, Y.Z. Xia, J.P. Zhang, A review on adsorption refrigeration technology and adsorption deterioration in physical adsorption systems, *Renewable and Sustainable Energy Reviews*, 14 (2010) 344-353.
- [22] A.O. Dieng, R.Z. Wang, Literature review on solar adsorption technologies for ice-making and air-conditioning purposes and recent developments in solar technology, *Renewable and Sustainable Energy Reviews*, 5 (2001) 313-342.
- [23] A. Sharafian, M. Bahrami, Assessment of adsorber bed designs in waste-heat driven adsorption cooling systems for vehicle air conditioning and refrigeration, *Renewable and Sustainable Energy Reviews*, 30 (2014) 440-451.
- [24] I. Sarbu, C. Sebarchievici, General review of solar-powered closed sorption refrigeration systems, *Energy Conversion and Management*, 105 (2015) 403-422.
- [25] A.A. Askalany, M. Salem, I.M. Ismail, A.H.H. Ali, M.G. Morsy, A review on adsorption cooling systems with adsorbent carbon, *Renewable and Sustainable Energy Reviews*, 16 (2012) 493-500.
- [26] R.P. Sah, B. Choudhury, R.K. Das, A review on adsorption cooling systems with silica gel and carbon as adsorbents, *Renewable and Sustainable Energy Reviews*, 45 (2015) 123-134.
- [27] W.S. Teng, K.C. Leong, A. Chakraborty, Revisiting adsorption cooling cycle from mathematical modelling to system development, *Renewable and Sustainable Energy Reviews*, 63 (2016) 315-332.
- [28] G. Restuccia, A. Freni, G. Maggio, A zeolite-coated bed for air conditioning adsorption systems: parametric study of heat and mass transfer by dynamic simulation, *Applied Thermal Engineering*, 22 (2002) 619-630.
- [29] Y. Zhong, T. Fang, K.L. Wert, An adsorption air conditioning system to integrate with the recent development of emission control for heavy-duty vehicles, *Energy*, 36 (2011) 4125-4135.
- [30] B.D. Dawoud, R. Gasper, T.D. Hocker, R.D. Lang, F. Marth, U. Marx, T. Miltkau, R. Prescha, M. Stricker, J. Wienen, Method of operating an adsorption heat pump, EP 1245910 B1, Vaillant GmbH (2003).
- [31] L.W. Wang, R.Z. Wang, R.G. Oliveira, A review on adsorption working pairs for refrigeration, *Renewable and Sustainable Energy Reviews*, 13 (2009) 518-534.

- [32] A. Kühn, F. Ziegler, Cycle basics of thermally driven heat pumps in: A. Kühn (ed.) Thermally driven heat pumps for heating and cooling, Universitätsverlag der TU Berlin, Berlin, 2013.
- [33] J.M. Corberan, M. Axell, R.d. Boer, A. Freni, U. Jakob, S. Landolina, P. Lundqvist, M. Monsberger, R. Nordman, T. Nowak, T. Oltersdorf, S. Spoelstra, F. Ziegler, Heat Pumps, in: Strategic Research Priorities for Cross-cutting Technology, Global CCS Institute, European Technology Platform on Renewable Heating and Cooling, Belgium, 2012, pp. 48-75.
- [34] U. Wittstadt, G. Földner, E. Laurenz, A. Warlo, A. Große, R. Herrmann, L. Schnabel, W. Mittelbach, A novel adsorption module with fiber heat exchangers: Performance analysis based on driving temperature differences, *Renewable Energy*, 110 (2016) 154-161.
- [35] L.F. Cabeza, P. Schossig, Advances in sorption systems for energy efficient heating and cooling, *Renewable Energy*, 110 (2017) 1-2.
- [36] M. Fumagalli, A. Sivieri, M. Aprile, M. Motta, M. Zanchi, Monitoring of gas driven absorption heat pumps and comparing energy efficiency on primary energy, *Renewable Energy*, 110 (2017) 115-125.
- [37] Y. Liu, K.C. Leong, The effect of operating conditions on the performance of zeolite/water adsorption cooling systems, *Applied Thermal Engineering*, 25 (2005) 1403-1418.
- [38] A.R.M. Rezk, R.K. Al-Dadah, Physical and operating conditions effects on silica gel/water adsorption chiller performance, *Applied Energy*, 89 (2012) 142-149.
- [39] W. Zheng, W.M. Worek, G. Nowakowski, Effect of Operating Conditions on the Performance of Two-Bed Closed-Cycle Solid-Sorption Heat Pump Systems, *Journal of Solar Energy Engineering*, 117 (1995) 181-186.
- [40] M.F. de Lange, B.L. van Velzen, C.P. Ottevanger, K.J.F.M. Verouden, L.-C. Lin, T.J.H. Vlugt, J. Gascon, F. Kapteijn, Metal–Organic Frameworks in Adsorption-Driven Heat Pumps: The Potential of Alcohols as Working Fluids, *Langmuir*, 31 (2015) 12783-12796.
- [41] E. Elsayed, R. Al-Dadah, S. Mahmoud, A. Elsayed, P.A. Anderson, Aluminium fumarate and CPO-27(Ni) MOFs: Characterization and thermodynamic analysis for adsorption heat pump applications, *Applied Thermal Engineering*, 99 (2016) 802-812.
- [42] M.D. Stricker, B.D. Dawoud, Vacuum sorption device and method for operating a vacuum sorption device, EP 1985948 B1, Viessmann Werke GmbH & Co. KG (2015).
- [43] S.K. Henninger, F.P. Schmidt, H.M. Henning, Water adsorption characteristics of novel materials for heat transformation applications, *Applied Thermal Engineering*, 30 (2010) 1692-1702.
- [44] T.J. Barton, L.M. Bull, W.G. Klemperer, D.A. Loy, B. McEnaney, M. Misono, P.A. Monson, G. Pez, G.W. Scherer, J.C. Vartuli, O.M. Yaghi, Tailored Porous Materials, *Chemistry of Materials*, 11 (1999) 2633-2656.
- [45] S.V. Shelton, W.J. Wepfer, D.J. Miles, Ramp Wave Analysis of the Solid/Vapor Heat Pump, *Journal of Energy Resources Technology*, 112 (1990) 69-78.
- [46] A. Freni, G. Maggio, A. Sapienza, A. Frazzica, G. Restuccia, S. Vasta, Comparative analysis of promising adsorbent/adsorbate pairs for adsorptive heat pumping, air conditioning and refrigeration, *Applied Thermal Engineering*, 104 (2016) 85-95.
- [47] R.E. Critoph, Performance estimation of convective thermal wave adsorption cycles, *Applied Thermal Engineering*, 16 (1996) 429-437.
- [48] L. Dong, H. Huang, N. Kobayashi, Development of an All-in-One Type Adsorption Heat Pump for Heating Application, *International Journal of Chemical Reactor Engineering*, 9 (2011).

- [49] R.E. Critoph, Adsorption Refrigeration Research at Warwick, 1st TECCS meeting, University of Warwick (2007).
- [50] A.R. Pacho, Innovation in carbon/ammonia adsorption heat pump technology: a case study, Institute of Refrigeration (IOR), United Kingdom (2015).
- [51] S.K. Henninger, S.-J. Ernst, L. Gordeeva, P. Bendix, D. Fröhlich, A.D. Grekova, L. Bonaccorsi, Y. Aristov, J. Jaenchen, New materials for adsorption heat transformation and storage, *Renewable Energy*, 110 (2017) 59-68.
- [52] Y.B. Gui, R.Z. Wang, W. Wang, J.Y. Wu, Y.X. Xu, Performance modeling and testing on a heat-regenerative adsorptive reversible heat pump, *Applied Thermal Engineering*, 22 (2002) 309-320.
- [53] R.Z. Wang, Adsorption refrigeration research in Shanghai Jiao Tong University, *Renewable and Sustainable Energy Reviews*, 5 (2001) 1-37.
- [54] T. Núñez, W. Mittelbach, H.-M. Henning, Development of an adsorption chiller and heat pump for domestic heating and air-conditioning applications, *Applied Thermal Engineering*, 27 (2007) 2205-2212.
- [55] B. Dawoud, P. Hofle, S. Chmielewski, Experimental Investigation of the Effect Of Zeolite Coating Thickness on the Performance of a Novel Zeolite-Water Adsorption Heat Pump Module, Tenth International Conference Enhanced Building Operations, Kuwait (2010).
- [56] T. Zanifé, F. Meunier, Experimental results of a zeolite-water heat pump installed in a slaughter house, *Heat Recovery Systems and CHP*, 12 (1992) 131-142.
- [57] A.S. Ülkü, M. Mobedi, Adsorption in Energy Storage, in: B. Kılıç, S. Kakaç (eds.) *Energy Storage Systems*, Springer Netherlands, Dordrecht, 1989, pp. 487-507.
- [58] L. Marletta, G. Maggio, A. Freni, M. Ingrassiotta, G. Restuccia, A non-uniform temperature non-uniform pressure dynamic model of heat and mass transfer in compact adsorbent beds, *International Journal of Heat and Mass Transfer*, 45 (2002) 3321-3330.
- [59] A. Tajima, Y. Ozawa, H. Kawaguchi, Hybrid Gas Water Heater Combined with Adsorption Heat Pump Cycle for Commercial Use, *HVAC&R Research*, 12 (2006) 783-796.
- [60] Mitsubishi Plastics - Zeolitic water vapor adsorbent AQSOA, http://www.mitsubishi-chemical.de/uploads/tx_mfcmcecommerce/Aqsoa.pdf, (accessed in 18.07.2017).
- [61] H. Kakiuchi, S. Shimooka, M. Iwade, K. Oshima, M. Yamazaki, S. Terada, H. Watanabe, T. Takewaki, Water Vapor Adsorbent FAM-Z02 and Its Applicability to Adsorption Heat Pump, *KAGAKU KOGAKU RONBUNSHU*, 31 (2005) 273-277.
- [62] L. Dong, Y. Suzuki, N. Kobayashi, A novel hybrid adsorption heat pump water heater, *The Canadian Journal of Chemical Engineering*, 87 (2009) 741-747.
- [63] B. Dawoud, Water vapor adsorption kinetics on small and full scale zeolite coated adsorbents; A comparison, *Applied Thermal Engineering*, 50 (2013) 1645-1651.
- [64] G. Földner, Performance evaluation and optimization of adsorption modules, *Sorption Friends 2015, Sicily* (2015).
- [65] Y.I. Aristov, G. Restuccia, G. Cacciola, V.N. Parmon, A family of new working materials for solid sorption air conditioning systems, *Applied Thermal Engineering*, 22 (2002) 191-204.
- [66] W. Dechang, W. Jingyi, S. Honggang, W. Ruzhu, Experimental study on the dynamic characteristics of adsorption heat pumps driven by intermittent heat source at heating mode, *Applied Thermal Engineering*, 25 (2005) 927-940.
- [67] S.J. Metcalf, R.E. Critoph, Z. Tamainot-Telto, Optimal cycle selection in carbon-ammonia adsorption cycles, *International Journal of Refrigeration*, 35 (2012) 571-580.

- [68] D.J. Miles, S.V. Shelton, Design and testing of a solid-sorption heat-pump system, *Applied Thermal Engineering*, 16 (1996) 389-394.
- [69] A.M. Rivero-Pacho, R.E. Critoph, S.J. Metcalf, Modelling and development of a generator for a domestic gas-fired carbon-ammonia adsorption heat pump, *Renewable Energy*, 110 (2017) 180-185.
- [70] D.B. Boman, D.C. Hoysall, D.G. Pahinkar, M.J. Ponkala, S. Garimella, Screening of working pairs for adsorption heat pumps based on thermodynamic and transport characteristics, *Applied Thermal Engineering*, 123 (2017) 422-434.
- [71] S.-J. Ernst, F. Jeremias, H.-J. Bart, S.K. Henninger, Methanol Adsorption on HKUST-1 Coatings Obtained by Thermal Gradient Deposition, *Industrial & Engineering Chemistry Research*, 55 (2016) 13094-13101.
- [72] F. Jeremias, D. Frohlich, C. Janiak, S.K. Henninger, Water and methanol adsorption on MOFs for cycling heat transformation processes, *New Journal of Chemistry*, 38 (2014) 1846-1852.
- [73] A. Freni, B. Dawoud, L. Bonaccorsi, S. Chmielewski, A. Frazzica, L. Calabrese, G. Restuccia, *Characterization of Zeolite-based Coatings for Adsorption Heat Pumps*, Springer International Publishing, 2015.
- [74] T.A. Fuller, W.J. Wepfer, S.V. Shelton, M.W. Ellis, A Two-Temperature Model of the Regenerative Solid-Vapor Heat Pump, *Journal of Energy Resources Technology*, 116 (1994) 297-304.
- [75] G. Cacciola, G. Restuccia, Reversible adsorption heat pump: a thermodynamic model, *International Journal of Refrigeration*, 18 (1995) 100-106.
- [76] N. Douss, F. Meunier, Experimental study of cascading adsorption cycles, *Chemical Engineering Science*, 44 (1989) 225-235.
- [77] N. Douss, F. Meunier, Effect of operating temperatures on the coefficient of performance of active carbon-methanol systems, *Heat Recovery Systems and CHP*, 8 (1988) 383-392.
- [78] A. Freni, Comparative thermodynamic analysis of promising adsorbent/adsorbate pairs for adsorptive heat pumping, air conditioning and refrigeration, *Seminar of advanced sorption technologies and their applications*, Empa, Dübendorf (2015).
- [79] G. Restuccia, Thermally driven adsorption heat pumps: recent advancements and future technical challenges, *Problématiques Scientifiques et Technologiques dans les Procédés Frigorifiques et Thermiques à Sorption*, Paris (2014).
- [80] M.J. Goldsworthy, Measurements of water vapour sorption isotherms for RD silica gel, AQSOA-Z01, AQSOA-Z02, AQSOA-Z05 and CECA zeolite 3A, *Microporous and Mesoporous Materials*, 196 (2014) 59-67.
- [81] B. Mette, H. Kerskes, H. Drück, H. Müller-Steinhagen, Experimental and numerical investigations on the water vapor adsorption isotherms and kinetics of binderless zeolite 13X, *International Journal of Heat and Mass Transfer*, 71 (2014) 555-561.
- [82] H.T. Chua, K.C. Ng, A. Chakraborty, N.M. Oo, M.A. Othman, Adsorption Characteristics of Silica Gel + Water Systems, *Journal of Chemical & Engineering Data*, 47 (2002) 1177-1181.
- [83] U. Wittstadt, G. Fuldner, O. Andersen, R. Herrmann, F. Schmidt, A New Adsorbent Composite Material Based on Metal Fiber Technology and Its Application in Adsorption Heat Exchangers, *Energies*, 8 (2015) 8431.
- [84] D. Frohlich, E. Pantatosaki, P.D. Kolokathis, K. Markey, H. Reinsch, M. Baumgartner, M.A. van der Veen, D.E. De Vos, N. Stock, G.K. Papadopoulos, S.K. Henninger, C. Janiak,

Water adsorption behaviour of CAU-10-H: a thorough investigation of its structure-property relationships, *Journal of Materials Chemistry A*, 4 (2016) 11859-11869.

[85] Y. Aristov, Concept of adsorbent optimal for adsorptive cooling/heating, *Applied Thermal Engineering*, 72 (2014) 166-175.

[86] BINE Information Service - Heating with gas adsorption heat pumps (2015), http://www.bine.info/fileadmin/content/Publikationen/Projekt-Infos/2015/Projekt_03-2015/ProjektInfo_0315_engl_internetx.pdf, (accessed in 20.09.2017).

[87] B.T. Nguyen, H.L. Nguyen, T.C. Nguyen, K.E. Cordova, H. Furukawa, High Methanol Uptake Capacity in Two New Series of Metal–Organic Frameworks: Promising Materials for Adsorption-Driven Heat Pump Applications, *Chemistry of Materials*, 28 (2016) 6243-6249.

[88] D. Frohlich, S.K. Henninger, C. Janiak, Multicycle water vapour stability of microporous breathing MOF aluminium isophthalate CAU-10-H, *Dalton Transactions*, 43 (2014) 15300-15304.

[89] H. Furukawa, F. Gándara, Y.-B. Zhang, J. Jiang, W.L. Queen, M.R. Hudson, O.M. Yaghi, Water Adsorption in Porous Metal–Organic Frameworks and Related Materials, *Journal of the American Chemical Society*, 136 (2014) 4369-4381.

[90] S.K. Henninger, F. Jeremias, H. Kummer, C. Janiak, MOFs for Use in Adsorption Heat Pump Processes, *European Journal of Inorganic Chemistry*, (2012) 2625-2634.

[91] B. Bozbiyik, T. Van Assche, J. Lannoeye, D.E. De Vos, G.V. Baron, J.F.M. Denayer, Stepped water isotherm and breakthrough curves on aluminium fumarate metal–organic framework: experimental and modelling study, *Adsorption*, 23 (2017) 185-192.

[92] F. Jeremias, A. Khutia, S.K. Henninger, C. Janiak, MIL-100(Al, Fe) as water adsorbents for heat transformation purposes-a promising application, *Journal of Materials Chemistry*, 22 (2012) 10148-10151.

[93] F. Jeremias, D. Frohlich, C. Janiak, S.K. Henninger, Advancement of sorption-based heat transformation by a metal coating of highly-stable, hydrophilic aluminium fumarate MOF, *RSC Advances*, 4 (2014) 24073-24082.

[94] P.M. Schoenecker, C.G. Carson, H. Jasuja, C.J.J. Flemming, K.S. Walton, Effect of Water Adsorption on Retention of Structure and Surface Area of Metal–Organic Frameworks, *Industrial & Engineering Chemistry Research*, 51 (2012) 6513-6519.

[95] H. Kummer, F. Jeremias, A. Warlo, G. Földner, D. Fröhlich, C. Janiak, R. Gläser, S.K. Henninger, A Functional Full-Scale Heat Exchanger Coated with Aluminum Fumarate Metal–Organic Framework for Adsorption Heat Transformation, *Industrial & Engineering Chemistry Research*, (2017).

[96] N. Al-Janabi, A. Alfutimie, F.R. Siperstein, X. Fan, Underlying mechanism of the hydrothermal instability of Cu₃(BTC)₂ metal-organic framework, *Frontiers of Chemical Science and Engineering*, 10 (2016) 103-107.

[97] E. Elsayed, H. Wang, P.A. Anderson, R. Al-Dadah, S. Mahmoud, H. Navarro, Y. Ding, J. Bowen, Development of MIL-101(Cr)/GrO composites for adsorption heat pump applications, *Microporous and Mesoporous Materials*, 244 (2017) 180-191.

[98] J. Bauer, T. Selvam, J. Ofili, E. Che, R. Herrmann, W. Schwieger, Stability of AlPO and SAPO molecular sieves during adsorption-desorption cycles of water vapor investigated by in-situ XRD measurements, *Studies in Surface Science and Catalysis*, 170 (2007) 837-844.

[99] A. Ristić, N.Z. Logar, S.K. Henninger, V. Kaučič, The Performance of Small-Pore Microporous Aluminophosphates in Low-Temperature Solar Energy Storage: The Structure–Property Relationship, *Advanced Functional Materials*, 22 (2012) 1952-1957.

- [100] L. Bonaccorsi, P. Bruzzaniti, L. Calabrese, A. Freni, E. Proverbio, G. Restuccia, Synthesis of SAPO-34 on graphite foams for adsorber heat exchangers, *Applied Thermal Engineering*, 61 (2013) 848-852.
- [101] L. Bonaccorsi, L. Calabrese, A. Freni, E. Proverbio, Hydrothermal and microwave synthesis of SAPO (CHA) zeolites on aluminium foams for heat pumping applications, *Microporous and Mesoporous Materials*, 167 (2013) 30-37.
- [102] L. Calabrese, L. Bonaccorsi, A. Freni, E. Proverbio, Synthesis of SAPO-34 zeolite filled macrocellular foams for adsorption heat pump applications: A preliminary study, *Applied Thermal Engineering*, 124 (2017) 1312-1318.
- [103] H.J. Chen, Q. Cui, Q.G. Li, K. Zheng, H.Q. Yao, Adsorption-desorption characteristics of water on silico-alumino-phosphate-34 molecular sieve for cooling and air conditioning, *Journal of Renewable and Sustainable Energy*, 5 (2013) 053129.
- [104] L.G. Gordeeva, Y.I. Aristov, Composites 'salt inside porous matrix' for adsorption heat transformation: a current state-of-the-art and new trends, *International Journal of Low-Carbon Technologies*, 7 (2012) 288-302.
- [105] Y. Yuan, H. Zhang, F. Yang, N. Zhang, X. Cao, Inorganic composite sorbents for water vapor sorption: A research progress, *Renewable and Sustainable Energy Reviews*, 54 (2016) 761-776.
- [106] Y.I. Aristov, New family of solid sorbents for adsorptive cooling: Material scientist approach, *Journal of Engineering Thermophysics*, 16 (2007) 63-72.
- [107] I. Glaznev, I. Ponomarenko, S. Kirik, Y. Aristov, Composites CaCl₂/SBA-15 for adsorptive transformation of low temperature heat: Pore size effect, *International Journal of Refrigeration*, 34 (2011) 1244-1250.
- [108] Y.I. Aristov, Challenging offers of material science for adsorption heat transformation: A review, *Applied Thermal Engineering*, 50 (2013) 1610-1618.
- [109] G. Cacciola, G. Restuccia, Progress on adsorption heat pumps, *Heat Recovery Systems and CHP*, 14 (1994) 409-420.
- [110] D. Schawe, Theoretical and experimental investigations of an adsorption heat pump with heat transfer between two adsorbers, PhD thesis, University of Stuttgart, Germany (2001).
- [111] B.O. Bolaji, Z. Huan, Ozone depletion and global warming: Case for the use of natural refrigerant – a review, *Renewable and Sustainable Energy Reviews*, 18 (2013) 49-54.
- [112] A. Ordaz-Flores, O. García-Valladares, V.H. Gómez, Findings to improve the performance of a two-phase flat plate solar system, using acetone and methanol as working fluids, *Solar Energy*, 86 (2012) 1089-1098.
- [113] B.B. Saha, I.I. El-Sharkawy, A. Chakraborty, S. Koyama, Study on an activated carbon fiber–ethanol adsorption chiller: Part I – system description and modelling, *International Journal of Refrigeration*, 30 (2007) 86-95.
- [114] Proklima Programme: Natural Refrigerants - Sustainable Ozone and Climate Friendly Alternatives to HCFCs, <https://www.epa.gov/sites/production/files/documents/en-gtz-proklima-natural-refrigerants.pdf>, (accessed in 6.11.2017).
- [115] R.E. Critoph, S.J. Metcalf, Development of a domestic adsorption gas-fired heat pump, in: A. Kühn (ed.) *Thermally driven heat pumps for heating and cooling*, Universitätsverlag der TU Berlin, Berlin, 2013.
- [116] H. Kummer, M. Baumgartner, P. Hügenell, D. Fröhlich, S.K. Henninger, R. Gläser, Thermally driven refrigeration by methanol adsorption on coatings of HKUST-1 and MIL-101(Cr), *Applied Thermal Engineering*, 117 (2017) 689-697.

- [117] European Heat Pump Market and Statistics Report 2015 - European Heat Pump Association (EHPA), <http://www.ehpa.org/about/news/article/european-heat-pump-market-and-statistics-report-soon-available/>, (accessed in 26.09.2017).
- [118] J. Wienen, M. Neubert, R. Lang, Results from the field test gas heat pump Zeotherm of Vaillant company, in: A. Kühn (ed.) Thermally driven heat pumps for heating and cooling, Universitätsverlag der TU Berlin, Berlin, 2013.
- [119] B. Dawoud, Gas-driven sorption heat pumps; a potential trend-setting heating technology, in: A. Kühn (ed.) Thermally driven heat pumps for heating and cooling, Universitätsverlag der TU Berlin, Berlin, 2013.
- [120] NIST Chemistry WebBook, <http://webbook.nist.gov/chemistry/>, (accessed in 31.08.2017).
- [121] J.M. Coulson, J.F. Richardson, Coulson & Richardson's Chemical Engineering: Vol. 1, Fluid flow, heat transfer and mass transfer, Pergamon Press, 1990.
- [122] A.K. Agarwal, A. Dhar, A. Gautam, A. Pandey, Locomotives and Rail Road Transportation: Technology, Challenges and Prospects, Springer Singapore, 2017.
- [123] G. Santori, C. Di Santis, Optimal fluids for adsorptive cooling and heating, Sustainable Materials and Technologies, 12 (2017) 52-61.
- [124] S. Wang, D. Zhu, Adsorption Heat Pump Using an Innovative Coupling Refrigeration Cycle, Adsorption, 10 (2004) 47-55.
- [125] N. Douss, F.E. Meunier, L.M. Sun, Predictive model and experimental results for a two-adsorber solid adsorption heat pump, Industrial & Engineering Chemistry Research, 27 (1988) 310-316.
- [126] J.M. Pinheiro, S. Salústio, A.A. Valente, C.M. Silva, Adsorption heat pump optimization by experimental design and response surface methodology, Applied Thermal Engineering, 138 (2018) 849-860.
- [127] F. Meunier, Solid sorption heat powered cycles for cooling and heat pumping applications, Applied Thermal Engineering, 18 (1998) 715-729.
- [128] R. Lang, M. Roth, M. Stricker, T. Westerfeld, Development of a modular zeolite-water heat pump, Heat and Mass Transfer, 35 (1999) 229-234.
- [129] L. Calabrese, V. Brancato, L. Bonaccorsi, A. Frazzica, A. Caprì, A. Freni, E. Proverbio, Development and characterization of silane-zeolite adsorbent coatings for adsorption heat pump applications, Applied Thermal Engineering, 116 (2017) 364-371.
- [130] Y.I. Aristov, Optimal adsorbent for adsorptive heat transformers: Dynamic considerations, International Journal of Refrigeration, 32 (2009) 675-686.
- [131] A. Li, K. Thu, A.B. Ismail, K.C. Ng, A heat transfer correlation for transient vapor uptake of powdered adsorbent embedded onto the fins of heat exchangers, Applied Thermal Engineering, 93 (2016) 668-677.
- [132] A. Frazzica, G. Földner, A. Sapienza, A. Freni, L. Schnabel, Experimental and theoretical analysis of the kinetic performance of an adsorbent coating composition for use in adsorption chillers and heat pumps, Applied Thermal Engineering, 73 (2014) 1022-1031.
- [133] A. Freni, L. Bonaccorsi, L. Calabrese, A. Caprì, A. Frazzica, A. Sapienza, SAPO-34 coated adsorbent heat exchanger for adsorption chillers, Applied Thermal Engineering, 82 (2015) 1-7.
- [134] J. Sauer, B. Dawoud, S. Chmielewski, H. Van Heyden, H. Klaschinsky, Adsorber element and method for producing an adsorber element, US 20110183835 A1, Viessmann Werke GmbH & Co.Kg (2011).
- [135] M. Schick Tanz, K.T. Witte, G. Földner, S.K. Henninger, A. Frazzica, A. Freni, Recent developments in adsorption materials and heat exchangers for thermally driven heat pumps

- in: A. Kühn (ed.) Thermally driven heat pumps for heating and cooling, Universitätsverlag der TU Berlin, Berlin, 2013.
- [136] A.M. Elsayed, A.A. Askalany, A.D. Shea, H.J. Dakkama, S. Mahmoud, R. Al-Dadah, W. Kaialy, A state of the art of required techniques for employing activated carbon in renewable energy powered adsorption applications, *Renewable and Sustainable Energy Reviews*, 79 (2017) 503-519.
- [137] A. Freni, A. Frazzica, B. Dawoud, S. Chmielewski, L. Calabrese, L. Bonaccorsi, Adsorbent coatings for heat pumping applications: Verification of hydrothermal and mechanical stabilities, *Applied Thermal Engineering*, 50 (2013) 1658-1663.
- [138] R.K. Shah, D.P. Sekulić, Classification of Heat Exchangers, in: *Fundamentals of Heat Exchanger Design*, John Wiley & Sons Inc., New Jersey, 2003, pp. 1-77.
- [139] Viessmann - Vitosorp 200-F gas adsorption heating appliance (2015), http://viessmann.com/com/content/dam/vi-corporate/COM/Download/Gas_adsorption_heating_appliance.pdf/_jcr_content/renditions/original.media.file.download_attachment.file/Gas_adsorption_heating_appliance.pdf, (accessed in 22.8.2017).
- [140] S. Santamaria, A. Sapienza, A. Frazzica, A. Freni, I.S. Gernik, Y.I. Aristov, Water adsorption dynamics on representative pieces of real adsorbents for adsorptive chillers, *Applied Energy*, 134 (2014) 11-19.
- [141] J.-Y. San, F.-K. Tsai, Testing of a lab-scale four-bed adsorption heat pump, *Applied Thermal Engineering*, 70 (2014) 274-281.
- [142] A. Freni, F. Russo, S. Vasta, M. Tokarev, Y.I. Aristov, G. Restuccia, An advanced solid sorption chiller using SWS-1L, *Applied Thermal Engineering*, 27 (2007) 2200-2204.
- [143] B. Dawoud, E.H. Amer, D.M. Gross, Experimental investigation of an adsorptive thermal energy storage, *International Journal of Energy Research*, 31 (2007) 135-147.
- [144] A. Li, K. Thu, A.B. Ismail, M.W. Shahzad, K.C. Ng, Performance of adsorbent-embedded heat exchangers using binder-coating method, *International Journal of Heat and Mass Transfer*, 92 (2016) 149-157.
- [145] I.S. Gernik, Y.I. Aristov, Dynamic optimization of adsorptive chillers: The “AQSOA™-FAM-Z02 – Water” working pair, *Energy*, 106 (2016) 13-22.
- [146] Y.I. Aristov, A. Sapienza, D.S. Ovoshchnikov, A. Freni, G. Restuccia, Reallocation of adsorption and desorption times for optimisation of cooling cycles, *International Journal of Refrigeration*, 35 (2012) 525-531.
- [147] M. Verde, L. Cortés, J.M. Corberán, A. Sapienza, S. Vasta, G. Restuccia, Modelling of an adsorption system driven by engine waste heat for truck cabin A/C. Performance estimation for a standard driving cycle, *Applied Thermal Engineering*, 30 (2010) 1511-1522.
- [148] U. Wittstadt, G. Földner, S. Vasta, R. Volmer, P. Bendix, L. Schnabel, W. Mittelbach, Adsorption Heat Pumps and Chillers – Recent Developments for Materials and Components, 12th IEA Heat Pump Conference, Rotterdam (2017).
- [149] I.S. Gernik, Y.I. Aristov, Dynamics of water vapour adsorption by a monolayer of loose AQSOA™-FAM-Z02 grains: Indication of inseparably coupled heat and mass transfer, *Energy*, 114 (2016) 767-773.
- [150] L. Rainer, Sorption heat pump with an ad/desorber heat exchanger, DE 19902695 B4, Vaillant GmbH (2016).
- [151] B. Dawoud, R. Lang, T. Miltkau, M. Stricker, Sorption heat pump, EP 1178269 B1, Vaillant GmbH (2003).
- [152] R. Kehl, R.D. Lang, F. Marth, U. Marx, J. Wienen, Adsorber /desorber heat exchanger, EP 1180650 B1, Vaillant GmbH (2003).

- [153] R. Lang, F. Marth, U. Marx, J. Wienen, Closed loop heating device, EP 1184629 B1, Vaillant GmbH (2008).
- [154] R.D. Lang, M. Leyendecker, F. Marth, U. Marx, J. Wienen, B.D. Dawoud, V.H. De, T. Miltkau, M. Stricker, Adsorber/desorber for heating apparatus using zeolite, EP 1239240 B1, Vaillant GmbH (2007).
- [155] T.D. Hocker, R.D. Lang, F. Marth, U. Marx, R. Prescha, J. Wienen, B.D. Dawoud, R. Gasper, T. Miltkau, Module of heat pump for an adsorption heat pump, EP 1278028 B1, Vaillant GmbH (2006).
- [156] J.L. Heim, T.D. Hocker, R.D. Lang, F. Marth, U. Marx, R. Prescha, J. Wienen, Process for operating an adsorption heat pump, EP 1279910 B1, Vaillant GmbH (2006).
- [157] J.L. Heim, T.D. Hocker, R.D. Lang, F. Marth, U. Marx, R. Prescha, J. Wienen, Adsorption heat pump, EP 1279909 B1, Vaillant GmbH (2003).
- [158] J.L. Heim, T. Hocker, R. Lang, F. Marth, U. Marx, R. Prescha, J. Wienen, Method for operating adsorption heat pump at low temperatures has secondary ambient heat exchangers in heating circuit, DE 10235737 A1, Vaillant GmbH (2003).
- [159] J.L. Heim, T.D. Hocker, R.D. Lang, F. Marth, U. Marx, R. Prescha, J. Wienen, A. Burgdorf, B.D. Dawoud, R. Gasper, Regulating method for an adsorption heat pump, EP 1288596 B1, Vaillant GmbH (2007).
- [160] J.L. Heim, H. Thomas, R. Lang, F. Marth, U. Marx, R. Prescha, J. Wienen, A method of reversing the phase of a sorption heat pump, and device for carrying out the method, DE 10242820 A1, Vaillant GmbH (2016).
- [161] M. Stricker, Foreign gas removal method for vacuum sorption device using intermediate phase in which overpressure is obtained by application of heat and blocking heat output of condenser, DE 10310748 B3, Viessmann Werke GmbH & Co Kg (2004).
- [162] S. Marc, Vacuum sorption, DE 102004049411 B4, Viessmann Werke GmbH & Co Kg (2015).
- [163] M. Stricker, The vacuum sorption, DE 102004049408 B4, Viessmann Werke GmbH & Co Kg (2006).
- [164] Sorption apparatus, DE 202004015674 U1, Viessmann Werke GmbH & Co Kg (2006).
- [165] M. Stricker, Vacuum sorption device, EP 1653168 B1, Viessmann Werke GmbH & Co KG (2009).
- [166] M. Stricker, Method of control for a periodically operating vacuum sorption device, EP 1645820 B1, Viessmann Werke GmbH & Co KG (2009).
- [167] A. Burgdorf, R. Lang, F. Marth, M. Neubert, J. Wienen, Sorber heat exchanger of an adsorption heat pump, EP 2058608 A2, Vaillant GmbH (2009).
- [168] B.D. Dawoud, A. Bornmann, Vacuum-sorption device, EP 2045547 B1, Viessmann Werke GmbH & Co. KG (2012).
- [169] B.D. Dawoud, A. Bornmann, S. Lohmöller, Vacuum sorption device, EP 2083231 B1, Viessmann Werke GmbH & Co. KG (2015).
- [170] B.D. Dawoud, A. Bornmann, S. Chmielewski, P. Höfle, Vacuum sorption device and method for operating same, EP 2309211 B1, Viessmann Werke GmbH & Co. KG (2015).
- [171] B. Dawoud, P. Hoefle, A. Bornmann, S. Chmielewski, C. Marburger, Vacuum sorption apparatus, US 8544293 B2, Viessmann Werke GmbH & Co. Kg (2013).
- [172] J.H. Sick, F. Salg, H.J. Spahn, Sorption heat pump, EP 2447623 A3, Vaillant GmbH (2014).
- [173] A. Bornmann, B. Dawoud, P. Hoefle, Vacuum sorption device, US 20120055194 A1, Viessmann Werke GmbH & Co. Kg (2012).
- [174] R.E. Critoph, State of the art in gas driven heat pumps, University of Warwick, 2013.

Chapter 2: Introduction

- [175] B. Critoph, I. Malenković, IEA Heat Pump Annex 43: Fuel driven sorption heat pumps - For residential and small scale commercial heating applications, IEA National Teams Meeting for the UK Heat Pump Industry, United Kingdom (2016).
- [176] Viessman Vitorsorp-200F - German prices (Loebbeshop), <http://www.loebbeshop.de/viessmann/gas-systeme/gas-brennwert-systeme/vitorsorp-200-f/index.htm>, (accessed in 27.09.2017).
- [177] IVT GEO 312C heat pump - technical datasheet, http://doc.ivt.se/download.asp?pt=se&fn=Pr_bl_Geo312C.pdf, (accessed in 27.09.2017).
- [178] M. Ally, High Efficiency, Residential Gas-Fired Adsorption Heat Pump Water Heater Development, Hot Water Forum - American Council for an Energy-Efficient Economy (ACEEE), Portland (2016).

Annex A2

Table A2.1 - Database of AHPs for heating applications: work domain (theoretical (*Theor*) and/or experimental (*Exp*)), working pairs, operating conditions (T_{evap} , T_2 , T_{cond} , T_4 , $T_{\text{heat source}}^{\text{low}}$, $T_{\text{heat source}}^{\text{high}}$, t_{cycle}), cycle features (basic (single-bed) or advanced (multi-bed) cycles), adsorbent configurations (loose grains, consolidated beds, coatings), adsorbent heat exchanger (AHEx) geometries (plate, tubular with or without fins, extended surface), and performance indicators (*COPs* and *SHPs*). Some additional notes are also provided.

Work domain (a)	Working pair	Operating conditions (T_{evap} , T_2 , T_{cond} , T_4) (K)	T of heat sources (K)		t_{cycle} (s) (b,c,d)	Cycle features (f)	Adsorbent configuration (e)	AHEx geometry	Performance indicator (b,d)		Observations	Ref.
			$T_{\text{heat source}}^{\text{low}}$	$T_{\text{heat source}}^{\text{high}}$					<i>COP</i>	<i>SHP</i> (W kg ⁻¹)		
Theor/ Exp	Activated carbon/methanol	---	271-284	353-403	900-1800 (H)	Heat recovery (2 beds in alternate operation)	Loose grains	Tubular (shell and finned tubes)	1.10 [*] -1.60 [*] 1.33-1.47 (1.39 [*] →1.47; 1.43 [*] →1.41; 1.40 [*] →1.35; 1.38 [*] →1.33)	150 [*] -550 [*] 281-487 (474 [*] →487; 396 [*] →383; 325 [*] →319; 286 [*] →281)	<ul style="list-style-type: none"> T of HTF at the condenser outlet: 293- 309 K. <i>SHPs</i> calculated considering the mass of adsorbent in one bed and t_{cycle} (H). 	[1]
Theor	(a) Zeolite 4A/water (b) Zeolite 13X/water (c) Activated carbon/methanol	(a), (b) 273 – 283, --- , 328, 383-503 (c) 275 – 283, --- , 328, 388-428	---	---	---	Heat recovery (2 beds in alternate operation)	---	---	(a) 1.10 – 1.60 (b) 1.10 – 1.65 (c) 1.05 – 1.55	---	---	[2]
Theor/ Exp	Zeolite/water	~ 283, 333, 328 - 333, 473	---	483	2100 – 5640 (H)	Heat recovery (2 beds in alternate operation)	Loose grains	---	1.42 [*] – 1.45 [*]	---	---	[3]

(Table A2.1 continues)

Chapter 2: Introduction – Annex A2

Theor/ Exp	Zeolite 13X/water	303, 358 – 383, 313 – 333, 473 - 513	---	up to 533	5280*→3 600 (F) 9420*→9 600 (F)	Heat recovery (2 beds in alternate operation)	Loose grains	Tubular (hairpin with finned tubes)	1.57 [*] → 1.35 1.62 [*] →1.45	138 [*] → 93 167 [*] →111	---	[4]
Theor/ Exp	Silica gel/water	---	281-305	353	(a) ~ 780 (F)	(a) 2 beds in alternate operation (b) 4 beds (2 beds performing adsorption and 2 beds in desorption stage)	Loose grains	Tubular (shell and finned tubes)	(a) 1.62 [*] → 1.37; 1.25-1.45 (b) 1.17 [*] → 1.07	---	<ul style="list-style-type: none"> ▪ Hybrid system combining a gas water heater with an AHP. ▪ The reported COPs do not include the contribution of the gas water heater. 	[5]
Exp	AQSOA [®] FAM- Z02/water	283-298, 298- 313, 283-298, 353	---	348 - 373	300-480	Basic (1 bed)	Coating ($\delta = 1.6 \times 10^{-4}$ m)	Extended surface (corrugate copper fins and flat iron tubes)	1.20-1.47	---	Authors intended to develop a two bed AHP working in phase shift mode; experimental results were obtained using only one bed.	[6]
Theor	ETS-10/water	278, 333, 333, 473	---	473	420-1680	Basic (1 bed)	Loose grains	Tubular (shell and tube without fins)	1.36-1.41	249-934	---	[7]
Theor	Zeolite 4A/water	280, 328, 328, 473	---	---	900	Basic (1 bed)	Consolidated bed ($\delta = 5 \times 10^{-3}$ m)	Tubular (shell and tube without fins)	1.37	---	---	[8]

(Table A2.1 continues)

Chapter 2: Introduction – Annex A2

Exp	Activated carbon/methanol	276-278, ~313, --, 362-373	279-281	up to 388	2520 (F)	Heat recovery (2 beds in alternate operation)	Loose grains	Tubular (shell and tube without fins)	1.19-1.31	76-111	<i>SHPs</i> where calculated considering the mass of two adsorbers.	[9]
Exp	AQSOA® FAM-ZO2/water	< 278-283, ---, --, 363-373	278-283	---	---	Basic (1 bed)	Coating ($\delta = 3 \times 10^{-4} - 5 \times 10^{-4}$ m)	Tubular (shell and longitudinal finned tubes)	1.14-1.35	820 – 2200	Using loose pellets in a finned tube AHEx, the <i>SHPs</i> are at most 1/4 of those measured using coatings (which corresponds to ~ 205-550 W kg ⁻¹).	[10]
Exp	AQSOA® FAM-ZO2/water	---, ---, ---, 363	278	---	---	Basic (1 bed)	Coating ($\delta = 1.5 \times 10^{-4} - 5 \times 10^{-4}$ m)	(a) Tubular (shell and longitudinal finned tubes) (b) Extended surface (extruded finned plate)	(a) 1.17 – 1.25 (b) 1.21 - 1.23	---	---	[11]
Exp	AQSOA® FAM-ZO2/water	---	---	358	ca. 300 (F)	(2 beds in alternate operation)	Loose grains	Extended surface (plate fin tube)	1.41 – 1.43	---	<ul style="list-style-type: none"> ▪ Hybrid AHP water heater including a gas boiler. ▪ <i>COPs</i> are for the AHP (Fig. 9 also includes the <i>COPs</i> for the hybrid system). 	[12]

(Table A2.1 continues)

Chapter 2: Introduction – Annex A2

Theor	(a) Zeolite 4A/water (b) Activated carbon/methanol	(a) 278, 313 – 328, 313 – 328, 458 (b) 278, 313, 313, 403	---	(a) 478 (b) 413	(a) 900 – 1080 (F) (b) 5880 (F)	Heat recovery (2 beds in alternate operation)	(a) Coating ($\delta = 1 \times 10^{-3}$ m) (b) Loose pellets	(a) Tubular (shell and tube without fins) (b) Tubular (shell and tube with fins)	(a) 1.41-1.46 (b) 1.52	(a) 878 -891 (b) 94	<ul style="list-style-type: none"> ▪ <i>SHPs</i> correspond to the generated useful heat per full cycle time and per unit mass of adsorbent. ▪ Changing from loose pellets to coatings led to the following changes in <i>COP</i>, <i>SHP</i> and full cycle time of the zeolite/water AHP, respectively: 1.44 to 1.41, 244 W kg⁻¹ to 878 W kg⁻¹, and 3540 to 900 s. 	[13]
Theor/ Exp	Zeolite/water	273-283, 323, 308-313, 473	---	up to 473	1620 (F)	Heat recovery ((a) 2 beds (in alternate operation) (b) 8 beds (4 beds in adsorption and the remaining 4 in desorption))	Loose pellets	Tubular (shell and gilled tubes)	(a) 1.22* – 1.60* (b) 1.10* – 2.00*	---	---	[14]
Theor	Zeolite 4A/water	278, 333, 328, 463	---	---	---	Heat recovery (2 beds in alternate operation)	---	---	1.30 - 1.50	up to ca. 3300	---	[15]

(Table A2.1 continues)

Chapter 2: Introduction – Annex A2

Exp	Silica gel/water	---, ≥ 301 , ---, ≤ 348	280 - 293	348-368	900-1800 (H)	Heat recovery (2 beds in alternate operation)	Loose grains	---	1.30 – 1.65	229-457	<ul style="list-style-type: none"> ▪ T of HTF at the condenser outlet and at the AHEx outlet (in adsorption stage) was, respectively: ~ 298 – 307 K and ~ 301 – 323 K. ▪ SHP_s were calculated in this work considering the values of average heating powers of 8 and 16 kW reported in ref. [16], which correspond to the useful heat divided by the full cycle time and by m_{ads} in one bed (35 kg). 	[16]
Exp	Activated carbon/ammonia	258-279, ---, 308 – 319, ---	259-281	~ 505	312 (F)	Thermal wave (2 beds in alternate operation)	Loose grains	Tubular (shell and tube without fins)	1.21-1.59	---	T of HTF at the AHEx outlet (in adsorption stage): ~ 311-366 K.	[17]
Theor	(a) Zeolite 13X/water (b) Zeolite 4A/water (c) ETS-10/water (d) Silica gel/water	278, 333, 333, 423-473	---	---	120-660	Basic (1 bed)	Loose grains	Tubular (shell and tube without fins)	(a) 1.48 (b) 1.40 (c) 1.37 (d) 1.02	(a) 1255 (b) 1258 (c) 768 (d) 802	---	[18]
Theor	Activated carbon/ammonia	278, ---, ---, 463	---	473	---	(a) Heat and mass recovery (i) 2 beds, (ii) 4 beds) (b) Thermal wave with mass recovery (60 beds)	Loose grains	Plate-type	(a) (i) 1.25-1.45 (ii) 1.30 – 1.65 (b) 1.20 -1.90	(a) (i) 2000 – 9000 (ii) 1000 – 4200 (b) up to ~ 5600	---	[19]

(Table A2.1 continues)

Chapter 2: Introduction – Annex A2

Theor/ Exp	Zeolite 13X/water	~ 293-298, 333, 313, 473	---	---	(b) <i>ca.</i> 10800 (H)	(a) Basic (1 bed) (b) Heat recovery (2 beds in alternate operation)	Loose grains	Tubular (hairpin with finned tubes)	(a) 1.38* - 1.49*; 1.38-1.39 (1.49* → 1.38) (b) 1.55* – 1.83*; 1.56-1.57 (1.83* → 1.57)	(b) ~ 176* → ~ 184	<i>SHPs</i> were calculated considering the average value of m_{ads} of the two beds reported in Table II of ref. [20] (25.5 kg), the theoretical and experimental output heats from AHEx and condenser (see Table III of that work), and t_{cycle} (H) of 10800 s (Fig. 9 of that work).	[20]
Theor	Zeolite/water	275-283, 333 – 348, 333 – 338, 548	---	---	---	(a) Basic (1 bed)	Loose grains	---	1.35 - 1.43	---	---	[21]
Theor	Activated carbon/ammonia	280, 316, 316, 505	---	---	---	Thermal wave (2 beds in alternate operation)	Loose grains	Tubular (shell and tube spiral)	1.5-3.5	---	---	[22]
Theor/ Exp	Zeolite 13X/water	281, 311, 305-333, 478	---	478	---	Thermal wave (2 beds in alternate operation)	Loose grains	---	1.45* – 1.60*	---	Seasonal heating <i>COPs</i> .	[23]
Theor	Zeolite/ammonia	255-289, 294-333, 294-333, 422 – 755	---	---	---	Thermal wave (2 beds in alternate operation)	Loose grains	Tubular (shell and tube without fins)	1.35 – 2.50	---	---	[24]
Theor	Zeolite/ammonia	255-289, 311-339, 311-339, 422 - 755	---	---	---	Thermal wave (2 beds in alternate operation)	Loose grains	Tubular (shell and tube without fins)	1.25 – 1.85	---	---	[25]

(Table A2.1 continues)

Chapter 2: Introduction – Annex A2

Theor/ Exp	(a) Zeolite 13X/water (b) Zeolite MgA/water (c) Zeolite 13X/methanol (d) Clinoptilolite/water (e) Silica gel/water	---	---	---	---	Basic (1 bed)	---	---	(a) 1.29 (b) 1.40 (c) 1.34 (d) 0.68-1.39 (e) 1.57	---	---	[26]
Exp	Activated carbon/methanol	---	275-283	373-383	1800-3600	Heat recovery (2 beds)	Loose grains	Extended surface (finned plate)	1.33-1.54	281-487	<i>SHP</i> was calculated dividing the heat pump power by the mass of activated carbon in one bed (26 kg).	[27]
Theor	(a) Zeolite 13X/water (b) Activated carbon/methanol	---, 313-323, 313-323, ---	---	(a) 493 - 563 (b) 423	---	(i) Heat recovery (2 beds in alternate operation) (ii) Thermal wave (2 beds in alternate operation)	---	---	(a)(i) 1.60-1.70 (a)(ii) 1.70-2.00 (b)(i) 1.45-1.60	---	---	[28]
Theor	Activated carbon/ammonia	274, 323, 323, 523	---	---	---	Forced convection (2 beds in alternate operation)	Loose grains	---	1.76	577	---	[29]
Theor	(a) Composite LiBr-silica/water (b) Zeolite 4A/water (c) AQSOA® FAM-Z02/water (d) Zeolite DDZ70/water (e) SAPO-34/water (f) Silica gel/water	283, 318, 318, 423	---	---	---	Basic (1 bed)	---	---	(a) 1.62 (b) 1.42 (c) 1.60 (d) 1.55 (e) 1.58 (f) 1.51	---	---	[30]

(Table A2.1 continues)

Chapter 2: Introduction – Annex A2

Theor	AQSOA® FAM-Z02/water	275-288, 303, 303, 363	---	---	---	Basic (1 bed)	---	---	1.57 - 1.62	---	---	[31]
Theor	(a) SWS-1L/water (b) Silica gel/water (c) Zeolite 13X/water	278, 308-330, 308-330, 368-453	---	---	---	Heat recovery (2 beds in alternate operation)	---	---	(a) 1.00-1.65 (b) 0.80 – 1.45 (c) 0.90 – 1.45	---	A heat recovery factor of 0.7 was considered.	[32]
Theor	(a) Silica gel/water (b) SWS-2L/water (c) SWS-1S/water	(a) 280, 328, 328, 388 – 433 (b) 280, 328, 328, 393 – 423 (c) 280, 328, 328, 373 – 408	---	---	---	Heat recovery (2 beds in alternate operation)	---	---	(a) 1.05-1.50 (b) 1.15 – 1.65 (c) 1.13 – 1.40	---	---	[33]
Theor	(a) CPO-27 (Ni)/water (b) Aluminium fumarate/water	278 -293, 303 – 318, 303 – 318, 343 - 383	---	---	---	Basic (1 bed)	---	---	(a) 1.10 – 1.70 (b) 1.15 – 1.80	---	---	[34]
Theor	Activated carbon/ammonia blend	278, 313, 313, 358-473	---	---	---	(i) Basic (1 bed) (ii) Heat recovery (2 beds in alternate operation)	---	---	(i) 1.00-1.25 (ii) 1.00 – 1.45	---	An azeotropic mixture of 60 % ammonia and 40 % dimethyl ether (R723) was used as refrigerant.	[35]

(Table A2.1 continues)

Chapter 2: Introduction – Annex A2

Exp	SAPO-34/water	285 – 294, 298 – 318, 298 – 318, 358 - 363	~ 294	up to ~ 363	420-600	Basic (1 bed)	Coating (direct crystallization)	Extended surface (aluminum fiber plate)	0.70 - 1.40	1136-3288	<ul style="list-style-type: none"> ▪ T of HTF at the condenser outlet and at the AHEx outlet (in adsorption stage), respectively: ~ 303-308 K and ~ 303-318 K. ▪ SHPs were calculated based on the information reported in Fig. 5 of that work, for m_{ads} of 3.3 kg. 	[36]
Theor	Activated carbon/ammonia	278, 313, 313, 353 - 473	---	---	---	(i) Basic (1 bed) (ii) 2 beds in alternate operation	(a) Monolith (b) Loose grains (c) Fiber and cloth (d) Powder (e) Compacted granular, fiber or cloth	---	(i) (a) 1.05-1.50 (i) (b) 1.10 – 1.50 (i) (c) 1.10 – 1.45 (i) (d) 1.10-1.50 (i) (e) 1.15-1.50 (ii) (a) 1.10-1.70 (ii) (b) 1.20 – 1.70 (ii) (c) 1.15 – 1.70 (ii) (d) 1.20 – 1.75 (ii) (e) 1.20 – 1.70	---	---	[37]
Theor	(a) CAU-3/methanol (b) UiO-67/methanol (c) ZIF-8/methanol (d) CAU-3/ethanol (e) UiO-67/ethanol (f) ZIF-8/ethanol	288, 318, 318, 355-395	---	---	---	Basic (1 bed)	---	---	(a) 1.20 – 1.60 (b) 1.10-1.60 (c) 1.20 – 1.60 (d) 1.10 – 1.55 (e) 1.05-1.50 (f) 1.05 – 1.50	---	---	[38]

(Table A2.1 continues)

Chapter 2: Introduction – Annex A2

Theor	(a) MOF-801 (Zr)/water (b) MIL-53(Cr)/methanol (c) Zn(BDC) (DABCO)/methanol (d) AQSOA® FAM-Z02/water (e) Activated carbon/methanol	(a), (d), (e) 288, 318, 318, 350-395 (b), (c) 288, 318, 318, 360-395	---	---	---	Basic (1 bed)	---	---	(a) 1.00 – 1.55 (b) 1.00 – 1.50 (c) 1.00 – 1.55 (d) 1.35 – 1.60 (e) 1.00 – 1.50	---	---	[39]
Exp	Activated carbon Busofit/ammonia	~ 255, 293 – 303, 323, 383-393	---	---	720 (H)	Heat recovery (2 beds in alternate operation)	Loose fibers	Tubular (shell and finned tubes)	---	350	---	[40]
Theor/ Exp	Activated carbon/ammonia	268 – 285, ---, 303 – 313, ---	---	396-443	120-420 (F)	Heat recovery (4 beds)	Loose grains (packed layer, $\delta = 9 \times 10^{-4}$ m)	Tubular (shell and tube without fins)	ca. 1.10* – 1.80* (1.67* → 1.31)	ca. 500* - 2250*	AHP intended for domestic environment (space and water heating) as replacer of gas condensing boilers	[41]
Theor/ Exp	Activated carbon/ammonia	---	253-293	---	---	Basic (1 bed)	Loose grains	---	---	---	Aiming at the development of a residential gas fired AHP water heater.	[42]
Exp	Activated carbon/ammonia	---	---	448 - 498	---	Forced convection (2 beds)	Loose grains	---	1.80	---	---	[43]
Theor	(a) Zeolite 4A/water (b) Activated carbon/methanol (c) Zeolite 13X/water (d) Activated carbon/Ammonia	(a) 278, 313-328, 313-328, 473 (b) 278, 313-328, 313-328, 413-423 (c) 278, 313-328, 313-328, 493-563 (d) 258, 313-328, 313-328, 523	---	---	---	(i) Heat recovery (2 beds in alternate operation) (ii) Thermal wave (2 beds in alternate operation)	---	---	(a)(i) 1.45 (b)(i) 1.45-1.60 (c)(i) 1.60-1.75 (c)(ii) 1.70-2.00 (d)(ii) 1.40-2.05	(a) (i) ca. 900 (b) (i) 100 – 450 (c)(i) 1000-1100 (c)(ii) 400 (d)(ii) 650-800	---	[44]

(Table A2.1 continues)

Chapter 2: Introduction – Annex A2

Exp	Zeolite 13X/water	---, ---, ---, 423	283 - 313	423	21600	Basic (1 bed)	Loose grains	Tubular (shell and finned tubes)	0.83-1.09	---	---	[45]
Theor/ Exp	(a) Silica gel/water (b) Zeolite 13X/water	(a) 280-273, 308-318, 311-321, 388-395 (b) 279, 379, 358, 546	---	---	(a) 2340 - 3060 (b) 2520	Basic (1 bed)	Loose grains	Tubular (shell and finned tubes)	(a) 1.26 [*] -1.41 [*] ; 0.90 – 1.07 (1.41 [*] →1.04; 1.34 [*] →0.96; 1.26 [*] →0.90; 1.39 [*] →1.07) (b) 1.31 [*] → 1.00	(a) 111 [*] -136 [*] 74-93 (136 [*] →85; 133 [*] →83; 111 [*] →74; 132 [*] →93) (b) 283 [*] → 237	COPs and SHPs were calculated using the theoretical and experimental data reported in Table 7.1 of that work.	[46]
Theor/ Exp	Activated carbon/methanol	---, 301, ---, 317	---	334	330* → 4920 (H)	2 beds (alternate operation)	Loose grains	Tubular (shell and spiral tube)	1.284 [*] →1.014	---	---	[47]
Exp	Silica gel/water	---	288 – 293	353 – 368	1140 – 17160 (F)	Heat recovery (2 beds in alternate operation)	Loose grains	Plate-type (lamella heat exchanger)	ca. 1.05 - 1.46	135 - 376	<ul style="list-style-type: none"> ▪ SHPs correspond to the ratio of the average heating powers divided by m_{ads} in one AHEx module (35 kg) (Tables 5 and 6 of that work). ▪ Experimental results obtained for two distinct control strategies (maximization of COP or power) were reported. 	[48]

(Table A2.1 continues)

Chapter 2: Introduction – Annex A2

Theor	SAPO-34/water	---	---	---	≤ 600	Basic (1 bed)	Coating (direct crystallization)	Extended surface (aluminum fiber plate)	1.10 – 1.60	---	Multicriterial Pareto optimisation performed.	[49]
Theor	Activated carbon/ammonia	---, 323, ---, 523	---	423 - 523	ca. 240 (F)	Forced convection (2 beds in alternate operation)	Loose grains	---	1.20 - 1.35	~ 1000 – 3000	---	[50]
Theor/ Exp	Silica gel/water	291, ---, 300, ---	---	345 (initial)	---	Basic (1 bed)	Loose grains	Plate-type (lamella heat exchanger)	1.19 - 1.32	---	$T_{\text{heat source}}^{\text{high}}$ depends on the stratification effects along the water storage tank (see Figs. 2 and 4 of that work).	[51]
Theor	Zeolite 13X/water	276 – 281, 311 – 316, 301 – 311, 477	---	---	---	Thermal wave (2 beds in alternate operation)	---	---	0.92 – 2.48	---	AHP combined with a boiler is referred in that work.	[52]
Theor	(a) Zeolite 13XBFK/water (b) Zeolite 13X/water (c) Zeolite NaYBFK/water	278, 308-328, 308-328, 398 - 448	---	398-448	900 - 3600	Basic (1 bed)	Loose grains	Tubular (shell and tube without fins)	(a) 1.00-1.41 (b) 1.06-1.39 (c) 1.05-1.63	(a) 40 - 322 (b) 47 – 344 (c) 48 - 621	---	[53]
Theor/ Exp	(a) Zeolite/Water (b) Activated carbon/methanol	298, ---, 308, 493	---	---	9840	Cascading (3 beds: 2 beds with zeolite, and 1 bed with activated carbon)	Loose pellets	Tubular (shell and finned tubes)	1.54* → 1.78	---	The indicated maximum bed T is for the zeolite/water beds. The low T heat from the zeolitic beds was used to regenerate the activated carbon bed (Fig. 4 of that work).	[54]

(Table A2.1 continues)

Chapter 2: Introduction – Annex A2

Theor/ Exp	Activated carbon/ammonia	278, ---, ca. 309 – 323, ---	---	423 - 443	~ 42* – 480* (F)	Heat recovery (2 beds in alternate operation)	(a) Loose grains and powder (b) Consolidated bed: composite with lignin binder (c) Consolidated bed: composite with silane binder (d) Consolidated bed: composite with expanded natural graphite	(i) Tubular (shell and tube without fins) (ii) Tubular (shell and tube with fins)	(a)(i) 1.18 – 1.30 (a)(i) ca. 1.15* - 1.29* (b)(i) ca. 1.17* - 1.28* (c)(i) ca. 1.15* - 1.26* (d)(i) ca. 1.22* - 1.27* (b)(ii) ca. 1.10* - 1.31*	---	<ul style="list-style-type: none"> Developed AHP is intended for space heating as replacer of gas condensing boilers. The system is to be driven by heat supplied by a gas burner and would use pressurized water as HTF. 	[55]
Theor	(a) MIL-101/ethanol (b) MIL-101/methanol (c) MIL-53-NH ₂ /methanol (d) Activated carbon AX-21/ammonia (e) Activated carbon LSZ30/methanol (f) Activated carbon MD5060/methanol (g) Activated carbon AS12/ammonia (h) Activated carbon Maxsorb III (KOH + H ₂)/ethanol (i) Activated carbon MD6070/methanol (j) SG(SP18)/CaCl ₂ (23 wt %)/methanol	250, 323, 323, ≥ 413	---	---	---	Basic (1 bed)	---	---	(a) 1.21 (b) 1.21 (c) 1.16 (d) 1.17 (e) 1.15 (f) 1.15 (g) 1.15 (h) 1.15 (i) 1.15 (j) 1.14	---	<ul style="list-style-type: none"> Around 80 pairs were analyzed. Most promising COPs were obtained for the following: CSPMs/methanol, activated carbons/ammonia, MOFs/methanol and MOFs/ethanol (Fig. 10 of that work). Activated carbons/ammonia are among the most promising pairs in terms of heating power (Fig. 14 of that work). 	[56]

(Table A2.1 continues)

Chapter 2: Introduction – Annex A2

Theor/ Exp	Activated carbon/methanol	247-278, 293 – 319, 288, 326 – 403	253 - 278	326 - 406	2760 - 8160	Basic (1 bed)	Loose grains	Tubular (hairpin with finned tubes)	1.06 – 1.55 (1.13* → 1.06 1.58* → 1.55)	---	---	[57]
Theor	(a) HKUST- 1/methanol (b) Activated carbon/methanol	263-275, 313- 323, 313-323, 353-413	---	---	---	Basic (1 bed)	(a) Coating (direct crystallization) (b) Loose grains/powder	---	(a) 1.00-1.50 (b) 1.00-1.56	---	---	[58]

- (a) *Theor* refers to studies reporting theoretical performances (obtained from simplified calculations or modelling and simulations), and *Exp* refers to experimental work and results obtained from AHP prototypes. *Theor/Exp* refers to the studies encompassing both theoretical and experimental work.
- (b) In the studies whose domain is *Theor/Exp*, the values indicated with * are theoretical or obtained from numerical simulations.
- (c) Due to the several different approaches in the literature regarding the specification of t_{cycle} for advanced cycles, whenever possible it is indicated whether it corresponds to a half cycle time (i.e., the time for one bed to perform half of an operating cycle) or to a full cycle time (i.e. the time for one bed to run a complete operating cycle). In the first case, the values of t_{cycle} are identified with *H* (half), and in the second case they are marked with *F* (full).
- (d) The symbol → was used to indicate the differences in the reported t_{cycle} , *COPs* and *SHPs* determined through theoretical calculations or simulations, and measured in prototypes/experimental setups, for the same working conditions (“theoretical/calculated value” → “experimental value”), to show the differences in results when going from theoretical to practical scenarios.
- (e) δ is the adsorbent bed thickness.
- (f) When performances were calculated from equilibrium data without any more information, cycle feature was considered basic.

References

- [1] Y.B. Gui, R.Z. Wang, W. Wang, J.Y. Wu, Y.X. Xu, Performance modeling and testing on a heat-regenerative adsorptive reversible heat pump, *Applied Thermal Engineering*, 22 (2002) 309-320.
- [2] G. Cacciola, G. Restuccia, Reversible adsorption heat pump: a thermodynamic model, *International Journal of Refrigeration*, 18 (1995) 100-106.
- [3] G.H.W. van Benthem, G. Cacciola, G. Restuccia, Regenerative adsorption heat pumps: Optimization of the design, *Heat Recovery Systems and CHP*, 15 (1995) 531-544.
- [4] T. Zanifé, F. Meunier, Experimental results of a zeolite-water heat pump installed in a slaughter house, *Heat Recovery Systems and CHP*, 12 (1992) 131-142.
- [5] A. Tajima, Y. Ozawa, H. Kawaguchi, Hybrid Gas Water Heater Combined with Adsorption Heat Pump Cycle for Commercial Use, *HVAC&R Research*, 12 (2006) 783-796.
- [6] L. Dong, H. Huang, N. Kobayashi, Development of an All-in-One Type Adsorption Heat Pump for Heating Application, *International Journal of Chemical Reactor Engineering*, 9 (2011).
- [7] J.M. Pinheiro, A.A. Valente, S. Salústio, N. Ferreira, J. Rocha, C.M. Silva, Application of the novel ETS-10/water pair in cyclic adsorption heating processes: Measurement of equilibrium and kinetics properties and simulation studies, *Applied Thermal Engineering*, 87 (2015) 412-423.
- [8] L. Marletta, G. Maggio, A. Freni, M. Ingrassiotta, G. Restuccia, A non-uniform temperature non-uniform pressure dynamic model of heat and mass transfer in compact adsorbent beds, *International Journal of Heat and Mass Transfer*, 45 (2002) 3321-3330.
- [9] W. Dechang, W. Jingyi, S. Honggang, W. Ruzhu, Experimental study on the dynamic characteristics of adsorption heat pumps driven by intermittent heat source at heating mode, *Applied Thermal Engineering*, 25 (2005) 927-940.
- [10] B. Dawoud, P. Hofle, S. Chmielewski, Experimental Investigation of the Effect Of Zeolite Coating Thickness on the Performance of a Novel Zeolite-Water Adsorption Heat Pump Module, *Tenth International Conference Enhanced Building Operations*, Kuwait (2010).
- [11] B. Dawoud, Water vapor adsorption kinetics on small and full scale zeolite coated adsorbers; A comparison, *Applied Thermal Engineering*, 50 (2013) 1645-1651.
- [12] L. Dong, Y. Suzuki, N. Kobayashi, A novel hybrid adsorption heat pump water heater, *The Canadian Journal of Chemical Engineering*, 87 (2009) 741-747.
- [13] G. Restuccia, G. Cacciola, Performances of adsorption systems for ambient heating and air conditioning, *International Journal of Refrigeration*, 22 (1999) 18-26.
- [14] R. Lang, M. Roth, M. Stricker, T. Westerfeld, Development of a modular zeolite-water heat pump, *Heat and Mass Transfer*, 35 (1999) 229-234.
- [15] G. Cacciola, G. Restuccia, G.H.W. van Benthem, Influence of the adsorber heat exchanger design on the performance of the heat pump system, *Applied Thermal Engineering*, 19 (1999) 255-269.
- [16] T. Núñez, W. Mittelbach, H.-M. Henning, Development of an adsorption chiller and heat pump for domestic heating and air-conditioning applications, *Applied Thermal Engineering*, 27 (2007) 2205-2212.

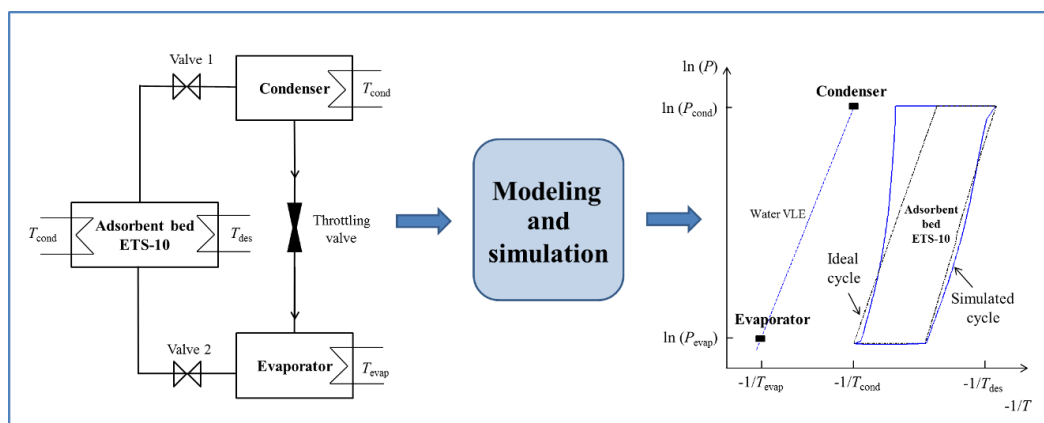
- [17] D.J. Miles, S.V. Shelton, Design and testing of a solid-sorption heat-pump system, *Applied Thermal Engineering*, 16 (1996) 389-394.
- [18] J.M. Pinheiro, S. Salústio, J. Rocha, A.A. Valente, C.M. Silva, Analysis of equilibrium and kinetic parameters of water adsorption heating systems for different porous metal/metalloid oxide adsorbents, *Applied Thermal Engineering*, 100 (2016) 215-226.
- [19] S.J. Metcalf, R.E. Critoph, Z. Tamainot-Telto, Optimal cycle selection in carbon-ammonia adsorption cycles, *International Journal of Refrigeration*, 35 (2012) 571-580.
- [20] N. Douss, F.E. Meunier, L.M. Sun, Predictive model and experimental results for a two-adsorber solid adsorption heat pump, *Industrial & Engineering Chemistry Research*, 27 (1988) 310-316.
- [21] F. Meunier, Theoretical performances of solid adsorbent cascading cycles using the zeolite-water and active carbon-methanol pairs: four case studies, *Journal of Heat Recovery Systems*, 6 (1986) 491-498.
- [22] T.A. Fuller, W.J. Wepfer, S.V. Shelton, M.W. Ellis, A Two-Temperature Model of the Regenerative Solid-Vapor Heat Pump, *Journal of Energy Resources Technology*, 116 (1994) 297-304.
- [23] D.I. Tchernev, Regenerative Zeolite Heat Pump, in: P.A. Jacobs, R.A. van Santen (eds.) *Studies in Surface Science and Catalysis*, Vol. 49, Elsevier, 1989, pp. 519-526.
- [24] S.V. Shelton, W.J. Wepfer, D.J. Miles, Square wave analysis of the solid-vapor adsorption heat pump, *Heat Recovery Systems and CHP*, 9 (1989) 233-247.
- [25] S.V. Shelton, W.J. Wepfer, D.J. Miles, Ramp Wave Analysis of the Solid/Vapor Heat Pump, *Journal of Energy Resources Technology*, 112 (1990) 69-78.
- [26] A.S. Ülkü, M. Mobedi, Adsorption in Energy Storage, in: B. Kılıkış, S. Kakaç (eds.) *Energy Storage Systems*, Springer Netherlands, Dordrecht, 1989, pp. 487-507.
- [27] R.Z. Wang, Adsorption refrigeration research in Shanghai Jiao Tong University, *Renewable and Sustainable Energy Reviews*, 5 (2001) 1-37.
- [28] M. Pons, F. Poyelle, Adsorptive machines with advanced cycles for heat pumping or cooling applications, *International Journal of Refrigeration*, 22 (1999) 27-37.
- [29] R.E. Critoph, Forced convection adsorption cycle with packed bed heat regeneration: Cycle à adsorption à convection forcée avec régénération thermique du lit fixe, *International Journal of Refrigeration*, 22 (1999) 38-46.
- [30] A. Freni, G. Maggio, A. Sapienza, A. Frazzica, G. Restuccia, S. Vasta, Comparative analysis of promising adsorbent/adsorbate pairs for adsorptive heat pumping, air conditioning and refrigeration, *Applied Thermal Engineering*, 104 (2016) 85-95.
- [31] A. Frazzica, A. Sapienza, A. Freni, Novel experimental methodology for the characterization of thermodynamic performance of advanced working pairs for adsorptive heat transformers, *Applied Thermal Engineering*, 72 (2014) 229-236.
- [32] T. Nunez, H.M. Henning, W. Mittelbach, Adsorption cycle modeling: Characterization and comparison of materials, *International Sorption Heat Pump Conference (ISHPC)*, München (1999).
- [33] Y.I. Aristov, G. Restuccia, G. Cacciola, V.N. Parmon, A family of new working materials for solid sorption air conditioning systems, *Applied Thermal Engineering*, 22 (2002) 191-204.
- [34] E. Elsayed, R. Al-Dadah, S. Mahmoud, A. Elsayed, P.A. Anderson, Aluminium fumarate and CPO-27(Ni) MOFs: Characterization and thermodynamic analysis for adsorption heat pump applications, *Applied Thermal Engineering*, 99 (2016) 802-812.

- [35] Z. Tamainot-Telto, Novel method using Dubinin-Astakhov theory in sorption reactor design for refrigeration and heat pump applications, *Applied Thermal Engineering*, 107 (2016) 1123-1129.
- [36] U. Wittstadt, G. Földner, E. Laurenz, A. Warlo, A. Große, R. Herrmann, L. Schnabel, W. Mittelbach, A novel adsorption module with fiber heat exchangers: Performance analysis based on driving temperature differences, *Renewable Energy*, 110 (2016) 154-161.
- [37] Z. Tamainot-Telto, S.J. Metcalf, R.E. Critoph, Y. Zhong, R. Thorpe, Carbon–ammonia pairs for adsorption refrigeration applications: ice making, air conditioning and heat pumping, *International Journal of Refrigeration*, 32 (2009) 1212-1229.
- [38] M.F. de Lange, B.L. van Velzen, C.P. Ottevanger, K.J.F.M. Verouden, L.-C. Lin, T.J.H. Vlugt, J. Gascon, F. Kapteijn, Metal–Organic Frameworks in Adsorption-Driven Heat Pumps: The Potential of Alcohols as Working Fluids, *Langmuir*, 31 (2015) 12783-12796.
- [39] M.F. de Lange, K.J.F.M. Verouden, T.J.H. Vlugt, J. Gascon, F. Kapteijn, Adsorption-Driven Heat Pumps: The Potential of Metal–Organic Frameworks, *Chemical Reviews*, 115 (2015) 12205-12250.
- [40] L.L. Vasiliev, D.A. Mishkinis, A.A. Antukh, L.L. Vasiliev Jr, Solar–gas solid sorption heat pump, *Applied Thermal Engineering*, 21 (2001) 573-583.
- [41] A.R. Pacho, Innovation in carbon/ammonia adsorption heat pump technology: a case study, Institute of Refrigeration (IOR), United Kingdom (2015).
- [42] M. Ally, High Efficiency, Residential Gas-Fired Adsorption Heat Pump Water Heater Development, Hot Water Forum - American Council for an Energy-Efficient Economy (ACEEE), Portland (2016).
- [43] R.E. Critoph, Adsorption Refrigeration Research at Warwick, 1st TECCS meeting, University of Warwick (2007).
- [44] M. Pons, F. Meunier, G. Cacciola, R.E. Critoph, M. Groll, L. Puigjaner, B. Spinner, F. Ziegler, Thermodynamic based comparison of sorption systems for cooling and heat pumping: Comparaison des performances thermodynamique des systèmes de pompes à chaleur à sorption dans des applications de refroidissement et de chauffage, *International Journal of Refrigeration*, 22 (1999) 5-17.
- [45] B. Dawoud, E.H. Amer, D.M. Gross, Experimental investigation of an adsorptive thermal energy storage, *International Journal of Energy Research*, 31 (2007) 135-147.
- [46] D. Schawe, Theoretical and experimental investigations of an adsorption heat pump with heat transfer between two adsorbers, PhD thesis, University of Stuttgart, Germany (2001).
- [47] A. Grzebielec, Experimental study on adsorption heat pump, *Archives of Thermodynamics*, 30 (2009) 189-200.
- [48] T. Núñez, W. Mittelbach, H.M. Henning, Development of a Small-Capacity Adsorption System for Heating and Cooling Applications, *HVAC&R Research*, 12 (2006) 749-765.
- [49] G. Földner, Performance evaluation and optimization of adsorption modules, Sorption Friends 2015, Sicily (2015).
- [50] R.E. Critoph, Forced convection enhancement of adsorption cycles, *Heat Recovery Systems and CHP*, 14 (1994) 343-350.
- [51] W. Li, Y. Chen, P. Xu, C. Joshi, F. Schmidt, Research on the performance of an adsorption heat pump in winter demand response, *Science and Technology for the Built Environment*, 23 (2017) 449-456.

- [52] A. Hajji, W.M. Worek, Simulation of a regenerative, closed-cycle adsorption cooling/heating system, *Energy*, 16 (1991) 643-654.
- [53] J.M. Pinheiro, S. Salústio, A.A. Valente, C.M. Silva, Adsorption heat pump optimization by experimental design and response surface methodology, *Applied Thermal Engineering*, 138 (2018) 849-860.
- [54] N. Douss, F. Meunier, Experimental study of cascading adsorption cycles, *Chemical Engineering Science*, 44 (1989) 225-235.
- [55] A.M. Rivero-Pacho, R.E. Critoph, S.J. Metcalf, Modelling and development of a generator for a domestic gas-fired carbon-ammonia adsorption heat pump, *Renewable Energy*, 110 (2017) 180-185.
- [56] D.B. Boman, D.C. Hoysall, D.G. Pahinkar, M.J. Ponkala, S. Garimella, Screening of working pairs for adsorption heat pumps based on thermodynamic and transport characteristics, *Applied Thermal Engineering*, 123 (2017) 422-434.
- [57] N. Douss, F. Meunier, Effect of operating temperatures on the coefficient of performance of active carbon-methanol systems, *Heat Recovery Systems and CHP*, 8 (1988) 383-392.
- [58] S.-J. Ernst, F. Jeremias, H.-J. Bart, S.K. Henninger, Methanol Adsorption on HKUST-1 Coatings Obtained by Thermal Gradient Deposition, *Industrial & Engineering Chemistry Research*, 55 (2016) 13094-13101.

Chapter 3: Adsorption heat pump based on ETS-10/water pair[†]

The ETS-10/water pair was explored for the first time for cyclic adsorption heating purposes, with modeling and simulation studies. Measurements of water adsorption equilibrium properties were carried out, and, for the first time, the effective thermal conductivity and specific heat capacity of ETS-10 were measured. The experimental results were used for the modeling and simulation of an adsorption heating unit. A model was developed, which contemplates adsorption equilibrium, one-dimensional heat and mass transfer in the bed, heat transfer in the external film, and intraparticle mass transport. From the numerical simulations, the coefficient of performance (*COP*) and specific heating power (*SHP*) were calculated, which allowed evaluating the heating performance of the adsorption unit. The bed thickness, adsorbent regeneration temperature, and heating thermal fluid temperature influence considerably the cycle time and cyclic adsorption loading swing, thus impacting on *COP* and *SHP*. For three simulated cycles differing in bed thickness, *COP* values in the range 1.36–1.39 were obtained, which are close to the estimated ideal value of 1.41; the corresponding *SHP* ranged from 934 to 249 W kg⁻¹. Based on sensitivity studies, a good compromise is required between the bed thickness, regeneration temperature, and the heating fluid temperature in order to meet superior performances of the system.



[†] Based on:

Joana M. Pinheiro, Anabela A. Valente, Sérgio Salústio, Nelson Ferreira, João Rocha, Carlos M. Silva, Application of the novel ETS-10/water pair in cyclic adsorption heating processes: measurement of equilibrium and kinetics properties and simulation studies, *Appl. Therm. Eng.*, 87 (2015), pp. 412-423.

3.1. Introduction

In recent years adsorption systems for heating/cooling applications have received much attention, since they are based on an environmentally friendly technology in comparison to the conventional vapor compression systems, and can be powered by thermal energy sources such as solar energy or waste heat [1-4]. The absence of moving parts, noise and vibration are also important features of adsorption systems [5].

A basic adsorption heating system (AHS) comprises an adsorbent bed operating in alternate connection to an evaporator or a condenser (Fig. 3.1(a)), depending on the stage of the cycle. The complete adsorption cycle consists of four stages (Fig. 3.1(b)): isobaric adsorption (1-2), isosteric heating (2-3), isobaric desorption (3-4), and isosteric cooling (4-1).

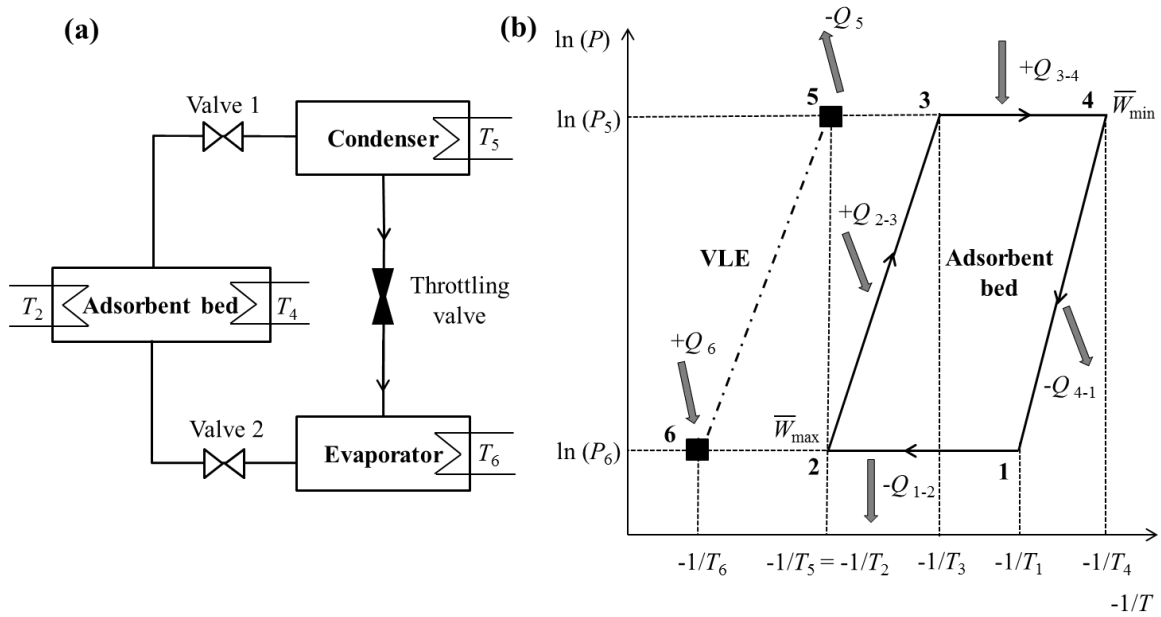


Fig. 3.1 - Simplified representation of an adsorption heating system and (b) corresponding Clapeyron diagram. Q_{1-2} , Q_{4-1} and Q_5 are the heats generated during adsorption stage, during isosteric cooling stage and in the condenser, respectively; Q_{2-3} , Q_{3-4} and Q_6 are the heats consumed during isosteric heating stage, during desorption stage and in the evaporator, respectively; P_5 and P_6 are the condenser and the evaporator pressures, respectively; T_5 and T_6 are the condenser and the evaporator temperatures, respectively; T_1 and T_2 are the initial and final temperatures of the bed during isobaric adsorption stage; T_3 and T_4 are the initial and final temperatures of the bed during isobaric desorption stage; \bar{W}_{\max} and \bar{W}_{\min} are the maximum and minimum average adsorbate loadings, respectively.

In the isobaric adsorption stage, the bed is connected to the evaporator, vapor is adsorbed on the adsorbent material and heat Q_{1-2} is released from the system, which can be used for heating purposes. Subsequently, in the isosteric heating (2-3) the adsorbent is isolated (closing valves 1 and 2) and heated (Q_{2-3}), which is accompanied by increasing pressure. When P_5 is reached, the adsorbent bed is opened to the condenser, and the isobaric desorption stage is initialized. Heat supply (Q_{3-4}) is required for regenerating the adsorbent; the desorbed vapor condenses inside the condenser, releasing heat (Q_5) which can be used for heating purposes. The adsorption cycle closes with the isosteric cooling stage in which the bed is isolated (closing valves 1 and 2) and cooled, which is accompanied by pressure drop. The sensible heat released by the system in this stage (Q_{4-1}) can also be used for heating purposes. When the bed pressure reaches P_6 , a new cycle can be initialized by reopening the adsorbent bed to the evaporator, etc.

The selection of the most appropriate working adsorbent/adsorbate pair is one of the main factors determining the efficiency of any AHS. Important requirements to be put on the adsorbent include good hydrothermal stability, considerable adsorption capacity, and easily regenerated. On the other hand, the refrigerant fluid should preferably have a large specific latent heat, good thermal stability, be non-toxic and not flammable [4]. Some of the pairs reported in the literature for heating applications include activated carbon/methanol [6], activated carbon/ammonia [7], zeolite/water [6]. There is a continuous search for novel materials aiming at the improvement of their heating performances [8, 9].

The Engelhard titanosilicate number 10 (ETS-10), firstly synthesised in 1989 [10], possesses an interesting framework structure and charge distribution, and unique adsorption properties [11]. This material is microporous and crystalline, and its structure consists of corner-sharing SiO_4 tetrahedra and TiO_6^{2-} octahedra linked through bridging oxygen atoms, forming a pore system which contains 12-membered ring channels. Since the titanium sites are located in small 7-membered ring channels, the interactions between water molecules inside the 12-membered ring channels and the framework are relatively weak in comparison to conventional zeolites, allowing facilitated regeneration of ETS-10 [12]. The potentiality of ETS-10 as adsorbent in cyclic processes for removing water has deserved patent applications [13], and it has also found increasing interest as desiccant in chlorofluorocarbon-free air conditioners based on evaporative and desiccant cooling [14].

In spite of its interesting water adsorption properties, ETS-10 has been under-investigated for cyclic adsorption heating purposes. This may be partly due to the fact that the design and optimisation of heating/cooling systems require the knowledge of various fundamental properties of the adsorbents, which unfortunately are not available for many promising materials including ETS-10.

In this work, a cyclic adsorption unit with the ETS-10/water pair was investigated for heating purposes. The process was simulated using a model, which includes the adsorption equilibrium, one-dimensional heat and mass transfer phenomena in the bed, heat transfer in the particle film, and mass transfer resistance inside the particles. Due to the lack of necessary kinetic and equilibrium data for the simulations, this work comprehended also an indispensable experimental component. The ETS-10/water isotherms were measured at different temperatures, and the data fitted with a reliable model for determination of the isosteric heat of adsorption; from the adsorption kinetics data, the intraparticle mass transfer coefficient was determined. In addition, thermophysical properties of ETS-10, specifically the effective thermal conductivity and specific heat capacity, were measured for the first time, along with the bed porosity and density of the adsorbent. Sensitivity studies were carried out in order to get insights into the influence of the bed thickness and the operating conditions on the overall heating performance of the system, which was evaluated by means of the coefficient of performance (*COP*) and specific heating power (*SHP*).

3.2. Materials and methods

The powdered ETS-10 sample was synthesised according to the titanium trichloride based method described previously [15]. The crystalline structure of the material was checked by powder X-ray diffraction, using a Philips X'Pert MPD diffractometer with CuK α radiation.

The porosity of the bed was determined by mercury porosimetry using an AutoPore IV Micromeritics equipment operating between $3.45 \times 10^3 - 2.07 \times 10^8$ Pa, (experimental error of 2-5 %). The adsorbent density was measured by helium pycnometry using a

Quantachrome Multipycnometer after pre-treatment of the sample at 383 K during 1h (*ca.* 4 % error).

The adsorption-desorption isotherms of water on ETS-10 were measured at 298, 323 and 348 K, by the gravimetric method, using a CI Electronics microbalance (experimental error of up to 5 %). Prior to analysis, the ETS-10 (*ca.* 65 mg) was outgassed at 573 K under vacuum ($<10^{-2}$ kPa) during *ca.* 2 h, and then cooled to the desired temperature. For each equilibrium point of the isotherms, the variation of mass with time was monitored using CI Electronics Labweigh software, and the pressure was monitored using Pfeiffer and Edwards Penning pressure sensors.

The effective thermal conductivity and specific heat capacity of pelletized ETS-10 were measured in the range 293–413 K, using a TPS 2500 hot diskAB sensor [16], with uncertainties of $\pm 0.004 \text{ W m}^{-1} \text{ K}^{-1}$ and $\pm 0.03 \text{ MJ m}^{-3} \text{ K}^{-1}$, respectively.

3.3. Mathematical modeling of the adsorption unit

3.3.1. Model description

The cyclic adsorption process using the ETS-10/water pair was investigated for the common cylindrical bed configuration represented in Fig. 3.2.

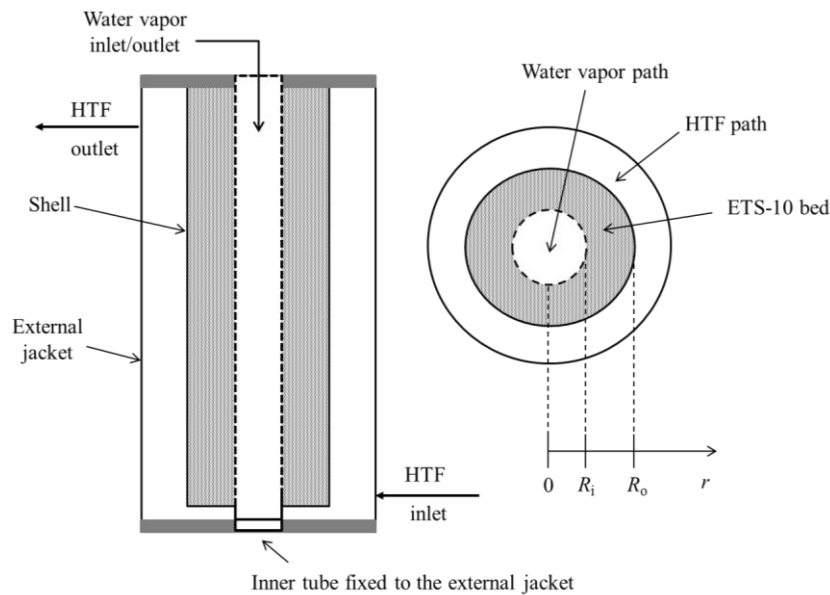


Fig. 3.2 - Schematic representation of the adsorption unit modeled in this work. HTF is the heat transfer fluid; the vapor inlet/outlet tube is connected to the condenser or to the evaporator.

The core of the unit is essentially composed of a central porous and empty tube, through which the water vapor is either evacuated to the condenser or feed from the evaporator; an external jacket where a heat transfer fluid (HTF) circulates for heating (temperature $T_{HTF,hot}$) or cooling (temperature $T_{HTF,cool}$) the adsorbent bed; a cylindrical shell, between the empty tube and the jacket, containing ETS-10. Both upper and bottom surfaces of the unit are insulated, and thus heat and mass transfer are assumed to occur only in the radial direction.

The following assumptions were introduced in the mathematical model: (i) the adsorbent bed is composed of uniformly-sized particles and constant porosity; (ii) there is resistance to mass transfer inside the particles; (iii) there is film resistance to heat transfer (around the particle); (iv) thermal conductivities and specific heat capacities of the solid and vapor, and the viscosity of the vapor are constants; (v) radiation heat transfer, viscous dissipation and the work done by pressure changes are negligible; (vi) thermal resistance between the HTF and the adsorbent bed is negligible, and there are no losses to the environment.

The mathematical model of the unsteady state cyclic unit was written for a differential volume element of radial thickness dr , and includes (Table 3.1): the material balance to the bed (Eq. (3.1)), which contemplates accumulation in the fluid domain (bed void) and in the solid particles, and convective transport through the bed; the material balance to the adsorbent particles (Eq. (3.2)), given by the Linear Driving Force (LDF) model which accounts for intra-particle mass transfer resistances, and provides a suitable description of the transport behavior [17, 18]; the energy balances to the adsorbent (Eq. (3.3)) and vapor (Eq. (3.4)); the equilibrium isotherm described by the Dubinin-Astakhov model (Eq. (3.5)) [19]; and the momentum balance, considering the fluid superficial velocity through the bed as described by Darcy's law (Eq. (3.6)) [20]. The set of initial and boundary conditions for each stage of the cycle are given in Table 3.2. The heating performance of the unit was evaluated by means of the *COP* (Eq. (3.15)) and *SHP* (Eq. (3.16)).

Chapter 3: Adsorption heat pump based on ETS-10/water pair

Table 3.1 - Mathematical model of the adsorption heating system investigated in this work.

Description	Equation	
Material balance to the adsorbent bed	$\varepsilon_b \frac{\partial \rho_v}{\partial t} + (1 - \varepsilon_b) \rho_s \frac{\partial W}{\partial t} + \frac{1}{r} \frac{\partial (r \rho_v u)}{\partial r} = 0$	(3.1)
Material balance to the adsorbent particles - Linear Driving Force (LDF) model	$\frac{\partial W}{\partial t} = K_{LDF} (W_{eq} - W)$	(3.2)
Energy balance to the adsorbent bed	$\rho_s (1 - \varepsilon_b) (C_{p,s} + W C_{p,a}) \frac{\partial T_s}{\partial t} = \frac{1}{r} \frac{\partial}{\partial r} \left(r \lambda_{eff,s} \frac{\partial T_s}{\partial r} \right) - a h_{sv} (T_s - T_v) + (1 - \varepsilon_b) \rho_s \frac{\partial W}{\partial t} Q_{ads}$	(3.3)
Energy balance to the vapor	$\varepsilon_b \frac{\partial}{\partial t} (\rho_v C_{p,v} T_v) + \frac{1}{r} \frac{\partial}{\partial r} (r u \rho_v C_{p,v} T_v) - (1 - \varepsilon_b) \rho_s C_{p,v} \frac{\partial W}{\partial t} (T_s - T_v) = \frac{1}{r} \frac{\partial}{\partial r} \left(r \lambda_{eff,v} \frac{\partial T_v}{\partial r} \right) + a h_{sv} (T_s - T_v)$	(3.4)
Dubinin-Astakhov (DA) isotherm ^(a)	$W_{eq} = W_0 \exp \left[-D \left(T \ln \frac{P_{sat}}{P} \right)^n \right]$	(3.5)
Momentum balance – Darcy’s Law	$u = -\frac{K}{\eta_v} \frac{\partial P}{\partial r}$	(3.6)
Blake-Kozeny model ^(b)	$K = \frac{d_p^2 \varepsilon_b^3}{150(1 - \varepsilon_b)^2}$	(3.7)
Clausius-Clapeyron model ^(c)	$\left[\frac{\partial \ln P}{\partial \left(\frac{1}{T} \right)} \right]_W = -\frac{Q_{ads} M}{\mathfrak{R}}$	(3.8)
External surface area of adsorbent spheres per unit bed volume	$a = \frac{6(1 - \varepsilon_b)}{d_p}$	(3.9)

(continuation in next page)

Chapter 3: Adsorption heat pump based on ETS-10/water pair

Description	Equation	
Dimensionless correlation for h_{sv} calculation ^(d)	$Nu = 2 + 1.8Pr^{0.33}Re^{0.5}$	(3.10)
Nusselt number ^(e)	$Nu = \frac{d_p h_{sv}}{\lambda_v}$	(3.11)
Prandtl number ^(e)	$Pr = \frac{\eta_v C_{p,v}}{\lambda_v}$	(3.12)
Reynolds number ^(e)	$Re = \frac{u \rho_v d_p}{\eta_v}$	(3.13)
Effective thermal conductivity of vapor	$\lambda_{eff,v} = \lambda_v \varepsilon_b$	(3.14)
Coefficient of heating performance (COP) ^(f)	$COP = \frac{ Q_{1-2} + Q_5 + Q_{4-1} }{Q_{3-4} + Q_{2-3}}$	(3.15)
Specific heating power (SHP) ^(f)	$SHP = \frac{ Q_{1-2} + Q_5 + Q_{4-1} }{m_s t_{cycle}}$	(3.16)
Heat released by the adsorbent bed in the isobaric adsorption ^(f)	$Q_{1-2} = \int_{T_1}^{T_2} [m_s (C_{p,s} + \bar{W} C_{p,a})] d\bar{T} + \int_{\bar{W}_{min}}^{\bar{W}_{max}} m_s (-Q_{ads}) d\bar{W}$	(3.17)
Heat supplied to the adsorbent bed in the isosteric heating ^(f)	$Q_{2-3} = \int_{T_2}^{T_3} [m_s (C_{p,s} + \bar{W} C_{p,a})] d\bar{T}$	(3.18)
Heat supplied to the adsorbent bed in the isobaric desorption ^(f)	$Q_{3-4} = \int_{T_3}^{T_4} [m_s (C_{p,s} + \bar{W} C_{p,a})] d\bar{T} + \left \int_{\bar{W}_{max}}^{\bar{W}_{min}} m_s Q_{ads} d\bar{W} \right $	(3.19)

(continuation in next page)

Chapter 3: Adsorption heat pump based on ETS-10/water pair

Description	Equation	
Heat released by the adsorbent bed in the isosteric cooling ^(f)	$Q_{4-1} = \int_{T_4}^{T_1} [m_s(C_{p,s} + \bar{W}C_{p,a})] d\bar{T}$	(3.20)
Heat produced in the condenser ^(f)	$Q_5 = -m_s \Delta \bar{W}_{\text{cycle}} \Delta H_v, \text{ where } \Delta \bar{W}_{\text{cycle}} = \bar{W}_{\text{max}} - \bar{W}_{\text{min}}$	(3.21)
Averages of temperature (\bar{T}), adsorbate loading (\bar{W}) and pressure (\bar{P})	$\bar{\varphi}(t) = \frac{\int_{R_i}^{R_o} 2r\varphi(t,r)dr}{(R_o^2 - R_i^2)}$	(3.22)

^(a) Saturation pressure (P_{sat}) was calculated by the Antoine equation [21]. ^(b) Equation available from reference [20]. ^(c) Equation available from reference [19]. The Clausius-Clapeyron equation was used to calculate Q_{ads} from the DA isotherm. ^(d) Equation available from reference [22]. ^(e) Equation available from reference [23]. ^(f) Nomenclature in accordance with Fig. 3.1.

Table 3.2 - Initial and boundary conditions of the model of the adsorption heating system investigated in this work.

Cycle stage	Inner boundary conditions ($r = R_i$)	Outer boundary conditions ($r = R_o$)	Initial conditions
Isobaric adsorption (1→2)	$\frac{\partial T_s}{\partial r}(t, R_i) = \frac{\partial T_v}{\partial r}(t, R_i) = 0$ $P(t, R_i) = P_{\text{evap}}$	$T_s(t, R_o) = T_v(t, R_o) = T_{\text{HTF,cool}}$ $\frac{\partial P}{\partial r}(t, R_o) = 0^{(a)}$	<p><i>Startup cycle:</i></p> $T_s(0, r) = T_v(0, r) = T_{\text{ini}}$ $P(0, r) = P_{\text{ini}}$ $W(0, r) = W_{\text{ini}}$ <p><i>Remaining cycles:</i> Final values of T_s, T_v, P and W of the isosteric cooling step</p>
Isosteric heating (2→3)	$\frac{\partial T_s}{\partial r}(t, R_i) = \frac{\partial T_v}{\partial r}(t, R_i) = 0$ $\frac{\partial P}{\partial r}(t, R_i) = 0^{(b)}$	$T_s(t, R_o) = T_v(t, R_o) = T_{\text{HTF,hot}}$ $\frac{\partial P}{\partial r}(t, R_o) = 0^{(a)}$	Final values of T_s , T_v , P and W of the isobaric adsorption step
Isobaric desorption (3→4)	$\frac{\partial T_s}{\partial r}(t, R_i) = \frac{\partial T_v}{\partial r}(t, R_i) = 0$ $P(t, R_i) = P_{\text{cond}}$	$T_s(t, R_o) = T_v(t, R_o) = T_{\text{HTF,hot}}$ $\frac{\partial P}{\partial r}(t, R_o) = 0^{(a)}$	Final values of T_s , T_v , P and W of the isosteric heating step
Isosteric cooling (4→1)	$\frac{\partial T_s}{\partial r}(t, R_i) = \frac{\partial T_v}{\partial r}(t, R_i) = 0$ $\frac{\partial P}{\partial r}(t, R_i) = 0^{(b)}$	$T_s(t, R_o) = T_v(t, R_o) = T_{\text{HTF,cool}}$ $\frac{\partial P}{\partial r}(t, R_o) = 0^{(a)}$	Final values of T_s , T_v , P and W of the isobaric desorption step

^(a) A zero pressure gradient is assumed since the shell wall is impermeable ($u = 0 \text{ m s}^{-1}$). ^(b) Since the bed is isolated from both condenser and evaporator, no pressure gradient exists.

3.3.2. Numerical approach

The highly coupled, complex and non-linear partial differential equations governing the adsorption cycle were solved by the method of lines [24]. The radial direction was discretised using second-order finite difference scheme, as commonly found in the literature [25]. The resulting set of ordinary differential equations was integrated using a variable order solver based on numerical differentiation formulas [26]. The computer simulation program was written in Matlab, and validated using literature data [27]. The dependence of *COP* and *SHP* results in relation to the grid size was evaluated using 35, 50 and 75 points of discretisation, and differences of less than 1 % were observed. Therefore, the trade-off between accuracy and computational cost favors the usage of 35 points. Different stopping criteria were applied for the four steps of the heating cycle. For the isobaric adsorption and desorption stages, the simulator stopped the integration when the average temperature of the bed (\bar{T}) was approximately equal to the outer boundary condition imposed in terms of temperature ($\bar{T} = T_{\text{HTF,cool}}$ for adsorption, and $\bar{T} = T_{\text{HTF,hot}}$ (or lower) for the regeneration; tolerance of 1 K). In the isosteric stages, the stopping criteria were defined in terms of pressure: the simulation stopped when the average pressure in the bed (\bar{P}) was equal to P_{cond} or P_{evap} for the isosteric heating and cooling stages, respectively.

3.4. Results and discussion

3.4.1. Synthesis, properties and isotherms of ETS-10

The powder XRD pattern of the synthesized ETS-10 is in agreement with literature data for this type of material (Fig. 3.3) [15].

The adsorption-desorption isotherms of water on ETS-10 at 298, 323 and 348 K (Fig. 3.4) are reversible and of Type I (IUPAC), characteristic of microporous solids (details are given in Annex A3, Section A3.1.1). For materials with micropore diameters smaller than 15 Å, the adsorption equilibrium is more adequately described by the micropore filling mechanism than the surface coverage mechanism. In this case, an appropriate equilibrium adsorption model is that of Dubinin-Astakhov (DA) (Eq. (3.5)) [19], which fitted

reasonably well the experimental data (Fig. 3.4). The DA model parameters W_0 , D and n , obtained by unconstrained nonlinear optimization, are 0.129 kg kg^{-1} , 4.1×10^{-7} and 1.98, respectively, with an average absolute relative deviation (AARD) of 5.1 % (see Table 3.3).

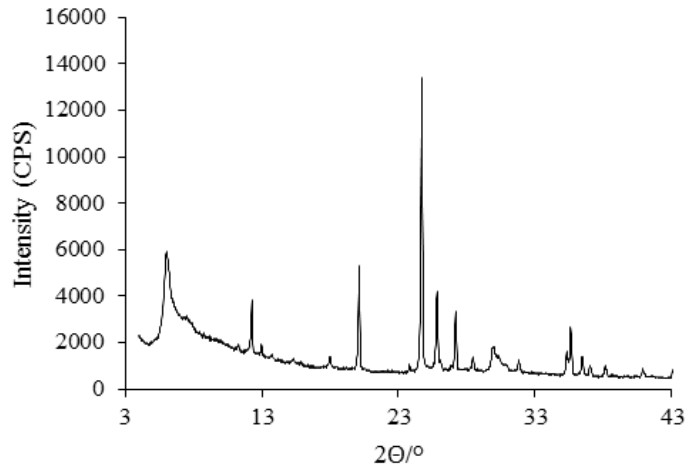


Fig. 3.3 - Powder X-ray diffraction pattern of ETS-10 sample.

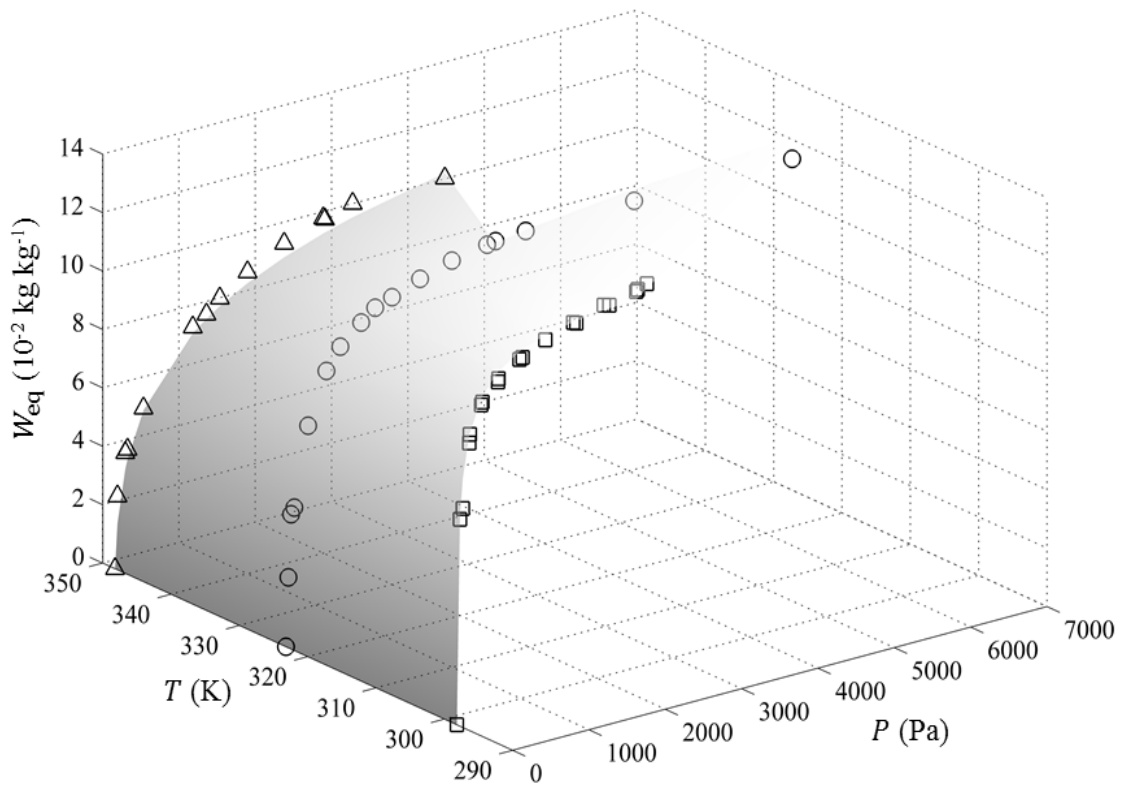


Fig. 3.4 - Water equilibrium adsorption isotherms for ETS-10 at 298 K (\square), 323 K (\circ) and 348 K (Δ). The surface is the Dubinin-Astakhov model (Eq. (3.5)), whose fitted parameters are listed in Table 3.3.

The isosteric heat of adsorption (Q_{ads}) determined using the DA isotherm and the Clausius-Clapeyron equation (Eq. (3.8)), is $3.042 \times 10^6 \text{ J kg}^{-1}$ at half coverage (*i.e.*, $W/W_0 = 0.5$) (Table 3.3, Section 3.4.2.1). The value of Q_{ads} is lower than literature data for different types of zeolites (4A and 13X, Q_{ads} around $4.4 \times 10^6 \text{ J kg}^{-1}$; 10A and mordenite, Q_{ads} about $4 \times 10^6 \text{ J kg}^{-1}$) [2]. High Q_{ads} is attractive in terms of heat generated during the adsorption stage, albeit a compromise is important since higher Q_{ads} can imply more demanding regeneration conditions of the adsorbent.

It has been demonstrated that the use of a constant value of the mass transfer coefficient (K_{LDF}) is sufficient to reproduce the operating conditions of amplifiers, chillers and adsorption heat pumps [28]. In this work, the K_{LDF} was determined by fitting Eq. (3.2) to the experimental kinetics data, giving a mean value of $1.5 \times 10^{-2} \text{ s}^{-1}$ in the temperature range 298-348 K (Table 3.3, Section 3.4.2.1). Exemplified experimental kinetics data of water adsorption on ETS-10, used for the K_{LDF} determination, are shown in Fig. 3.5.

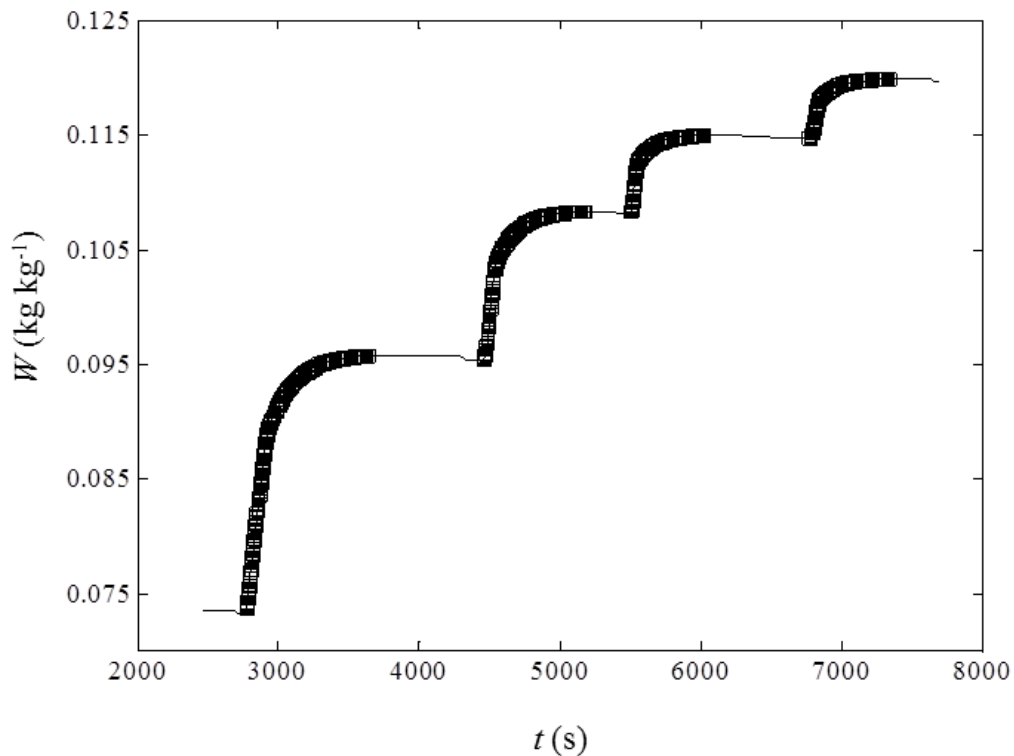


Fig. 3.5 - Kinetics of water adsorption on ETS-10 at 298 K (—), which contributed to the determination of K_{LDF} (■) using Eq. (3.2). The value of K_{LDF} used in the simulations was the average of the values obtained for different water loadings and temperatures (298, 323 and 348 K).

The adsorbent density (ρ_s) and porosity of the bed (ε_b) are 2553 kg m^{-3} and 0.58, respectively (Table 3.3). The effective thermal conductivities ($\lambda_{\text{eff},s}$) and the heat capacities ($C_{p,s}$) of ETS-10, measured in the range 293-413 K, are shown in Fig. 3.6. Details on the measurements of ρ_s , ε_b , $\lambda_{\text{eff},s}$ and $C_{p,s}$ are given in Annex A3 (Sections A3.1.2-A3.1.4). The effective thermal conductivity of the adsorbent contemplates the lattice thermal conductivity, effects associated with packing voids, heat transported by the filling gas, adsorbed water, and thermal resistance associated with boundaries. The average values in the range 333-413 K are $\lambda_{\text{eff},s} = 0.24 \text{ W m}^{-1} \text{ K}^{-1}$ and $C_{p,s} = 800 \text{ J kg}^{-1} \text{ K}^{-1}$ (see Table 3.3), which are similar to those reported for zeolites such as 4A and 13X: Dawoud *et al.* [29] pointed $\lambda_{\text{eff},s}$ between 0.12 and $0.25 \text{ W m}^{-1} \text{ K}^{-1}$ for zeolite 4A in the range 298-473 K, and Jakubinek *et al.* [30] reported 0.16 - $0.22 \text{ W m}^{-1} \text{ K}^{-1}$ for zeolite 13X in the interval 300-400K; Qiu *et al.* [31] reported $C_{p,s}$ around 915 and $948 \text{ J kg}^{-1} \text{ K}^{-1}$ for zeolite 4A in the range 299-311 K.

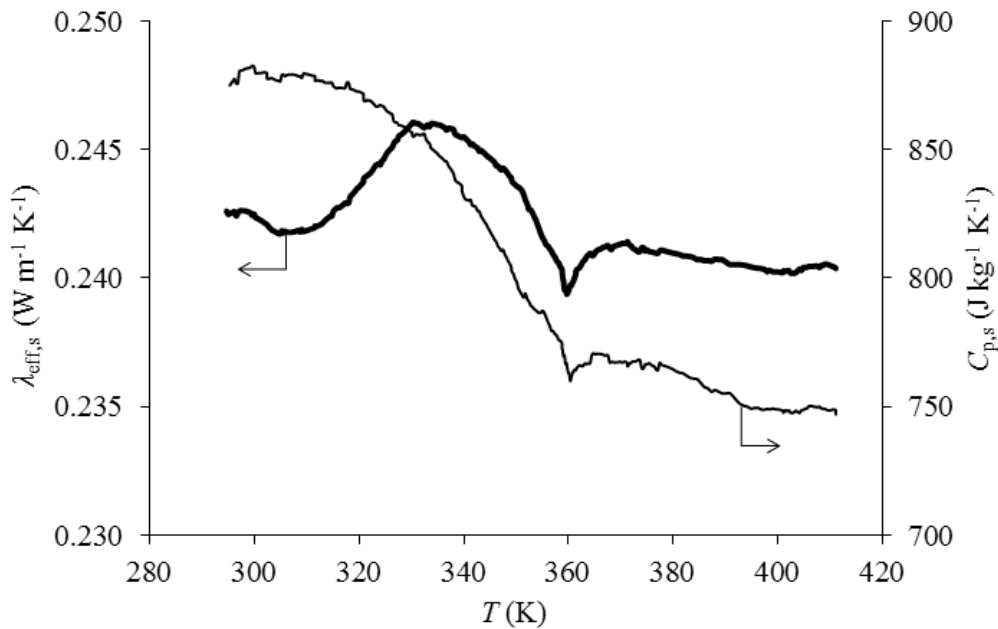


Fig. 3.6 - Effective thermal conductivity and specific heat capacity of ETS-10 as a function of T.

3.4.2. Simulation of the ETS-10/water heating system, and sensitivity studies

The results from the modeling and simulation of the ETS-10/water adsorption heating system are discussed ahead. On the other hand, sensitivity studies are provided in order to get insights into the influence of the bed thickness and operating conditions upon the overall heating performance of the system.

3.4.2.1. Simulation of the ETS-10/water heating system

The most relevant input data used for modeling and simulation of the ETS-10/water system are given in Table 3.3.

Table 3.3 - Main features and properties necessary for the simulations.

Adsorbent		Adsorber dimensions	
$C_{p,s}$ (J kg ⁻¹ K ⁻¹)	800	R_i (m)	0.0050
$\lambda_{eff,s}$ (W m ⁻¹ K ⁻¹)	0.24	R_o (m)	0.0070
d_p (μm)	170	Operating conditions	
ε_b	0.58	P_{ini} (Pa)	500
ρ_s (kg m ⁻³)	2553	T_{ini} (K)	333
Equilibrium and kinetics data		W_{ini} (kg kg ⁻¹)	0
Q_{ads} (J kg ⁻¹)	3.042×10^6	$T_{HTF,cool}$ (K)	333
W_0 (kg kg ⁻¹)	0.129	$T_{HTF,hot}^{(a)}$ (K)	473
D	4.1×10^{-7}	P_{cond} (Pa)	19921
n	1.98	P_{evap} (Pa)	870
K_{LDF} (s ⁻¹)	1.5×10^{-2}	T_{cond} (K)	333
		T_{evap} (K)	278

^(a) The final regeneration temperature of the bed (T_4 in Fig. 3.1) is coincident with $T_{HTF,hot}$.

The modeled adsorption system can represent an application concerning heating purposes where the production of heat at 333 K is desirable, using a heat source

temperature ($T_{\text{HTF,hot}}$) at 473 K to regenerate the adsorbent. A heating design temperature of 333 K was considered in the simulations, as it is the temperature defined for the condenser, also corresponding to the minimum temperature of the cycle. The chosen value of $T_{\text{HTF,hot}}$ lies within the range of temperatures reported in the literature for low grade heat sources, typically between ambient temperature and 523 K [32]. The chosen $T_{\text{HTF,hot}}$ can also correspond to the usage of exhaust gas as a heat source.

The simulated cycles for three different bed thicknesses are compared to the ideal cycle in Fig. 3.7. For the ideal cycle, it is assumed that the temperature and pressure in the bed are uniform, and that the internal mass transfer and heat resistances are negligible.

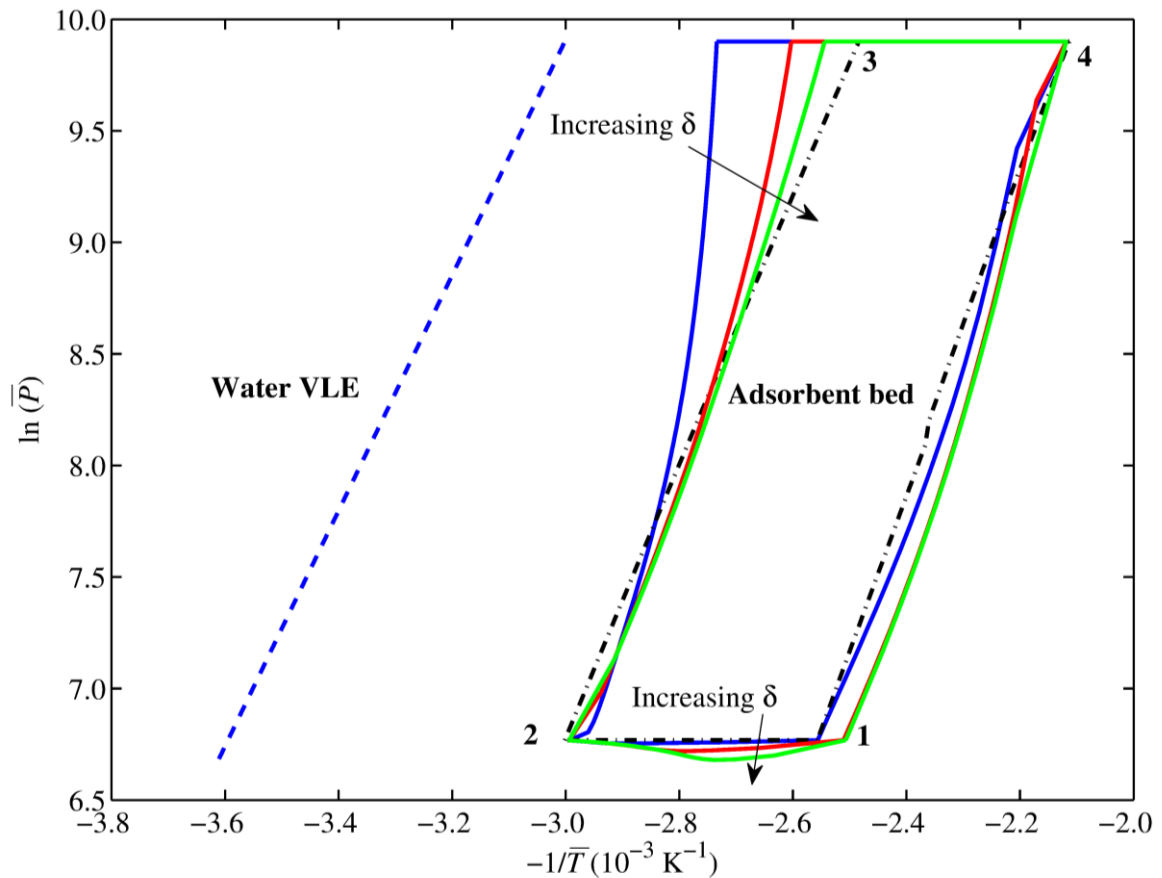


Fig. 3.7 - Operational cycles for bed thicknesses $\delta = 2$ (—), 4 (—) and 6 (—) mm, and ideal cycle (---). Numbers correspond to those of Fig. 3.1. Data for the calculations are given in Table 3.3.

For a bed thickness $\delta = 2$ mm, the simulated cycle is close to the ideal one, except in the isosteric heating stage, which is related to the existence of vapor transport and thermal

resistances within the bed. The transient curves of the bulk and adsorbent temperatures (T_v , T_s), pressure (P) and adsorbate loading (W) for different bed positions, at each cycle stage are shown in Figs. 3.8-3.11. These curves are graphed for an established steady-state cycle. The T_s and T_v versus time functions are nearly overlapped in all stages of the cycle, and thus the adsorbent and the vapor can be considered in thermal equilibrium.

Adsorption stage (1-2). For a HTF temperature of 333 K, the adsorbent bed is cooled and the generated heat of adsorption is removed. The duration of the adsorption stage is *ca.* 240 s, after which the bed temperature is uniform (*ca.* $T_{\text{HTF,cool}}$) (Fig. 3.8(a)). Initially, an abrupt decrease of P from 870 to 851 Pa at $r = R_o = 0.0070$ m occurs (Fig. 3.8(b)), since R_o corresponds to the coldest position of the bed where water adsorption is enhanced. As the evaporator feeds continuously the bed, the bed pressure approaches P_{evap} . The pressure gradients are not drastic, and thus the conditions are approximately isobaric. The adsorbate loading (W) increases with time, reaching approximately equilibrium capacity in all radial positions at the end of the stage ($W_{\text{eq}} = 0.0875$ kg kg⁻¹ for $T = T_{\text{HTF,cool}} = 333$ K; $P = P_{\text{evap}} = 870$ Pa), Fig. 3.8(c).

Isosteric heating stage (2-3). Initially, the instantaneous increase of T_{HTF} from 333 K to 473 K is set (Fig. 3.9(a)); water is desorbed from the solid, leading to fast uniform pressurisation of the bed from P_{evap} to P_{cond} (Fig. 3.9(b)). This stage lasts less than 1 s, ending with large temperature gradients inside the bed (Fig. 3.9(a)). The adsorbate loading remains nearly constant (Fig. 3.9(c)), consistent with an isosteric process.

Desorption stage (3-4). During this step, the bed is heated by the HTF at 473 K, in order to be regenerated. After *ca.* 180 s, the bed is uniformly heated to $T_{\text{HTF,hot}}$ (Fig. 3.10(a)). Pressure gradients are negligible, and thus conditions can be considered isobaric (Fig. 3.10(b)). With increasing temperature, the adsorbate loading (W) decreases uniformly with time, and at the end of the stage it is similar to W_{eq} , which is 0.0274 kg kg⁻¹ for $T = T_{\text{HTF,hot}} = 473$ K and $P = P_{\text{cond}} = 19921$ Pa (Fig. 3.10(c)).

Isosteric cooling stage (4-1). Initially, the abrupt decrease of T_{HTF} from 473 K to 333 K is set (Fig. 3.11(a)). This isosteric stage leads to uniform depressurisation of the system from P_{cond} to P_{evap} , and lasts *ca.* 3 s (Fig. 3.11(b)). At the hotter positions of the bed, water desorbs from the adsorbent, which, in turn, becomes adsorbed at coldest positions, resulting in an approximately constant average value of W (Fig. 3.11(c)).

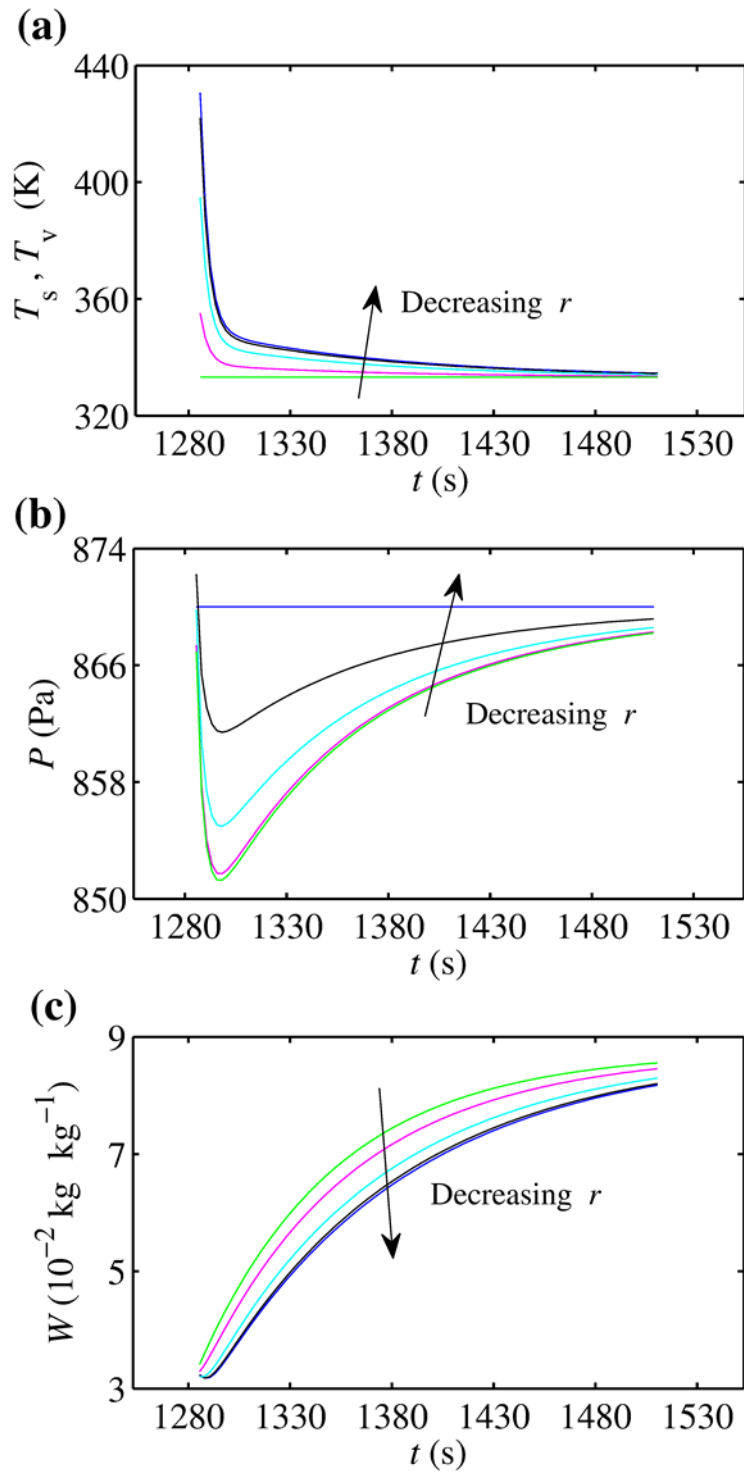


Fig. 3.8 - Evolution of (a) temperatures of adsorbent (solid lines) and vapor (dashed lines), (b) pressure and (c) adsorbate loading against time, for different bed positions ($r = R_1 = 0.0050$ m, $r = 0.0055$ m, $r = 0.0061$ m, $r = 0.0067$ m, $r = R_0 = 0.0070$ m) during the adsorption stage ($T_{\text{HTF,cool}} = 333$ K and $P_{\text{evap}} = 870$ Pa). Data for the calculations are given in Table 3.3.

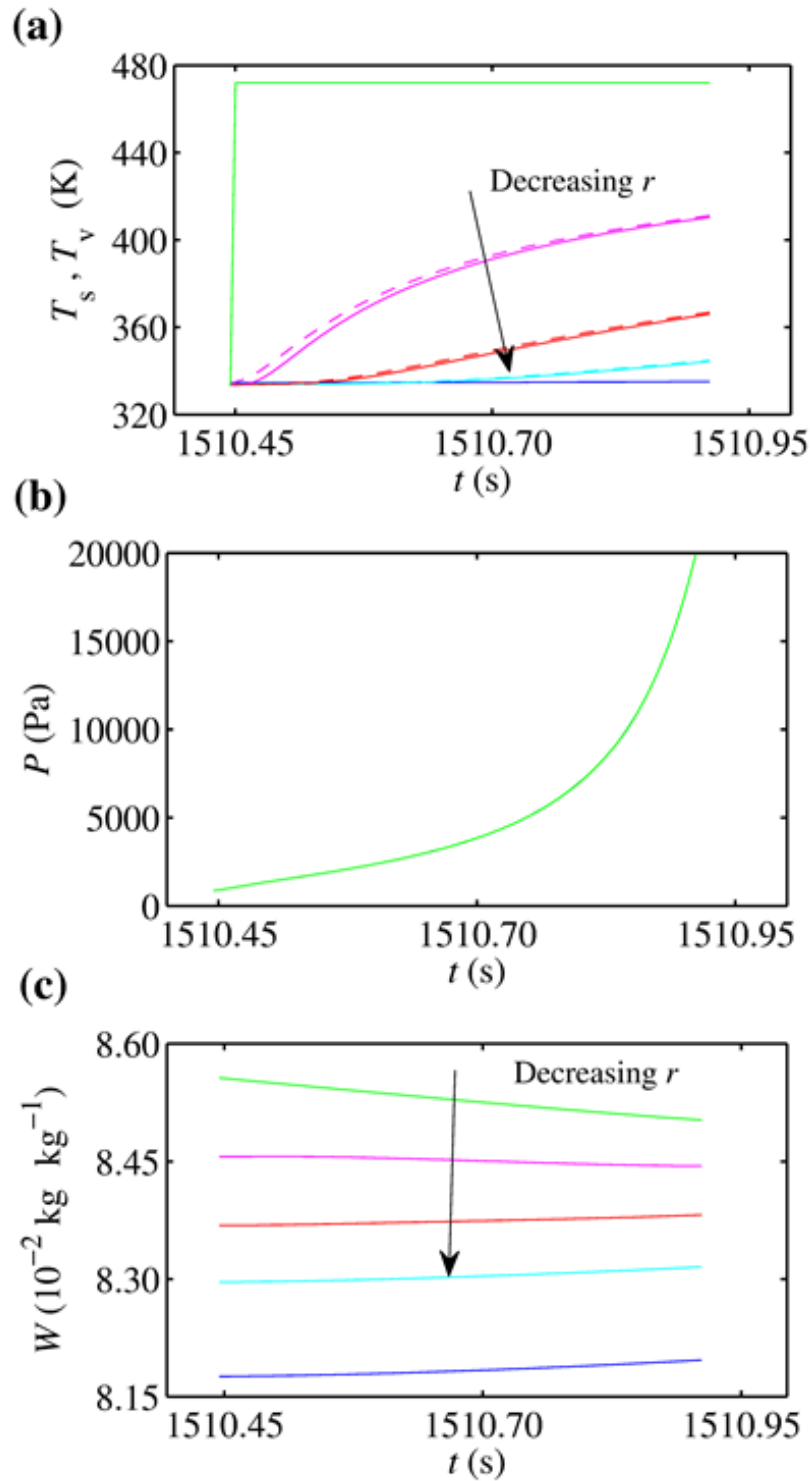


Fig. 3.9 - Curves of (a) adsorbent (solid lines) and vapor (dashed lines) temperatures, (b) pressure and (c) adsorbate loading against time, for different bed positions ($r = R_i = 0.0050$ m, $r = 0.0061$ m, $r = 0.0064$ m, $r = 0.0067$ m, $r = R_o = 0.0070$ m), during isosteric heating stage. Data for the calculations are given in Table 3.3.

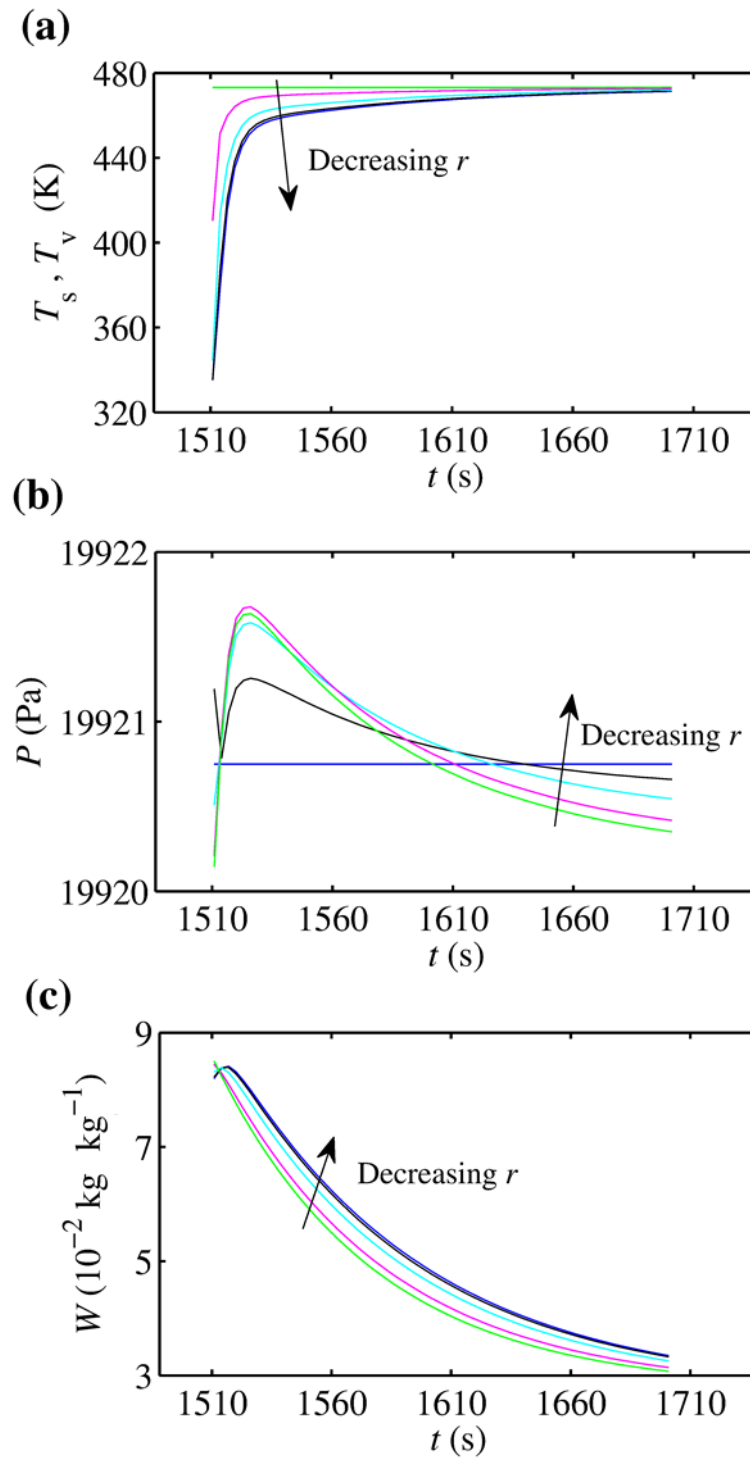


Fig. 3.10 - Evolution of (a) temperatures of adsorbent (solid lines) and vapor (dashed lines), (b) pressure and (c) adsorbate loading against time, for different bed positions ($r = R_i = 0.0050 \text{ m}$, $r = 0.0055 \text{ m}$, $r = 0.0061 \text{ m}$, $r = 0.0067 \text{ m}$, $r = R_o = 0.0070 \text{ m}$), during desorption stage ($T_{\text{HTF,hot}} = 473 \text{ K}$ and $P_{\text{cond}} = 19921 \text{ Pa}$). Data for the calculations are given in Table 3.3.

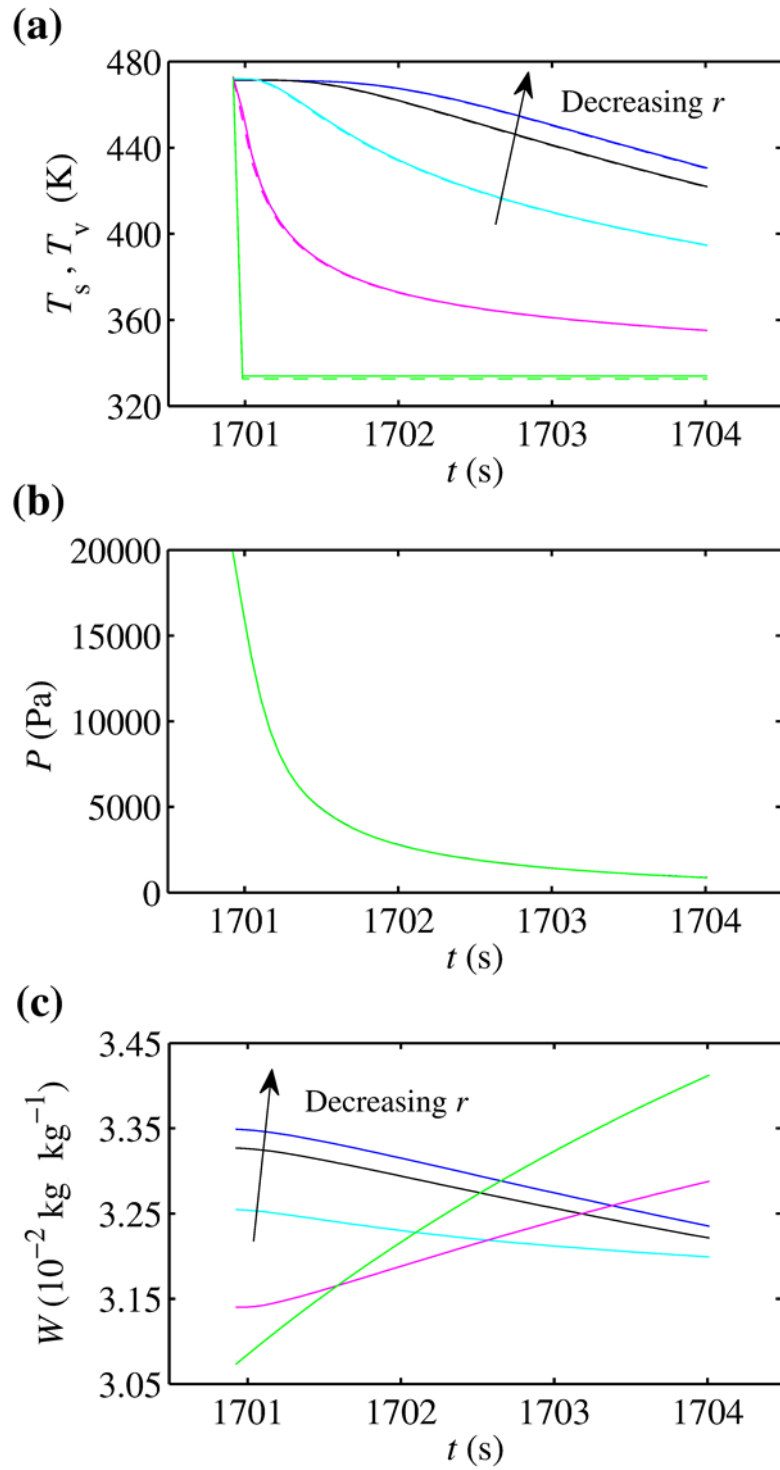


Fig. 3.11 - Curves of (a) temperature of adsorbent (solid lines) and vapor (dashed lines), (b) pressure and (c) adsorbate loading against time, for different bed positions ($r = R_i = 0.0050$ m, $r = 0.0055$ m, $r = 0.0061$ m, $r = 0.0067$ m, $r = R_o = 0.0070$ m), during the isosteric cooling stage. Data for the calculations are given in Table 3.3.

Evaluation of the heating performance. Fig. 3.12 shows the evolutions of \bar{T}_s , \bar{T}_v , \bar{P} and \bar{W} during the first four cycles.

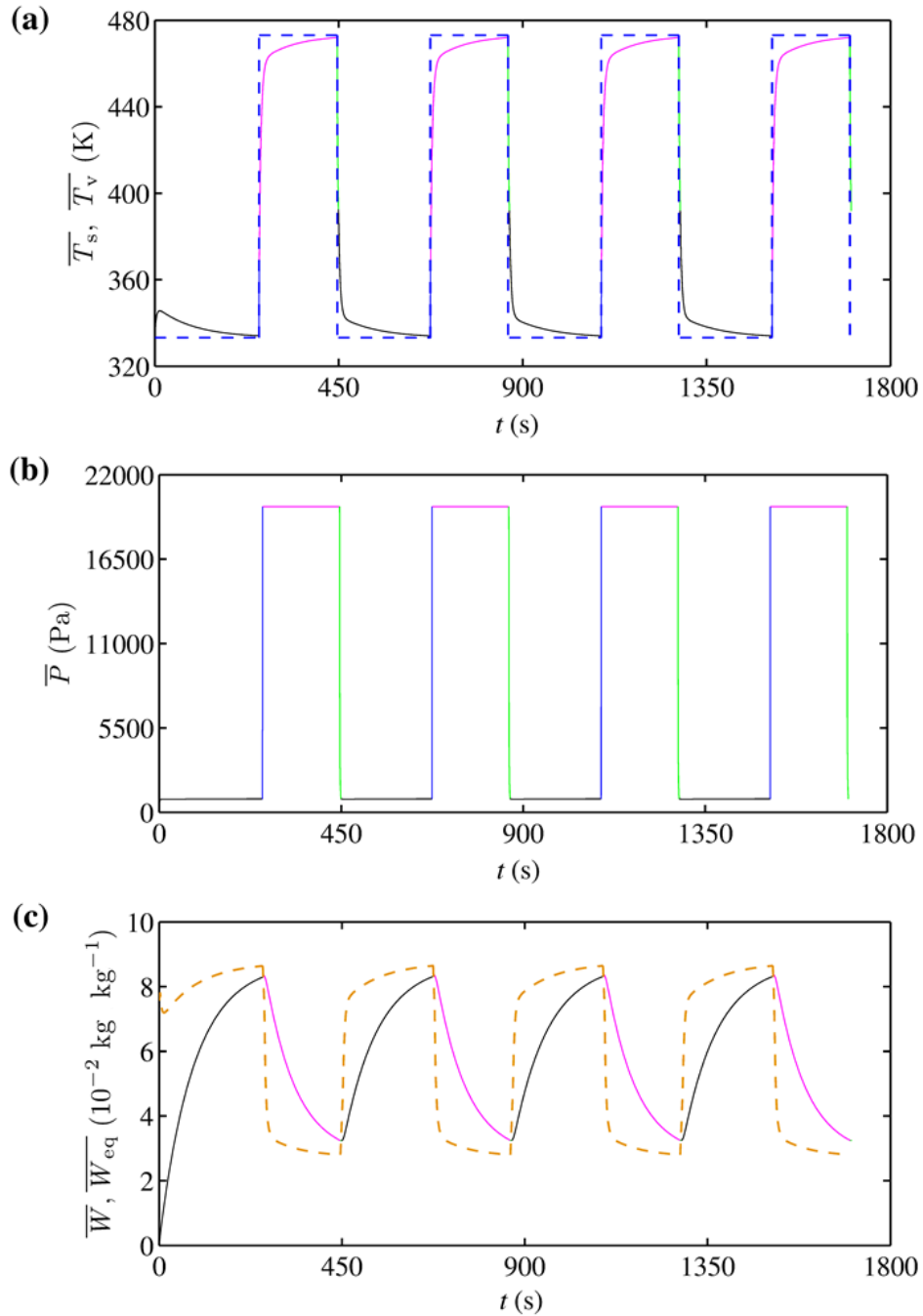


Fig. 3.12 - Evolution of the (a) average temperatures of adsorbent and vapor, (b) average pressure and (c) average adsorbate loading, for the first 4 cycles (— isobaric adsorption, — isosteric heating, — isobaric desorption, — isosteric cooling). The \bar{T}_s and \bar{T}_v versus time curves are coincident. — — T_{HTF} , — — \bar{W}_{eq} . Data for the calculations are given in Table 3.3.

The process rapidly reaches a cyclic steady state, with a cycle time of *ca.* 415 s. As the average bed temperatures become closer to T_{HTF} , the heat transfer becomes slower (Fig. 3.12(a)). On the other hand, the bed pressure spreads more rapidly than the bed temperature, indicating that the heat transfer resistances are more pronounced than the vapor transport limitations (Fig. 3.12(b)). The cyclic adsorption loading swing ($\Delta\bar{W}_{cycle}$) is approximately 0.05 kg kg^{-1} , which is close to the maximum value of *ca.* 0.06 kg kg^{-1} (Fig. 3.12(c)). The $\Delta\bar{W}_{cycle}$ has a considerable influence on the amount of heat generated by the unit, consequently impacting on *COP* and *SHP*, which equal 1.36 and 934 W kg^{-1} , respectively, for the case under study ($\delta = 2 \text{ mm}$; Table 3.4). These results are comparable to those reported for AHS using zeolites: Marletta *et al.* [33] reported *COP* = 1.37 for $\delta = 5 \text{ mm}$, using the zeolite 4A/water pair under similar operating conditions; Restuccia *et al.* [34] reported *COP* = 1.44 and *SHP* = 878 W kg^{-1} for a zeolite 4A/water heating system, operating two beds with internal heat recovery; Meunier [35] reported *COP* = 1.36 for a zeolite/water heating unit.

3.4.2.2. Sensitivity studies

3.4.2.2.1. Effect of the adsorbent bed thickness

The bed thickness (δ) is an important factor influencing the heating performance of an adsorption system, since it is directly related with the path for vapor and heat transport. Fig. 3.7 (Section 3.4.2.1) compares the simulated cycles for $\delta = 2, 4$ and 6 mm , and Table 3.4 lists the corresponding cycle times, cyclic adsorption loading swings, *COP* and *SHP* values, and also the ideal $\Delta\bar{W}_{cycle}$ and *COP* values. Fig. 3.7 shows that the major differences appear in the isosteric heating for thinner beds, for which the resistances are lower, leading to faster pressurisation until P_{cond} . A small deviation from the isobaric conditions during adsorption stage (1-2) occurs for $\delta = 6 \text{ mm}$, due to increased vapor transport resistance. Increasing δ , lead to higher values of $\Delta\bar{W}_{cycle}$ and t_{cycle} (Table 3.4). Larger thicknesses increase the resistances inside the bed, leading to longer cycle times; since the adsorption and desorption stages are extended, higher \bar{W}_{max} and lower \bar{W}_{min} are reached, thus enhancing $\Delta\bar{W}_{cycle}$. The *COP* tends to increase with increasing δ , since it is

partly influenced by $\Delta\bar{W}_{\text{cycle}}$. Conversely, *SHP* decreases because the increment in $\Delta\bar{W}_{\text{cycle}}$ is largely counterbalanced by the increased t_{cycle} (Eq. (3.16)). The cycle times obtained are comparable to literature data for the zeolite 4A/water pair: Marletta *et al.* [33] reported t_{cycle} of 460, 926 and 1547 s for $\delta = 3, 5$ and 7 mm, respectively.

Table 3.4 - Influence of the bed thickness (δ) on the performance of the adsorption heating system. The $\Delta\bar{W}_{\text{cycle}}$ and *COP* of the ideal cycle are also listed for comparison.

δ (mm)	t_{cycle} (s)	\bar{W}_{min} (kg kg ⁻¹)	\bar{W}_{max} (kg kg ⁻¹)	$\Delta\bar{W}_{\text{cycle}}$ (kg kg ⁻¹)	<i>COP</i>	<i>SHP</i> (W kg ⁻¹)
2	415	0.0329	0.0834	0.0505	1.36	934
4	960	0.0291	0.0858	0.0567	1.38	434
6	1707	0.0285	0.0861	0.0576	1.39	249
Ideal cycle		0.0274	0.0875	0.0601	1.41	-

3.4.2.2.2. Effect of final regeneration temperature and heating fluid temperature

The regeneration temperature of the bed (\bar{T}_4 in Fig. 3.7) and the heating fluid temperature ($T_{\text{HTF,hot}}$) are important factors influencing the overall performance of an adsorption unit. Their effects on $\Delta\bar{W}_{\text{cycle}}$, *COP* and *SHP* are represented in Fig. 3.13. For the same $T_{\text{HTF,hot}}$, increasing \bar{T}_4 leads to: (i) improved regeneration of the bed as evidenced by the enhanced $\Delta\bar{W}_{\text{cycle}}$ (Fig. 3.13(a)), and thus increasing *COP* (Fig. 3.13(b)); (ii) a longer desorption stage, and thus higher t_{cycle} , contributing to lower *SHP* (Fig. 3.13(c)). For a given \bar{T}_4 , higher $T_{\text{HTF,hot}}$ leads to faster heat transfer between the HTF and the bed, contributing to low values of $\Delta\bar{W}_{\text{cycle}}$ (Fig. 3.13(a)) and t_{cycle} (based on stopping criteria indicated in Section 3.3.2); these trends result in lower *COP* (Fig. 3.13(b)) and higher *SHP* (Fig. 3.13(c)). The maximum *COP* values are achieved for $\bar{T}_4 = T_{\text{HTF,hot}}$; the *COP* increases with increasing temperature, reaching a maximum for $\bar{T}_4 = T_{\text{HTF,hot}} = 473$ K (Fig. 3.13(b)). This plateau-like behavior parallels that reported in the literature for AHS using the pairs zeolite 13X/water, zeolite 4A/water and activated carbon/methanol [6].

Overall, it is worth emphasizing that both \bar{T}_4 and $T_{\text{HTF,hot}}$ impart a strong effect upon the heating performance of an AHS.

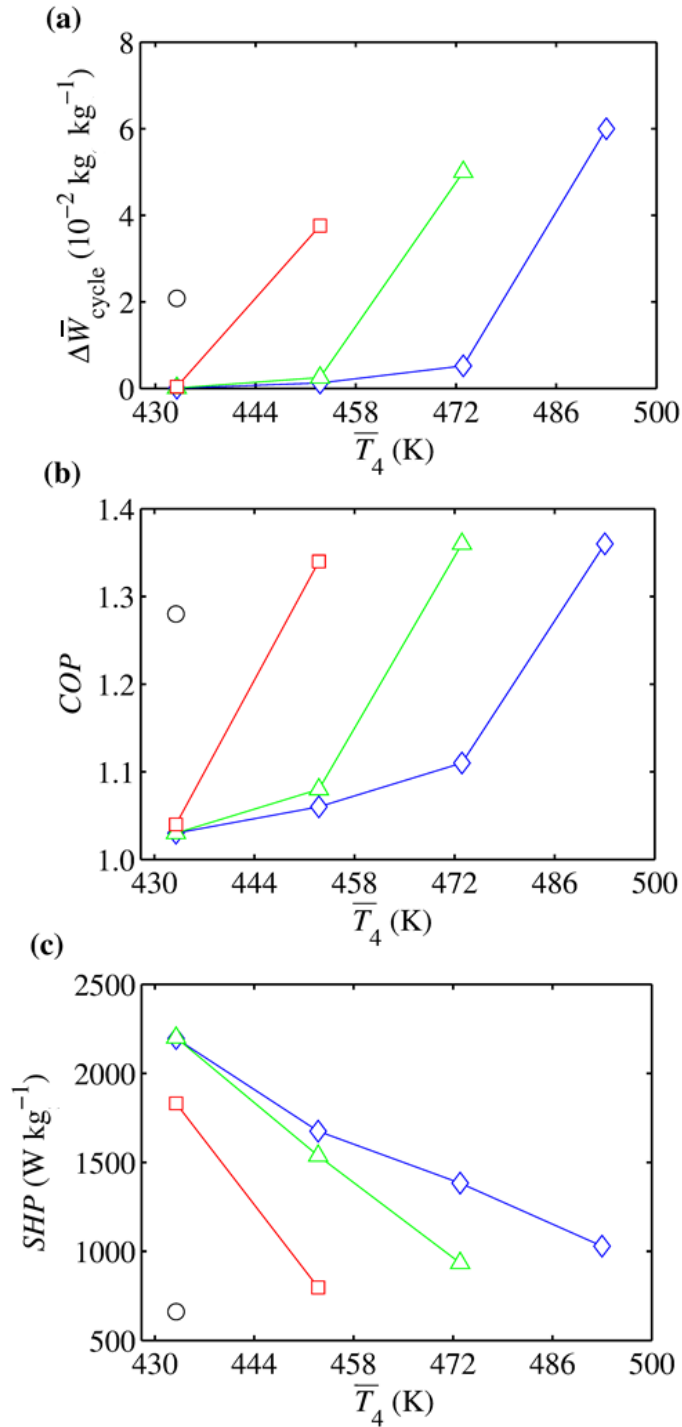


Fig. 3.13 - Variation of (a) $\Delta \bar{W}_{\text{cycle}}$, (b) COP and (c) SHP with the final regeneration temperature of the bed (\bar{T}_4 in Fig. 3.7), for different heating fluid temperatures ($T_{\text{HTF,hot}} = 433 \text{ K}$ (o), $T_{\text{HTF,hot}} = 453 \text{ K}$ (\square), $T_{\text{HTF,hot}} = 473 \text{ K}$ (\triangle), $T_{\text{HTF,hot}} = 493 \text{ K}$ (\diamond)). The lines are visual guides. Data for the calculations are given in Table 3.3 (Section 3.4.2.1).

3.5. Conclusions

A cyclic adsorption heating process using the ETS-10/water pair was modeled and simulated for the first time. Firstly, several properties of ETS-10 were experimentally measured, specifically, effective thermal conductivities, heat capacities, intraparticle LDF mass transfer coefficient, adsorbent density and bed porosity. In the range of 333-413 K, the average values $\lambda_{\text{eff},s} = 0.24 \text{ W m}^{-1} \text{ K}^{-1}$ and $C_{p,s} = 800 \text{ J kg}^{-1} \text{ K}^{-1}$ were obtained, and in the interval 298-348 K an average $K_{\text{LDF}} = 1.5 \times 10^{-2} \text{ s}^{-1}$ was determined. The ETS-10/water isotherms were also measured in the range 298-348 K, and the Dubinin-Astakhov model was accurately fitted to data.

From the modeling and simulation studies performed, a cycle time of *ca.* 415 s, $COP = 1.36$ and $SHP = 934 \text{ W kg}^{-1}$ were obtained for the ETS-10/water adsorption heating system. The sensitivity studies showed that: (i) the thicker the bed, the higher the COP while SHP decreases significantly; (ii) for the same temperature of the heating thermal fluid, increasing the bed regeneration temperature (\bar{T}_4) enhances COP and decreases SHP . If $T_{\text{HTF,hot}}$ is increased, for a given \bar{T}_4 , SHP is enhanced but COP decreases. Hence, a good compromise must exist between the bed thickness and the operating conditions, in order to maximise the performance of the system.

Nomenclature

a	External surface area of adsorbent per unit bed volume (m^{-1})
AARD	$= \frac{\sum_{i=1}^n \left \frac{\text{Value}_{\text{calculated},i} - \text{Value}_{\text{experimental},i}}{\text{Value}_{\text{experimental},i}} \right }{N_{\text{data}}}$
	Average Absolute Relative Deviation (%)
C_p	Specific heat capacity ($\text{J kg}^{-1} \text{K}^{-1}$)
COP	Coefficient of heating performance
d_p	Adsorbent particle diameter (m)
D	Parameter of Dubinin-Astakhov equation, related to the characteristic energy
DA	Dubinin-Astakhov
h_{sv}	Solid/vapor convective heat transfer coefficient ($\text{W m}^{-2} \text{K}^{-1}$)
HTF	Heat transfer fluid
K	Permeability of the adsorbent bed (m^2)
K_{LDF}	Intraparticle mass transfer coefficient (s^{-1})
m	Mass (kg)
M	Molar mass of the adsorbate (kg mol^{-1})
n	Parameter of Dubinin-Astakhov equation, related to the surface heterogeneity
Nu	Nusselt number
P	Pressure (Pa)
P_{sat}	Saturation pressure (Pa)
Pr	Prandtl number
Q	Heat (J)
Q_{ads}	Isosteric heat of adsorption (J kg^{-1})
r	Spatial coordinate (m)
R	Radial position in the adsorbent bed (m)
\bar{R}	Universal gas constant ($\text{J mol}^{-1} \text{K}^{-1}$)
Re	Reynolds number
SHP	Specific heating power (W kg^{-1})

t	Time (s)
t_{cycle}	Cycle time (s)
T	Temperature (K)
u	Fluid superficial velocity (m s^{-1})
W	Adsorbate loading (kg kg^{-1})
W_0	Adsorbate loading at saturation pressure (kg kg^{-1})

Greek symbols

ΔH_c	Heat of condensation (J kg^{-1})
ΔW_{cycle}	Cyclic adsorption loading swing (kg kg^{-1})
η	Dynamic viscosity ($\text{kg m}^{-1} \text{s}^{-1}$)
ε_b	Porosity of the bed
δ	Bed thickness (m)
λ	Thermal conductivity ($\text{W m}^{-1} \text{K}^{-1}$)
ρ	Density (kg m^{-3})
φ	Generic notation of T , W and P
$\bar{\varphi}$	Generic notation of \bar{T} , \bar{W} and \bar{P}

Subscripts

a	Adsorbed vapor
cond	Condenser
eff	Effective
eq	Equilibrium
evap	Evaporator
i	Internal boundary of the bed
ini	Initial
max	Maximum
min	Minimum
o	External boundary of the bed
s	Adsorbent
v	Vapor phase

References

- [1] R.Z. Wang, Adsorption refrigeration research in Shanghai Jiao Tong University, *Renewable and Sustainable Energy Reviews*, 5 (2001) 1-37.
- [2] H. Demir, M. Mobedi, S. Ülkü, A review on adsorption heat pump: Problems and solutions, *Renewable and Sustainable Energy Reviews*, 12 (2008) 2381-2403.
- [3] F. Meunier, Adsorption heat powered heat pumps, *Applied Thermal Engineering*, 61 (2013) 830-836.
- [4] D.C. Wang, Y.H. Li, D. Li, Y.Z. Xia, J.P. Zhang, A review on adsorption refrigeration technology and adsorption deterioration in physical adsorption systems, *Renewable and Sustainable Energy Reviews*, 14 (2010) 344-353.
- [5] F. Ziegler, State of the art in sorption heat pumping and cooling technologies, *International Journal of Refrigeration*, 25 (2002) 450-459.
- [6] G. Cacciola, G. Restuccia, Reversible adsorption heat pump: a thermodynamic model, *International Journal of Refrigeration*, 18 (1995) 100-106.
- [7] Z. Tamainot-Telto, R.E. Critoph, Monolithic carbon for sorption refrigeration and heat pump applications, *Applied Thermal Engineering*, 21 (2001) 37-52.
- [8] Y. Aristov, Concept of adsorbent optimal for adsorptive cooling/heating, *Applied Thermal Engineering*, (2014) 166-175.
- [9] Y.I. Aristov, Challenging offers of material science for adsorption heat transformation: A review, *Applied Thermal Engineering*, 50 (2013) 1610-1618.
- [10] S.M. Kuznicki, Large-pored crystalline titanium molecular sieve zeolites, US4853202, (1989).
- [11] X. Liu, J.K. Thomas, Synthesis of microporous titanosilicates ETS-10 and ETS-4 using solid TiO₂ as the source of titanium, *Chemical Communications*, (1996) 1435-1436.
- [12] X. Yang, R.E. Truitt, ¹²⁹Xe NMR Investigation of ETS-10 Titanosilicate Molecular Sieves, *The Journal of Physical Chemistry*, 100 (1996) 3713-3718.
- [13] H.M. Garfinkel, S.M. Kuznicki, K.A. Thrush, Use of crystalline molecular sieves containing charged octahedral sites in cyclic desiccating processes, EP0544892B1, (1993).
- [14] P.S. Zurer, Looming Ban on Production of CFCs, Halons Spurs Switch to Substituteas, *Chemical & Engineering News Archive*, 71 (1993) 12.
- [15] J. Rocha, A. Ferreira, Z. Lin, M.W. Anderson, Synthesis of microporous titanosilicate ETS-10 from TiCl₃ and TiO₂: a comprehensive study, *Microporous and Mesoporous Materials*, 23 (1998) 253-263.
- [16] Y. He, Rapid thermal conductivity measurement with a hot disk sensor: Part 1. Theoretical considerations, *Thermochimica Acta*, 436 (2005) 122-129.
- [17] S. Sircar, J.R. Hufton, Why Does the Linear Driving Force Model for Adsorption Kinetics Work?, *Adsorption*, 6 (2000) 137-147.
- [18] D.M. Ruthven, *Principles of Adsorption and Adsorption Processes*, first ed., John Wiley & Sons, USA, 1984.
- [19] D.D. Duong, *Adsorption Analysis: Equilibria and Kinetics*, first ed., Imperial College Press, London, 1998.
- [20] J.O. Wilkes, S.G. Bickel, *Fluid Mechanics for Chemical Engineers*, second ed., Prentice Hall PTR, New Jersey, 1999.
- [21] R.C. Reid, J.M. Prausnitz, B.E. Poling, *The Properties of Gases and Liquids*, fourth ed., McGraw-Hill, New York, 1987.
- [22] A. Bejan, *Convection Heat Transfer*, first ed., John Wiley & Sons, New York, 1984.

- [23] S. Middleman, *An Introduction to Mass and Heat Transfer: Principles of Analysis and Design*, first ed., John Wiley & Sons, New York, 1998.
- [24] W.E. Schiesser, *The Numerical Method of Lines: Integration of Partial Differential Equations*, third ed., Academic Press, San Diego, 1991.
- [25] A. Allouhi, T. Kousksou, A. Jamil, Y. Zeraoui, Modeling of a thermal adsorber powered by solar energy for refrigeration applications, *Energy*, 75 (2014) 589-596.
- [26] J.D. Hoffman, S. Frankel, *Numerical Methods for Engineers and Scientists*, second ed., Taylor & Francis, New York, 2001.
- [27] İ. Solmuş, D.A.S. Rees, C. Yamalı, D. Baker, B. Kaftanoğlu, Numerical investigation of coupled heat and mass transfer inside the adsorbent bed of an adsorption cooling unit, *International Journal of Refrigeration*, 35 (2012) 652-662.
- [28] Y. Zhong, T. Fang, K.L. Wert, An adsorption air conditioning system to integrate with the recent development of emission control for heavy-duty vehicles, *Energy*, 36 (2011) 4125-4135.
- [29] B. Dawoud, M.I. Sohel, A. Freni, S. Vasta, G. Restuccia, On the effective thermal conductivity of wetted zeolite under the working conditions of an adsorption chiller, *Applied Thermal Engineering*, 31 (2011) 2241-2246.
- [30] M.B. Jakubinek, B.-Z. Zhan, M.A. White, Temperature-dependent thermal conductivity of powdered zeolite NaX, *Microporous and Mesoporous Materials*, 103 (2007) 108-112.
- [31] L. Qiu, V. Murashov, M.A. White, Zeolite 4A: heat capacity and thermodynamic properties, *Solid State Sciences*, 2 (2000) 841-846.
- [32] C.W. Chan, J. Ling-Chin, A.P. Roskilly, Reprint of "A review of chemical heat pumps, thermodynamic cycles and thermal energy storage technologies for low grade heat utilisation", *Applied Thermal Engineering*, 53 (2013) 160-176.
- [33] L. Marletta, G. Maggio, A. Freni, M. Ingrassiotta, G. Restuccia, A non-uniform temperature non-uniform pressure dynamic model of heat and mass transfer in compact adsorbent beds, *International Journal of Heat and Mass Transfer*, 45 (2002) 3321-3330.
- [34] G. Restuccia, G. Cacciola, Performances of adsorption systems for ambient heating and air conditioning, *International Journal of Refrigeration*, 22 (1999) 18-26.
- [35] F. Meunier, Theoretical performances of solid adsorbent cascading cycles using the zeolite-water and active carbon-methanol pairs: four case studies, *Journal of Heat Recovery Systems*, 6 (1986) 491-498.

Annex A3

A3.1. Experimental measurements

A3.1.1. Sorption isotherms

The sorption isotherms of water on ETS-10 measured at 298, 323 and 348 K are shown in Fig. A3.1.

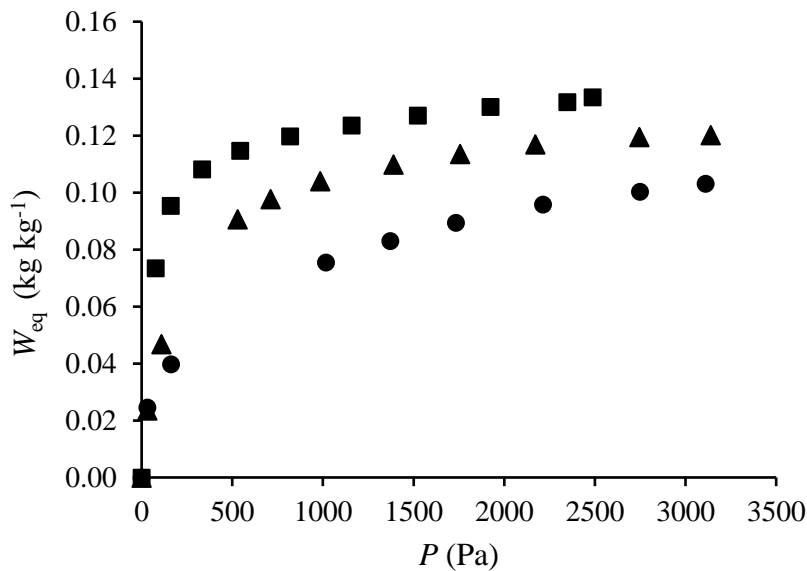


Fig. A3.1 - Sorption isotherms of water on ETS-10 at 298 (■), 323 (▲) and 348 (●) K, measured in this work.

A3.1.2. Bed porosity – Mercury porosimetry

Table A3.1 lists the data obtained from mercury porosimetry, used to determine the porosity of the bed. V_{pen} is the penetrometer volume, ρ_{Hg} is the density of mercury, m_{ass} is the assembly weight, m_{pen} is the penetrometer weight, m_s is the mass of the sample of ETS-10, V_{Hg} and m_{Hg} are the volume and the weight of mercury (not intruded into the

sample), $V_{s,bulk}$ and $\rho_{s,bulk}$ are, respectively, the bulk volume and the bulk density of the sample, $V_{i,total}$ is the total intrusion volume, $V_{s,app}$ is the apparent (skeletal) volume and $\rho_{s,app}$ is the apparent (skeletal) density. Using bulk and apparent (skeletal) densities, the porosity of the bed is determined.

Table A3.1 - Mercury porosimetry measurements used to calculate the porosity of the bed.

V_{pen} (mL)	ρ_{Hg} (g mL ⁻¹)	m_{ass} (g)	m_{pen} (g)	m_s (g)	V_{Hg} (mL)
5.3905	13.5413	142.59	70.855	0.073	5.2921
m_{Hg} (g)	$V_{s,bulk}$ (mL)	$\rho_{s,bulk}$ (g mL ⁻¹)	$V_{i,total}$ (mL g ⁻¹)	$V_{s,app}$ (mL)	$\rho_{s,app}$ (g mL ⁻¹)
71.66	0.0984	0.7419	0.7854	0.0411	1.778

A3.1.3. Adsorbent density – Helium pycnometry

Helium pycnometry data considered in the determination of the ETS-10 density are given in Table A3.2. The m is the mass of the sample, V_{sc} denotes the volume of the sample chamber, V_{ec} is the volume of the expansion chamber, P_1 is the pressure in the sample chamber after pressurization, P_2 is the pressure in the sample chamber after opening the expansion valve, and V_s is the volume of the solid (excluding intra and inter-particle pores). From V_s and m , the ETS-10 density is determined.

Table A3.2 - Helium pycnometry data for calculating ETS-10 density.

m (g)	V_{sc} (cm ³)	V_{ec} (cm ³)	P_1 (psi)	P_2 (psi)	V_s (cm ³)	V_s (cm ³) (average)	ρ_s (kg/m ³)
3.02	12.851	5.324	15.309	4.785	1.142	1.183	2553
	12.851	5.324	15.540	4.872	1.193		
	12.851	5.324	15.221	4.778	1.215		

A3.1.4. Specific heat capacity and thermal conductivity – hot disk

The raw data of the thermal conductivity and specific heat capacity of ETS-10, measured using a hot disk equipment, are listed in Table A3.3.

Table A3.3 - Thermal conductivity and specific heat capacity data of ETS-10 measured using the hot disk technique.

T (K)	$\lambda_{\text{eff},s}$ ($\text{W m}^{-1} \text{K}^{-1}$)	$C_{p,s}$ ($\text{MJ m}^{-3} \text{K}^{-1}$)	T (K)	$\lambda_{\text{eff},s}$ ($\text{W m}^{-1} \text{K}^{-1}$)	$C_{p,s}$ ($\text{MJ m}^{-3} \text{K}^{-1}$)
294.72	0.24261	1.54911	304.32	0.24176	1.55918
295.02	0.24248	1.55364	304.63	0.24174	1.55897
295.33	0.24251	1.55572	304.95	0.24172	1.55859
295.63	0.24254	1.55748	305.27	0.24185	1.56300
295.94	0.24257	1.55879	305.58	0.24176	1.56318
296.25	0.24258	1.56017	305.90	0.24183	1.56208
296.56	0.24242	1.55706	306.22	0.24179	1.56287
296.86	0.24254	1.55701	306.53	0.24178	1.56318
297.17	0.24261	1.56553	306.85	0.24178	1.56311
297.48	0.24262	1.56610	307.16	0.24179	1.56326
298.09	0.24262	1.56697	307.48	0.24180	1.56323
298.40	0.24261	1.56722	307.80	0.24181	1.56307
298.71	0.24259	1.56769	308.11	0.24183	1.56254
299.02	0.24256	1.56769	308.43	0.24186	1.56197
299.33	0.24253	1.56835	308.75	0.24180	1.56213
299.64	0.24243	1.56934	309.06	0.24190	1.56085
299.94	0.24250	1.56876	309.38	0.24181	1.56391
300.25	0.24236	1.56413	309.70	0.24183	1.56382
300.56	0.24233	1.56409	310.01	0.24185	1.56342
300.87	0.24229	1.56423	310.33	0.24187	1.56336
301.18	0.24225	1.56431	310.65	0.24190	1.56301
301.48	0.24222	1.56437	310.96	0.24192	1.56263
301.79	0.24217	1.56471	311.28	0.24194	1.56237
302.10	0.24213	1.56470	311.59	0.24197	1.56210
302.41	0.24209	1.56420	311.60	0.24204	1.55902
302.42	0.24208	1.56060	311.92	0.24202	1.55914
302.74	0.24200	1.56017	312.24	0.24204	1.55944
303.05	0.24193	1.56064	312.56	0.24207	1.55869
303.37	0.24187	1.56062	312.88	0.24211	1.55900
303.68	0.24184	1.56019	313.20	0.24217	1.55828
304.00	0.24180	1.55946	313.52	0.24224	1.55758

(continuation in next page)

T (K)	$\lambda_{\text{eff},s}$ (W m ⁻¹ K ⁻¹)	$C_{p,s}$ (MJ m ⁻³ K ⁻¹)	T (K)	$\lambda_{\text{eff},s}$ (W m ⁻¹ K ⁻¹)	$C_{p,s}$ (MJ m ⁻³ K ⁻¹)
313.84	0.24230	1.55740	326.31	0.24508	1.53584
314.16	0.24235	1.55740	326.63	0.24524	1.53102
314.48	0.24241	1.55738	326.95	0.24534	1.53019
314.80	0.24241	1.55771	327.28	0.24536	1.53006
315.12	0.24261	1.55514	327.60	0.24552	1.52810
315.44	0.24267	1.55428	327.92	0.24557	1.52808
315.76	0.24274	1.55362	328.24	0.24561	1.52761
316.07	0.24273	1.55415	328.56	0.24568	1.52724
316.39	0.24276	1.55403	328.89	0.24574	1.52643
316.71	0.24281	1.55401	329.21	0.24582	1.52557
317.03	0.24287	1.55377	329.53	0.24588	1.52473
317.35	0.24293	1.55387	329.86	0.24597	1.52364
317.67	0.24291	1.55755	330.18	0.24603	1.52286
317.99	0.24292	1.55769	330.19	0.24606	1.52092
318.31	0.24317	1.55337	330.51	0.24606	1.52027
318.63	0.24323	1.55301	330.84	0.24601	1.52179
318.95	0.24331	1.55265	331.16	0.24603	1.52190
319.27	0.24339	1.55223	331.49	0.24599	1.52144
319.58	0.24348	1.55147	331.81	0.24595	1.52141
319.90	0.24353	1.55147	332.14	0.24589	1.52180
320.22	0.24360	1.55113	332.47	0.24585	1.52221
320.54	0.24368	1.55048	332.80	0.24591	1.51855
320.86	0.24373	1.54986	333.13	0.24597	1.51667
320.86	0.24386	1.54595	333.46	0.24589	1.51546
321.18	0.24394	1.54467	333.78	0.24602	1.51214
321.50	0.24397	1.54565	334.11	0.24601	1.51144
321.82	0.24403	1.54522	334.44	0.24601	1.51011
322.14	0.24407	1.54523	334.76	0.24598	1.50936
322.46	0.24416	1.54423	335.09	0.24597	1.50804
322.78	0.24426	1.54308	335.41	0.24596	1.50672
323.10	0.24437	1.54165	335.74	0.24593	1.50572
323.42	0.24441	1.54098	336.07	0.24588	1.50481
323.74	0.24445	1.54138	336.40	0.24585	1.50329
324.06	0.24440	1.54232	336.72	0.24576	1.50312
324.38	0.24456	1.54141	337.05	0.24583	1.50039
324.70	0.24462	1.54126	337.38	0.24583	1.49856
325.02	0.24475	1.53935	337.70	0.24581	1.49680
325.34	0.24487	1.53794	338.03	0.24579	1.49472
325.66	0.24495	1.53716	338.36	0.24559	1.49031
325.99	0.24503	1.53634	338.69	0.24557	1.48904

(continuation in next page)

T (K)	$\lambda_{\text{eff},s}$ (W m ⁻¹ K ⁻¹)	$C_{p,s}$ (MJ m ⁻³ K ⁻¹)	T (K)	$\lambda_{\text{eff},s}$ (W m ⁻¹ K ⁻¹)	$C_{p,s}$ (MJ m ⁻³ K ⁻¹)
339.01	0.24553	1.48821	351.76	0.24304	1.41190
339.34	0.24549	1.48734	352.10	0.24290	1.40807
339.67	0.24546	1.48602	352.43	0.24267	1.40635
339.68	0.24547	1.48256	352.76	0.24266	1.40369
340.01	0.24550	1.47881	353.09	0.24255	1.40255
340.33	0.24544	1.47695	353.42	0.24240	1.40116
340.66	0.24537	1.47646	353.76	0.24227	1.40016
340.98	0.24530	1.47605	354.09	0.24208	1.39897
341.31	0.24519	1.47656	354.42	0.24190	1.39833
341.64	0.24523	1.47265	354.76	0.24170	1.39878
341.96	0.24515	1.47246	355.09	0.24156	1.39991
342.29	0.24511	1.47157	355.42	0.24144	1.39800
342.62	0.24507	1.46902	355.75	0.24129	1.39515
342.94	0.24494	1.46873	356.09	0.24125	1.39203
343.27	0.24498	1.46562	356.42	0.24114	1.38928
343.59	0.24491	1.46364	356.75	0.24105	1.38602
343.92	0.24487	1.46158	357.09	0.24091	1.38572
344.25	0.24480	1.46003	357.42	0.24082	1.38367
344.57	0.24472	1.45757	357.76	0.24066	1.38272
344.90	0.24469	1.45567	358.09	0.24060	1.37985
345.22	0.24463	1.45321	358.43	0.24044	1.37907
345.55	0.24458	1.45151	358.76	0.24034	1.37737
345.87	0.24451	1.44906	358.77	0.24026	1.37343
346.20	0.24437	1.44755	358.86	0.24009	1.37305
346.53	0.24437	1.44451	358.95	0.23994	1.36988
346.85	0.24427	1.44310	359.04	0.23990	1.36833
347.18	0.24421	1.44121	359.13	0.23968	1.36943
347.50	0.24429	1.44215	359.22	0.23956	1.36893
347.82	0.24423	1.43897	359.32	0.23952	1.36653
348.15	0.24414	1.43683	359.41	0.23951	1.36294
348.47	0.24405	1.43434	359.50	0.23949	1.36382
348.79	0.24395	1.43232	359.59	0.23946	1.36374
349.12	0.24390	1.42956	359.68	0.23937	1.36297
349.12	0.24380	1.42722	359.78	0.23942	1.36002
349.45	0.24370	1.42560	359.87	0.23944	1.35857
349.78	0.24365	1.42187	359.96	0.23948	1.35713
350.11	0.24358	1.41978	360.05	0.23953	1.35645
350.44	0.24354	1.41514	360.14	0.23959	1.35597
350.77	0.24349	1.41292	360.23	0.23966	1.35376
351.10	0.24341	1.41078	360.32	0.23973	1.35121
351.43	0.24326	1.40910	360.42	0.23975	1.35175

(continuation in next page)

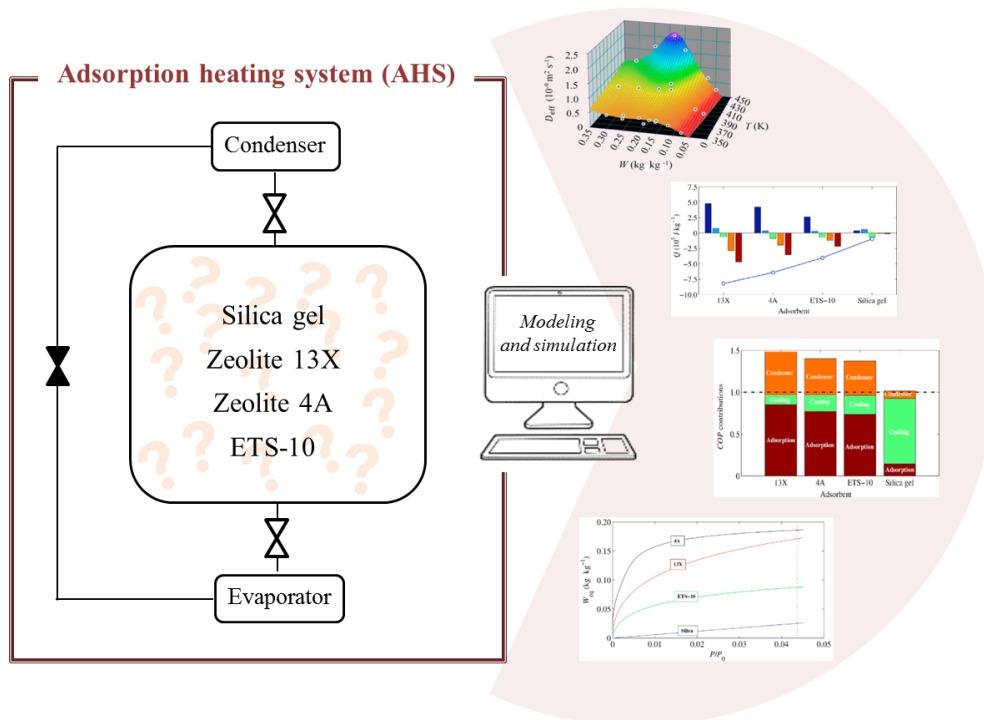
T (K)	$\lambda_{\text{eff},s}$ (W m ⁻¹ K ⁻¹)	$C_{p,s}$ (MJ m ⁻³ K ⁻¹)	T (K)	$\lambda_{\text{eff},s}$ (W m ⁻¹ K ⁻¹)	$C_{p,s}$ (MJ m ⁻³ K ⁻¹)
360.51	0.23975	1.35349	371.26	0.24142	1.36141
360.60	0.23973	1.35495	371.60	0.24130	1.36303
360.69	0.23982	1.35583	371.94	0.24126	1.36406
360.78	0.23983	1.35732	372.28	0.24117	1.36474
360.87	0.23986	1.35754	372.62	0.24113	1.36473
360.96	0.23989	1.35801	372.96	0.24108	1.36503
361.05	0.23998	1.35800	373.30	0.24103	1.36589
361.14	0.23999	1.35911	373.64	0.24104	1.36576
361.23	0.24005	1.35894	373.98	0.24118	1.36002
361.32	0.24011	1.35840	374.32	0.24118	1.36003
361.41	0.24017	1.35944	374.67	0.24105	1.36283
361.41	0.24028	1.35919	375.01	0.24110	1.36272
361.75	0.24036	1.36110	375.35	0.24104	1.36358
362.09	0.24040	1.36219	375.69	0.24103	1.36271
362.43	0.24053	1.36172	376.03	0.24102	1.36183
362.77	0.24065	1.36162	376.37	0.24099	1.36138
363.11	0.24071	1.36342	376.72	0.24098	1.35947
363.45	0.24084	1.36305	377.06	0.24096	1.35870
363.79	0.24090	1.36330	377.40	0.24106	1.36384
364.13	0.24097	1.36354	377.74	0.24110	1.36249
364.47	0.24088	1.36938	378.42	0.24106	1.36169
364.81	0.24089	1.37049	379.11	0.24102	1.36072
365.15	0.24103	1.36971	379.79	0.24098	1.35971
365.49	0.24107	1.37007	380.48	0.24096	1.35812
365.82	0.24112	1.36992	381.16	0.24093	1.35704
366.16	0.24113	1.36986	381.84	0.24086	1.35661
366.50	0.24119	1.36960	382.53	0.24086	1.35497
366.84	0.24121	1.36903	383.21	0.24084	1.35346
367.18	0.24124	1.36900	383.89	0.24080	1.35295
367.52	0.24127	1.36908	384.58	0.24072	1.35256
367.86	0.24116	1.36409	385.26	0.24072	1.34989
368.20	0.24112	1.36453	385.95	0.24068	1.34704
368.54	0.24122	1.36438	386.63	0.24069	1.34619
368.88	0.24126	1.36404	387.32	0.24066	1.34395
369.21	0.24128	1.36418	388.00	0.24075	1.34497
369.55	0.24131	1.36432	388.69	0.24072	1.34386
369.89	0.24131	1.36459	389.37	0.24072	1.34269
370.23	0.24135	1.36407	390.05	0.24063	1.34255
370.57	0.24135	1.36449	390.74	0.24054	1.34300
370.91	0.24134	1.36455	391.42	0.24052	1.34066
371.25	0.24137	1.36354	392.11	0.24053	1.33779

(continuation in next page)

T (K)	$\lambda_{\text{eff},s}$ (W m ⁻¹ K ⁻¹)	$C_{p,s}$ (MJ m ⁻³ K ⁻¹)	T (K)	$\lambda_{\text{eff},s}$ (W m ⁻¹ K ⁻¹)	$C_{p,s}$ (MJ m ⁻³ K ⁻¹)
392.79	0.24053	1.33534	408.96	0.24055	1.33197
393.48	0.24051	1.33417	409.30	0.24055	1.33129
394.16	0.24048	1.33352	409.64	0.24052	1.33090
94.85	0.24043	1.33213	409.99	0.24050	1.33092
395.53	0.24041	1.33267	410.33	0.24046	1.33143
396.22	0.24038	1.33267	410.67	0.24044	1.33137
396.90	0.24037	1.33145	411.02	0.24040	1.33118
397.59	0.24032	1.33158	411.02	0.24038	1.32941
397.93	0.24025	1.33210	411.02	0.24037	1.32812
398.27	0.24031	1.33167	411.02	0.24035	1.32681
398.61	0.24028	1.33181			
398.96	0.24025	1.33226			
399.30	0.24024	1.33190			
399.64	0.24025	1.33169			
399.99	0.24024	1.33167			
400.33	0.24024	1.33145			
400.68	0.24022	1.33101			
401.02	0.24022	1.33065			
401.02	0.24028	1.32930			
401.37	0.24028	1.33102			
401.71	0.24028	1.33036			
402.06	0.24029	1.33107			
402.40	0.24019	1.32928			
402.75	0.24020	1.32918			
403.09	0.24019	1.32965			
403.44	0.24022	1.33075			
403.78	0.24029	1.32977			
404.13	0.24035	1.32920			
404.47	0.24030	1.33112			
404.82	0.24042	1.33107			
405.16	0.24041	1.33223			
405.51	0.24042	1.33219			
405.85	0.24046	1.33377			
406.20	0.24046	1.33395			
406.54	0.24045	1.33385			
406.89	0.24047	1.33349			
407.23	0.24047	1.33333			
407.58	0.24047	1.33307			
407.92	0.24041	1.33360			
408.27	0.24050	1.33229			
408.61	0.24050	1.33207			

Chapter 4: Comparison of different porous metal/metalloid oxides[†]

The performances of well-known porous metal/metalloid oxides adsorbents (zeolite 13X, zeolite 4A and silica gel) and less explored Engelhard titanosilicate ETS-10 for water adsorption heating systems (AHSs) were compared with the aid of computational modeling and simulations. The developed model contemplated adsorption equilibrium, one-dimensional heat and mass transfer in the bed, external heat transfer limitations, and intraparticle mass transport. The pair zeolite 13X/water seemed most promising for the AHS partly due to a higher amount of heat generated per cycle, and favourable water-adsorption isotherm features. Based on sensitivity studies, for zeolite particle diameters in the range 0.2-0.6 mm, the coefficient of performance was 1.48 and the specific heating power was in the range 1141-1254 W kg⁻¹. Aiming at inferior computational and numerical efforts, the impact of considering some simplified postulations (*e.g.*, constant thermal conductivity of the adsorbent; constant isosteric heat of adsorption; constant linear driving force coefficient) while ensuring comparable predictions of the performances of the AHSs, was successfully investigated.



[†] Based on:

Joana M. Pinheiro, Sérgio Salústio, João Rocha, Anabela A. Valente, Carlos M. Silva, Analysis of equilibrium and kinetic parameters of water adsorption heating systems for different porous metal/metalloid oxide adsorbents, Appl. Therm. Eng., 100 (2016), pp. 215-226.

4.1. Introduction

During the last 35 years thermally-driven adsorption cycles have been widely investigated, namely adsorption systems for heating/cooling applications, due to their lower environmental impact compared to that of conventional vapor compression systems. While the latter use hydrochlorofluorocarbons (HCFCs) and hydrofluorocarbons (HFCs), adsorption-based systems utilize benign refrigerants, such as water, which have zero global warming potential, and can be powered by solar energy or waste heat instead of mechanical power [1-3].

In terms of energy demand in Europe, almost 50 % of the final energy consumption is used for heating and cooling. The building sector accounts for more than 35 % of the overall consumption, of which 75 % is for domestic hot water production and room heating [4]. Therefore, efficient and cost effective heat production is important not only to meet the market needs, but also to decrease the consumption of fossil fuels in the building sector. In this respect, adsorption-based heating systems using, for instance, porous metal/metalloid oxides as adsorbents, such as zeolites/zeotype materials, have been pointed as promising technology [1, 4, 5].

The cyclic operation of an adsorption heating system (AHS), such as an adsorption heat pump (AHP), consists of four stages (Fig. 4.1), namely, isobaric adsorption (1→2), isosteric heating (2→3), isobaric desorption (3→4), and isosteric cooling (4→1). A detailed description of the working principles of adsorption cycles can be found elsewhere [6, 7].

The selection of the most appropriate working adsorbent/adsorbate pair is one of the main factors determining the efficiency of adsorption systems, and it depends on various factors such as the desirable operating conditions and the heat source temperature. It is important that the solid possesses a large adsorption capacity, is easily regenerated, and exhibits good hydrothermal stability, while the refrigerant fluid should have a large specific latent heat of condensation, good thermal stability, no toxicity and no flammability [8]. An important parameter to evaluate working pairs is the heat of adsorption (Q_{ads}) which has a direct influence on the cycled heat [9]. While a high value is favorable for generating heat in the adsorption stage, this may be levelled-off by more demanding conditions required for the regeneration of the adsorbent, and thus good compromises between the two are important for improved performances of heating processes.

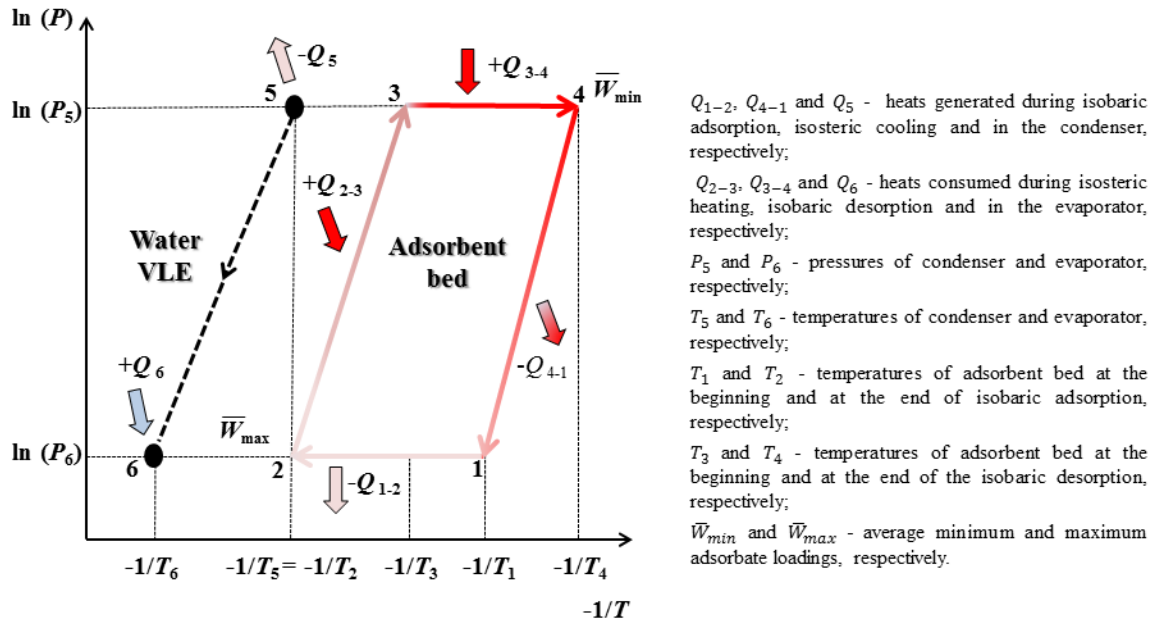


Fig. 4.1 - Clapeyron diagram of an adsorption heating system (AHS).

Zeolites, namely those of the faujasite framework type (X and Y zeolites), have been considered for AHP applications since the 1980s [9]. In particular, zeolite/water pairs have been reported as very suitable for AHPs due to their fairly high water adsorption capacity even at low pressures [10]. Other investigated pairs include activated carbon/methanol [11] and activated carbon/ammonia [12], albeit the use of eco-friendlier adsorbates is desirable.

Relatively high adsorption capacities of zeolites result at least partly from relatively strong adsorbent/adsorbate interactions, and therefore high desorption temperatures may be required (200-300 °C), presenting limitations for many applications [13]. More recently, efforts have been made to develop zeolitic adsorbents requiring less demanding regeneration conditions for AHPs, such as zeolite DDZ-70 from UOP and AQSOA™-FAM-Z02 from Mitsubishi Plastics [14]. The use of Engelhard titanosilicate number 10 (ETS-10) with water as adsorbate for use in AHSs has been recently reported [15]. The isotherms of the ETS-10/water pair feature benefits in terms of moderate regeneration conditions.

The overall performance of an AHS depends on the equilibrium properties of the pair and also on the mass and heat transfer processes within the adsorbent bed. Concerning equilibrium, large adsorption capacity at low relative pressures (characteristic of Type I isotherms) and desorption of most of the adsorbate even at high relative pressures are

particularly important [10]. Regarding mass transfer processes, adsorption kinetics can strongly affect the dynamic behaviour of an AHS and hence its specific heating power (*SHP*). The Linear Driving Force (LDF) model has often been used for describing intraparticle mass transfer kinetics. It includes an overall mass transfer coefficient (K_{LDF}) dependent on the effective diffusivity (D_{eff}) of the adsorbate in the porous solid [16, 17]. The D_{eff} not only varies with temperature but also with adsorbate loading, which tends to be discarded [18, 19]. Intraparticle mass transport and vapor permeability through the bed are both affected by particle diameter (d_p); larger particle sizes increase internal diffusion limitations, and, on the other hand, decrease the vapor transport resistances through the bed. Previous studies have reported on the strong impact of d_p on the mass transfer processes in adsorbent beds [2, 16, 20]. Regarding thermophysical properties, the thermal conductivity of the adsorbent ($\lambda_{eff,s}$) influences the efficiency of adsorbent beds [10, 21]. It may vary along the cycle, depending on adsorbate loading, temperature and pressure [21-23], although most modeling and simulation studies of adsorption refrigeration systems reported in the literature consider constant $\lambda_{eff,s}$ [10, 24, 25].

In this work, modeling and simulation studies were carried out aiming at the comparison of the heating performance of ETS-10, zeolites 13X and 4A, and silica gel for AHSs with water as adsorbate. The cyclic adsorption process was rigorously simulated, and the overall heating performance of each system was evaluated by means of the coefficient of performance (*COP*) and specific heating power (*SHP*). A comparison of the heat generated and consumed on the different stages of the cycle by each working pair was carried out, and the heating performances were discussed accounting for the shape of the isotherms. In addition, given the importance of equilibrium, kinetic and thermophysical parameters for the estimation of the performance of AHSs, simulation studies were carried out in order to gain insights into the influence of using: constant or variable $\lambda_{eff,s}$; constant Q_{ads} or adsorbate loading-dependent Q_{ads} ; D_{eff} varying with temperature and adsorbate loading; constant K_{LDF} in the whole adsorption cycle. A sensitivity analysis was made in order to investigate the impact of the particle size on the overall heating performance of an AHS.

4.2. Mathematical modeling of the adsorption unit

4.2.1. Model description and estimations of heating performance

The cyclic adsorption process for each adsorbent was investigated using the cylindrical bed configuration represented in Fig. 4.2. The adsorption unit, which is alternately connected to the evaporator or to the condenser, is essentially composed of a central porous and empty tube, through which the water vapor flows; adsorbent grains located in the space between the concentric cylinders; an external jacket where a heat transfer fluid (HTF) circulates which is accompanied by heating or cooling the adsorbent bed. Both upper and bottom surfaces of the unit are insulated, and thus heat and mass transfer occur only in the radial direction.

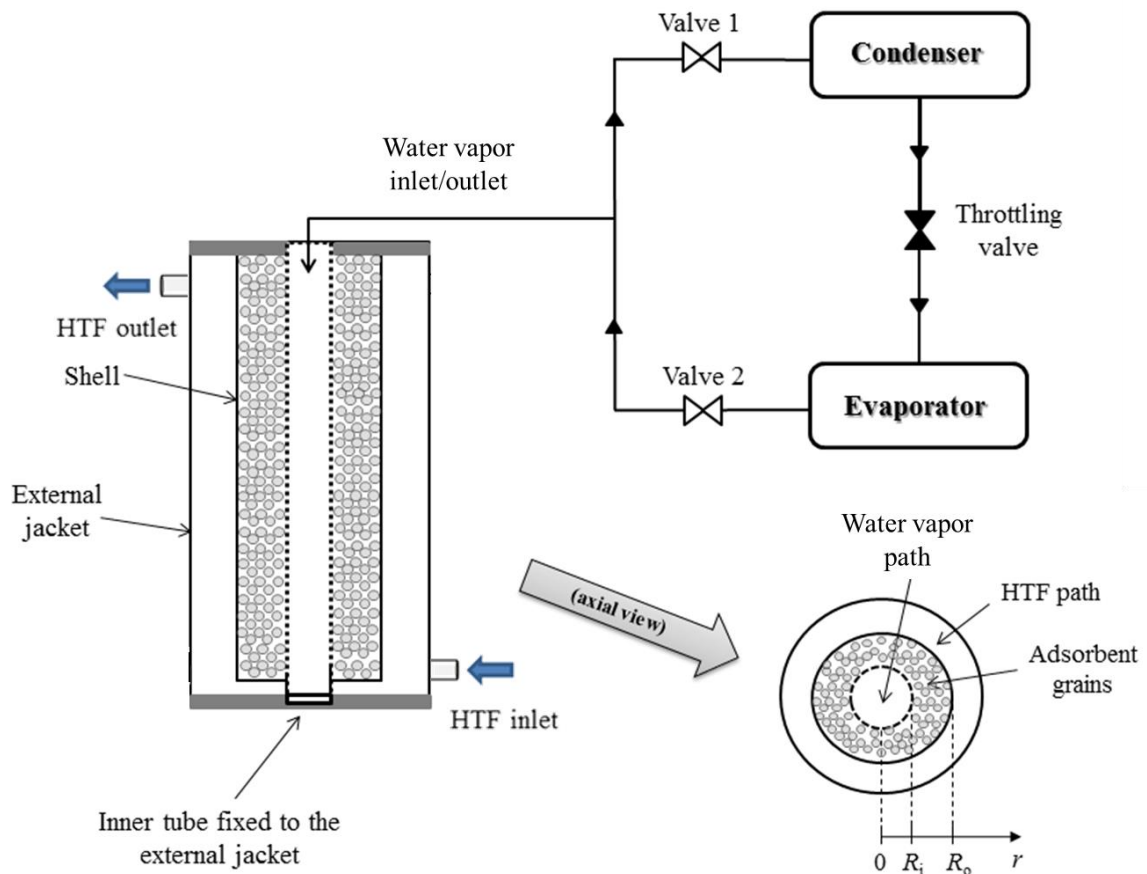


Fig. 4.2 - Schematic representation of the AHS modeled in this work. HTF is the heat transfer fluid; the water vapor inlet/outlet tube of the adsorbent bed is connected to the condenser or to the evaporator.

The following assumptions were introduced in the mathematical model: (i) the adsorbent bed is composed of uniformly-sized particles and its porosity is constant; (ii) there is resistance to mass transfer inside the particles; (iii) there is film resistance to heat transfer; (iv) the thermal conductivities and specific heat capacities of the solid and vapor, and the viscosity of the vapor are constants; (v) radiation heat transfer, viscous dissipation and the work done by pressure changes are negligible; (vi) the thermal resistance between the HTF and the adsorbent bed is negligible, and there are no losses to the environment.

The mathematical model of the unsteady state cyclic unit was written for a differential volume element of radial thickness dr , whose equations are given in Table 4.1. The model also includes the equilibrium isotherms for each working pair (Section 4.3.1.1, Eqs. (4.17)-(4.20), Table 4.3). The set of initial and boundary conditions for each stage of the cycle are given in Table 4.2.

4.2.2. Estimation of the heating performance

The heating performance of each working pair was evaluated by means of the coefficient of performance (COP) and the specific heating power (SHP), calculated using Eqs. (4.9)-(4.10), respectively (nomenclature in accordance with Fig. 4.1):

$$COP = \frac{|Q_{1-2} + Q_5 + Q_{4-1}|}{Q_{3-4} + Q_{2-3}} \quad (4.9)$$

$$SHP = \frac{|Q_{1-2} + Q_5 + Q_{4-1}|}{m_s t_{\text{cycle}}} \quad (4.10)$$

Chapter 4: Comparison of different porous metal/metalloid oxides

Table 4.1 - Mathematical model of the adsorption systems investigated in this work.

Description	Equation	
Material balance to the adsorbent bed	$\varepsilon_b \frac{\partial \rho_v}{\partial t} + (1 - \varepsilon_b) \rho_s \frac{\partial W}{\partial t} + \frac{1}{r} \frac{\partial (r \rho_v u)}{\partial r} = 0$	(4.1)
Material balance to the adsorbent particles - Linear Driving Force (LDF) model ^(a)	$\frac{\partial W}{\partial t} = K_{LDF} (W_{eq} - W)$, with $K_{LDF} = 15 \frac{D_{eff}}{R_p^2}$	(4.2)
Energy balance to the adsorbent	$\rho_s (1 - \varepsilon_b) (C_{p,s} + W C_{p,a}) \frac{\partial T_s}{\partial t} = \frac{1}{r} \frac{\partial}{\partial r} \left(r \lambda_{eff,s} \frac{\partial T_s}{\partial r} \right) - a h_{sv} (T_s - T_v) + (1 - \varepsilon_b) \rho_s \frac{\partial W}{\partial t} Q_{ads}$	(4.3)
Energy balance to the vapor	$\varepsilon_b \frac{\partial}{\partial t} (\rho_v C_{p,v} T_v) + \frac{1}{r} \frac{\partial}{\partial r} (r u \rho_v C_{p,v} T_v) - (1 - \varepsilon_b) \rho_s C_{p,v} \frac{\partial W}{\partial t} (T_s - T_v) = \frac{1}{r} \frac{\partial}{\partial r} \left(r \lambda_{eff,v} \frac{\partial T_v}{\partial r} \right) + a h_{sv} (T_s - T_v)$	(4.4)
Momentum balance (Darcy's Law) ^(b)	$u = -\frac{K}{\eta_v} \frac{\partial P}{\partial r}$, with $K = \frac{d_p^2 \varepsilon_b^3}{150(1-\varepsilon_b)^2}$	(4.5)
External surface area of adsorbent spheres per unit bed volume	$a = \frac{6(1 - \varepsilon_b)}{d_p}$	(4.6)
Dimensionless correlation for h_{sv} calculation ^(c)	$Nu = 2 + 1.8 Pr^{0.33} Re^{0.5}$, with $Nu = \frac{d_p h_{sv}}{\lambda_v}$, $Pr = \frac{\eta_v C_{p,v}}{\lambda_v}$, $Re = \frac{u \rho_v d_p}{\eta_v}$	(4.7)
Effective thermal conductivity of vapor	$\lambda_{eff,v} = \lambda_v \varepsilon_b$	(4.8)

^(a) The equation used to calculate K_{LDF} is given in reference [24]. For ETS-10/water pair, a constant value of K_{LDF} , available from reference [15], was used in the simulations. ^(b) The equation used to calculate K is given in reference [26]. ^(c) Dimensionless correlation available from reference [27]; equations used to calculate Nu, Pr and Re numbers are available from reference [28].

Table 4.2 - Initial and boundary conditions of the model of the adsorption heating systems investigated in this work.

Cycle stage	Inner boundary conditions ($r = R_i$)	Outer boundary conditions ($r = R_o$)	Initial conditions
Isobaric adsorption (1→2)	$\frac{\partial T_s}{\partial r}(t, R_i) = \frac{\partial T_v}{\partial r}(t, R_i) = 0$ $P(t, R_i) = P_{\text{evap}}$	$T_s(t, R_o) = T_v(t, R_o) = T_{\text{HTF,cool}}$ $\frac{\partial P}{\partial r}(t, R_o) = 0^{(a)}$	<p><i>Startup cycle:</i></p> $T_s(0, r) = T_v(0, r) = T_{\text{ini}}$ $P(0, r) = P_{\text{ini}}$ $W(0, r) = W_{\text{ini}}$ <p><i>Remaining cycles:</i></p> <p>Final values of T_s, T_v, P and W of the isosteric cooling step</p>
Isosteric heating (2→3)	$\frac{\partial T_s}{\partial r}(t, R_i) = \frac{\partial T_v}{\partial r}(t, R_i) = 0$ $\frac{\partial P}{\partial r}(t, R_i) = 0^{(b)}$	$T_s(t, R_o) = T_v(t, R_o) = T_{\text{HTF,hot}}$ $\frac{\partial P}{\partial r}(t, R_o) = 0^{(a)}$	<p>Final values of T_s, T_v, P and W of the isobaric adsorption step</p>
Isobaric desorption (3→4)	$\frac{\partial T_s}{\partial r}(t, R_i) = \frac{\partial T_v}{\partial r}(t, R_i) = 0$ $P(t, R_i) = P_{\text{cond}}$	$T_s(t, R_o) = T_v(t, R_o) = T_{\text{HTF,hot}}$ $\frac{\partial P}{\partial r}(t, R_o) = 0^{(a)}$	<p>Final values of T_s, T_v, P and W of the isosteric heating step</p>
Isosteric cooling (4→1)	$\frac{\partial T_s}{\partial r}(t, R_i) = \frac{\partial T_v}{\partial r}(t, R_i) = 0$ $\frac{\partial P}{\partial r}(t, R_i) = 0^{(b)}$	$T_s(t, R_o) = T_v(t, R_o) = T_{\text{HTF,cool}}$ $\frac{\partial P}{\partial r}(t, R_o) = 0^{(a)}$	<p>Final values of T_s, T_v, P and W of the isobaric desorption step</p>

^(a) A zero pressure gradient is assumed since the shell wall is impermeable ($u = 0 \text{ m s}^{-1}$). ^(b) Since the bed is isolated from both condenser and evaporator, no pressure gradient exists.

The heats involved in the process were computed by:

$$Q_{1-2} = \int_{T_1}^{T_2} [m_s(C_{p,s} + \bar{W}C_{p,a})] d\bar{T} + \int_{\bar{W}_{\min}}^{\bar{W}_{\max}} m_s (-Q_{\text{ads}}) d\bar{W} \quad (4.11)$$

$$Q_{2-3} = \int_{T_2}^{T_3} [m_s(C_{p,s} + \bar{W}C_{p,a})] d\bar{T} \quad (4.12)$$

$$Q_{3-4} = \int_{T_3}^{T_4} [m_s(C_{p,s} + \bar{W}C_{p,a})] d\bar{T} + \left| \int_{\bar{W}_{\max}}^{\bar{W}_{\min}} m_s Q_{\text{ads}} d\bar{W} \right| \quad (4.13)$$

$$Q_{4-1} = \int_{T_4}^{T_1} [m_s(C_{p,s} + \bar{W}C_{p,a})] d\bar{T} \quad (4.14)$$

$$Q_5 = -m_s \Delta \bar{W}_{\text{cycle}} \Delta H_v, \text{ where } \Delta \bar{W}_{\text{cycle}} = \bar{W}_{\max} - \bar{W}_{\min} \quad (4.15)$$

The average temperature, pressure and adsorbate loading in the bed (\bar{T} , \bar{P} , and \bar{W} , respectively), generically denoted by $\bar{\varphi}$, were calculated as follows,

$$\bar{\varphi}(t) = \frac{\int_{R_i}^{R_o} 2r\varphi(t,r)dr}{(R_o^2 - R_i^2)} \quad (4.16)$$

4.2.3. Numerical approach

The highly coupled and non-linear set of partial differential equations governing the adsorption cycle were solved by the method of lines [29]. The radial direction was discretised using second-order finite difference scheme, and the resulting system of ordinary differential equations was integrated using a variable order solver based on numerical differentiation formulas [30]. The computer simulation program was written in Matlab and validated previously using literature data [24]. Concerning the grid size, 35 points of discretisation allowed a good trade-off between accuracy and computational cost.

Details on the stopping criteria applied in the simulations are given in Annex A4 (Section A4.1).

4.3. Results and discussion

In this section the determination of the isotherm equation for zeolite 13X/water pair (Section 4.3.1.1), the equations used to calculate $Q_{\text{ads}} = Q_{\text{ads}}(W)$ of working pairs (Section 4.3.1.2), and the expressions of $D_{\text{eff}} = D_{\text{eff}}(T, W)$ of water on zeolites 13X, 4A and silica gel (Section 4.3.1.3) are described. Results from the modeling and simulation of the cyclic adsorption heating process using water as refrigerant and different adsorbents - ETS-10, zeolites 13X and 4A, and silica gel - are presented, including a comparison of their heating performances, which are discussed accounting for the shape of the isotherms of each pair (Section 4.3.2). The impact of considering constant or variable $\lambda_{\text{eff},s}$ in the simulations is evaluated, along with the effect of using a constant Q_{ads} or $Q_{\text{ads}} = Q_{\text{ads}}(W)$. The influence of considering $D_{\text{eff}} = D_{\text{eff}}(T, W)$ in the calculation of K_{LDF} , and the impact of using a constant K_{LDF} in the simulations is also assessed. A sensitivity study provided insights into the influence of the particle size on the overall heating performance of an AHS.

4.3.1. Equilibrium and kinetic properties of the working pairs

4.3.1.1. Adsorption isotherms

In order to carry out the simulations, the mathematical expressions of water adsorption isotherms are required. In the case of ETS-10, silica gel and zeolite 4A they were taken from the literature, while for zeolite 13X it was determined in this work (Eqs. (4.17)-(4.20), Table 4.3).

Chapter 4: Comparison of different porous metal/metalloid oxides

Table 4.3 - Mathematical expressions of the water adsorption isotherms of ETS-10, zeolite 13X (obtained in this work), zeolite 4A and silica gel considered in the simulations, equations for the calculation of $Q_{\text{ads}} = Q_{\text{ads}}(W)$, and equations obtained in this work for the determination of D_{eff} of water on zeolite 13X, zeolite 4A and silica gel as a function of temperature and adsorbate loading. Clausius-Clapeyron model is also given.

ETS-10/water isotherm (Dubinin-Astakhov model) ^(a)	$W_{\text{eq}} = 0.129 \exp \left[-4.1 \times 10^{-7} \left(T \ln \frac{P_{\text{sat}}}{P} \right)^{1.98} \right]$	(4.17)
Zeolite 13X/water isotherm (Dubinin-Astakhov model) ^(b)	$W_{\text{eq}} = 0.295 \exp \left[-8.68 \left(\frac{T}{T_{\text{sat}}} - 1 \right)^{1.71} \right]$	(4.18)
Zeolite 4A/water isotherm ^(c)	$\ln P = 14.898 + 95.408 W - 636.66 W^2 + 1848.8 W^3 + \frac{-7698.9 + 21498 W - 184598 W^2 + 512605 W^3}{T}$	(4.19)
Silica gel/water isotherm (Toth's model) ^(d)	$W_{\text{eq}} = \frac{7.30 \times 10^{-13} P \exp \left(\frac{5.8 \times 10^3}{T} \right)}{\left\{ 1 + \left[1.62 \times 10^{-12} P \exp \left(\frac{5.8 \times 10^3}{T} \right) \right]^{12} \right\}^{1/12}}$	(4.20)
Isosteric heat of adsorption of 13X/water as function of adsorbate loading ^(e)	$Q_{\text{ads}} = \frac{5.678 \times 10^4}{M} + \frac{-3.21 \times 10^2}{M} W$	(4.21)
Isosteric heat of adsorption of 4A/water as function of adsorbate loading ^(f)	$Q_{\text{ads}} = \frac{1000 R (-7698.9 + 21498W - 184598 W^2 + 512605W^3)}{M}$	(4.22)
Isosteric heat of adsorption of ETS-10/water as function of adsorbate loading (W)	$Q_{\text{ads}} = -8.155 \times 10^6 W + 3.586 \times 10^6$	(4.23)

(Table 4.3 continues)

Chapter 4: Comparison of different porous metal/metalloid oxides

Clausius-Clapeyron model ^(g)	$\left[\frac{\partial \ln P}{\partial \left(\frac{1}{T} \right)} \right]_W = - \frac{Q_{\text{ads}} M}{R}$	(4.24)
Effective diffusivity of water on zeolite 13X (D_{eff})	$D_{\text{eff}} = \exp(-27.889 + 4.420 \times 10^{-4} T^{1.5} - 284.341 W^2 - \frac{107.152 W}{\ln W} + 3.839 W^{0.5} - \frac{4.042 \times 10^{-3}}{W^{1.5}})$	(4.25)
Effective diffusivity of water on zeolite 4A (D_{eff})	$D_{\text{eff}} = -7.915 \times 10^{-9} + 2.026 \times 10^{-9} \ln T - 9.907 \times 10^{-10} \ln W - 1.197 \times 10^{-10} (\ln T)^2 - 7.707 \times 10^{-11} (\ln W)^2 + 1.209 \times 10^{-10} \ln T \ln W$	(4.26)
Effective diffusivity of water on silica gel (D_{eff})	$D_{\text{eff}} = \exp(-238.011 - \frac{3790.810}{T} + 157.667 W - 42.783 W \ln W + 222.302 \exp(-W))$	(4.27)

^(a) Equation available from reference [15]. Saturation pressure (P_{sat}) was calculated by the Antoine equation [34]. ^(b) Equation obtained in this work using experimental data reported in reference [33]. Saturation temperature (T_{sat}) was calculated by the Antoine equation [34]. ^(c) Equation available from reference [35]. The P is in mbar. ^(d) Equation available from reference [36]. ^(e) Equation available from reference [5]. ^(f) Equation available from reference [35]. ^(g) Equation available from reference [37].

The Dubinin-Astakhov (DA) model, which has been widely used to describe the adsorption equilibrium in microporous materials by the micropore filling mechanism [31, 32], was fitted to the experimental data reported by Garfinkel *et al.* [33] for water adsorption on zeolite 13X in the range 294-355 K (Fig. 4.3). The parameters W_0 , C and n of the DA model, obtained by unconstrained nonlinear optimization, are 0.295 kg kg⁻¹, -8.68 and 1.71, respectively (Eq. (4.18)), with an average absolute relative deviation (AARD) of 6.6 %.

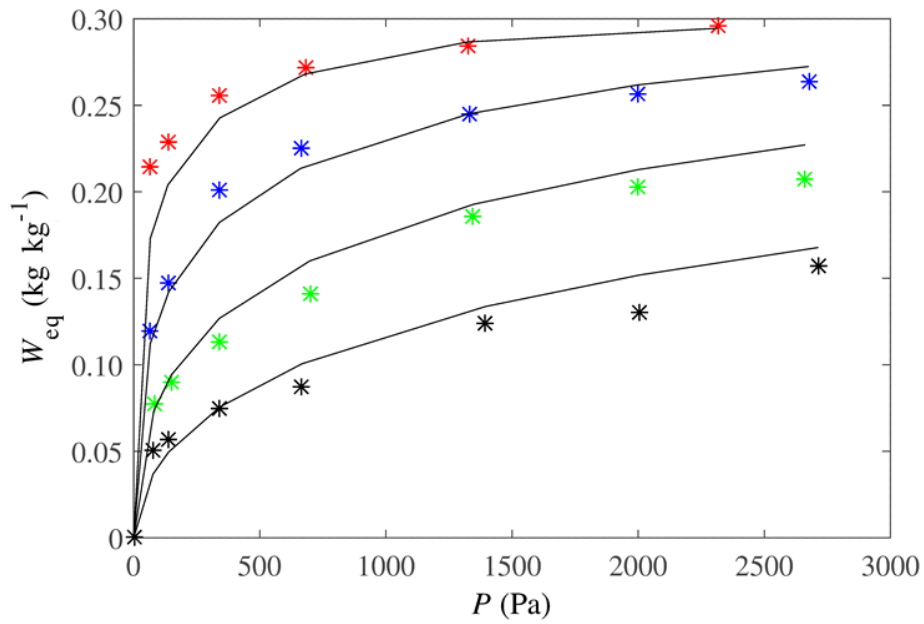


Fig. 4.3 - Adsorption isotherms of water on zeolite 13X: Experimental data at 294 (*), 314 (*), 333 (*) and 355 K (*) taken from ref. [33]; lines are Dubinin-Astakhov model (Eq. (4.18), Table 4.3).

4.3.1.2. Estimation of $Q_{ads} = Q_{ads}(W)$ for zeolites 13X, 4A and ETS-10

The expressions collected from the literature to calculate $Q_{ads} = Q_{ads}(W)$ for zeolite 13X/water [5] and zeolite 4A/water [35] are given in Table 4.3 (Eqs. (4.21) and (4.22), respectively). According to the isotherm of zeolite 13X/water pair (Eq. (4.18)), W at half coverage is $0.295/2 = 0.148$ kg kg⁻¹ and the corresponding Q_{ads} estimated by Eq. (4.21) is *ca.* 3.2×10^6 J kg⁻¹, which is coincident with the constant value taken from the literature and indicated in Table 4.4 (Section 4.3.2). For zeolite 4A/water pair, the isotherm equation

(Eq. (4.19)) gives $W_{eq} = 0.219 \text{ kg kg}^{-1}$ at $T = T_{min,cycle} = 333 \text{ K}$ and $P = P_{sat}^{333 K} = 19921 \text{ Pa}$, which was assumed to be the maximum W achievable. At half coverage, *i.e.*, $0.219/2 = 0.1095 \text{ kg kg}^{-1}$, Q_{ads} given by Eq. (4.22) is *ca.* $3.2 \times 10^6 \text{ J kg}^{-1}$, which is close to the value in Table 4.4, collected from the literature. Fig. 4.4 shows Q_{ads} as function of W for ETS-10/water pair, whose data was estimated using the isotherm (Eq. (4.17)) and the Clausius-Clapeyron model (Eq. (4.24)). The Q_{ads} vs. W relation obtained from linear fitting with $R^2 = 0.996$ is given in Table 4.3 (Eq. (4.23)).

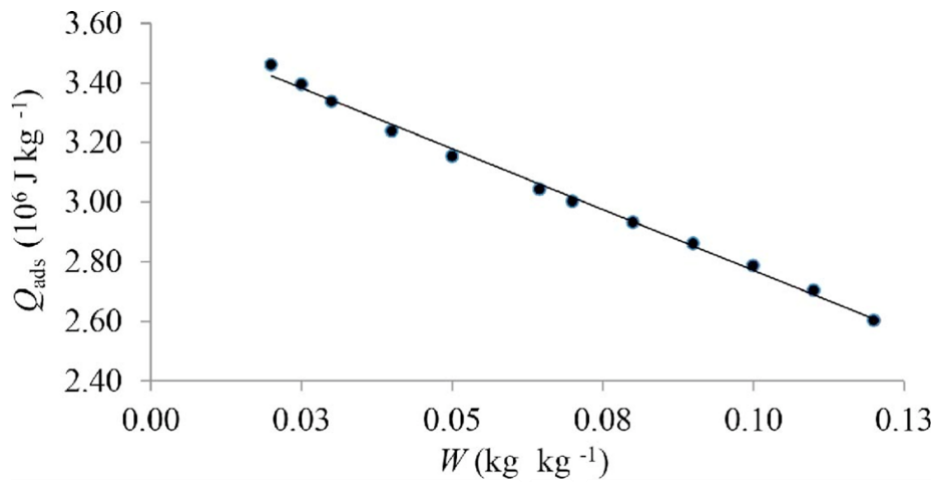


Fig. 4.4 - Isosteric heat of adsorption of ETS-10/water pair as function of W : (•) data calculated using the isotherm equation and the Clausius – Clapeyron model; (-) linear fitting (Eq. (4.23), Table 4.3).

4.3.1.3. Estimation of $D_{eff} = D_{eff}(T, W)$ of water on zeolites 13X, 4A and silica gel

The expressions used to calculate $D_{eff} = D_{eff}(T, W)$ of water on zeolites 13X, 4A and on silica gel, which are given in Table 4.3 (Eqs. (4.25)-(4.27)), were determined by surface fitting to experimental data available in the literature (Fig. 4.5) [18, 19, 38]. The quality indicators obtained from the fittings in Fig. 4.5 are: zeolite 13X/water - $R^2 = 0.968$, $R^2_{adjusted} = 0.960$; zeolite 4A/water - $R^2 = 0.977$, $R^2_{adjusted} = 0.960$; silica gel/water - $R^2 = 0.999$, $R^2_{adjusted} = 0.999$. According to the classification of Kärger and Pfeifer [39] for the dependence of intracrystalline self-diffusion on concentration, the water diffusion in zeolites 13X and 4A is of Type IV (*i.e.*, D_{eff} has a maximum value near half coverage),

and in silica gel it is of Type III (*i.e.*, D_{eff} monotonically increases with adsorbate loading, reaching a *plateau* for a given W).

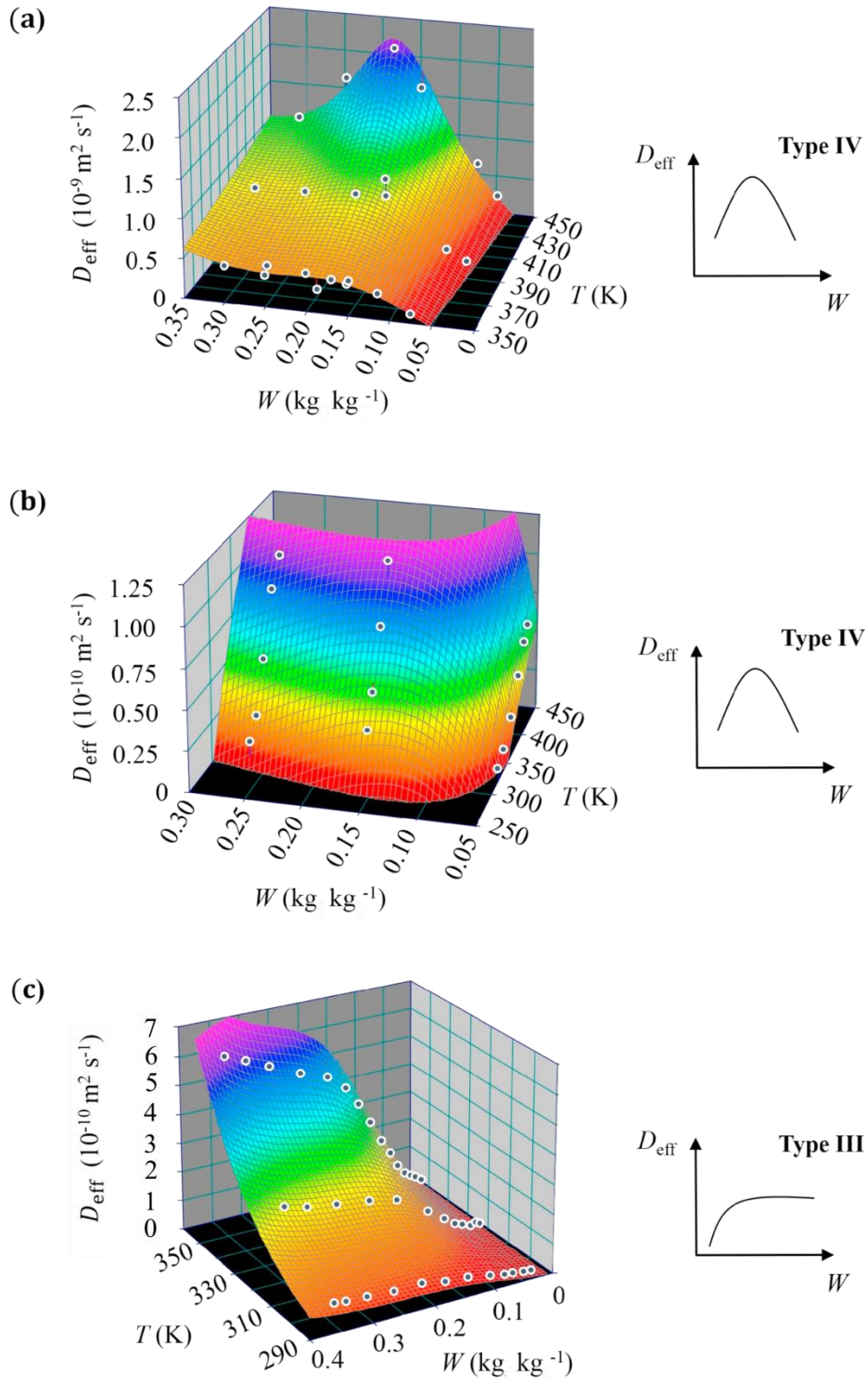


Fig. 4.5 - $D_{\text{eff}} = D_{\text{eff}}(T, W)$ of water on: (a) zeolite 13X. Surface fitted to literature data (dots) taken from ref. [18] is given by Eq. (4.25); (b) zeolite 4A. Surface fitted to literature data (dots) taken from ref. [38] is

given by Eq. (4.26); (c) silica gel type RD. Surface fitted to literature data (dots) taken from ref. [19] is given by Eq. (4.27). For zeolites 13X and 4A, D_{eff} vs. W curves are of type IV, while for silica is of type III, according to the classification of Kärger and Pfeifer [39].

4.3.2. Simulation of the heating performance of the working pairs

The main properties of the working pairs, cylindrical adsorbent bed dimensions and the operating conditions considered in the simulations are given in Table 4.4.

The modeled AHS aims at the production of heat at 333 K, using a heat source temperature ($T_{\text{HTF,hot}}$) at 473 K (or 423 K in the case of silica gel) to regenerate the adsorbent. The chosen value of $T_{\text{HTF,hot}}$ lies within the range of temperatures of low grade heat sources, typically between room temperature and 523 K [45]. The chosen $T_{\text{HTF,hot}}$ can also correspond to the usage of exhaust gas as a heat source.

To exemplify the operating cycle of the AHS, the simulated cycles for three different particle sizes of zeolite 13X are given in Fig. 4.6, along with the corresponding ideal cycle. For the ideal cycle, it is assumed that the temperature and pressure in the bed are uniform, and the absence of heat and mass transfer resistances. Fig. 4.6 includes three pie charts indicating the time spent on each stage of the cycle for the three particle sizes. For $d_p = 2.0 \times 10^{-4}$ m some deviations from the ideal cycle occur, particularly during the adsorption stage due to vapor transport resistance inside the bed; a minimum \bar{P} of about 764 Pa is achieved, which corresponds to a deviation of *ca.* 12 % in relation to the value of P_{evap} .

Table 4.5 indicates the results obtained for the cycle times, minimum and maximum average adsorbate loadings achieved in the bed, average adsorption loading swings, *COP* and *SHP* values for each adsorbent.

Chapter 4: Comparison of different porous metal/metalloid oxides

Table 4.4 - Main properties of the adsorbents, operating conditions and adsorbent bed dimensions considered in the simulations.

	ETS-10	Ref.	Zeolite 13X	Ref.	Zeolite 4A	Ref.	Silica gel	Ref.
$C_{p,s}$ (J kg ⁻¹ K ⁻¹) ^(a)	800	[15]	836	[16]	920	[40]	921	[36]
$\lambda_{eff,s}$ (W m ⁻¹ K ⁻¹) ^(a)	0.24		0.20 ^(b)	[41]	0.20 ^(c)	[21]	0.20	
d_p (m)	3.5×10 ⁻⁴	[42]	3.5×10 ⁻⁴	---	3.5×10 ⁻⁴	---	3.5×10 ⁻⁴	---
ε_b	0.40		0.40	---	0.40	---	0.40	---
ρ_s (kg m ⁻³)	2553		2561 ^(b)	[43]	2391 ^(b)	[43]	2027	[36]
Q_{ads} (J kg ⁻¹)	3.042×10 ⁶	[15]	3.200×10 ⁶	[16]	3.300×10 ⁶	[6]	2.693×10 ⁶	[36]
K_{LDF} (s ⁻¹)	1.5×10 ⁻²		---		---		---	
<i>Operating conditions</i>								
P_{ini} (Pa); T_{ini} (K); W_{ini} (kg kg ⁻¹)				500; 333; ≈ 0				
$T_{HTF,cool}$ (K); $T_{HTF,hot}$ (K) ^(d)				333; 473 (or 423)				
P_{cond} (Pa); T_{cond} (K)				19921; 333				
P_{evap} (Pa); T_{evap} (K)				870; 278				
<i>Adsorbent bed dimensions</i> - R_i ; R_o (m)				0.0050; 0.0070				

^(a) Further details on the used values are given in Section A4.2 (Annex A4). ^(b) Average values between 333 K and 473 K. ^(c) Average value between 333 K and 473 K, considering the operating pressures of 870 and 19921 Pa, respectively. ^(d) The final regeneration temperature of the bed (T_4 in Fig. 4.1) is coincident with $T_{HTF,hot}$. According to ref. [44], 423 K corresponds to the maximum recommended temperature for the regeneration of silica gel. For the remaining adsorbents, $T_{HTF,hot}$ = 473 K was considered in the simulations.

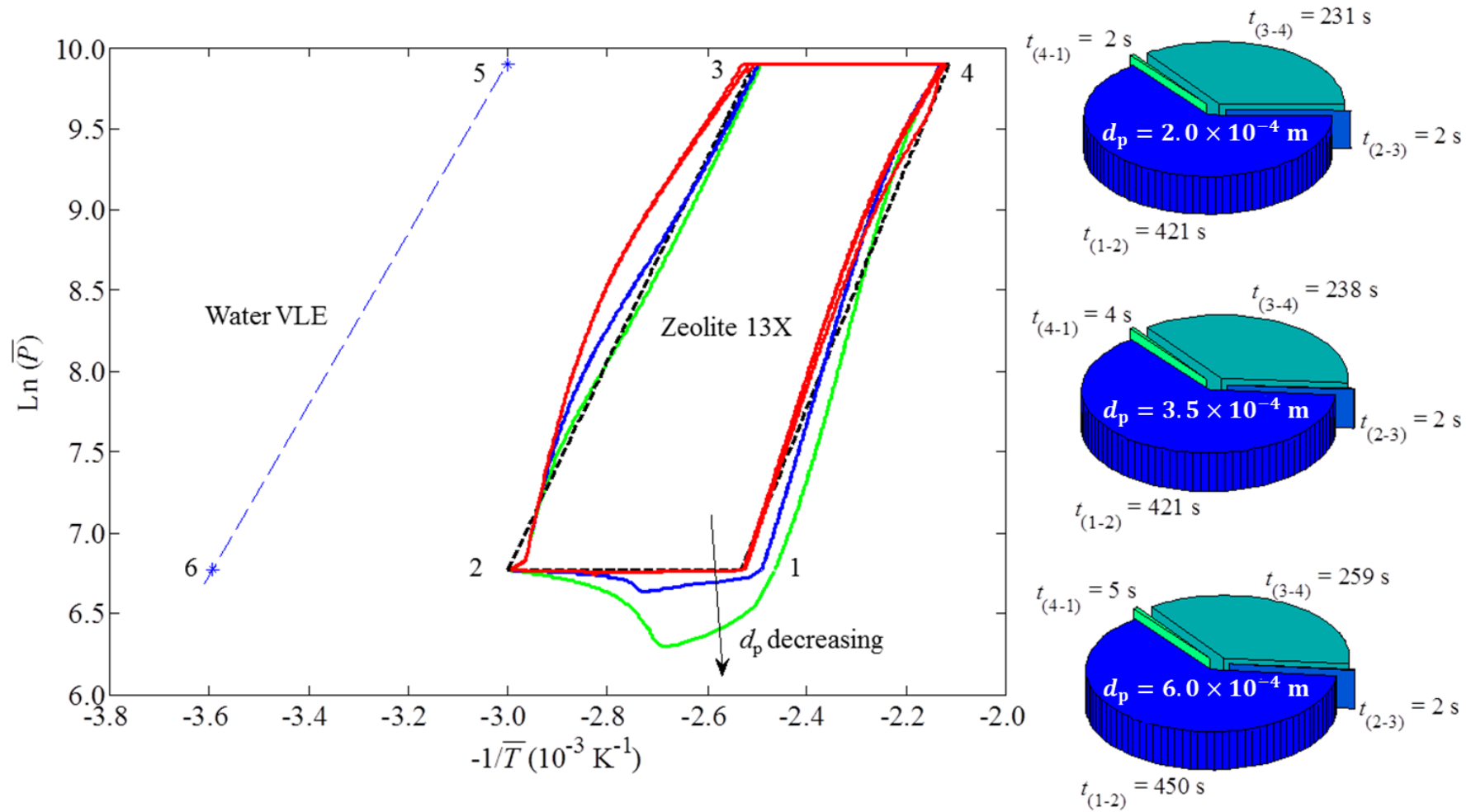


Fig. 4.6 - Operational cycles for different particle sizes of zeolite 13X: $d_p = 2.0 \times 10^{-4}$ (—), 3.5×10^{-4} (—) and 6.0×10^{-4} m (—), and ideal cycle (— —). Water vapor-liquid equilibrium (VLE) (— —). The stage numbers (1-4) match those of Fig. 4.1. Pie charts indicate the time spent on each stage of the heating cycle for each particle size (t_{1-2} , t_{2-3} , t_{3-4} and t_{4-1} are the durations of isobaric adsorption, isosteric heating, isobaric desorption, and isosteric cooling, respectively).

Table 4.5 - Results obtained from the simulations for the different adsorbents. Performance values for ideal cycles are given for comparison.

Adsorbent		t_{cycle} (s)	\bar{W}_{min} (kg kg ⁻¹)	\bar{W}_{max} (kg kg ⁻¹)	$\Delta\bar{W}_{\text{cycle}}$ (kg kg ⁻¹)	COP	SHP (W kg ⁻¹)
ETS-10	Simulated cycle	523	0.0311	0.0843	0.0532	1.37	768
	Ideal cycle	---	0.0274 ^(a)	0.0875 ^(c)	0.0601	1.41	---
Zeolite 13X	Simulated cycle	666	0.0425	0.169	0.126	1.48	1232
	Ideal cycle	---	0.0411 ^(a)	0.171 ^(c)	0.130	1.49	---
Zeolite 4A	Simulated cycle	512	0.0979	0.185	0.0869	1.40	1248
	Ideal cycle	---	0.0961 ^(a)	0.186 ^(c)	0.0899	1.41	---
Silica gel	Simulated cycle	119	0.0153	0.0166	0.00131	1.02	802
	Ideal cycle	---	0.0140 ^(b)	0.0253 ^(c)	0.0113	1.20	---

^(a) Obtained from the isotherm at 473 K. ^(b) Obtained from the isotherm at 423 K. ^(c) Obtained from the isotherm at 333 K.

The most promising adsorbent is the zeolite 13X, followed by zeolite 4A, ETS-10 and, lastly, silica gel. Silica gel exhibits poor potential due to its low COP value (1.02). The results obtained for zeolite 13X and 4A are roughly comparable to those reported in the literature: Marletta *et al.* [25] pointed $COP = 1.37$ for zeolite 4A/water pair with $\delta = 5$ mm, under similar operating conditions; Restuccia *et al.* [46] reported $COP = 1.44$ and $SHP = 878 \text{ W kg}^{-1}$ for a zeolite 4A/water heating system, operating two beds with internal heat recovery; Cacciola *et al.* [11] pointed $COP = 1.60$ for a double-bed system using zeolite 13X/water pair under similar operating conditions, which is consistently in agreement with the lower value of 1.48 obtained in this work for a single bed.

The heats generated or consumed in the four stages of the cycle by each pair, along with the different contributions to the COP value, are shown in Fig. 4.7. Zeolite 13X led to the highest heat production per cycle, despite the fact that the heat required for its regeneration was highest (Fig. 4.7(a)). The heats involved in the isobaric adsorption (Q_{1-2}) and desorption (Q_{3-4}) stages include a sensible heat component and a latent heat component (Eqs. (4.11) and (4.13)). For zeolites 13X and 4A, and ETS-10, the heat involved in these stages was mostly latent heat (*e.g.*, for the zeolite 13X/water pair, sensible heat contribution was only *ca.* 15 %). Fig. 4.7(b) shows that for zeolites 13X, 4A and ETS-10,

the isobaric adsorption is the stage that impacts more on COP , followed by condenser, and a minor contribution of the cooling stage since it only involves sensible heat (Eq. (4.14)). Once that $Q_{1-2} + Q_{4-1} \approx Q_{3-4} + Q_{2-3}$, the heat generated by the condenser (Q_5) gives the main contribution to obtain $COP > 1$. On the other hand, the usage of silica gel/water pair leads to low heat production per cycle due to extremely low $\Delta\bar{W}_{cycle}$ ($0.00131 \text{ kg kg}^{-1}$, Table 4.5); the main contribution to COP was provided by the cooling stage, and to much lower extents by the adsorption stage and condenser, which is not attractive for application in AHSs.

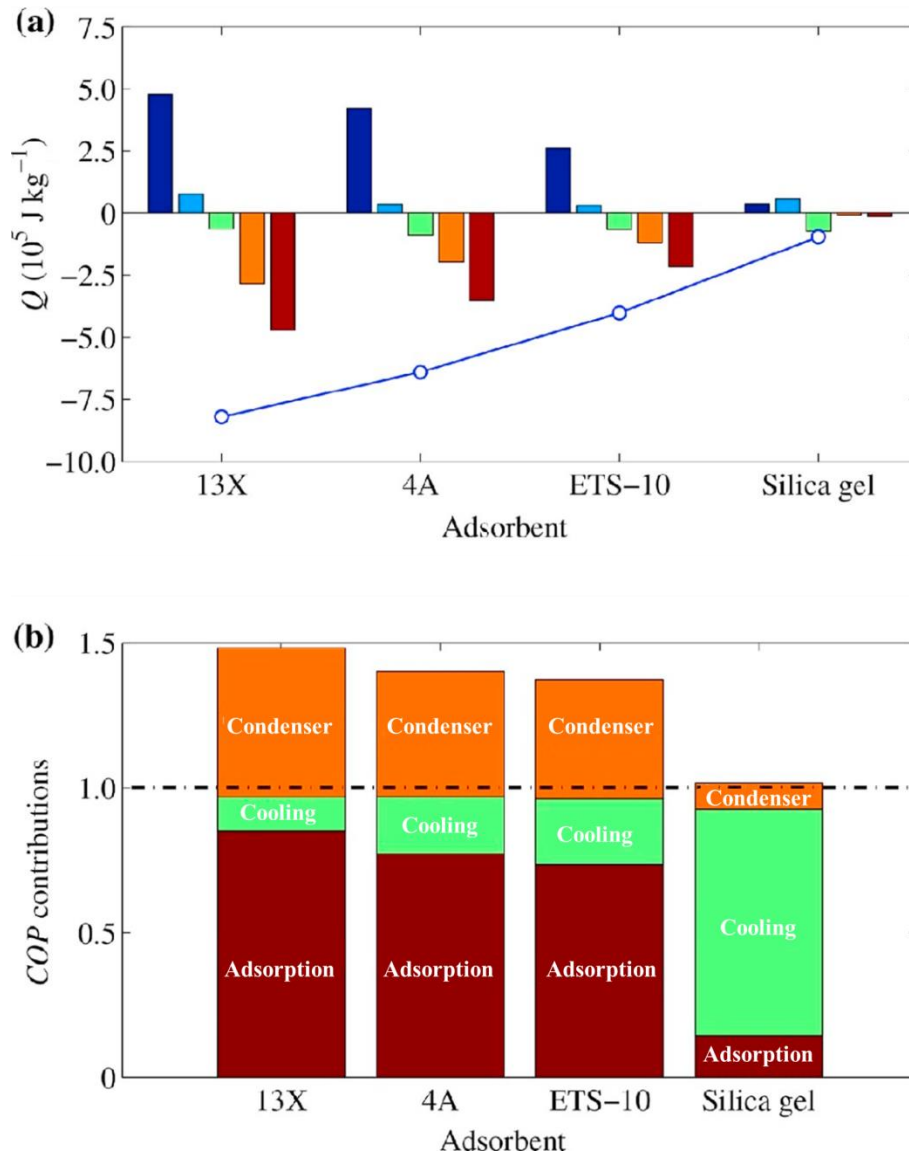


Fig. 4.7 - (a) Heats generated (negative) or supplied (positive) to the AHS during each stage of the cycle, for each adsorbent: dark blue bars – isobaric desorption (3→4); light blue bars – isosteric heating (2→3); green

bars – isosteric cooling (4→1); orange bars – condenser (5); brown bars – isobaric adsorption (1→2). Symbol ‘o’ denotes the total heat generated by each AHS; line (–) is a visual guide. (b) Contribution of different cycle stages to the COP: isobaric adsorption: $COP_{\text{contribution } 1-2} = \frac{Q_{1-2}}{Q_{3-4}+Q_{2-3}}$; condenser: $COP_{\text{contribution } 5} = \frac{Q_5}{Q_{3-4}+Q_{2-3}}$; isosteric cooling: $COP_{\text{contribution } 4-1} = \frac{Q_{4-1}}{Q_{3-4}+Q_{2-3}}$.

The isotherms at $T = 333$ K and at $T = 473$ K (or 423 K for silica gel) for each pair are given in Fig. 4.8. Silica gel has a low adsorption capacity up to $P/P_0 = 0.0437$, and water adsorption occurs mainly at very high relative pressures (Fig. 4.8(a)). The linear trend of the silica gel isotherms is unfavourable for the application under study, leading to poor heating performance (Table 4.5 and Fig. 4.7). In fact, silica gel has been essentially investigated for cooling rather than heating purposes [8, 24]. Zeolites 13X and 4A, and ETS-10 exhibit Type I isotherms (Fig. 4.8), adsorbing higher amounts of water at low relative pressures; the adsorption isotherms reach a *plateau* at a low relative pressures, after which W_{eq} becomes almost independent of pressure. These equilibrium adsorption features, together with their temperature dependency (important for good adsorbent regeneration upon heating), lead to higher ΔW_{eq} and hence better heating performances than in the case of silica gel. Despite the less demanding regeneration of ETS-10 and its lower heat of adsorption in comparison to classical aluminosilicates [15], zeolites, particularly 13X, led to higher ΔW_{eq} , contributing to superior heating performance (Table 4.5 and Fig. 4.7). These results are in agreement with those reported by Tatlier *et al.* [10] for various zeolites, which pointed out 13X with superior performance for adsorption heat pumping applications, due to its higher water adsorption capacity.

Concerning heating applications, for given evaporator and regeneration temperatures, the higher the desired heating temperature (T_{cond}) the lower the maximum P/P_0 achieved in isobaric adsorption (considering $T_{\text{cond}} = T_{\text{min,cycle}}$) and the higher the minimum P/P_0 achieved in the isobaric desorption. On the other hand, a steep increase of the adsorbate loading at low P/P_0 implies high heats of adsorption and also high heat source temperatures, which may not be available in the most of the applications [9, 13].

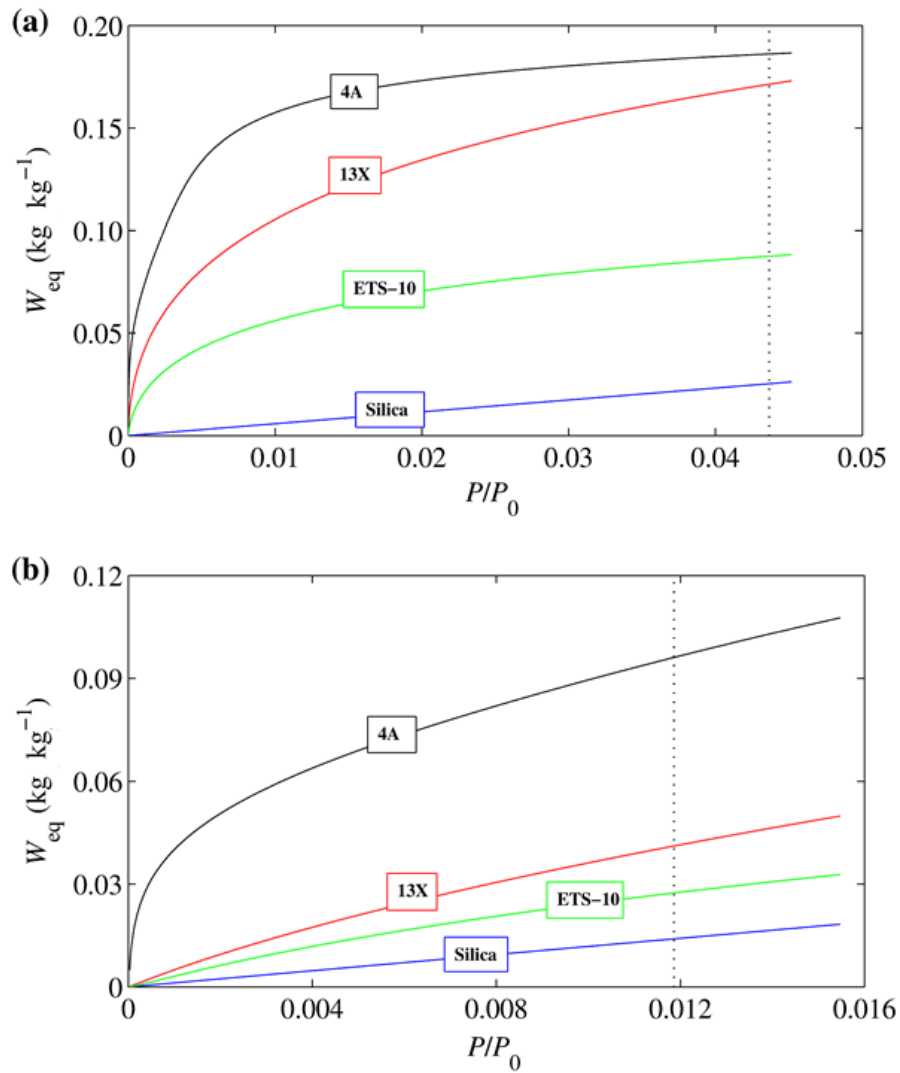


Fig. 4.8 - (a) Water adsorption isotherms of zeolite 13X (—), zeolite 4A (—), ETS-10 (—) and silica gel (—) at 333 K; the vertical line (--) is the maximum relative pressure achieved in the isobaric adsorption ($\frac{P}{P_0} = \frac{P_{\text{evap}}}{P_{\text{sat}}(T_{\text{min,cycle}=333 \text{ K}})} = 0.0437$). (b) Water adsorption isotherms of zeolite 13X (—), zeolite 4A (—) and ETS-10 (—) at 473 K and of silica gel (—) at 423 K; the vertical line (--) is the minimum relative pressure achieved in the isobaric desorption when using zeolite 13X, 4A and ETS-10 ($\frac{P}{P_0} = \frac{P_{\text{cond}}}{P_{\text{sat}}(T_{\text{max,cycle}=473 \text{ K}})} = 0.0119$).

4.3.2.1. Effect of using constant or variable thermal conductivity

The impact of considering constant or variable $\lambda_{\text{eff,s}}$ along the cycle was studied for the case of zeolite 4A/water pair. The simulation results showed no differences in COP and only 4.6 % variation in SHP (details are given in Annex A4, Section A4.3). Accordingly,

the usage of a constant $\lambda_{\text{eff},s}$ seems a fairly good approach to estimate the performance of AHSs.

4.3.2.2. Effect of using constant or variable Q_{ads}

The isosteric heat of adsorption decreases as the adsorbate loading increases, as explained by Saha *et al.* [32] for Maxsorb III/n-butane pair, considering the mechanism of the diffusion of n-butane in the pores of the adsorbent. Conventional zeolites and ETS-10 possess micropores with different sizes, and the adsorbate molecules may primarily penetrate into the narrower ones, resulting in stronger interaction between the adsorbate and the adsorbent, and hence higher Q_{ads} at lower loadings. When the smaller micropores are completely full, the adsorbate is gradually accommodated in the larger ones, in which the average adsorption affinity becomes weaker, leading to lower Q_{ads} with increasing W [31, 32]. Literature on modeling and simulation studies of adsorption refrigeration systems reports on the usage of a constant Q_{ads} [16, 47], or the calculation of Q_{ads} as a function of W [24, 35].

The impact of using constant or variable Q_{ads} (dependence on W) in modeling the AHS was investigated for zeolites 13X, 4A and for ETS-10, using the values in Table 4.4 or the equations in Table 4.3, respectively. The results of COP and SHP for each adsorbent were: (i) zeolite 13X: 1.49 and 1242 W kg⁻¹, respectively; (ii) zeolite 4A: 1.41 and 1261 W kg⁻¹, respectively; (iii) ETS-10: 1.36 and 769 W kg⁻¹, respectively. These results are similar to those obtained considering constant Q_{ads} (Table 4.5). Hence, the usage of a constant Q_{ads} seems a fairly good approach to estimate the performance of AHSs.

4.3.2.3. Modeling the intraparticle mass transfer kinetics

4.3.2.3.1. Effect of assuming $D_{\text{eff}} = D_{\text{eff}}(T, W)$ in the simulations

Fig. 4.9 shows the variation of D_{eff} and K_{LDF} of zeolite 13X/water pair over four adsorption cycles, calculated by Eqs. (4.25) and (4.2), respectively (corresponding heating performance results are given in Table 4.5).

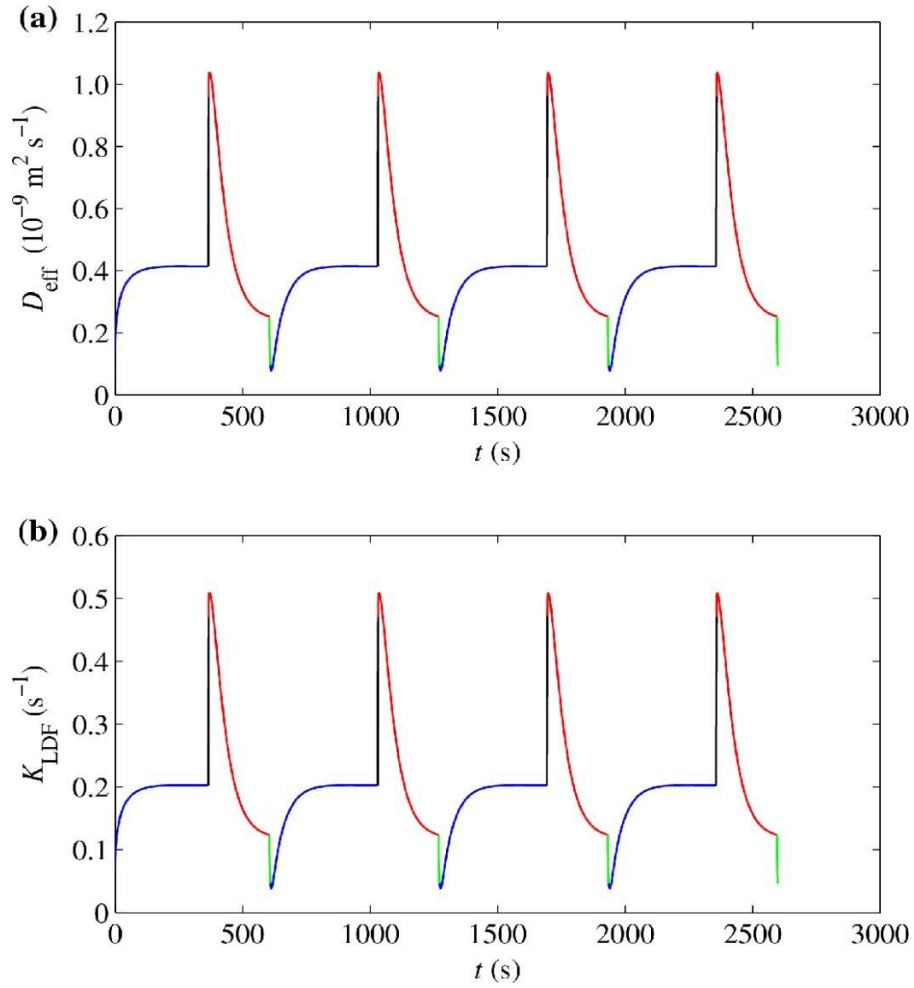


Fig. 4.9 - (a) D_{eff} vs. time curves and (b) variation of K_{LDF} along time for each stage of the heating cycle, for zeolite 13X/water pair. (—) Isobaric adsorption, (—) Isobaric desorption, (—) Isosteric heating, (—) Isosteric cooling. Average adsorbate loadings (\bar{W}) and average temperatures (\bar{T}) were considered in Eq. (4.25) to calculate the D_{eff} values in (a), and K_{LDF} dependence on time (b) was then calculated using Eq. (4.2).

During a whole cycle, D_{eff} and K_{LDF} vary in the range 0.1×10^{-9} – $1.0 \times 10^{-9} \text{ m}^2 \text{ s}^{-1}$, and $0.04 - 0.5 \text{ s}^{-1}$, respectively. During isobaric adsorption, where temperature decreases and W increases, D_{eff} and K_{LDF} initially increase with time, as a result of incrementing W , reaching a constant value near the half time of the stage. The *plateau* is reached when W is close to the corresponding half coverage, which is somewhat in accordance with the Type IV profile of D_{eff} versus W obtained for zeolite 13X/water pair. On the other hand, during isobaric desorption, the kinetics parameters initially increase and then start to decrease until the end of the stage, owing to the impact of the W decrease. The turnover of the D_{eff} and K_{LDF} versus t curves occurs when W approximates the half coverage. During isosteric stages, since W is practically unchanged, D_{eff} and K_{LDF} variations are attributed to the

sharp increase (isosteric heating) or decrease (isosteric cooling) of the temperature of the bed.

Fig. 4.10 shows the values of $D_{\text{eff}} = D_{\text{eff}}(T, W)$ obtained for zeolite 4A/water over 3 cycles, which are consistently lower than those for zeolite 13X/water pair, ranging from 1.9×10^{-10} to $8.2 \times 10^{-11} \text{ m}^2 \text{ s}^{-1}$ due to the smaller pore sizes of the former adsorbent ($4.1 \times 4.1 \text{ \AA}$ for zeolite 4A, and $7.4 \times 7.4 \text{ \AA}$ for 13X [48]).

The heating performance of zeolite 4A/water pair was evaluated using an Arrhenius equation to describe D_{eff} solely as a function of temperature, as reported by Tatlier *et al.* [10]. The *COP* and *SHP* (1.40 and 1334 W kg^{-1} , respectively) were similar to those obtained using $D_{\text{eff}} = D_{\text{eff}}(T, W)$ (Table 4.5).

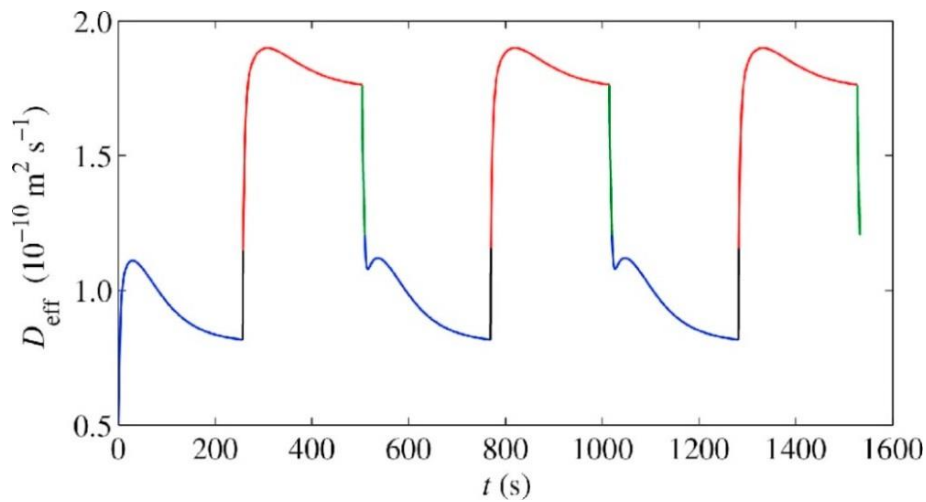


Fig. 4.10 - D_{eff} versus time curve for each stage of the cycle, for zeolite 4A/water pair. (—) Isobaric adsorption, (—) Isosteric heating, (—) Isobaric desorption, (—) Isosteric cooling. Average adsorbate loadings (\bar{W}) and average temperatures (\bar{T}) were considered in Eq. (4.26) to calculate the D_{eff} values.

4.3.2.3.2. Effect of using a constant K_{LDF} in the simulations

In order to evaluate the impact of using a constant K_{LDF} in the simulations, an average between the maximum and the minimum values achieved during the adsorption cycle was considered for both zeolites 13X and 4A. Table 4.6 shows the average K_{LDF} values used and the results of heating performance obtained for each pair. Comparing the results in

Tables 4.5 and 4.6, neither t_{cycle} and $\Delta\bar{W}_{\text{cycle}}$, nor COP and SHP present major differences. Thus, it seems that the use of a constant K_{LDF} does not compromise the performance estimations, which is in accordance with the data reported by Zhong *et al.* [40].

Table 4.6 – Average value of K_{LDF} considered in the simulations for the operating conditions under study and corresponding results obtained from the simulations of zeolite 13X/water and zeolite 4A/water pairs.

Adsorbent	$K_{\text{LDF}}^{(a)}$ (s^{-1})	t_{cycle} (s)	$\Delta\bar{W}_{\text{cycle}}$ (kg kg^{-1})	COP	SHP (W kg^{-1})
Zeolite 13X	0.273	654	0.126	1.48	1255
Zeolite 4A	0.067	509	0.0871	1.40	1258

^(a) Average between the maximum and the minimum values achieved during the whole adsorption cycle.

4.3.3. Sensitivity study - effect of the particle size on the performance of the AHS

The particle size is an important factor influencing the performance of an AHS, since it impacts directly on the internal mass transfer kinetics (K_{LDF}) and on the vapor permeability within the bed (K). Fig. 4.6 compares the operational cycles of the AHS using zeolite 13X/water pair for $d_p = 2.0 \times 10^{-4}$, 3.5×10^{-4} , and 6.0×10^{-4} m. The major differences appear in the isobaric adsorption stage for smaller d_p , which is associated with lower vapor permeability values ($K = 4.74 \times 10^{-11}$, 1.45×10^{-10} and $4.27 \times 10^{-10} \text{m}^2$ for $d_p = 2.0 \times 10^{-4}$, 3.5×10^{-4} and 6.0×10^{-4} m, respectively), leading to higher pressure drop. The pie charts (Fig. 4.6) show that the cycle times for $d_p = 2.0 \times 10^{-4}$ and 3.5×10^{-4} m are similar, while for $d_p = 6.0 \times 10^{-4}$ m the time increases slightly.

Fig. 4.11 shows the evolution of the average adsorbate loading (\bar{W}) during the first four cycles for each above-mentioned d_p .

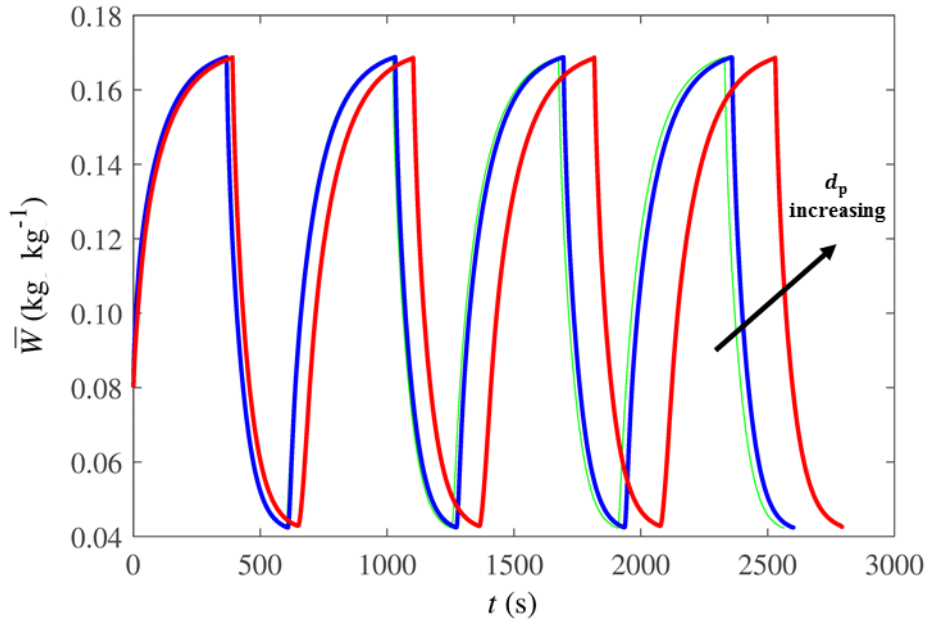


Fig. 4.11 - Evolution of the average water loading (\bar{W}) in zeolite 13X, during the first four cycles, for three distinct particle sizes ($- d_p = 2.0 \times 10^{-4}$ m, $- d_p = 3.5 \times 10^{-4}$ m, $- d_p = 6.0 \times 10^{-4}$ m). Increasing and decreasing \bar{W} branches with time correspond to the isobaric adsorption and desorption stages, respectively.

Concerning the internal mass transfer resistances, Fig. 4.11 shows that the higher the d_p , the slower the kinetics, in accordance with Eq. (4.2). For example, for $t = 2000$ s, while in the cases of $d_p = 2.0 \times 10^{-4}$ and 3.5×10^{-4} m the fourth adsorption stage is ongoing, for $d_p = 6.0 \times 10^{-4}$ m, the bed is ending the isobaric desorption of the third cycle. The slower kinetics for $d_p = 6.0 \times 10^{-4}$ m is consistent with the increased cycle time observed in Fig. 4.6. The results obtained for the heating performance were: for $d_p = 2.0 \times 10^{-4}$ m, $COP = 1.48$ and $SHP = 1254$ W kg $^{-1}$; for $d_p = 6.0 \times 10^{-4}$ m, $COP = 1.48$ and $SHP = 1141$ W kg $^{-1}$. Comparing with the results obtained for $d_p = 3.5 \times 10^{-4}$ m (Table 4.5), COP values are equal and SHP values differ less than 10 %. Overall, it seems that the variation of d_p in the range $2.0 \times 10^{-4} - 6.0 \times 10^{-4}$ m has no drastic influence on the performance of the AHS. These results are somewhat in agreement with those reported by Leong *et al.* [16]; the variation of d_p in the range $1.0 \times 10^{-4} - 5.0 \times 10^{-4}$ m had a negligible effect on the performance of cooling cycles, because the intraparticle mass transfer resistance was counterbalanced by the opposite effect of vapor permeability in the bed.

4.4. Conclusions

Modeling and simulation studies were carried out in order to compare the performances of different porous metal/metalloid oxides - zeolite 13X, zeolite 4A, ETS-10 and silica gel - for adsorption heating applications using water as refrigerant. The AHS using zeolite 13X/water pair seemed most promising for the production of heat at 333 K considering a regeneration temperature of 473 K, presenting a cycle time of 666 s, $COP = 1.48$, $SHP = 1232 \text{ W kg}^{-1}$, as well as higher heat generation per cycle. The superior overall heating performance of this pair can be partly explained by the favourable shape of the isotherms (Type I) for the required operating conditions (high condenser temperature).

In order to evaluate the impact of important equilibrium, kinetic and thermophysical parameters on the performance of an AHS, simulation studies were carried out to gain insights into the influence of using: (i) a constant or variable $\lambda_{\text{eff},s}$; (ii) a constant value of Q_{ads} or a Q_{ads} versus W dependence; (iii) D_{eff} as a function of both temperature and loading in the calculation of K_{LDF} ; (iv) a constant K_{LDF} value in the whole adsorption cycle. These studies indicated that the use of constant Q_{ads} , approximately the value corresponding to half coverage, provides reliable estimations of the performance of the AHSs. Despite the dependence of D_{eff} on temperature and adsorbate loading, it was shown that the use of an average constant value of K_{LDF} is sufficient to predict the heating performance of adsorption systems. These two simplifications are very helpful to accomplish AHSs simulations with inferior computational and numerical effort, while ensuring similarly accurate results.

A sensitivity study was carried out in order to investigate the impact of varying the particle size on the overall performance of the AHS using zeolite 13X/water pair. It was shown that a variation of d_p in the range $2.0 \times 10^{-4} - 6.0 \times 10^{-4} \text{ m}$ has no significant impact on the COP and SHP values of the AHS. The enhanced intraparticle transport with decreasing d_p is levelled-off by the reduction of vapor permeability through the bed.

Nomenclature

a	External surface area of adsorbent per unit bed volume ($\text{m}^2 \text{m}^{-3}$)
AARD	$= \frac{\sum_{i=1}^n \left \frac{\text{value}_{\text{calculated},i} - \text{value}_{\text{experimental},i}}{\text{value}_{\text{experimental},i}} \right }{N_{\text{data}}}$ Average Absolute Relative Deviation (%)
C	Parameter of Dubinin-Astakhov isotherm
C_p	Specific heat capacity ($\text{J kg}^{-1} \text{K}^{-1}$)
COP	Coefficient of performance
d_p	Adsorbent particle diameter (m)
D_{eff}	Effective diffusivity ($\text{m}^2 \text{s}^{-1}$)
h_{sv}	Solid/vapor convective heat transfer coefficient ($\text{W m}^{-2} \text{K}^{-1}$)
HTF	Heat transfer fluid
K	Permeability of the adsorbent bed (m^2)
K_{LDF}	Intraparticle mass transfer coefficient (s^{-1})
m	Mass (kg)
M	Molar mass of adsorbate (kg mol^{-1})
n	Parameter of Dubinin-Astakhov isotherm
Nu	Nusselt number
P	Pressure (Pa)
Pr	Prandtl number
Q	Heat (J)
Q_{ads}	Isosteric heat of adsorption (J kg^{-1})
r	Spatial coordinate (m)
R	Radial position in the adsorbent bed (m)
\mathfrak{R}	Universal gas constant ($\text{J mol}^{-1} \text{K}^{-1}$).
R_p	Adsorbent particle radius (m)
Re	Reynolds number
SHP	Specific heating power (W kg^{-1})
t	Time (s)
t_{cycle}	Cycle time (s)

Chapter 4: Comparison of different porous metal/metalloid oxides

T	Temperature (K)
u	Fluid superficial velocity (m s^{-1})
W	Adsorbate loading (kg kg^{-1})
W_0	Adsorbate loading at saturation temperature (kg kg^{-1})

Greek symbols

ΔH_v	Latent heat of evaporation (J kg^{-1})
$\Delta \bar{W}_{\text{cycle}}$	Cyclic adsorption loading swing (kg kg^{-1})
η	Dynamic viscosity ($\text{kg m}^{-1} \text{s}^{-1}$)
ε_b	Porosity of the bed
λ	Thermal conductivity ($\text{W m}^{-1} \text{K}^{-1}$)
ρ	Density (kg m^{-3})
φ	Generic notation of T , W and P
$\bar{\varphi}$	Generic notation of \bar{T} , \bar{W} and \bar{P}

Subscripts

a	Adsorbate
cond	Condenser
eff	Effective
eq	Equilibrium
evap	Evaporator
i	Internal boundary of the bed
ini	Initial
max	Maximum
min	Minimum
o	External boundary of the bed
s	Adsorbent
sat	Saturation
v	Vapor phase

References

- [1] B. Dawoud, On the development of an innovative gas-fired heating appliance based on a zeolite-water adsorption heat pump; system description and seasonal gas utilization efficiency, *Applied Thermal Engineering*, 72 (2014) 323-330.
- [2] H. Niazmand, H. Talebian, M. Mahdavihah, Effects of particle diameter on performance improvement of adsorption systems, *Applied Thermal Engineering*, 59 (2013) 243-252.
- [3] F. Meunier, Adsorption heat powered heat pumps, *Applied Thermal Engineering*, 61 (2013) 830-836.
- [4] B. Mette, H. Kerskes, H. Drück, H. Müller-Steinhagen, Experimental and numerical investigations on the water vapor adsorption isotherms and kinetics of binderless zeolite 13X, *International Journal of Heat and Mass Transfer*, 71 (2014) 555-561.
- [5] S. Narayanan, S. Yang, H. Kim, E.N. Wang, Optimization of adsorption processes for climate control and thermal energy storage, *International Journal of Heat and Mass Transfer*, 77 (2014) 288-300.
- [6] L.W. Wang, R.Z. Wang, R.G. Oliveira, A review on adsorption working pairs for refrigeration, *Renewable and Sustainable Energy Reviews*, 13 (2009) 518-534.
- [7] H. Demir, M. Mobedi, S. Ülkü, A review on adsorption heat pump: Problems and solutions, *Renewable and Sustainable Energy Reviews*, 12 (2008) 2381-2403.
- [8] D.C. Wang, Y.H. Li, D. Li, Y.Z. Xia, J.P. Zhang, A review on adsorption refrigeration technology and adsorption deterioration in physical adsorption systems, *Renewable and Sustainable Energy Reviews*, 14 (2010) 344-353.
- [9] S.K. Henninger, F.P. Schmidt, H.M. Henning, Water adsorption characteristics of novel materials for heat transformation applications, *Applied Thermal Engineering*, 30 (2010) 1692-1702.
- [10] M. Tatlier, B. Tantekin-Ersolmaz, A. Erdem-Şenatalar, A novel approach to enhance heat and mass transfer in adsorption heat pumps using the zeolite-water pair, *Microporous and Mesoporous Materials*, 27 (1999) 1-10.
- [11] G. Cacciola, G. Restuccia, Reversible adsorption heat pump: a thermodynamic model, *International Journal of Refrigeration*, 18 (1995) 100-106.
- [12] Z. Tamainot-Telto, R.E. Critoph, Monolithic carbon for sorption refrigeration and heat pump applications, *Applied Thermal Engineering*, 21 (2001) 37-52.
- [13] Y.I. Aristov, Challenging offers of material science for adsorption heat transformation: A review, *Applied Thermal Engineering*, 50 (2013) 1610-1618.
- [14] Y. Aristov, Concept of adsorbent optimal for adsorptive cooling/heating, *Applied Thermal Engineering*, 72 (2014) 166-175.
- [15] J.M. Pinheiro, A.A. Valente, S. Salústio, N. Ferreira, J. Rocha, C.M. Silva, Application of the novel ETS-10/water pair in cyclic adsorption heating processes: Measurement of equilibrium and kinetics properties and simulation studies, *Applied Thermal Engineering*, 87 (2015) 412-423.
- [16] K.C. Leong, Y. Liu, Numerical modeling of combined heat and mass transfer in the adsorbent bed of a zeolite/water cooling system, *Applied Thermal Engineering*, 24 (2004) 2359-2374.
- [17] Y.I. Aristov, Optimal adsorbent for adsorptive heat transformers: Dynamic considerations, *International Journal of Refrigeration*, 32 (2009) 675-686.

- [18] P. Demontis, H. Jobic, M.A. Gonzalez, G.B. Suffritti, Diffusion of Water in Zeolites NaX and NaY Studied by Quasi-Elastic Neutron Scattering and Computer Simulation, *The Journal of Physical Chemistry C*, 113 (2009) 12373-12379.
- [19] J.-Y. San, C.-C. Ni, S.-H. Hsu, Validity of solid-side mass diffusivity in simulation of water vapor adsorbed by silica gel in packed beds, *International Journal of Thermal Sciences*, 41 (2002) 41-49.
- [20] I.S. Glaznev, Y.I. Aristov, The effect of cycle boundary conditions and adsorbent grain size on the water sorption dynamics in adsorption chillers, *International Journal of Heat and Mass Transfer*, 53 (2010) 1893-1898.
- [21] B. Dawoud, M.I. Sohel, A. Freni, S. Vasta, G. Restuccia, On the effective thermal conductivity of wetted zeolite under the working conditions of an adsorption chiller, *Applied Thermal Engineering*, 31 (2011) 2241-2246.
- [22] A. Freni, M.M. Tokarev, G. Restuccia, A.G. Okunev, Y.I. Aristov, Thermal conductivity of selective water sorbents under the working conditions of a sorption chiller, *Applied Thermal Engineering*, 22 (2002) 1631-1642.
- [23] E. Tsotsas, H. Martin, Thermal conductivity of packed beds: A review, *Chemical Engineering and Processing: Process Intensification*, 22 (1987) 19-37.
- [24] İ. Solmuş, D.A.S. Rees, C. Yamalı, D. Baker, B. Kaftanoğlu, Numerical investigation of coupled heat and mass transfer inside the adsorbent bed of an adsorption cooling unit, *International Journal of Refrigeration*, 35 (2012) 652-662.
- [25] L. Marletta, G. Maggio, A. Freni, M. Ingrasciotta, G. Restuccia, A non-uniform temperature non-uniform pressure dynamic model of heat and mass transfer in compact adsorbent beds, *International Journal of Heat and Mass Transfer*, 45 (2002) 3321-3330.
- [26] J.O. Wilkes, S.G. Bibe, *Fluid Mechanics for Chemical Engineers*, 2nd ed., Prentice Hall PTR, New Jersey, 1999.
- [27] A. Bejan, *Convection Heat Transfer*, first ed., John Wiley & Sons, New York, 1984.
- [28] S. Middleman, *An Introduction to Mass and Heat Transfer: Principles of Analysis and Design*, 1st ed., John Wiley & Sons, New York, 1998.
- [29] W.E. Schiesser, *The Numerical Method of Lines: Integration of Partial Differential Equations*, 3rd ed., Academic Press, San Diego, 1991.
- [30] J.D. Hoffman, S. Frankel, *Numerical Methods for Engineers and Scientists*, second ed., Taylor & Francis, New York, 2001.
- [31] İ. Solmuş, C. Yamalı, B. Kaftanoğlu, D. Baker, A. Çağlar, Adsorption properties of a natural zeolite–water pair for use in adsorption cooling cycles, *Applied Energy*, 87 (2010) 2062-2067.
- [32] B.B. Saha, A. Chakraborty, S. Koyama, S.-H. Yoon, I. Mochida, M. Kumja, C. Yap, K.C. Ng, Isotherms and thermodynamics for the adsorption of n-butane on pitch based activated carbon, *International Journal of Heat and Mass Transfer*, 51 (2008) 1582-1589.
- [33] H.M. Garfinkel, S.M. Kuznicki, K.A. Thrush, Use of crystalline molecular sieves containing charged octahedral sites in cyclic desiccating processes, Eur. Patent 0544892B1, (1993).
- [34] R.C. Reid, J.M. Prausnitz, B.E. Poling, *The Properties of Gases and Liquids*, 4th ed., McGraw-Hill, New York, 1987.
- [35] G. Cacciola, G. Restuccia, G.H.W. van Benthem, Influence of the adsorber heat exchanger design on the performance of the heat pump system, *Applied Thermal Engineering*, 19 (1999) 255-269.

- [36] H.T. Chua, K.C. Ng, A. Chakraborty, N.M. Oo, M.A. Othman, Adsorption Characteristics of Silica Gel + Water Systems, *Journal of Chemical & Engineering Data*, 47 (2002) 1177-1181.
- [37] D.D. Duong, *Adsorption Analysis: Equilibria and Kinetics*, 1st ed., Imperial College Press, London, 1998.
- [38] H. Paoli, A. Méthivier, H. Jobic, C. Krause, H. Pfeifer, F. Stallmach, J. Kärger, Comparative QENS and PFG NMR diffusion studies of water in zeolite NaCaA, *Microporous and Mesoporous Materials*, 55 (2002) 147-158.
- [39] J. Kärger, H. Pfeifer, N.m.r. self-diffusion studies in zeolite science and technology, *Zeolites*, 7 (1987) 90-107.
- [40] Y. Zhong, T. Fang, K.L. Wert, An adsorption air conditioning system to integrate with the recent development of emission control for heavy-duty vehicles, *Energy*, 36 (2011) 4125-4135.
- [41] M.B. Jakubinek, B.-Z. Zhan, M.A. White, Temperature-dependent thermal conductivity of powdered zeolite NaX, *Microporous and Mesoporous Materials*, 103 (2007) 108-112.
- [42] L. Lv, Y. Zhang, K. Wang, A.K. Ray, X.S. Zhao, Modeling of the adsorption breakthrough behaviors of Pb²⁺ in a fixed bed of ETS-10 adsorbent, *Journal of Colloid and Interface Science*, 325 (2008) 57-63.
- [43] P. Malbrunot, D. Vidal, J. Vermesse, R. Chahine, T.K. Bose, Adsorbent Helium Density Measurement and Its Effect on Adsorption Isotherms at High Pressure, *Langmuir*, 13 (1997) 539-544.
- [44] E. Tsotsas, A.S. Mujumdar, *Modern Drying Technology, Energy Savings*, Wiley, 2011.
- [45] C.W. Chan, J. Ling-Chin, A.P. Roskilly, Reprint of "A review of chemical heat pumps, thermodynamic cycles and thermal energy storage technologies for low grade heat utilisation", *Applied Thermal Engineering*, 53 (2013) 160-176.
- [46] G. Restuccia, G. Cacciola, Performances of adsorption systems for ambient heating and air conditioning, *International Journal of Refrigeration*, 22 (1999) 18-26.
- [47] L. Yong, K. Sumathy, Comparison between heat transfer and heat mass transfer models for transportation process in an adsorbent bed, *International Journal of Heat and Mass Transfer*, 47 (2004) 1587-1598.
- [48] C. Baerlocher, L.B. McCusker, D.H. Olson, *Atlas of Zeolite Framework Types*, Elsevier Science, 2007.

Annex A4

A4.1. Stopping criteria applied in the simulation studies

Different stopping criteria were applied for the four steps of the heating cycle. For the isobaric adsorption and desorption stages, the integration was stopped when the average temperature of the bed (\bar{T}) was approximately equal to the outer boundary condition imposed in terms of temperature ($\bar{T} = T_{\text{HTF,cool}}$ for adsorption, and $\bar{T} = T_{\text{HTF,hot}}$ for the regeneration; tolerance of 1 K). In the isosteric stages, the stopping criteria were defined in terms of pressure: the simulation stopped when the average pressure in the bed (\bar{P}) was equal to P_{cond} or P_{evap} in the isosteric heating and cooling stages, respectively.

A4.2. Effective thermal conductivity and specific heat capacity values used in the simulations

The effective thermal conductivity and specific heat capacity values considered for ETS-10 were previously reported for the temperature range 293-413 [1].

Specific heat capacity of zeolite 13X was taken from ref. [2] (no details were given on the bed conditions at which the value was measured/estimated). The effective thermal conductivity of zeolite 13X was based on measurements reported by Jakubinek *et al.* [3] for evacuated packed beds ($P < 10^{-5}$ kPa); the value $0.20 \text{ W m}^{-1} \text{ K}^{-1}$ is the average of the value $\sim 0.167 \text{ W m}^{-1} \text{ K}^{-1}$ at 333 K (Fig. 2 of ref. [3]) and *ca.* $0.223 \text{ W m}^{-1} \text{ K}^{-1}$ at 473 K (obtained by linear extrapolation using the data published by Jakubinek *et al.* [3] (see Fig. A4.1)). The values for different conditions differ *ca.* 11-17 % of the used average value.

For zeolite 4A, the specific heat capacity was that reported by Zhong *et al.* [4] (no details were given on the bed conditions at which the value was measured/estimated). The effective thermal conductivity of zeolite 4A used in the simulations ($0.20 \text{ W m}^{-1} \text{ K}^{-1}$) is the average of the value at 333 K and 870 Pa (*ca.* $0.182 \text{ W m}^{-1} \text{ K}^{-1}$), and the value at 473 K and 19921 Pa ($\lambda_{\text{eff,s}} \sim 0.225 \text{ W m}^{-1} \text{ K}^{-1}$) reported by Dawoud *et al.* [5] (see thermal

conductivity chart for wet 4A, in Fig. 6 of that work). The values for different conditions differ *ca.* 9-12 % of the used average value.

Regarding silica gel, the two thermophysical parameters were taken from ref. [6] (no details were given on the bed conditions at which the value was measured/estimated; it was reported that the values were indicated by the supplier).

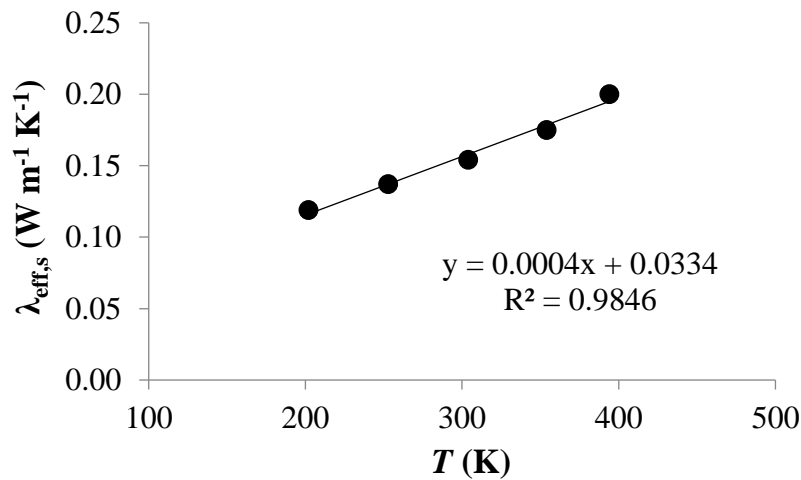


Fig. A4.1 – Effective thermal conductivity of zeolite 13X as a function of temperature. Data measured by Jakubinek *et al.* [3] (•) and linear fitting performed in this work (-).

A4.2.1. Effect of constant or variable $\lambda_{\text{eff},s}$ along the adsorption heating cycle

The mathematical lumped dependencies of $\lambda_{\text{eff},s}$ on temperature for zeolite 4A/water under the operating conditions of interest ($T_{\text{evap}} = 278$ K, $T_{\text{cond}} = T_{\text{min,cycle}} = 333$ K and $T_{\text{max,cycle}} = 473$ K) were obtained using data from Dawoud *et al.* [5] (see Fig. 6 of that work), and are shown in Fig. A4.2 (ideal cycle conditions were assumed). The introduction of $\lambda_{\text{eff},s} = f(T)$ in the simulations was performed by manipulating the energy balance to the adsorbent (Eq. (4.3), Table 4.1) as follows:

$$\frac{1}{r} \frac{\partial}{\partial r} \left(r \lambda_{\text{eff},s} \frac{\partial T_s}{\partial r} \right) = \frac{\lambda_{\text{eff},s}}{r} \frac{\partial T_s}{\partial r} + \frac{\partial \lambda_{\text{eff},s}}{\partial r} \frac{\partial T_s}{\partial r} + \lambda_{\text{eff},s} \frac{\partial^2 T_s}{\partial r^2} \quad (\text{A4.1})$$

where,

$$\frac{\partial \lambda_{\text{eff},s}}{\partial r} = 3.56 \times 10^{-5} \frac{\partial T_s}{\partial r} \quad - \text{ Isobaric adsorption stage}$$

$$\frac{\partial \lambda_{\text{eff},s}}{\partial r} = 4.80 \times 10^{-4} \frac{\partial T_s}{\partial r} \quad - \text{ Isosteric heating stage}$$

$$\frac{\partial \lambda_{\text{eff},s}}{\partial r} = 1.63 \times 10^{-4} \frac{\partial T_s}{\partial r} \quad - \text{ Isobaric desorption stage}$$

$$\frac{\partial \lambda_{\text{eff},s}}{\partial r} = 4.77 \times 10^{-4} \frac{\partial T_s}{\partial r} \quad - \text{ Isosteric cooling stage}$$

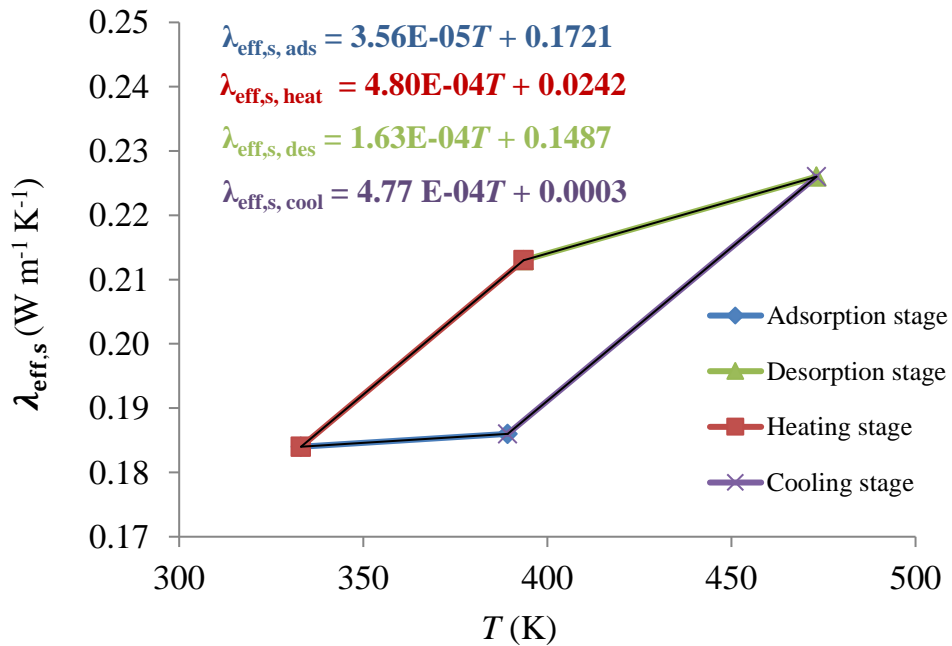


Fig. A4.2 – Variation of $\lambda_{\text{eff},s}$ along the ideal adsorption heating cycle of zeolite 4A/water pair, for $T_{\text{evap}} = 278$ K, $T_{\text{cond}} = T_{\text{min,cycle}} = 333$ K and $T_{\text{max,cycle}} = 473$ K, here expressed as function of temperature, on the basis of data from ref. [5].

The simulated results are given in Table A4.1 and show no major differences in the estimated *COP* and *SHp* values (< 5 %).

Table A4.1 - Results obtained for the heating performance of zeolite 4A/water pair considering constant and variable $\lambda_{\text{eff},s}$ in the simulations, at $T_{\text{evap}} = 278$ K, $T_{\text{cond}} = T_{\text{min,cycle}} = 333$ K and $T_{\text{max,cycle}} = 473$ K (K_{LDF} and Q_{ads} are assumed constant).

$\lambda_{\text{eff},s}$	t_{cycle} (s)	$\Delta\bar{W}_{\text{cycle}}$ (kg kg ⁻¹)	<i>COP</i>	<i>SHP</i> (W kg ⁻¹)
Constant ^(a)	509	0.0871	1.40	1258
Variable ^(b)	486	0.0869	1.40	1316

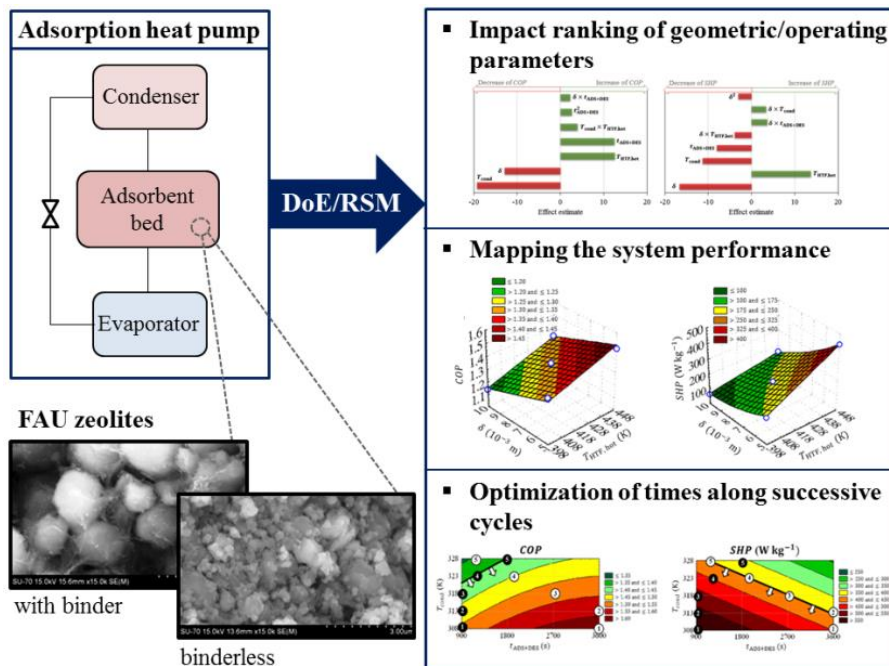
^(a) Data given in Table 4.6. ^(b) Linear relations presented in Fig. A4.2.

References

- [1] J.M. Pinheiro, A.A. Valente, S. Salústio, N. Ferreira, J. Rocha, C.M. Silva, Application of the novel ETS-10/water pair in cyclic adsorption heating processes: Measurement of equilibrium and kinetics properties and simulation studies, *Applied Thermal Engineering* 87 (2015) 412-423.
- [2] K.C. Leong, Y. Liu, Numerical modeling of combined heat and mass transfer in the adsorbent bed of a zeolite/water cooling system, *Applied Thermal Engineering* 24 (2004) 2359-2374.
- [3] M.B. Jakubinek, B.-Z. Zhan, M.A. White, Temperature-dependent thermal conductivity of powdered zeolite NaX, *Microporous and Mesoporous Materials* 103 (2007) 108-112.
- [4] Y. Zhong, T. Fang, K.L. Wert, An adsorption air conditioning system to integrate with the recent development of emission control for heavy-duty vehicles, *Energy* 36 (2011) 4125-4135.
- [5] B. Dawoud, M.I. Sohel, A. Freni, S. Vasta, G. Restuccia, On the effective thermal conductivity of wetted zeolite under the working conditions of an adsorption chiller, *Applied Thermal Engineering* 31 (2011) 2241-2246.
- [6] H.T. Chua, K.C. Ng, A. Chakraborty, N.M. Oo, M.A. Othman, Adsorption Characteristics of Silica Gel + Water Systems, *Journal of Chemical & Engineering Data* 47 (2002) 1177-1181.

Chapter 5: Phenomenological modeling and statistical optimization[†]

The performance of commercial zeolites, with and without binder in its formulation (SYLOBEAD[®] MS C 548: 13X with binder; Köstrolith[®] 13XBFK and NaYBFK: 13X and NaY without binder, respectively), for water adsorption heating applications was compared in this work. Accounting for a Box-Behnken design with four factors (time of adsorption and desorption, $t_{\text{ADS+DES}}$; condensation temperature, T_{COND} ; heat source temperature, $T_{\text{HTF,hot}}$; bed thickness, δ) and three levels, a set of 25 simulations per adsorbent was accomplished, and the performance of the adsorption units was evaluated through the coefficient of performance (COP) and the specific heating power (SHP). The results suggested that the presence of the binder in the formulation of 13X does not penalize the zeolite performance significantly, and that NaYBFK is the most promising material. For the latter solid, statistical outcomes were analyzed and insights about their usefulness to optimize the design and operation of adsorption heat pumps are provided. Pareto charts displaying the impact ranking of the factors upon COP and SHP are discussed, and simple equations are provided for the expeditious estimation of both indicators. Such models were utilized to map system performance and to select optimal geometric/operating parameters that meet specific performance requirements.



[†] Based on:

J.M. Pinheiro, S. Salústio, A.A. Valente, C.M. Silva, Adsorption heat pump optimization by experimental design and response surface methodology, Applied Thermal Engineering, 138 (2018) 849-860.

5.1. Introduction

The increasing energy global demands, the dependency of modern society on fossil fuels and the need for reducing greenhouse gas emissions and ozone depletion have motivated the development of eco-friendly technologies based on renewable sources or powered by waste energy [1, 2]. Worldwide energy consumption for heating purposes in the building sector represents a significant portion of energy demands. In residential and commercial buildings, respectively, space heating accounts for 32 % and 33 % of the total energy use, while domestic hot water consumption represents 24 % and 12 % [3]. It is important to develop cost-effective technologies, allying energetic and environmental sustainability with market needs and human comfort. Focus has been put on cooling/heating technologies based on adsorption [4, 5] for the potential replacement of conventional vapor-compression systems (VCS), avoiding the negative impact of fluorocarbon type refrigerants through the usage of eco-friendly fluids such as water. Additionally, adsorption-based systems may be powered by renewable energy sources such as solar energy or waste heat (conversely, VCS use electricity), and present no noise nor vibration problems [2, 6, 7].

Adsorption cooling/heating systems, specifically adsorption heat pumps (AHPs), consist of four main units: an adsorbent heat exchanger (AHEX), condenser, evaporator and expansion valve [8]. The operating cycle of AHPs involves four stages: isobaric adsorption, isosteric heating, isobaric desorption and isosteric cooling [6, 9]. The efficiency and cost-effectiveness of AHPs are strongly influenced by the performance of the adsorbent/adsorbate working pairs. Several studies regarding the analysis of pairs for AHPs have been reported in the literature. For example, Boman *et al.* [10] analyzed approximately eighty pairs for heating applications, namely activated carbons with alcohols or ammonia as adsorbates, and MOFs/alcohols. Frazzica and Freni [11] investigated working pairs for solar thermal energy storage such as zeolite 13X/water, composites of multi-wall carbon nanotubes and LiCl for adsorption of water and methanol, and silica-alumina phosphate AQSOA[®] FAM-Z02/water, and concluded that the latter two pairs were promising for heating applications. Freni *et al.* [12] identified potential adsorbents using water as adsorbate and compared their heating performances, namely the composite LiBr-silica, silica-alumina phosphates SAPO-34 and AQSOA[®] FAM-Z02, and

standard commercial zeolite 4A, and obtained higher *COPs* for the composite and silica-alumina phosphates. The investigation of the composite adsorbents is essentially in an academic scope, which hinders the industrialization of AHPs incorporating these materials in the short to medium term. Regarding silica-alumina phosphates, a general issue is the high costs of the synthesis process in relation to standard commercial zeolites, and has not reached production in relatively large scale [12]. On the other hand, zeolites (crystalline microporous aluminosilicates) such as 4A and 13X are cheaper and widely available in the market, albeit their use in AHPs requires demanding regeneration conditions [12]. Zeolites are often commercialized as binder based granules, but the binder introduces passive mass in the AHEx, may reduce the adsorption capacity and hinder intraparticle mass transfer [13]. Aiming at materials with improved performances, the company Chemiewerk Bad Köstritz GmbH (CWK) developed binderless formulated zeolites of the type NaX, NaA and more recently NaY for thermochemical energy storage applications [14, 15], which exhibit improved water adsorption capacity and kinetics in comparison to conventional zeolite beads [13, 16]. Particularly, NaY zeolite presents a higher molar ratio Si/Al than NaX, which contributes to facilitated regeneration of the adsorbent [17].

In order to compete with VCS, AHPs require improvements in terms of coefficient of performance (*COP*), power per unit mass of adsorbent (specific heating power, *SHP*) and/or per unit AHEx volume (*VSHP*), and costs, as they are still too big and heavy appliances [18, 19]. Research and development priorities have been identified, which include novel adsorbents, compact AHEx designs, and advanced control strategies allowing the system to adapt to changes in operating conditions and user requirements [19]. The performance of AHPs is strongly dependent on the operating conditions (*e.g.*, cycle time, temperatures of condensation and adsorbent regeneration) and geometric factors (for instance, adsorbent configuration - coatings or loose grains - and bed thickness) [6, 20-24]. The cycle time, for instance, may impact conversely on *COP* and power [25-27], which turns it an important optimization parameter. Nonetheless, the study of AHPs is difficult due to the high complexity of the heat, mass and momentum transfer phenomena occurring simultaneously in the adsorbent bed [28], and to the challenging optimization of the system to fit variable working conditions or thermal demands [29].

The optimization of the AHP's design and operation can be performed using phenomenological models (usually coupled with complex numerical optimization tools)

[28-35], experimental setups/prototypes [18, 36-39] or a combination of both [40, 41], which may often become a difficult and lengthy task. Specifically, (i) it may be very time consuming, since a significant number of experiments or delayed simulations may be necessary to determine optimal parameters in a broad range of conditions; (ii) it may be very complex or even impossible to identify optimal combinations of operating/geometric parameters to meet pre-established performance requisites; (iii) assessing the impact ranking of several parameters on the performance may not be straightforward. In this regard, statistical methodologies can be combined with phenomenological modeling or experiments in order to perform optimizations much more easily and efficiently.

The design of experiments (DoE) and response surface methodology (RSM) are powerful statistical tools to help identify the main factors and interactions influencing key indicators of a process and for performing expeditious optimizations [7, 42]. These tools are versatile and have been used in distinct fields, allowing a considerable reduction of the number of experiments or simulations required for establishing optimal conditions; *e.g.*, chromatography [43], supercritical fluid extraction [44], coagulation-ultrafiltration for drinking water treatment [45], and synthesis of materials [46]. Despite the great potential of these methodologies, very few studies were related to adsorption-based technologies (and aimed specifically at cooling applications) [7, 8, 42, 47].

This work comprehends two distinct parts. Firstly, formulated zeolites with FAU topologies, specifically binderless zeolite NaY (Köstrolith® NAYBFK) and 13X (Köstrolith® 13XBFK) from Chemiewerk Bad Köstritz GmbH (CWK), and binder-containing 13X (SYLOBEAD® MS C 548, denoted by 13XB for simplicity) from Grace were compared through modeling and simulation for adsorption heating applications, using water as adsorbate. The necessary data for the AHPs simulations included: isosteric heats of adsorption (Q_{ads}) assessed from experimental water adsorption isotherms; thermal conductivities ($\lambda_{eff,s}$) of the adsorbents determined as function of temperature; measured solid densities (ρ_s). The cyclic adsorption process was simulated accounting for a Box-Behnken design with four factors and three levels per factor: time of adsorption and desorption steps ($t_{ADS+DES}$), temperature of condensation (T_{COND}), temperature of the heat transfer fluid (HTF) in the desorption stage ($T_{HTF,hot}$), and bed thickness (δ). In the second part of this work, the statistical outcomes from DoE/RSM were analyzed, as: Pareto charts for assessing concomitant impact of operating/geometric parameters on *COP* and *SHP*, and

polynomial equations for expeditious performance predictions as function of the factors (and *vice-versa*). Insights into the usefulness of these outcomes for the optimization of AHEx designs and control strategies of AHPs are provided for NaYBFK, which was the best material found in terms of both *COP* and *SHP*.

5.2. Materials and methods

Zeolite NaY (Köstrolith® NaYBFK) was kindly provided by Chemiewerk Bad Köstritz GmbH (CWK), which also commercializes 13X (Köstrolith® 13XBFK). The material 13XB (SYLOBEAD® MS C 548) contains a mineral clay binder (inorganic), and was kindly provided by Grace.

The density (ρ_s) of NaYBFK and 13XB was measured by helium pycnometry using a Quantachrome Multipycnometer after pre-treatment of the powders at 473 K during 150 min (*ca.* 4 % error).

Pellets of NaYBFK and 13XB with 1 cm diameter and 0.5 cm thickness were prepared to measure the effective thermal conductivities ($\lambda_{\text{eff},s}$) of the solid in the range 298.15–388.15 K, using the Gustafsson Probe method (or hot disk [48]) with a thermal constant analyzer TPS 2500S, and the samples temperature was controlled using a Thermo Scientific AC 200 immersion circulator. Prior to the data recording at a given temperature, the samples were maintained at constant temperature during 30 min. The accuracy of the measurements is *ca.* 5 %.

5.3. System description and mathematical modeling

5.3.1. Adsorbent Heat Exchanger (AHEx) geometry

The simulations were performed for the AHEx unit schematically shown in Fig. 5.1. Amongst various designs reported in the literature [49], this simple geometry was chosen since it is representative for modeling and simulation, and well-studied in the literature [21,

35, 50], allowing to correctly evaluate trends and compare distinct adsorbent/adsorbate pairs.

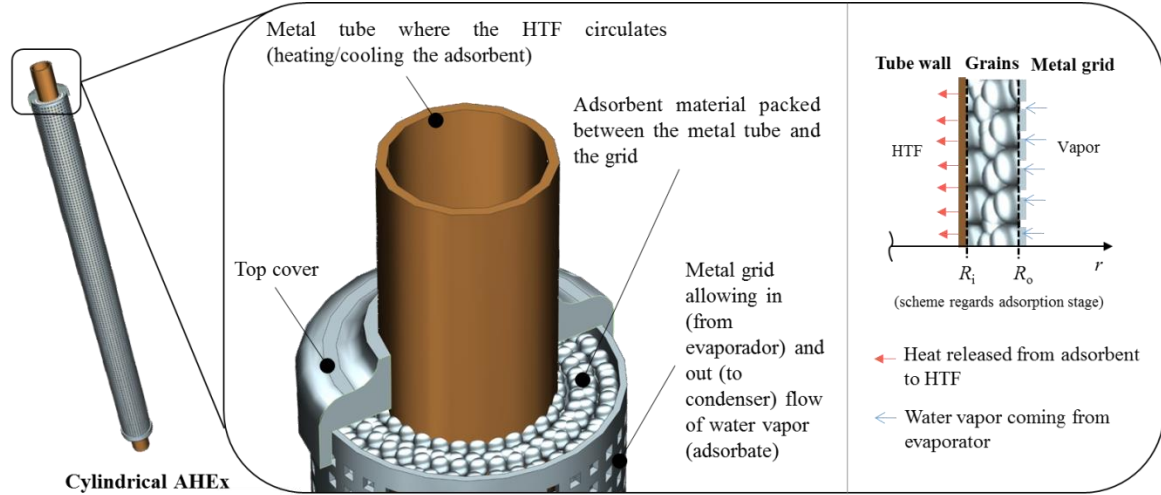


Fig. 5.1 - Schematic representation of the cylindrical adsorbent heat exchanger (AHEx) studied in this work.

5.3.2. Modeling and performance indicators

The mathematical model of the unsteady state AHEx unit was written for a differential volume element of radial thickness dr , and contemplates the material balance to the bed, the material balance to the adsorbent particle given by the Linear Driving Force (LDF) model, the energy balances to the adsorbent and vapor, the equilibrium isotherms, and the momentum balance given by Darcy's law. The corresponding equations, assumptions, initial and boundary conditions, and numerical approach are given in the Annex A5 (Section A5.2). The adsorption isotherms for each working pair together with the linear driving force (LDF) model for mass transfer are given in Section 5.4.1.1 (Table 5.2, Eqs. (5.11)-(5.14)). The LDF model is an approximation to the material balance to the adsorbent particle, which, in its unapproximated form, embodies Fick's law [51]. Since it is simultaneously analytic, simple and physically consistent, the LDF model has been frequently and successfully used to describe gas and liquid adsorption kinetics [51-54]. Moreover, it has been successfully applied to describe intraparticle mass transfer kinetics

in a fixed bed adsorption process with zeolite Köstrolith® 13XBFK (used in this work) [55].

For assessing the overall heating performance of each pair, the coefficient of performance and the specific heating power were calculated as follows:

$$COP = \frac{|Q_{ADS} + Q_{cond} + Q_{COOL}|}{Q_{DES} + Q_{HEAT}} \quad (5.1)$$

$$SHP = \frac{|Q_{ADS} + Q_{cond} + Q_{COOL}|}{m_s t_{cycle}} \quad (5.2)$$

where Q_{ADS} , Q_{COOL} and Q_{cond} are, respectively, the heats released during isobaric adsorption, isosteric cooling and by the condenser, and Q_{DES} and Q_{HEAT} are the heats supplied to the bed during the isobaric desorption and isosteric heating stages, respectively; m_s is the mass of the adsorbent and t_{cycle} is the cycle time. The heats involved in the cycle were computed as follows:

$$Q_{ADS} = \int_{T_{ADS,ini}}^{T_{ADS,fin}} [m_s(C_{p,s} + \bar{W}C_{p,a})] d\bar{T} + \int_{\bar{W}_{min}}^{\bar{W}_{max}} m_s (-Q_{ads}) d\bar{W} \quad (5.3)$$

$$Q_{HEAT} = \int_{T_{HEAT,ini}}^{T_{HEAT,fin}} [m_s(C_{p,s} + \bar{W}C_{p,a})] d\bar{T} \quad (5.4)$$

$$Q_{DES} = \int_{T_{DES,ini}}^{T_{DES,fin}} [m_s(C_{p,s} + \bar{W}C_{p,a})] d\bar{T} + \left| \int_{\bar{W}_{max}}^{\bar{W}_{min}} m_s Q_{ads} d\bar{W} \right| \quad (5.5)$$

$$Q_{COOL} = \int_{T_{COOL,ini}}^{T_{COOL,fin}} [m_s(C_{p,s} + \bar{W}C_{p,a})] d\bar{T} \quad (5.6)$$

$$Q_{cond} = -m_s \Delta \bar{W}_{cycle} \Delta H_v, \quad \text{where } \Delta \bar{W}_{cycle} = \bar{W}_{max} - \bar{W}_{min} \quad (5.7)$$

where $C_{p,s}$ and $C_{p,a}$ are, respectively, the specific heat capacities of the adsorbent and adsorbate, Q_{ads} is the isosteric heat of adsorption, $\Delta \bar{W}_{cycle}$ is the cyclic average loading and ΔH_v is the latent heat of vaporization of the refrigerant. The mass of the metal components of the AHEx was not considered in Eqs. (5.3)-(5.6), in order to extract specific

information regarding the influence of distinct adsorbents. The metal contribution hinders *COP*, albeit the major *COP* trends may be similar with or without this contribution [56, 57].

The average temperature (\bar{T}), pressure (\bar{P}) and loading (\bar{W}) in the bed along time (generically denoted by $\bar{\varphi}$) were given by:

$$\bar{\varphi}(t) = \frac{\int_{R_i}^{R_o} 2r\varphi(t,r)dr}{(R_o^2 - R_i^2)} \quad (5.8)$$

where t denotes time, r is the spatial coordinate, and R_o and R_i are, respectively, the external and internal boundaries of the adsorbent bed (Fig. 5.1).

5.3.3. Design of experiments and response surface methodology (DoE/RSM)

DoE/RSM consists of a set of mathematical and statistical methods which fit empirical models to experimental data (or simulation results). For applying this technique, it is necessary to specify the factors (independent variables), the responses (dependent variables), the levels of the factors (degrees of variation), the experimental domain (minimum and maximum limits of the factors) and the experimental design method [58]. In this work, a Box-Behnken design was adopted, which is efficient and economical, requiring a number of simulations given by $N = 2k(k - 1) + cp$, where cp is the number of central points and k is the number of factors, and is adequate when data may present curvatures [58]. Due to the importance of both operating conditions and geometric parameters in the performance of AHPs, the statistical studies considered the time of the adsorption and desorption stages ($t_{\text{ADS+DES}}$), the condensation and heat source temperatures (T_{cond} and $T_{\text{HTF,hot}}$, respectively), and the bed thickness (δ), with three levels per factor, as summarized in Table 5.1. The values of the independent variables were codified according to Eq. (5.9), for ranging between -1 and 1:

$$X_k = \frac{x_k - x_0}{\Delta x_k} \quad (5.9)$$

where X_k and x_k are, respectively, the codified and real values of the independent variable, x_0 is its real value at the central point, and Δx_k is its step change.

Table 5.1 - Factors, levels and codification considered for the Box-Behnken design.

Factor	Level		
	Low (-1)	Medium (0)	High (+1)
$t_{\text{ADS+DES}}$ (s) ^(a)	900 (15 min)	2250 (37.5 min)	3600 (60 min)
T_{cond} (K)	308.15	318.15	328.15
$T_{\text{HTF,hot}}$ (K)	398.15	423.15	448.15
δ (m)	5×10^{-3}	7.5×10^{-3}	10×10^{-3}

^(a) Isobaric adsorption and desorption are the longest stages, therefore $t_{\text{ADS+DES}}$ is similar to t_{cycle} .

The T_{cond} is between 308.15 and 328.15 K, which allows the utilization of the heat produced by the AHP for hot water production, while $T_{\text{HTF,hot}}$ ranges from 398.15 K (which enables the use of water as HTF) to 448.15 K (that implies alternative HTFs such as thermal oils, due to pressure constraints in circuits).

The results submitted to the RSM analysis are usually well represented by a second order polynomial. In the case of our simulations, the same equations are adopted:

$$Y = \beta_0 + \sum_{i=1}^k \beta_i X_i + \sum_{i=1}^k \beta_{ii} X_i^2 + \sum_{1 \leq i < j}^k \beta_{ij} X_i X_j \quad (5.10)$$

where Y is the response (COP or SHP), X_i and X_j are the codified factors ($t_{\text{ADS+DES}}$, T_{cond} , $T_{\text{HTF,hot}}$, δ), β_0 is a constant including the residual, and β_i , β_{ii} and β_{ij} are model coefficients related to linear, quadratic and pair interaction effects, respectively.

STATISTICA software (version 5.1, StatSoft Inc., Tulsa, USA) was used for statistical modeling and treatment of the simulation results. An analysis of variance (ANOVA) was performed to assess the statistical significance of factors and interactions using Fisher's test and its associated probability level (p -value) for a confidence interval of 95 %. For judging

the significance of the estimated coefficients β_i , β_{ii} , β_{ij} , t -tests were performed. The coefficient of determination (R^2) and its adjusted value (R_{adj}^2) were used to evaluate the goodness of fit of the regression models.

5.4. Results and discussion

5.4.1. Measurement and determination of properties of NaYBFK and 13XB

The Dubinin-Astakhov model was fitted to equilibrium data of water vapor onto zeolites NaYBFK and 13XB, from which heats of adsorption were calculated, and the solid densities and temperature dependency of thermal conductivities were measured. For NaYBFK and 13XB, morphological data (SEM images) were obtained, and textural data (N_2 isotherms, and specific surface area and pore volume) are given in Annex A5 (Section A5.3.1), and for 13XB are reported in Schumann *et al.* [59]. The properties necessary for the simulations using the latter adsorbent were collected from Mette *et al.* [55].

5.4.1.1. Morphology, equilibrium isotherms, heats of adsorption and adsorption kinetics

Fig. 5.2 shows SEM images of NaYBFK and 13XB. For the latter, a binding compound (glue-like aspect) is observed between pseudo-spherical particles.

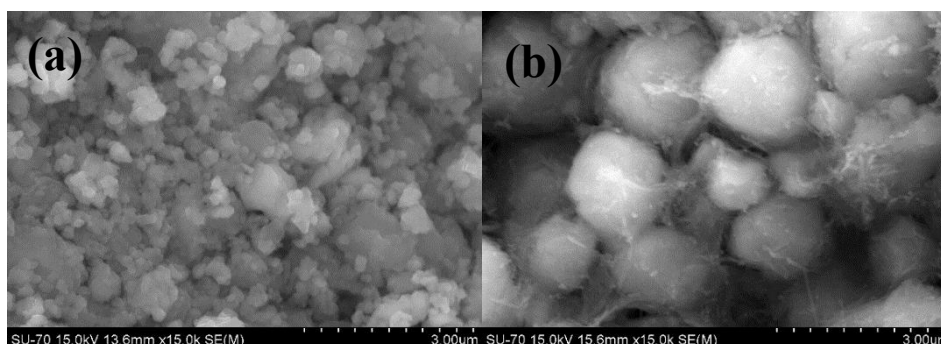


Fig. 5.2 - SEM images of (a) NaYBFK and (b) 13XB (crushed particle).

For 13XBFK, the water adsorption isotherm in the temperature range 298.15 – 523.15 K was taken from literature [55] (Eq. (5.11), Table 5.2). In the case of the other two adsorbents, the Dubinin-Astakhov (DA) model, often used to describe the adsorption equilibrium in zeolites and zeotypes [2, 55, 60], was accurately fitted to data provided by Chemiewerk Bad Köstritz GmbH (CWK) for NaYBFK in the range 298.15 – 353.15 K (Fig. 5.3), and to data from Grace for 13XB in the range 298.15 – 423.15 K (Fig. 5.4). For NaYBFK, the parameters of the model obtained by unconstrained nonlinear optimization are: $W_0 = 0.301 \text{ kg kg}^{-1}$, $C = 2.62 \times 10^{-8} \text{ K}^{-2.33}$ and $n = 2.33$ (see Eq. (5.12), Table 5.2), with an average absolute relative deviation (AARD) of 3.5 %. In the case of 13XB, they are: $W_0 = 0.231 \text{ kg kg}^{-1}$, $C = 6.28 \times 10^{-9} \text{ K}^{-2.41}$ and $n = 2.41$ (see Eq. (5.13), Table 5.2), with AARD = 6.2 %.

Table 5.2 - Dubinin-Astakhov (DA) isotherms of water vapor on 13XBFK, NaYBFK and 13XB, and expressions for the linear driving force (LDF) global coefficient (K_{LDF}).

Description	Equation	Eq.
13XBFK/water isotherm (DA model) ^(a,b)	$W_{\text{eq}} = 3.4103 \times 10^{-4} \rho_a \exp \left[- \left(\frac{\mathfrak{R}T}{1.1923 \times 10^6 M} \ln \frac{P_{\text{sat}}}{P} \right)^{1.55} \right],$ <p>where $\rho_a = \frac{\rho_{\text{water},293.15 \text{ K}}}{1 + \beta_{\text{water},293.15 \text{ K}}(T - 293.15)}$</p>	(5.11)
NaYBFK/water isotherm (DA model)	$W_{\text{eq}} = 0.301 \exp \left[-2.62 \times 10^{-8} \left(T \ln \frac{P_{\text{sat}}}{P} \right)^{2.33} \right]$	(5.12)
13XB /water isotherm (DA model)	$W_{\text{eq}} = 0.231 \exp \left[-6.28 \times 10^{-9} \left(T \ln \frac{P_{\text{sat}}}{P} \right)^{2.41} \right]$	(5.13)
Linear driving force (LDF) global mass transfer coefficient ^(c)	$K_{\text{LDF}} = \frac{\Omega D_{\text{eff}}}{R_p^2 H}, \text{ where } \Omega = 15 \text{ (for spheres),}$ $D_{\text{eff}} = \frac{\varepsilon_p}{\tau_p} \left(\frac{1}{D_K} + \frac{1}{D_m} \right)^{-1} \text{ and } H = \rho_p \frac{\mathfrak{R}T}{M} \frac{\partial W_{\text{eq}}}{\partial P}$	(5.14)

^(a) The $\beta_{\text{water},293.15 \text{ K}}$ is the thermal expansion coefficient of water at 293.15 K, which is $2.07 \times 10^{-4} \text{ K}^{-1}$ according with the Mugele model reported in Fig. 1(b) of ref. [61]. ^(b) The maximum loading (W_0) corresponds to the term $3.4103 \times 10^{-4} \rho_a$ (in kg kg^{-1}). ^(c) The equations for D_K and D_m are given in Annex A5 (Section A5.3.3.1).

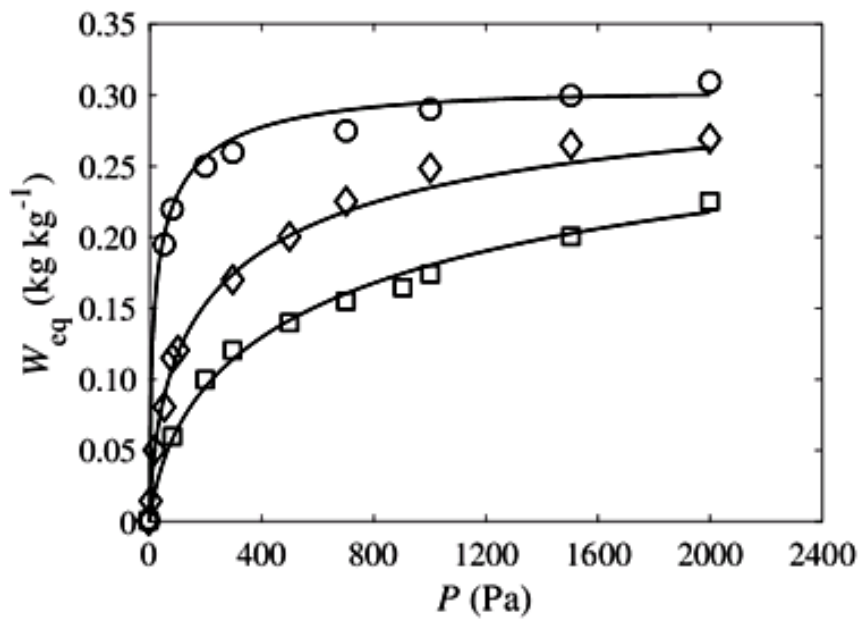


Fig. 5.3 - Adsorption isotherms of water vapor on zeolite NaYBFK: experimental data at 298.15 (o), 333.15 (◊) and 353.15 K (◻) provided by Chemiewerk Bad Köstritz GmbH (CWK); lines are the Dubinin-Astakhov model fitting.

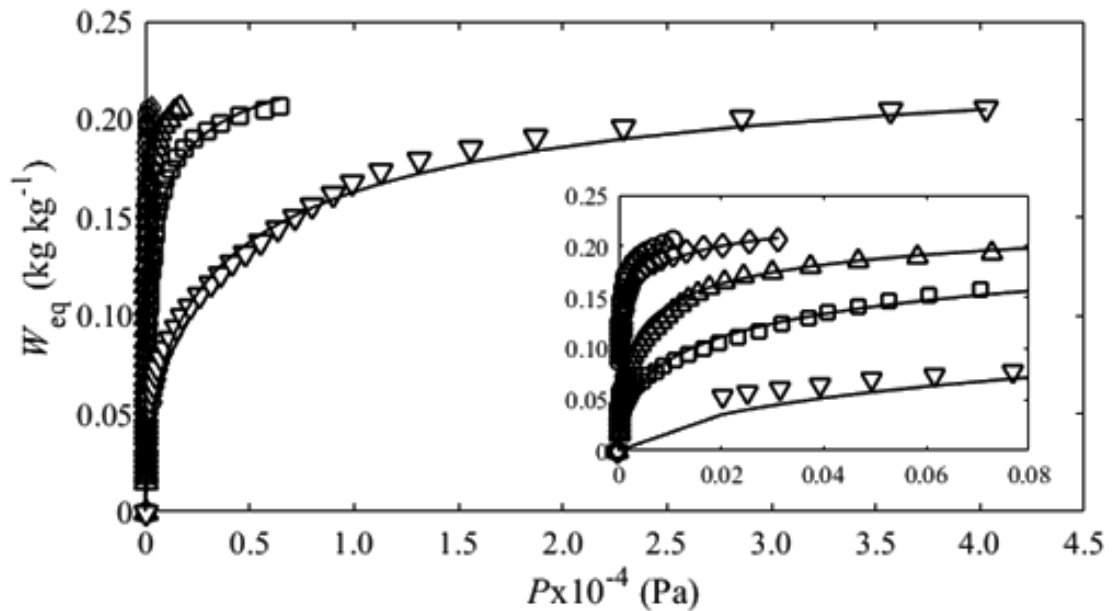


Fig. 5.4 - Adsorption isotherms of water vapor on zeolite 13XB: experimental data at 298.15 (o), 313.15 (◊), 338.15 K (Δ), 368.15 K (◻) and 423.15 K (∇) provided by Grace [61]; lines are the Dubinin-Astakhov model fitting.

The isosteric heats of adsorption (Q_{ads}) at half coverage for NaYBFK and 13XB were determined using the isotherm model and the Clausius-Clapeyron equation (Annex A5, Section A5.3.2), and are equal to $3.05 \times 10^6 \text{ J kg}^{-1}$ and $3.34 \times 10^6 \text{ J kg}^{-1}$, respectively, which are in close agreement (less than 10 % differences) with literature data [62, 63]. For 13XBFK, $Q_{\text{ads}} = 3.50 \times 10^6 \text{ J kg}^{-1}$ is reported by Mette *et al.* [55].

Regarding kinetics, an estimation of the mass transfer resistances inside the porous structure highlighted greater resistances in macropores and mesopores than in micropores (detailed in Annex A5, Section A5.3.3.1). Hence, Eq. (5.14) (Table 5.2) is appropriate for calculating K_{LDF} [51].

5.4.1.2. Solid densities (ρ_s) and thermal conductivities ($\lambda_{\text{eff},s}$)

The measured values of ρ_s for NaYBFK and 13XB are 2475 and 2447 kg m^{-3} , respectively (Table 5.3, Section 5.4.2), which are in agreement with literature data for zeolites [64] (details in Annex A5, Section A5.3.4).

Fig. 5.5 shows $\lambda_{\text{eff},s}$ of NaYBFK ($\lambda_{\text{eff,NaYBFK}}$) and 13XB ($\lambda_{\text{eff,13XB}}$) measured as function of temperature in the range 298.15-388.15 K, and corresponding linear fittings (details in Annex A5, Section A5.3.5.1).

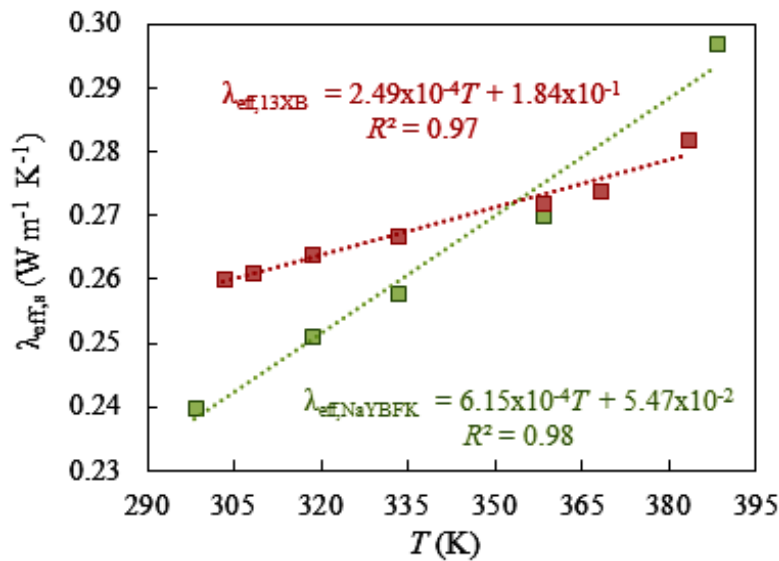


Fig. 5.5 - Variation of $\lambda_{\text{eff},s}$ of 13XB and NaYBFK with temperature. Squares are experimental results (using the Gustafsson probe method), and lines are the corresponding linear fittings.

In the simulations, average values of $\lambda_{\text{eff},s}$ between the minimum and the maximum temperatures of the bed were used, which are in the range $0.272 - 0.293 \text{ W m}^{-1} \text{ K}^{-1}$ and $0.272 - 0.281 \text{ W m}^{-1} \text{ K}^{-1}$ for NaYBFK and 13XB, respectively (Table 5.3, Section 5.4.2). These results are in agreement with literature data for zeolites, generally in the range $0.2-0.4 \text{ W m}^{-1} \text{ K}^{-1}$ [65, 66].

5.4.2. Simulation studies and optimization through DoE/RSM

In the first part of this section, the performances of NaYBFK, 13XBFK and 13XB for adsorption heating applications are investigated by carrying out a set of simulations, defined according to a Box-Behnken design with four factors ($t_{\text{ADS+DES}}$, T_{cond} , $T_{\text{HTF,hot}}$ and δ) and three levels (Table 5.1). The main properties of the adsorbent/adsorbate pairs considered in the simulations are given in Table 5.3.

Table 5.3 - Main properties of the adsorbents, bed dimensions and operating conditions considered in the simulations.

	NaYBFK	Ref.	13XBFK	Ref.	13XB	Ref.
$C_{p,s}$ ($\text{J kg}^{-1} \text{ K}^{-1}$)	855 – 898 ^(a)	[67]	880		910 – 945 ^(a)	[67]
$\lambda_{\text{eff},s}$ ($\text{W m}^{-1} \text{ K}^{-1}$)	0.272 – 0.293 ^(b)	This work	0.24 ^(c)	[55]	0.272 – 0.281 ^(b)	This work
Q_{ads} (J kg^{-1})	3.05×10^6 ^(d)		3.50×10^6 ^(d)		3.34×10^6 ^(d)	
ρ_s (kg m^{-3})	2475 ^(e)		2875 ^(f)	This work	2447 ^(e)	
ρ_p (kg m^{-3})	1117 ^(g)		1150	[55]	1117 ^(g)	
$\varepsilon_p; \tau_p$	0.55; 3.8 ^(g)		0.60; 4.0		0.54; 3.9 ^(g)	
d_p (m); ε_b	$0.5 \times 10^{-3}; 0.40$ ^(h)					
<i>Adsorbent bed dimensions and operating conditions</i>						
R_i (m)	7.5×10^{-3}					
T_{evap} (K); P_{evap} (Pa)	278.15; 870					
$T_{\text{HTF,cool}}$ (K) ⁽ⁱ⁾	308.15 – 328.15					

^(a) Details given in Annex A5 (Section A5.3.5.2). ^(b) Details given in Annex A5 (Section A5.3.5.1).

- ^(c) Obtained considering $\lambda_{\text{eff},s} = \lambda_s(1 - \varepsilon_b)$, using $\lambda_s = 0.4 \text{ W m}^{-1} \text{ K}^{-1}$ as reported in ref. [55].
^(d) Details given in Annex A5 (Section A5.3.2). ^(e) Details given in Annex A5 (Section A5.3.4).
^(f) Calculated using data reported in ref. [55] for particle density (ρ_p) and porosity (ε_p) of 1150 kg m^{-3} and 0.6, respectively, as follows: $\rho_s = \frac{\rho_p}{(1 - \varepsilon_p)}$. ^(g) Details given in Annex A5 (Section A5.3.3.2.1).
^(h) The porosity of undisturbed random beds of spheres normally lies between 0.36-0.42, as reported in ref. [68]. ⁽ⁱ⁾ $T_{\text{HTF,cool}}$ was coincident with T_{cond} .

In the second part, the statistical outcomes from DoE/RSM obtained for NaYBFK are presented and discussed, which include: Pareto charts showing the ranking of effects on *COP* and *SHP*; polynomial equations from RSM for predicting the AHP performance as function of the factors (and *vice-versa*). Examples of the usefulness of these equations to map the system performance and to easily select optimal operation times and geometric AHEx parameters are presented.

5.4.2.1. Comparison of NaYBKF, 13XBFK and 13XB beds

Table 5.4 shows the set of simulations run for the conditions established by the Box-Behnken design of four factors ($t_{\text{ADS+DES}}$, T_{cond} , $T_{\text{HTF,hot}}$ and δ) and three levels listed in Table 5.1, along with the results of *COP* and *SHP* obtained for NaYBFK, 13XBFK and 13XB. The material NaYBFK seems to lead to superior AHP performances than 13XBFK and 13XB, which is closely related to the higher values of $\Delta\bar{W}_{\text{cycle}}$ within the range of operating conditions under study. The two latter materials led to roughly comparable results, suggesting that the presence of the clay binder in 13XB does not affect considerably its performance. Based on these results, the formulation used to produce commercial 13XB seems very efficient, avoiding loss of material performance.

Table 5.4 - Box-Behnken design matrix of four factors ($t_{\text{ADS+DES}}$, T_{cond} , $T_{\text{HTF,hot}}$, δ) and three levels, and results of *COP* and *SHP* for NaYBFK, 13XBFK and 13XB beds.

Run	$t_{\text{ADS+DES}}$ (s) ^(a)	T_{cond} (K) ^(a)	$T_{\text{HTF,hot}}$ (K) ^(a)	δ (m) ^(a)	NaYBFK		13XBFK		13XB	
					<i>COP</i>	<i>SHP</i> (W kg ⁻¹)	<i>COP</i>	<i>SHP</i> (W kg ⁻¹)	<i>COP</i>	<i>SHP</i> (W kg ⁻¹)
1	900 (-1)	308.15 (-1)	423.15 (0)	7.5x10 ⁻³ (0)	1.38	322	1.26	238	1.27	248
2	3600 (1)	308.15 (-1)	423.15 (0)	7.5x10 ⁻³ (0)	1.51	201	1.38	150	1.38	150
3	900 (-1)	328.15 (1)	423.15 (0)	7.5x10 ⁻³ (0)	1.05	141	1.00	105	1.06	129
4	3600 (1)	328.15 (1)	423.15 (0)	7.5x10 ⁻³ (0)	1.26	95	1.18	76	1.19	76
5	900 (-1)	318.15 (0)	398.15 (-1)	7.5x10 ⁻³ (0)	1.10	128	1.05	102	1.08	113
6	3600 (1)	318.15 (0)	398.15 (-1)	7.5x10 ⁻³ (0)	1.32	87	1.21	72	1.19	79
7	900 (-1)	318.15 (0)	448.15 (1)	7.5x10 ⁻³ (0)	1.31	333	1.20	245	1.21	265
8	3600 (1)	318.15 (0)	448.15 (1)	7.5x10 ⁻³ (0)	1.47	220	1.33	153	1.37	164
9	2250 (0)	308.15 (-1)	398.15 (-1)	7.5x10 ⁻³ (0)	1.41	159	1.30	124	1.30	126
10	2250 (0)	328.15 (1)	398.15 (-1)	7.5x10 ⁻³ (0)	1.05	48	1.01	40	1.09	47
11	2250 (0)	308.15 (-1)	448.15 (1)	7.5x10 ⁻³ (0)	1.51	308	1.38	223	1.39	247
12	2250 (0)	328.15 (1)	448.15 (1)	7.5x10 ⁻³ (0)	1.34	196	1.17	138	1.25	155
13	2250 (0)	318.15 (0)	423.15 (0)	7.5x10 ⁻³ (0)	1.36	171	1.23	129	1.26	139
14	2250 (0)	308.15 (-1)	423.15 (0)	10x10 ⁻³ (1)	1.40	148	1.27	110	1.29	118
15	2250 (0)	328.15 (1)	423.15 (0)	10x10 ⁻³ (1)	1.10	68	1.03	52	1.07	62
16	3600 (1)	318.15 (0)	423.15 (0)	10x10 ⁻³ (1)	1.34	91	1.21	70	1.24	78
17	900 (-1)	318.15 (0)	423.15 (0)	10x10 ⁻³ (1)	1.12	142	1.04	105	1.07	111
18	2250 (0)	318.15 (0)	448.15 (1)	10x10 ⁻³ (1)	1.33	154	1.22	113	1.24	127
19	2250 (0)	318.15 (0)	398.15 (-1)	10x10 ⁻³ (1)	1.14	62	1.06	50	1.13	56
20	2250 (0)	318.15 (0)	398.15 (-1)	5x10 ⁻³ (-1)	1.36	176	1.26	146	1.24	124
21	2250 (0)	318.15 (0)	448.15 (1)	5x10 ⁻³ (-1)	1.48	431	1.35	318	1.36	304
22	900 (-1)	318.15 (0)	423.15 (0)	5x10 ⁻³ (-1)	1.36	427	1.24	322	1.26	344
23	3600 (1)	318.15 (0)	423.15 (0)	5x10 ⁻³ (-1)	1.47	224	1.36	177	1.33	136
24	2250 (0)	308.15 (-1)	423.15 (0)	5x10 ⁻³ (-1)	1.53	412	1.41	311	1.39	275
25	2250 (0)	328.15 (1)	423.15 (0)	5x10 ⁻³ (-1)	1.32	192	1.22	155	1.22	137

^(a) Values inside parenthesis are the codified levels of each variable under the context of DoE.

5.4.2.2. Statistical outcomes from DoE/RSM for NaYBKF and insights into AHPs optimization

5.4.2.2.1. Impact of operating/geometric factors on COP and SHP

Pareto charts allow the identification and classification of the factors and interactions with (negative or positive) impact on a response variable. Fig. 5.6 shows the Pareto charts of *COP* and *SHP* for the Box-Behnken design matrix of Table 5.4, with confidence interval of 95 %, where factors with positive and negative effects are ranked.

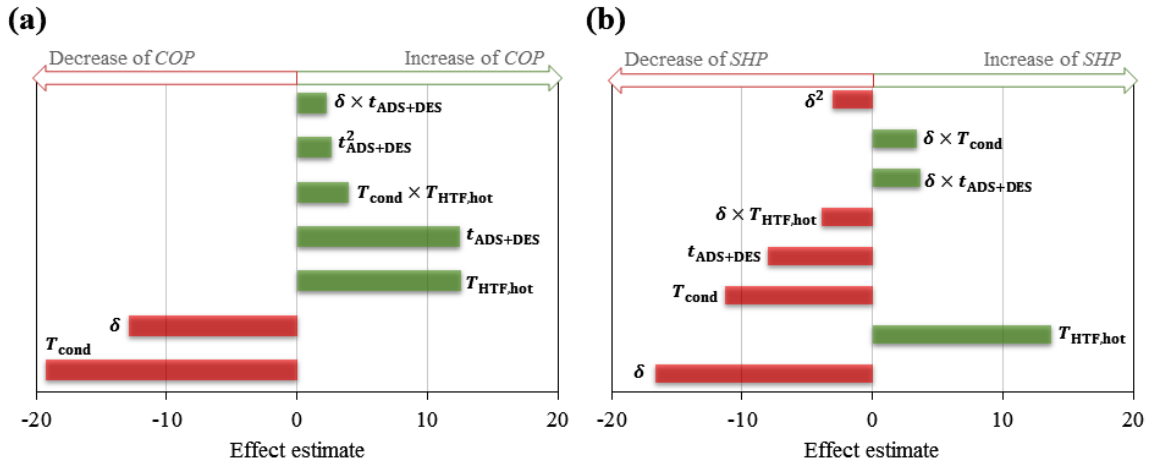


Fig. 5.6 - Pareto charts of (a) *COP* and (b) *SHP* for NaYBFK considering the Box-Behnken design of Table 5.4 with confidence interval of 95 %.

The increase of T_{cond} has negative influence on the performance parameters, being the greatest impacting variable on *COP* (Fig. 5.6(a)). As T_{cond} increases, the pressure during desorption stage increases, leading to the decrease of the average loading swing ($\Delta\bar{W}_{\text{cycle}}$) and of the heats generated per cycle. The bed thickness (δ) is the second most important factor on *COP*, and its increase predominantly reduces *SHP*. Incrementing δ increases the resistance to heat transfer along the adsorbent bed, influencing the heating/cooling rates of the adsorbent, and ultimately the adsorption/desorption rates of water vapor. Higher $T_{\text{HTF,hot}}$ impacts favorably on the AHEx operation, since it allows better adsorbent regeneration and thus higher $\Delta\bar{W}_{\text{cycle}}$. The $t_{\text{ADS+DES}}$ (ranked in fourth place in both Pareto charts) influences *COP* positively, since more time is given to heat and mass transfer, approximating the system to equilibrium state, which enlarges the differences between adsorption and desorption steps ($\Delta\bar{W}_{\text{cycle}}$). However, higher $t_{\text{ADS+DES}}$ accounts for reduced *SHP*. There are quadratic ($t_{\text{ADS+DES}}^2, \delta^2$) and interaction effects ($T_{\text{cond}} \times T_{\text{HTF,hot}}, \delta \times t_{\text{ADS+DES}}$) with statistical significance for *COP* and *SHP*, albeit less important. The Pareto charts for 13XBFK and 13XB present similar trends to those for NaYBFK (Annex A5, Section A5.4.2). Overall, these results show that DoE/RSM can be successfully applied for the evaluation of impact of operating conditions and geometric parameters on the performance of AHPs.

5.4.2.2.2. RSM models for COP and SHP

The RSM results of *COP* and *SHP*, for which $R_{COP}^2 = 0.981$, $R_{adj,COP}^2 = 0.973$, $R_{SHP}^2 = 0.978$ and $R_{adj,SHP}^2 = 0.967$, are:

$$COP = 29.905 + 6.686 \times 10^{-5} t_{ADS+DES} - 9.390 \times 10^{-2} T_{cond} - 5.692 \times 10^{-2} T_{HTF,hot} - 54.667\delta - 1.403 \times 10^{-8} t_{ADS+DES}^2 + 8.148 \times 10^{-3} t_{ADS+DES}\delta + 1.900 \times 10^{-4} T_{cond} T_{HTF,hot} \quad (5.15)$$

$$SHP = 3015.673 - 1.199 \times 10^{-1} t_{ADS+DES} - 17.250 T_{cond} + 8.163 T_{HTF,hot} - 295411\delta + 4044096\delta^2 + 11.259 t_{ADS+DES}\delta + 1400 T_{cond}\delta - 652 T_{HTF,hot}\delta \quad (5.16)$$

These simple equations are very useful for expeditious performance predictions since considerable number of experiments or time consuming simulations are avoided, for example, when a significant number of grid points need to be used to eliminate numerical instabilities due to the non-linearity and stiffness of the equations, or even when the isotherms are described by non-linear algebraic expressions (which greatly prolongs the simulation time). Examples of the usefulness of these equations are presented in the following.

(i) Mapping the AHP performance and assessing trends

The Eqs. (5.15)-(5.16) enable mapping the system performance within a range of conditions, based on the small number of simulations accomplished above. This may be visualized using *e.g.*, surface plots, which show the shape of the response surfaces, and allow assessing trends and identifying minima and maxima when existent. As illustrative case, the surface plots of *COP* and *SHP* as function of $T_{HTF,hot}$ and δ , with fixed $T_{cond} = 318.15$ K and $t_{ADS+DES} = 2250$ s, are given in Fig. 5.7.

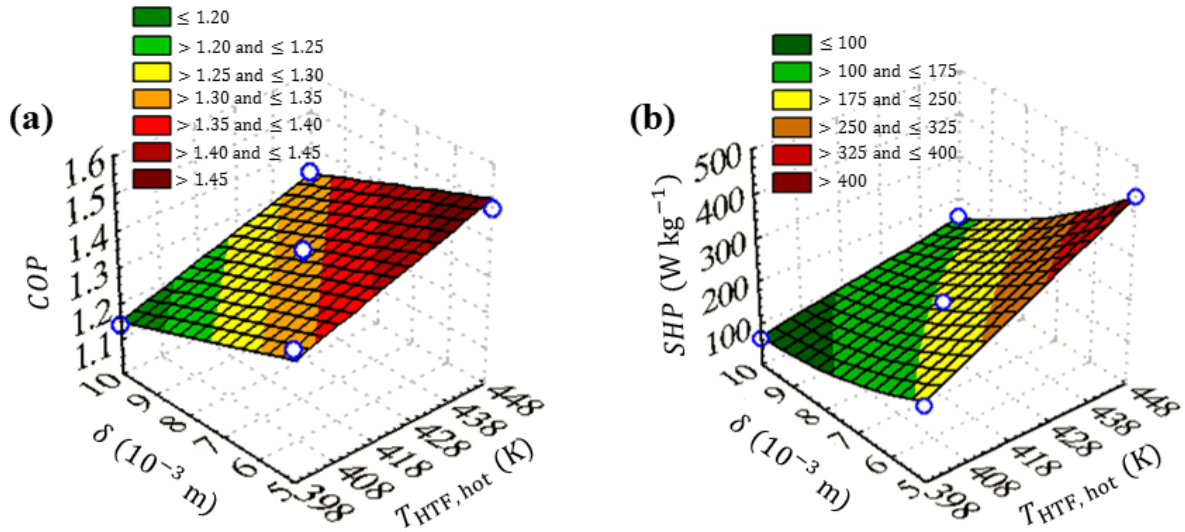


Fig. 5.7 - Surface plots of (a) COP (Eq. (5.15)) and (b) SHP (Eq. (5.16)) as function of $T_{HTF,hot}$ and δ obtained for NaYBFK with $T_{cond} = 318.15$ K and $t_{ADS+DES} = 2250$ s. Dots are simulation results (Table 5.4, runs 13 and 18-21).

As side remark, maximum values of COP and SHP around 1.50 and 400 W kg^{-1} , respectively, are achievable for $T_{HTF,hot} = 448.15$ K and $\delta = 5 \times 10^{-3}$ m, which indicates somewhat limited performances (namely in terms of power) for NaYBFK. Besides, $T_{HTF,hot} = 448.15$ K mimics a practical scenario requiring the use of thermal oils or even exhaust gases for bed regeneration. This may turn the concept of the AHP unfeasible in some applications, due to technical complexity, maintenance efforts (*e.g.*, need for periodical oil replacement) and costs. Regarding δ , the results reiterate the need for developing coated AHExs, for example using dip coating or spray coating techniques, for which $\delta < 1$ mm is commonly found [69], or even through the synthesis of thin adsorbent coatings (with dozens or hundreds of microns) directly on the heat exchangers [69, 70], in order to increase the technical and economic viability of AHPs (albeit a good compromise in terms of metal to adsorbent mass ratio is necessary to not significantly hinder COP s). Coated AHExs enable SHP s $> 1000 \text{ W kg}^{-1}$, while loose grains or pellets generally do not exceed the order of hundreds: *e.g.*, Dawoud [5], Restuccia and Cacciola [21] and Dawoud *et al.* [23] report SHP values in the range of *ca.* $900 - 2200 \text{ W kg}^{-1}$ for coatings of zeolites/zeotypes, while for beds of loose pellets they were roughly in the interval $160 - 550 \text{ W kg}^{-1}$. The latter range of SHP s is somewhat in agreement with the values in Figs. 5.7-5.8 in the interval *ca.* $100 - 600 \text{ W kg}^{-1}$.

(ii) Optimum times to fulfill performance requirements - insights into AHP control strategies

In this section, the selection of optimum times to meet specific performance requisites under variable T_{cond} is exemplified, envisaging two distinct control strategies, in which either *SHP* or *COP* are to be maximized. Fig. 5.8(a)-(b) shows the contour plots of *COP* and *SHP* (Eqs. (5.15)-(5.16)) as function of T_{cond} and $t_{\text{ADS+DES}}$, under fixed $T_{\text{HTF,hot}} = 448.15$ K and $\delta = 5 \times 10^{-3}$ m, from which optimum times of operation can be extracted.

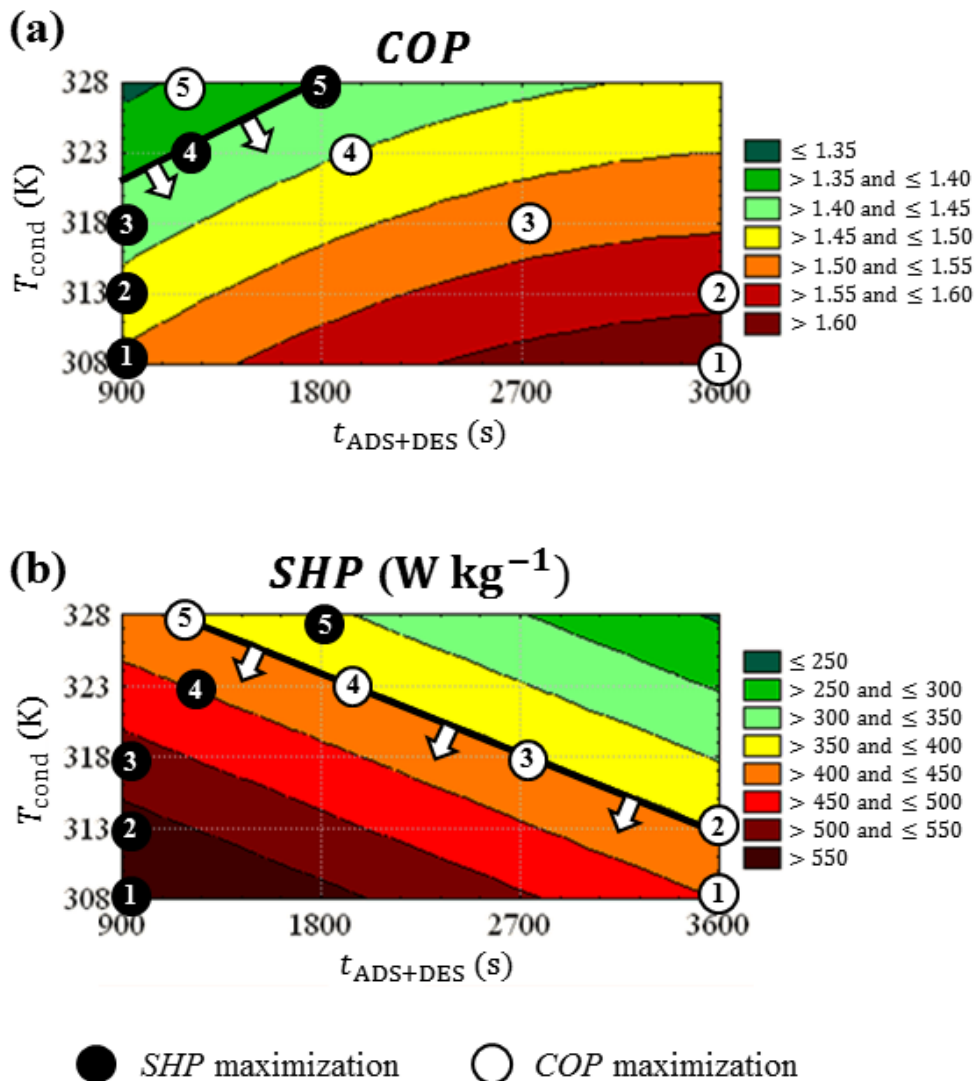


Fig. 5.8 - Contour plots of (a) *COP* (Eq. (5.15)) and (b) *SHP* (Eq. (5.16)) obtained for NaYBFK as function of T_{cond} and $t_{\text{ADS+DES}}$, for fixed $T_{\text{HTF,hot}} = 448.15$ K and $\delta = 5 \times 10^{-3}$ m. Filled black circles to the specification requiring $\text{COP} \geq 1.40$ and the simultaneous maximization of *SHP* in all cycles; Open white circles concern the requisite of $\text{SHP} \geq 400 \text{ W kg}^{-1}$ and the concomitant maximization of *COP* in all cycles.

In the following discussion it is always assumed that T_{cond} should range from 308.15 to 328.15 K in order to meet consumer needs (this mimics the domestic hot water production, in which the water temperature inside the tank rises along time).

Control strategy for maximizing SHP. If along the heating process $COP \geq 1.40$ and the highest SHP are simultaneously required, the evolution of $(t_{\text{ADS+DES}}, T_{\text{cond}})$ pair can be easily designed as shown in Fig. 5.8(a) (filled circles). In the first 3 cycles ($308.15 \leq T_{\text{cond}}(\text{K}) \leq 318.15$), an optimum $t_{\text{ADS+DES}}$ of 900 s is identified, and a progressive decrease in the performance occurs ($COP: 1.51 > 1.47 > 1.42$; calculated from Eq. (5.15)), for which the corresponding SHP s (W kg^{-1}) in Fig. 5.8(b) are: $621 > 570 > 519$; calculated from Eq. (5.16). In the fourth and fifth cycles ($T_{\text{cond}} = 323.15$ and 328.15 K, respectively), $t_{\text{ADS+DES}}$ needs to be increased to *ca.* 1260 s and 1800 s, in order to meet $COP = 1.40$ and maximum SHP values around 450 and 360 W kg^{-1} (Fig. 5.8(b)), respectively.

Control strategy for maximizing COP. Fixing $SHP \geq 400 \text{ W kg}^{-1}$ and seeking for the highest COP values at each moment during the heating process, the resulting evolution of $t_{\text{ADS+DES}}$ can be easily established from Fig. 5.8(b) (open white circles). In the first and second heating cycles (T_{cond} of 308.15 K and 313.15 K, respectively), $t_{\text{ADS+DES}} = 3600$ s allows $SHP \geq 400 \text{ W kg}^{-1}$ and maximizes COP (which attains, respectively, 1.63 and 1.59 (Fig. 5.8(a))). From the second to the third cycle, $t_{\text{ADS+DES}}$ needs to be reduced from 3600 to *ca.* 2700 s, while in the fourth cycle ($T_{\text{cond}} = 323.15$ K) it must be further decreased to *ca.* 1980 s. The heating process ends in the fifth cycle ($T_{\text{cond}} = 328.15$ K), for which $t_{\text{ADS+DES}}$ rounds 1170 s, SHP is *ca.* 400 W kg^{-1} and COP approaches 1.36 (Fig. 5.8(a)).

Overall, DoE/RSM methodologies may aid the development of advanced AHP control strategies allowing adaptations to changes in working conditions and/or user requirements, while simultaneously meeting performance requisites.

(iii) Optimal $(\delta, t_{\text{ADS+DES}})$ pairs to meet performance requirements - insights into the development of optimized AHExs

Fig. 5.9(a)-(c) shows (SHP, COP) pairs estimated using Eqs. (5.15)-(5.16) for $T_{\text{HTF,hot}} = 448.15$ K, δ in the range $5 \times 10^{-3} - 10 \times 10^{-3}$ m, $t_{\text{ADS+DES}}$ between 900 s and

3600 s, and T_{cond} of 308.15 K, 318.15 K and 328.15 K. Exemplified requisites of $COP \geq 1.40$ and $SHP \geq 400 \text{ W kg}^{-1}$ are marked. The δ vs. $t_{\text{ADS+DES}}$ values considered in the performance estimations for each T_{cond} are also shown, where the combinations that satisfy COP and SHP requisites are highlighted with orange border.

For $T_{\text{cond}} = 308.15 \text{ K}$ (Fig. 5.9(a)), the performance requisites are met for $\delta = 5 \times 10^{-3} \text{ m}$ in a broad range of $t_{\text{ADS+DES}}$ (900 – 3600 s), and for $\delta = 6.25 \times 10^{-3} \text{ m}$ with $t_{\text{ADS+DES}}$ lower than $\sim 2750 \text{ s}$. Incrementing T_{cond} to 318.15 K (Fig. 5.9(b)), only $\delta = 5 \times 10^{-3} \text{ m}$ with $t_{\text{ADS+DES}} < 2750 \text{ s}$ allows fulfilling the COP and SHP requirements. For $T_{\text{cond}} = 328.15 \text{ K}$ (Fig. 5.9(c)), the pre-established performance requisites are no longer met for any evaluated ($\delta, t_{\text{ADS+DES}}$) pairs evaluated. This example shows the importance of analyzing the complete range of temperature conditions when seeking for optimal AHEx geometry and operating parameters.

In the whole, DoE/RSM can easily aid the identification of optimal combinations of operating and geometric features for meeting pre-established performance requisites.

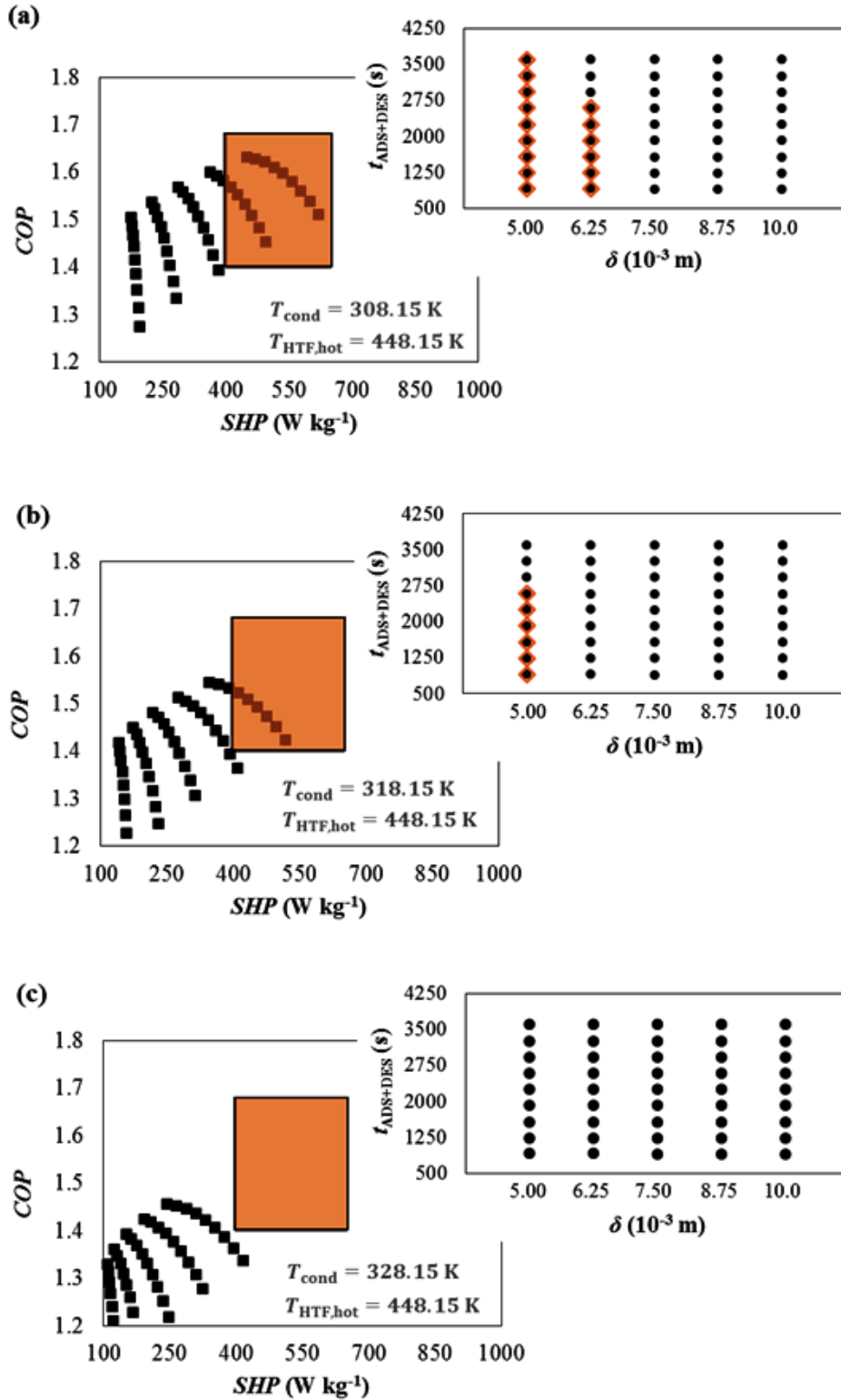


Fig. 5.9 – Pairs of SHP and COP estimated using Eqs. (5.15)-(5.16) for $T_{\text{HTF,hot}} = 448.15$ K, δ and $t_{\text{ADS+DES}}$ in the range $5 \times 10^{-3} - 10 \times 10^{-3}$ m and 900 - 3600 s, respectively, and T_{cond} of (a) 308.15 K, (b) 318.15 K and (c) 328.15 K. Exemplified performance requisites of $\text{COP} \geq 1.40$ and $\text{SHP} \geq 400$ W kg^{-1} are marked (orange squares). The $(\delta, t_{\text{ADS+DES}})$ pairs considered for the performance estimations at each T_{cond} are also shown (black circles), where the combinations that allow meeting the COP and SHP requisites are highlighted (diamonds with orange border).

5.5. Conclusions

Modeling and simulation studies were accomplished to compare the performance of binderless NaY (NaYBfK), binderless 13X (13XBfK), and binder-containing 13X (13XB) for adsorption heating applications using water as refrigerant. Equilibrium, kinetic and thermophysical properties were measured and/or estimated to carry out 25 simulations per adsorbent totally. With this purpose, four factors and three levels were studied according to a Box-Behnken design: $t_{\text{ADS+DES}}$ between 900 and 3600 s; T_{cond} from 308.15 to 328.15 K; $T_{\text{HTF,hot}}$ from 398.15 to 448.15 K; and δ between 5×10^{-3} and 10×10^{-3} m. The NaYBfK was the most promising adsorbent, with *COP* values up to 1.63 and *SHP* around 620 W kg^{-1} . The 13XBfK and 13XB materials achieved similar *COP* and *SHP* results, which means that the mineral clay binder of 13XB does not hinder its performance within the studied range of conditions.

In a second part of the work, the statistical outcomes from DoE/RSM for NaYBfK beds were analyzed, and insights into their usefulness for the optimization of adsorption heating pumps (AHPs) were illustrated. Simple models for the quick estimation of *COP* and *SHP* were developed, allowing for: (i) mapping system performance in a broad range of conditions with small number of simulations; (ii) the selection of optimal operating times and geometric features of adsorption heat exchangers (AHExs) under pre-established performance requirements. Overall, DoE/RSM can aid the successful development of optimized AHExs and advanced AHP control strategies.

Nomenclature

AARD	$= \frac{\sum_{i=1}^n \left \frac{\text{Value}_{\text{calculated},i} - \text{Value}_{\text{experimental},i}}{\text{Value}_{\text{experimental},i}} \right }{N_{\text{data}}}$
	Average Absolute Relative Deviation (%)
cp	Number of central points in Box-Behnken design
C	Parameter of Dubinin-Astakhov isotherm
C_p	Specific heat capacity ($\text{J kg}^{-1} \text{K}^{-1}$)
COP	Coefficient of performance
d_p	Adsorbent particle diameter (m)
D_{eff}	Effective diffusivity ($\text{m}^2 \text{s}^{-1}$)
D_K	Knudsen diffusivity ($\text{m}^2 \text{s}^{-1}$)
D_m	Molecular diffusivity ($\text{m}^2 \text{s}^{-1}$)
H	Equilibrium constant
k	Number of factors in the Box-Behnken design
K_{LDF}	Linear driving force (LDF) global mass transfer coefficient (s^{-1})
m	Mass (kg)
M	Molar mass of adsorbate (kg mol^{-1})
n	Parameter of Dubinin-Astakhov isotherm
N	Number of runs in Box-Behnken design
P	Pressure (Pa)
Q	Heat (J)
Q_{ads}	Isosteric heat of adsorption (J kg^{-1})
Q_{ADS}	Heat released during the isobaric adsorption stage (J),
Q_{COOL}	Heat released during the isosteric cooling stage (J)
Q_{cond}	Heat released by the condenser (J)
Q_{DES}	Heat supplied during the isobaric desorption stage (J)
Q_{HEAT}	Heat supplied during the isosteric heating stage (J)
r	Spatial coordinate (m)
R	Radial position in the adsorbent bed (m)
\mathfrak{R}	Universal gas constant ($\text{J mol}^{-1} \text{K}^{-1}$).

R^2	Coefficient of determination
R_{adj}^2	Adjusted coefficient of determination
R_p	Adsorbent particle radius (m)
SHP	Specific heating power (W kg^{-1})
t	Time (s)
t_{cycle}	Cycle time (s)
T	Temperature (K)
$T_{\text{HTF,cool}}$	Temperature of the cool heat transfer fluid (K)
$T_{\text{HTF,hot}}$	Temperature of the hot heat transfer fluid (K)
W	Adsorbate loading (kg kg^{-1})
W_0	Adsorbate loading at saturation pressure (kg kg^{-1})
x_0	Real value of the factor at the central point in DoE/RSM
x_k	Real value of the factor in DoE/RSM analysis
X_k, X_i, X_j	Codified value of the factor in DoE/RSM analysis
Y	Response variable in DoE/RSM analysis

Greek symbols

β_0	RSM model constant including the residual
β_i	RSM model coefficient related to linear effects
β_{ii}	RSM model coefficient related to quadratic effects
β_{ij}	RSM model coefficient related to pair interaction effects
β_{water}	Thermal expansion coefficient of water (K^{-1})
δ	Adsorbent bed thickness (m)
ΔH_v	Latent heat of vaporization (J kg^{-1})
$\Delta \bar{W}_{\text{cycle}}$	Cyclic average adsorption loading swing (kg kg^{-1})
Δx_k	Step change of the real value of the factor in DoE/RSM
ε_b	Porosity of the bed
ε_p	Porosity of the particle
λ	Thermal conductivity ($\text{W m}^{-1} \text{K}^{-1}$)
Ω	LDF model constant dependent on the particle geometry
ρ	Density (kg m^{-3})

τ_p	Tortuosity of the particle
φ	Generic notation of T , W and P
$\bar{\varphi}$	Generic notation of \bar{T} , \bar{W} and \bar{P}

Subscripts

a	Adsorbate
ADS	Isobaric adsorption stage
cond	Condenser
COOL	Isosteric cooling stage
DES	Isobaric desorption stage
eff	Effective
eq	Equilibrium
evap	Evaporator
fin	Final
HEAT	Isosteric heating stage
i	Internal boundary of the bed
ini	Initial
max	Maximum
min	Minimum
o	External boundary of the bed
p	Particle
s	Adsorbent
sat	Saturation

References

- [1] B.O. Bolaji, Z. Huan, Ozone depletion and global warming: Case for the use of natural refrigerant – a review, *Renewable and Sustainable Energy Reviews*, 18 (2013) 49-54.
- [2] J.M. Pinheiro, S. Salústio, J. Rocha, A.A. Valente, C.M. Silva, Analysis of equilibrium and kinetic parameters of water adsorption heating systems for different porous metal/metalloid oxide adsorbents, *Applied Thermal Engineering*, 100 (2016) 215-226.
- [3] D. Üрге-Vorsatz, L.F. Cabeza, S. Serrano, C. Barreneche, K. Petrichenko, Heating and cooling energy trends and drivers in buildings, *Renewable and Sustainable Energy Reviews*, 41 (2015) 85-98.
- [4] F. Meunier, Adsorption heat powered heat pumps, *Applied Thermal Engineering*, 61 (2013) 830-836.
- [5] B. Dawoud, On the development of an innovative gas-fired heating appliance based on a zeolite-water adsorption heat pump; system description and seasonal gas utilization efficiency, *Applied Thermal Engineering*, 72 (2014) 323-330.
- [6] J.M. Pinheiro, A.A. Valente, S. Salústio, N. Ferreira, J. Rocha, C.M. Silva, Application of the novel ETS-10/water pair in cyclic adsorption heating processes: Measurement of equilibrium and kinetics properties and simulation studies, *Applied Thermal Engineering*, 87 (2015) 412-423.
- [7] J.K. Kiplagat, R.Z. Wang, R.G. Oliveira, T.X. Li, M. Liang, Experimental study on the effects of the operation conditions on the performance of a chemisorption air conditioner powered by low grade heat, *Applied Energy*, 103 (2013) 571-580.
- [8] G. Restuccia, A. Freni, G. Maggio, A zeolite-coated bed for air conditioning adsorption systems: parametric study of heat and mass transfer by dynamic simulation, *Applied Thermal Engineering*, 22 (2002) 619-630.
- [9] H. Demir, M. Mobedi, S. Ülkü, A review on adsorption heat pump: Problems and solutions, *Renewable and Sustainable Energy Reviews*, 12 (2008) 2381-2403.
- [10] D.B. Boman, D.C. Hoysall, D.G. Pahinkar, M.J. Ponkala, S. Garimella, Screening of working pairs for adsorption heat pumps based on thermodynamic and transport characteristics, *Applied Thermal Engineering*, 123 (2017) 422-434.
- [11] A. Frazzica, A. Freni, Adsorbent working pairs for solar thermal energy storage in buildings, *Renewable Energy*, 110 (2017) 87-94.
- [12] A. Freni, G. Maggio, A. Sapienza, A. Frazzica, G. Restuccia, S. Vasta, Comparative analysis of promising adsorbent/adsorbate pairs for adsorptive heat pumping, air conditioning and refrigeration, *Applied Thermal Engineering*, 104 (2016) 85-95.
- [13] S.K. Henninger, S.-J. Ernst, L. Gordeeva, P. Bendix, D. Fröhlich, A.D. Grekova, L. Bonaccorsi, Y. Aristov, J. Jaenchen, New materials for adsorption heat transformation and storage, *Renewable Energy*, 110 (2017) 59-68.
- [14] Chemiewerk Bad Köstritz GmbH (CWK) Products, Köstrolith zeolite molecular sieves. <http://www.cwk-bk.de/en/produkte/molekularsiebe/zeolithe/>, 2017 (accessed 20.01.2017).
- [15] B. Alfons, K. Schumann, U. Baldur, Bindemittelfreies zeolithisches Granulat mit Faujasitstruktur und Verfahren zur Herstellung eines derartigen bindemittelfreien zeolithischen Granulats nebst Verwendung, DE102012010109 A1, Chemiewerk Bad Köstritz GmbH (2012).
- [16] J. Jänchen, K. Schumann, E. Thrun, A. Brandt, B. Unger, U. Hellwig, Preparation, hydrothermal stability and thermal adsorption storage properties of binderless zeolite beads, *International Journal of Low-Carbon Technologies*, 7 (2012) 275-279.

- [17] B. Jha, D.N. Singh, Basics of Zeolites, in: Fly Ash Zeolites: Innovations, Applications, and Directions, Springer Singapore, Singapore, 2016, pp. 5-31.
- [18] P. Bendix, G. Földner, M. Möllers, H. Kummer, L. Schnabel, S. Henninger, H.-M. Henning, Optimization of power density and metal-to-adsorbent weight ratio in coated adsorbents for adsorptive heat transformation applications, Applied Thermal Engineering, 124 (2017) 83-90.
- [19] J.M. Corberan, M. Axell, R.d. Boer, A. Freni, U. Jakob, S. Landolina, P. Lundqvist, M. Monsberger, R. Nordman, T. Nowak, T. Oltersdorf, S. Spoelstra, F. Ziegler, Heat Pumps, in: Strategic Research Priorities for Cross-cutting Technology, Global CCS Institute, European Technology Platform on Renewable Heating and Cooling, Belgium, 2012, pp. 48-75.
- [20] Y.B. Gui, R.Z. Wang, W. Wang, J.Y. Wu, Y.X. Xu, Performance modeling and testing on a heat-regenerative adsorptive reversible heat pump, Applied Thermal Engineering, 22 (2002) 309-320.
- [21] G. Restuccia, G. Cacciola, Performances of adsorption systems for ambient heating and air conditioning, International Journal of Refrigeration, 22 (1999) 18-26.
- [22] A. Sapienza, S. Santamaria, A. Frazzica, A. Freni, Influence of the management strategy and operating conditions on the performance of an adsorption chiller, Energy, 36 (2011) 5532-5538.
- [23] B. Dawoud, P. Hofle, S. Chmielewski, Experimental Investigation of the Effect Of Zeolite Coating Thickness on the Performance of a Novel Zeolite-Water Adsorption Heat Pump Module, Tenth International Conference Enhanced Building Operations, Kuwait (2010).
- [24] M. Tatlier, G. Munz, G. Földner, S.K. Henninger, Effect of zeolite A coating thickness on adsorption kinetics for heat pump applications, Microporous and Mesoporous Materials, 193 (2014) 115-121.
- [25] G. Zhang, D.C. Wang, J.P. Zhang, Y.P. Han, W. Sun, Simulation of operating characteristics of the silica gel-water adsorption chiller powered by solar energy, Solar Energy, 85 (2011) 1469-1478.
- [26] H.T. Chua, K.C. Ng, W. Wang, C. Yap, X.L. Wang, Transient modeling of a two-bed silica gel-water adsorption chiller, International Journal of Heat and Mass Transfer, 47 (2004) 659-669.
- [27] Y.I. Aristov, A. Sapienza, D.S. Ovoshchnikov, A. Freni, G. Restuccia, Reallocation of adsorption and desorption times for optimisation of cooling cycles, International Journal of Refrigeration, 35 (2012) 525-531.
- [28] A. Pesaran, H. Lee, Y. Hwang, R. Radermacher, H.-H. Chun, Review article: Numerical simulation of adsorption heat pumps, Energy, 100 (2016) 310-320.
- [29] M. Verde, K. Harby, R. de Boer, J.M. Corberán, Performance evaluation of a waste-heat driven adsorption system for automotive air-conditioning: Part II - Performance optimization under different real driving conditions, Energy, 115 (2016) 996-1009.
- [30] S. Narayanan, S. Yang, H. Kim, E.N. Wang, Optimization of adsorption processes for climate control and thermal energy storage, International Journal of Heat and Mass Transfer, 77 (2014) 288-300.
- [31] G.H.W. van Benthem, G. Cacciola, G. Restuccia, Regenerative adsorption heat pumps: Optimization of the design, Heat Recovery Systems and CHP, 15 (1995) 531-544.
- [32] M. Verde, K. Harby, J.M. Corberán, Optimization of thermal design and geometrical parameters of a flat tube-fin adsorbent bed for automobile air-conditioning, Applied Thermal Engineering, 111 (2017) 489-502.

- [33] F. Lanzerath, U. Bau, J. Seiler, A. Bardow, Optimal design of adsorption chillers based on a validated dynamic object-oriented model, *Science and Technology for the Built Environment*, 21 (2015) 248-257.
- [34] M. Gräber, C. Kirches, H.G. Bock, J.P. Schlöder, W. Tegethoff, J. Köhler, Determining the optimum cyclic operation of adsorption chillers by a direct method for periodic optimal control, *International Journal of Refrigeration*, 34 (2011) 902-913.
- [35] A.M. Rivero-Pacho, R.E. Critoph, S.J. Metcalf, Modelling and development of a generator for a domestic gas-fired carbon-ammonia adsorption heat pump, *Renewable Energy*, 110 (2017) 180-185.
- [36] Y.I. Aristov, I.S. Glaznev, I.S. Girnik, Optimization of adsorption dynamics in adsorptive chillers: Loose grains configuration, *Energy*, 46 (2012) 484-492.
- [37] I.S. Girnik, A.D. Grekova, L.G. Gordeeva, Y.I. Aristov, Dynamic optimization of adsorptive chillers: Compact layer vs. bed of loose grains, *Applied Thermal Engineering*, 125 (2017) 823-829.
- [38] A. Sapienza, I.S. Glaznev, S. Santamaria, A. Freni, Y.I. Aristov, Adsorption chilling driven by low temperature heat: New adsorbent and cycle optimization, *Applied Thermal Engineering*, 32 (2012) 141-146.
- [39] J.-Y. San, F.-K. Tsai, Testing of a lab-scale four-bed adsorption heat pump, *Applied Thermal Engineering*, 70 (2014) 274-281.
- [40] S. Graf, F. Lanzerath, A. Sapienza, A. Frazzica, A. Freni, A. Bardow, Prediction of SCP and COP for adsorption heat pumps and chillers by combining the large-temperature-jump method and dynamic modeling, *Applied Thermal Engineering*, 98 (2016) 900-909.
- [41] A. Frazzica, G. Földner, A. Sapienza, A. Freni, L. Schnabel, Experimental and theoretical analysis of the kinetic performance of an adsorbent coating composition for use in adsorption chillers and heat pumps, *Applied Thermal Engineering*, 73 (2014) 1022-1031.
- [42] S.W. Hong, S.H. Ahn, O.K. Kwon, J.D. Chung, Optimization of a fin-tube type adsorption chiller by design of experiment, *International Journal of Refrigeration*, 49 (2015) 49-56.
- [43] J.P.S. Aniceto, S.P. Cardoso, C.M. Silva, General optimization strategy of simulated moving bed units through design of experiments and response surface methodologies, *Computers & Chemical Engineering*, 90 (2016) 161-170.
- [44] R.M.A. Domingues, M.M.R. de Melo, E.L.G. Oliveira, C.P. Neto, A.J.D. Silvestre, C.M. Silva, Optimization of the supercritical fluid extraction of triterpenic acids from *Eucalyptus globulus* bark using experimental design, *The Journal of Supercritical Fluids*, 74 (2013) 105-114.
- [45] A.W. Zularisam, A.F. Ismail, M.R. Salim, M. Sakinah, T. Matsuura, Application of coagulation-ultrafiltration hybrid process for drinking water treatment: Optimization of operating conditions using experimental design, *Separation and Purification Technology*, 65 (2009) 193-210.
- [46] M.V. Ponte, L.P. Rivoira, J. Cussa, M.L. Martínez, A.R. Beltramone, O.A. Anunziata, Optimization of the synthesis of SBA-3 mesoporous materials by experimental design, *Microporous and Mesoporous Materials*, 227 (2016) 9-15.
- [47] A. Freni, G. Maggio, S. Vasta, G. Santori, F. Polonara, G. Restuccia, Optimization of a solar-powered adsorptive ice-maker by a mathematical method, *Solar Energy*, 82 (2008) 965-976.
- [48] Y. He, Rapid thermal conductivity measurement with a hot disk sensor: Part 1. Theoretical considerations, *Thermochimica Acta*, 436 (2005) 122-129.

- [49] U. Wittstadt, G. Fuldner, V. S., R. Volmer, P. Bendix, L. Schnabel, W. Mittelbach, Adsorption Heat Pumps and Chillers – Recent Developments for Materials and Component, 12th IEA Heat Pump Conference, Rotterdam (2017).
- [50] L. Marletta, G. Maggio, A. Freni, M. Ingrasciotta, G. Restuccia, A non-uniform temperature non-uniform pressure dynamic model of heat and mass transfer in compact adsorbent beds, *International Journal of Heat and Mass Transfer*, 45 (2002) 3321-3330.
- [51] J.P.S. Aniceto, C.M. Silva, Preparative Chromatography: batch and continuous, in: *Analytical Separation Science*, Vol. 4, Wiley, Germany, 2015.
- [52] S. Sircar, Linear-driving-force model for non-isothermal gas adsorption kinetics, *Journal of the Chemical Society, Faraday Transactions 1: Physical Chemistry in Condensed Phases*, 79 (1983) 785-796.
- [53] E. Glueckauf, Theory of chromatography. Part 10 – Formulae for diffusion into spheres and their application to chromatography, *Trans. Faraday Soc.*, 51 (1955) 1540-1551.
- [54] J.P.S. Aniceto, C.M. Silva, Simulated Moving Bed Strategies and Designs: From Established Systems to the Latest Developments, *Separation & Purification Reviews*, 44 (2015) 41-73.
- [55] B. Mette, H. Kerskes, H. Drück, H. Müller-Steinhagen, Experimental and numerical investigations on the water vapor adsorption isotherms and kinetics of binderless zeolite 13X, *International Journal of Heat and Mass Transfer*, 71 (2014) 555-561.
- [56] M.F. de Lange, K.J.F.M. Verouden, T.J.H. Vlugt, J. Gascon, F. Kapteijn, Adsorption-Driven Heat Pumps: The Potential of Metal–Organic Frameworks, *Chemical Reviews*, 115 (2015) 12205-12250.
- [57] M. Tathier, A. Erdem-Şenatalar, Effects of metal mass on the performance of adsorption heat pumps utilizing zeolite 4A coatings synthesized on heat exchanger tubes, *International Journal of Refrigeration*, 23 (2000) 260-268.
- [58] D.C. Montgomery, *Design and Analysis of Experiments*, eight ed., John Wiley & Sons Inc, New Jersey, 2012.
- [59] K. Schumann, B. Unger, A. Brandt, F. Scheffler, Investigation on the pore structure of binderless zeolite 13× shapes, *Microporous and Mesoporous Materials*, 154 (2012) 119-123.
- [60] İ. Solmuş, C. Yamalı, B. Kaftanoğlu, D. Baker, A. Çağlar, Adsorption properties of a natural zeolite–water pair for use in adsorption cooling cycles, *Applied Energy*, 87 (2010) 2062-2067.
- [61] C. Lehmann, S. Beckert, R. Gläser, O. Kolditz, T. Nagel, Assessment of adsorbate density models for numerical simulations of zeolite-based heat storage applications, *Applied Energy*, 185, Part 2 (2017) 1965-1970.
- [62] Y. Liu, K.C. Leong, The effect of operating conditions on the performance of zeolite/water adsorption cooling systems, *Applied Thermal Engineering*, 25 (2005) 1403-1418.
- [63] J. Jänchen, H. Stach, Shaping adsorption properties of nano-porous molecular sieves for solar thermal energy storage and heat pump applications, *Solar Energy*, 104 (2014) 16-18.
- [64] P. Malbrunot, D. Vidal, J. Vermesse, R. Chahine, T.K. Bose, Adsorbent Helium Density Measurement and Its Effect on Adsorption Isotherms at High Pressure, *Langmuir*, 13 (1997) 539-544.

- [65] D.B. Riffel, U. Wittstadt, F.P. Schmidt, T. Núñez, F.A. Belo, A.P.F. Leite, F. Ziegler, Transient modeling of an adsorber using finned-tube heat exchanger, *International Journal of Heat and Mass Transfer*, 53 (2010) 1473-1482.
- [66] P. Tatsidjodoung, N. Le Pierrès, J. Heintz, D. Lagre, L. Luo, F. Durier, Experimental and numerical investigations of a zeolite 13X/water reactor for solar heat storage in buildings, *Energy Conversion and Management*, 108 (2016) 488-500.
- [67] L. Qiu, *Thermal Properties of Framework Materials: Selected Zeolites, Clathrates and an Organic Diol*, PhD thesis, Dalhousie University, Canada, 2000.
- [68] M. Winterberg, E. Tsotas, Correlations for effective heat transport coefficients in beds packed with cylindrical particles, *Chemical engineering science*, 55 (2000) 5937-5943.
- [69] A. Freni, B. Dawoud, L. Bonaccorsi, S. Chmielewski, A. Frazzica, L. Calabrese, G. Restuccia, *Characterization of Zeolite-based Coatings for Adsorption Heat Pumps*, Springer, New York, 2015.
- [70] L. Bonaccorsi, L. Calabrese, A. Freni, E. Proverbio, G. Restuccia, Zeolites direct synthesis on heat exchangers for adsorption heat pumps, *Applied Thermal Engineering*, 50 (2013) 1590-1595.

Annex A5

A5.1. Publications regarding DoE/RSM

Fig. A5.1 shows the evolution of the number of publications on DoE/RSM along the last 20 years, where a significant increase in the use of these methods can be observed in the last 10 years.

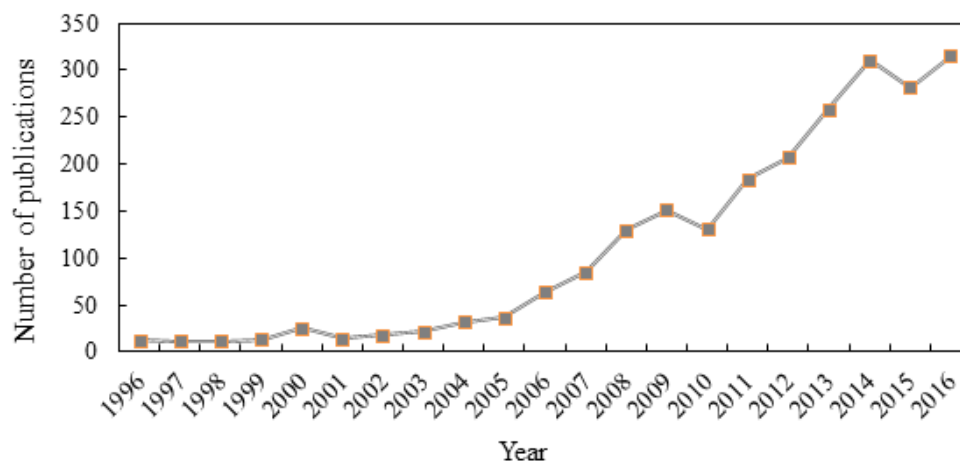


Fig. A5.1 - Evolution of the number of publications (regular articles and reviews) in the last 20 years, regarding the use of DoE/RSM. Data obtained from search in Scopus using the keywords: experimental design, design of experiments, response surface methodology.

A5.2. Mathematical modeling

A5.2.1. Model of the AHEx unit

The mathematical model of the unsteady state AHEx unit was written for a differential volume element of radial thickness dr , whose equations are given in Table A5.1, and the set of boundary conditions for each stage of the cycle are shown in Table A5.2. The startup cycle is initiated in the isobaric adsorption stage considering the values of $T_s(0, r) = T_v(0, r) = T_{\text{cond}}$, $P(0, r) \approx P_{\text{evap}}$ and $W(0, r) = W_{\text{ini}}$. In the remaining cycles, the final values of T_s , T_v , P and W of the isosteric cooling stage are the initial conditions for the adsorption step, whose final values are the initial conditions for the isosteric heating, etc.

The following simplifications were assumed in the model: (i) the bed is composed of uniformly-sized particles and its porosity is constant; (ii) there is resistance to mass transfer inside the particles; (iii) there is film resistance to heat transfer; (iv) the thermal conductivities and specific heat capacities of the solid and vapor, and the viscosity of the vapor are constants; (v) radiation heat transfer, viscous dissipation and the work done by pressure changes are negligible; (vi) the thermal resistance between the HTF and the adsorbent bed is negligible, and there are no losses to the environment.

A5.2.1.1. Validity of Darcy law for estimating the superficial velocity in the bed (u)

Darcy law describes correctly the velocity of water vapor through porous media in laminar flow conditions, which corresponds to Reynolds (Re) numbers up to about 10 [1]. Figs. A5.2(a) and (b) show, respectively, the average values of superficial velocity (\bar{u}) (calculated using Eq. (5.8)) and Reynolds number (\overline{Re}) in the bed of NaYBFK, for run 9 (Table 5.4), where laminar flow conditions are observed. Similar results were obtained for the remaining simulations.

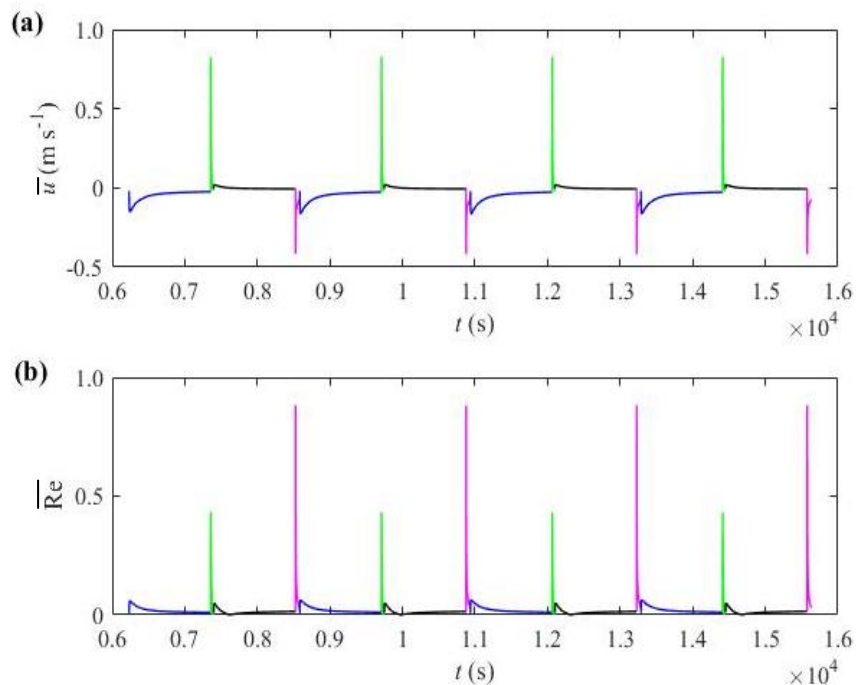


Fig. A5.2 – Average values of (a) superficial velocity of vapor in the bed and (b) Reynolds number ($\overline{Re} = \frac{\bar{u} \rho_v d_p}{(1-\varepsilon_b) \eta_v}$) along four cycles for run 9 using NaYBFK. Isobaric adsorption (—), isosteric heating (—), isobaric desorption (—), isosteric cooling (—).

Table A5.1 - Mathematical model of the AHEx unit investigated in this work.

Description	Equation	
Material balance to the adsorbent bed	$\varepsilon_b \frac{\partial \rho_v}{\partial t} + (1 - \varepsilon_b) \rho_s \frac{\partial W}{\partial t} + \frac{1}{r} \frac{\partial (r \rho_v u)}{\partial r} = 0$	(A5.1)
Material balance to the adsorbent particle - Linear Driving Force (LDF) model	$\frac{\partial W}{\partial t} = K_{LDF} (W_{eq} - W)$	(A5.2)
Energy balance to the adsorbent	$\rho_s (1 - \varepsilon_b) (C_{p,s} + W C_{p,a}) \frac{\partial T_s}{\partial t} = \frac{1}{r} \frac{\partial}{\partial r} \left(r \lambda_{eff,s} \frac{\partial T_s}{\partial r} \right) - a h_{sv} (T_s - T_v) + (1 - \varepsilon_b) \rho_s \frac{\partial W}{\partial t} Q_{ads}$	(A5.3)
Energy balance to the vapor	$\varepsilon_b \frac{\partial}{\partial t} (\rho_v C_{p,v} T_v) + \frac{1}{r} \frac{\partial}{\partial r} (r u \rho_v C_{p,v} T_v) - (1 - \varepsilon_b) \rho_s C_{p,v} \frac{\partial W}{\partial t} (T_s - T_v) = \frac{1}{r} \frac{\partial}{\partial r} \left(r \lambda_{eff,v} \frac{\partial T_v}{\partial r} \right) + a h_{sv} (T_s - T_v)$	(A5.4)
Momentum balance (Darcy Equation) ^(a)	$u = -\frac{K}{\eta_v} \frac{\partial P}{\partial r} \quad \text{with } K = \frac{d_p^2 \varepsilon_b^3}{150(1 - \varepsilon_b)^2}$	(A5.5)
External surface area of adsorbent spheres per unit bed volume	$a = \frac{6(1 - \varepsilon_b)}{d_p}$	(A5.6)
Dimensionless correlation for h_{sv} calculation ^(b)	$Nu = 2 + 1.8 Pr^{0.33} Re^{0.5}, \quad \text{with } Nu = \frac{d_p h_{sv}}{\lambda_v}, \quad Pr = \frac{\eta_v C_{p,v}}{\lambda_v}, \quad Re = \frac{u \rho_v d_p}{\eta_v}$	(A5.7)
Effective thermal conductivity of vapor	$\lambda_{eff,v} = \lambda_v \varepsilon_b$	(A5.8)

^(a) Equation available from ref. [2]. ^(b) Equations available from ref. [3].

Table A5.2 - Boundary conditions of the model of the adsorption unit investigated in this work.

Cycle stage	Inner boundary conditions ($r = R_i$) (HTF side)	Outer boundary conditions ($r = R_o$) (Water vapor side)
Isobaric adsorption (ADS)	$T_s(t, R_i) = T_v(t, R_i) = T_{\text{HTF,cool}}$ $\frac{\partial P}{\partial r}(t, R_i) = 0$ ^(a)	$\frac{\partial T_s}{\partial r}(t, R_o) = \frac{\partial T_v}{\partial r}(t, R_o) = 0$ ^(b) $P(t, R_o) = P_{\text{evap}}$
Isosteric heating (HEAT)	$T_s(t, R_i) = T_v(t, R_i) = T_{\text{HTF,hot}}$ $\frac{\partial P}{\partial r}(t, R_i) = 0$ ^(a)	$\frac{\partial T_s}{\partial r}(t, R_o) = \frac{\partial T_v}{\partial r}(t, R_o) = 0$ ^(b) $\frac{\partial P}{\partial r}(t, R_o) = 0$ ^(c)
Isobaric desorption (DES)	$T_s(t, R_i) = T_v(t, R_i) = T_{\text{HTF,hot}}$ $\frac{\partial P}{\partial r}(t, R_i) = 0$ ^(a)	$\frac{\partial T_s}{\partial r}(t, R_o) = \frac{\partial T_v}{\partial r}(t, R_o) = 0$ ^(b) $P(t, R_o) = P_{\text{cond}}$
Isosteric cooling (COOL)	$T_s(t, R_i) = T_v(t, R_i) = T_{\text{HTF,cool}}$ $\frac{\partial P}{\partial r}(t, R_i) = 0$ ^(a)	$\frac{\partial T_s}{\partial r}(t, R_o) = \frac{\partial T_v}{\partial r}(t, R_o) = 0$ ^(b) $\frac{\partial P}{\partial r}(t, R_o) = 0$ ^(c)

^(a) A zero pressure gradient is assumed since the wall of the HTF tube is impermeable ($u = 0 \text{ m s}^{-1}$).

^(b) Derivatives of T with respect to radial position are zero since that from R_o onwards there is no adsorbent bed (no heat transport by conduction). ^(c) Since the bed is isolated from both condenser and evaporator, no pressure gradient exists.

A5.2.2. Numerical approach and stopping criteria adopted in the simulations

The highly coupled and non-linear set of partial differential equations governing the adsorption cycle were solved by the method of lines [4]. The radial direction was discretised using a second-order finite difference scheme, and the resulting set of ordinary differential equations was integrated along time using a variable order solver based on numerical differentiation formulas [5]. The computer simulation program was written in Matlab and validated previously using literature data [6].

In order to ensure that the results of COP and SHP were independent of the grid size, a number of points of discretization ranging from 35 to 100 was adopted in the simulations, which allowed a good trade-off between accuracy and computational cost.

Different stopping criteria were applied for the four steps of the heating cycle. For the isobaric adsorption and desorption stages, the integration was stopped when time was $\frac{1}{2} t_{\text{ADS+DES}}$. In the isosteric stages, the stopping criteria were defined in terms of pressure: the simulation stopped when the average pressure in the bed (\bar{P}) was equal to P_{cond} or P_{evap} in the isosteric heating and cooling stages, respectively.

A5.3. Estimation and measurement of properties of the zeolites

A5.3.1. Textural properties

The adsorption-desorption isotherms of nitrogen on the zeolites NaYBFK and 13XB at 77 K are given in Figs. A5.3 and A5.4, respectively, where no significant hysteresis effects are observed. The materials exhibit Type I N_2 adsorption isotherms, characteristic of microporous materials, according to the IUPAC classification. From the data in Table A5.3, the microcrystalline materials possess high S_{BET} (somewhat higher in the case of NaYBFK) and low S_{ext} , and, for each material, V_{micro} is similar to V_p , indicating that both possess essentially an internal micropore structure.

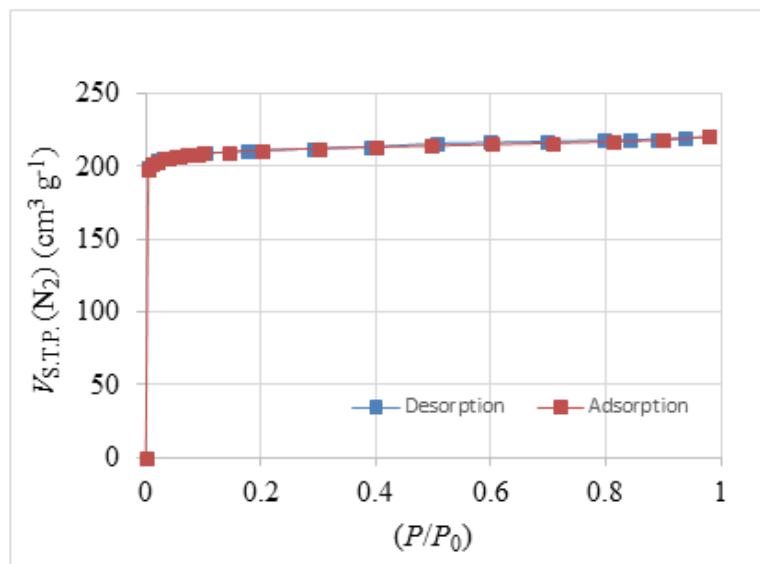


Fig. A5.3 – Nitrogen adsorption-desorption isotherms at 77 K, for zeolite NaYBFK.

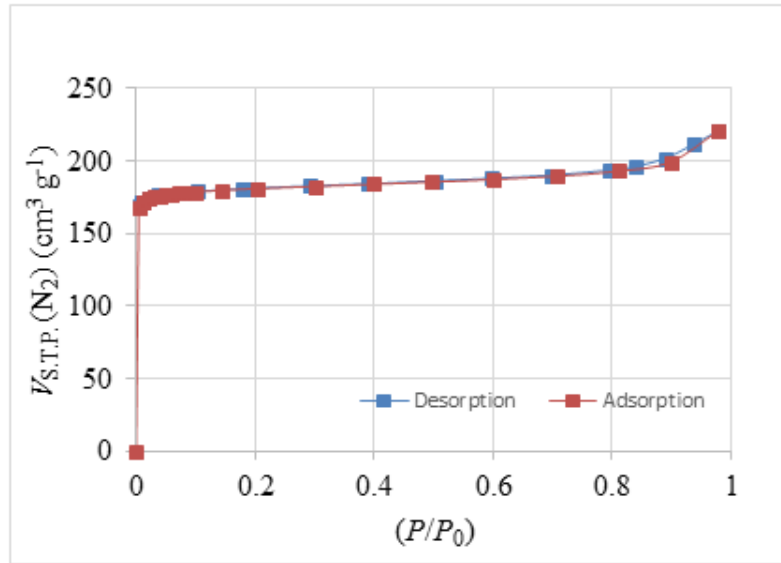


Fig. A5.4 – Nitrogen adsorption-desorption isotherms at 77 K, for zeolite 13XB.

Table A5.3- Textural properties of NaYBFK and 13XB obtained from N₂ adsorption isotherms at 77 K.

Sample	S_{BET} ($\text{m}^2 \text{g}^{-1}$)	V_{p} ($\text{cm}^3 \text{g}^{-1}$)	V_{micro} ($\text{cm}^3 \text{g}^{-1}$)	S_{ext} ($\text{m}^2 \text{g}^{-1}$)
NaYBFK	870	0.34	0.32	17
13XB	739	0.34	0.27	30

A5.3.2. Isothermic heats of adsorption (Q_{ads})

The values of Q_{ads} at half coverage ($W = W_{\theta=0.5}$) for NaYBFK and 13XB were estimated using the isotherm equations obtained in this work (Table 5.2, Eqs. (5.12) and (5.13), respectively) and the Clausius-Clapeyron model, which is given by,

$$\left[\frac{\partial \ln P}{\partial \left(\frac{1}{T} \right)} \right]_W = - \frac{Q_{\text{ads}} M}{\mathfrak{R}} \quad (\text{A5.9})$$

The plots of $\ln(P)$ versus $1/T$ obtained for NaYBFK and 13XB in the range 308.15 - 448.15 K are shown in Figs. A5.5 and A5.6, respectively. The Q_{ads} considered in the simulations for 13XBFK is the value at half coverage ($W \sim 0.170 \text{ kg kg}^{-1}$) reported by B. Mette *et al.* [7] (see Fig. 2 of that work).

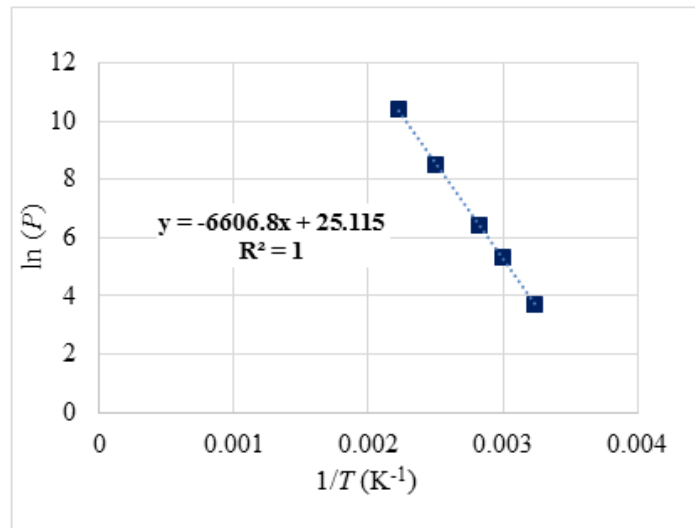


Fig. A5.5 – Relation between $\ln(P)$ and $1/T$ obtained for NaYBFK in the range 308.15 - 448.15 K at half coverage ($W = 0.151 \text{ kg kg}^{-1}$), for estimating Q_{ads} using Eq. (A5.9).

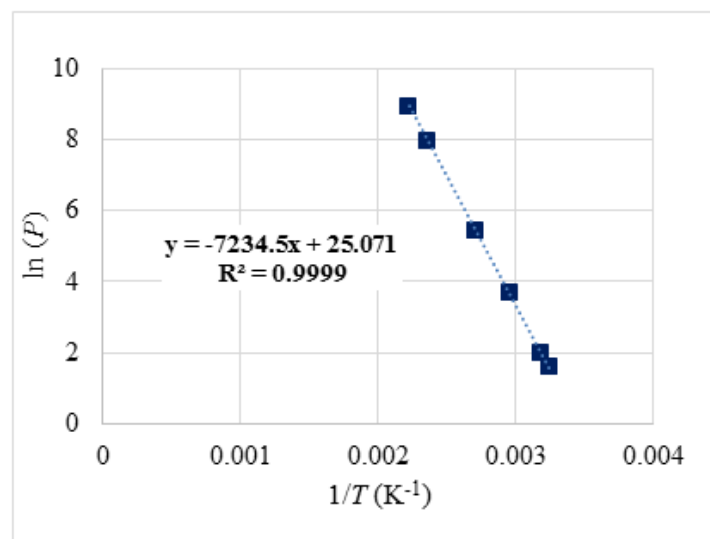


Fig. A5.6 – Relation between $\ln(P)$ and $1/T$ obtained for 13XB in the range 308.15 - 448.15 K at half coverage ($W = 0.116 \text{ kg kg}^{-1}$), for estimating Q_{ads} using Eq. (A5.9).

A5.3.3. Intraparticle mass transfer kinetics

A5.3.3.1. Estimation of the mass transfer resistances in a bidisperse particle

When using the linear driving force (LDF) model for bidisperse pore structures, where both macropore and micropore diffusion occurs, the global mass transfer coefficient (K_{LDF}) may be estimated using Eq. (A5.10), which represents an additivity of mass transfer resistances [8]:

$$\frac{1}{K_{\text{LDF}}} = \frac{H}{k_f a_p} + \frac{HR_p^2}{\Omega D_{\text{eff}}} + \frac{R_c^2}{\Omega D_c} \quad (\text{A5.10})$$

where $\frac{H}{k_f a_p}$ is the term of resistance in the film around the particle, $\frac{HR_p^2}{\Omega D_{\text{eff}}}$ regards the resistance in macropores and mesopores, and $\frac{R_c^2}{\Omega D_c}$ is the term of resistance inside the micropores. For pure component as in this case, where only water vapor is present, the first term of Eq. (A5.10) is zero. The effective diffusivity (D_{eff}) includes Knudsen diffusivity (D_K), which prevails in mesopores, and molecular diffusivity (D_m), which dominates in macropores, and it is computed as follows [8],

$$D_{\text{eff}} = \frac{\varepsilon_p}{\tau_p} \left(\frac{1}{D_K} + \frac{1}{D_m} \right)^{-1} \quad (\text{A5.11})$$

The D_K and D_m expressed in $\text{m}^2 \text{s}^{-1}$ are given by [8, 9],

$$D_K = 0.97 \bar{r}_{\text{pore}} \left(\frac{T}{M} \right)^{1/2} \quad (\text{A5.12})$$

$$D_m = 2.628 \times 10^{-7} \frac{\sqrt{T^3/M}}{P \sigma^2 \Omega^{(1,1)}(T^*)}, \text{ where } T^* = T \frac{k}{\xi} \quad (\text{A5.13})$$

where the molar mass (M) is in g/mol, the pressure (P) is in atm, the temperature (T) is in K, the average pore radius (\bar{r}_{pore}) is in cm, the potential energy parameter (σ) is in Å, and

the collision integral ($\Omega^{(1,1)}$) is dimensionless ($\Omega^{(1,1)}$ vs T^* plot is given in Section 3.3.2.2, Fig. A5.8). The equilibrium constant H in Eq. (A5.10) is obtained as follows:

$$H = \rho_p \frac{\Re T}{M} \frac{\partial W_{\text{eq}}}{\partial P} \quad (\text{A5.14})$$

and, for NaYBFK/water pair, the isotherm derivative in relation to pressure ($\frac{\partial W_{\text{eq}}}{\partial P}$) is computed as,

$$\frac{\partial W_{\text{eq}}}{\partial P} = 0.301 \left\{ \exp \left[-2.62 \times 10^{-8} \left(T \ln \frac{P_{\text{sat}}}{P} \right)^{2.33} \right] \times \frac{6.10 \times 10^{-8} T^{2.33}}{P} \left(\ln \frac{P_{\text{sat}}}{P} \right)^{1.33} \right\} \quad (\text{A5.15})$$

The water vapor diffusivity in the micropores of NaYBFK (D_c) was calculated using an equation fitted to the data reported by Demontis *et al.* [10] for zeolite NaY (see Table S3 of that work) in the range 330 – 530 K, at half coverage, as shown in Fig. A5.7.

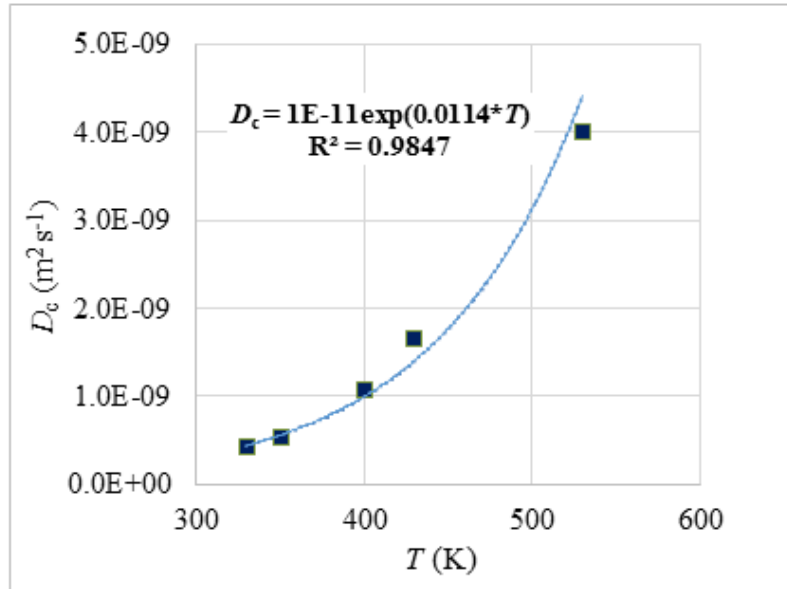


Fig. A5.7 – Intracrystalline diffusivity (D_c) of water vapor in zeolite NaY as function of temperature in the range 330 – 530 K, at half coverage. Data from ref. [10] (■) and fitting (—).

From Fig. 5.2(a), the average crystallite size was assumed to be $R_c = 0.2 \mu\text{m}$ for estimating the mass transfer resistance inside the micropores (last term of Eq. (A5.10)). The values obtained for the terms of mass transfer resistances in the macropores and mesopores $\left(\frac{HR_p^2}{\Omega D_{\text{eff}}}\right)$ and in micropores $\left(\frac{R_c^2}{\Omega D_c}\right)$ of NaYBFK, along with the values of all the parameters necessary for their estimations are given in Table A5.4.

Table A5.4 – Values of the terms of Eq. (A5.10) that regard the mass transfer resistances inside macropores and mesopores $\left(\frac{HR_p^2}{\Omega D_{\text{eff}}}\right)$ and micropores $\left(\frac{R_c^2}{\Omega D_c}\right)$ of a bidisperse particle, calculated for NaYBFK in this work, along with the values of the parameters considered for their estimations.

Parameter	Value	Reference
T (K)	308.15	---
P (Pa)	870	---
H	4515	This work
R_p (m)	2.5×10^{-4}	---
R_c (m)	0.1×10^{-6}	This work
Ω	15 (for spheres)	[8]
ε_p	0.55	This work
τ_p	3.8	
\bar{r}_{pore} (cm)	2.5×10^{-5}	[11]
σ (Å)	2.641	[9]
$\Omega^{(1,1)}(T^* = 0.81)$	1.6015 ^(a)	
D_K (m ² s ⁻¹)	1.00×10^{-4}	This work
D_m (m ² s ⁻¹)	3.47×10^{-3}	
D_{eff} (m ² s ⁻¹)	1.40×10^{-5}	
D_c (m ² s ⁻¹)	3.35×10^{-10}	
$\frac{HR_p^2}{\Omega D_{\text{eff}}}$ (s)	1.35	
$\frac{R_c^2}{\Omega D_c}$ (s)	1.99×10^{-6}	
K_{LDF} (s ⁻¹)	7.41×10^{-1}	

^(a) Calculated from the equation reported in Fig. A5.8 (Section A5.3.3.2.2).

The results reported in Table A5.4 show that the resistance to mass transfer inside macropores and mesopores largely superimposes that in the micropores, and the same conclusions were obtained for the remaining adsorbents under study. The Eq. (A5.10) discarding the terms of film resistance to mass transfer and resistance in micropores was then used to estimate the K_{LDF} values in the simulations.

A5.3.3.2. Properties necessary for the estimation of K_{LDF} in the simulations

A5.3.3.2.1. Density, porosity and tortuosity of the adsorbent particles

For the zeolites 13XB and NaYBFBK, the particle density (ρ_p), porosity (ε_p) and tortuosity (τ_p) reported in Table 5.3 and used in Eq. (5.14) (Table 5.2) were obtained as follows [8], respectively,

$$\rho_p = \frac{\rho_b}{1 - \varepsilon_b} \quad (A5.16)$$

$$\varepsilon_p = 1 - \frac{\rho_p}{\rho_s} \quad (A5.17)$$

$$\tau_p = \frac{(2 - \varepsilon_p)^2}{\varepsilon_p} \quad (A5.18)$$

where $\rho_b = 670 \text{ kg m}^{-3}$ for both 13XB and NaYBFBK (average between 630 and 710 kg m^{-3}), as indicated by the suppliers.

A5.3.3.2.2. Knudsen (D_K) and molecular (D_m) diffusivities

The contribution of Knudsen diffusivity for Eq. (5.14) (Table 5.2) was calculated using Eq. (A5.12) (Section A5.3.3.1), for which the average pore radius (\bar{r}_{pore}) of the particles is needed. For NaYBFBK and 13XB, \bar{r}_{pore} of 2.5×10^{-5} and 0.75×10^{-5} cm were used, respectively, based on mercury porosimetry data reported in refs. [11] and [12], while for

13XBFK, $\bar{r}_{\text{pore}} = 1.5 \times 10^{-5}$ cm was considered according to ref. [7]. The values of D_m for Eq. (5.14) (Table 5.2) were obtained from Eq. (A5.13) using $\sigma = 2.641 \text{ \AA}$ and $\frac{k}{\xi} = 1/380 \text{ K}^{-1}$, as reported for water in ref. [9]. Fig. A5.8 shows the values of $\Omega^{(1,1)}$ as function of T^* ($T^* = T \frac{k}{\xi}$), collected from ref. [9], along with the fitting of a polynomial to the data, that was used to calculate $\Omega^{(1,1)}$ as function of T in the simulations.

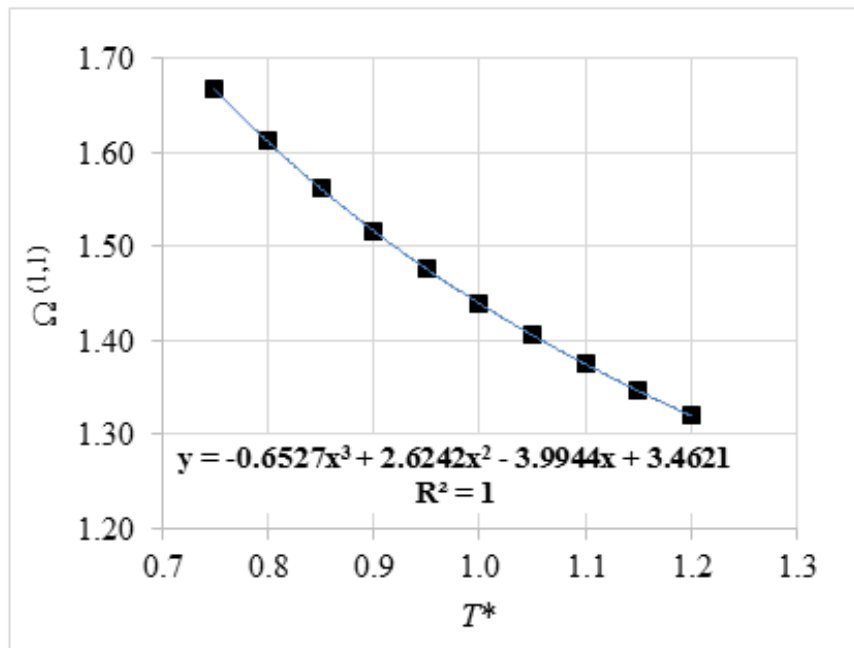


Fig. A5.8 - Values of $\Omega^{(1,1)}$ as function of T^* for determining D_m using Eq. (A5.13). Data from ref. [9] (■) and fitting (—). The minimum and maximum temperatures of the bed covered by the statistical study correspond, respectively, to T^* of 0.81 and 1.18 (308.15 and 448.15 K).

A5.3.4. Solid densities (ρ_s) determined by helium pycnometry

The raw data obtained from the helium pycnometry for determining ρ_s of NaYBFK and 13XB are given in Table A5.5.

Table A5.5 – Raw data obtained in this work by helium pycnometry to determine ρ_s of NaYBFK and 13XB.

Adsorbent	m (g)	V_{sc} (cm ³)	V_{ec} (cm ³)	P_1 (psi)	P_2 (psi)	V_s (cm ³)	V_s (cm ³) (average)	ρ_s (kg/m ³)
NaYBFK	3.158	12.851	5.324	15.154	4.778	1.289	1.276	2475
				15.225	4.795	1.270		
				15.637	4.924	1.268		
13XB	3.008	12.851	5.234	15.182	4.776	1.251	1.229	2447
				15.417	4.837	1.206		
				15.591	4.899	1.231		

The m is the mass of the sample, V_{sc} denotes the volume of the sample chamber, V_{ec} is the volume of the expansion chamber, P_1 is the pressure in the sample chamber after pressurization, P_2 is the pressure in the sample chamber after opening the expansion valve, and V_s is the volume of the solid (excluding intra and inter-particle pores). From V_s and m , the densities are determined. The values of V_s used to calculate ρ_s of each adsorbent are the mean values of three replicates.

A5.3.5. Thermophysical data of NaYBFK and 13XB

A5.3.5.1. Effective thermal conductivities ($\lambda_{eff,s}$)

The $\lambda_{eff,s} = f(T)$ measured for NaYBFK and for 13XB using the Gustafsson probe method in the range 298.15-388.15 K are listed in Table A5.6 (the results are mean values of ten replicates).

Table A5.6 – Effective thermal conductivities ($\lambda_{\text{eff},s}$) of NaYBFK and 13XB as function of temperature in the range 298.15-388.15 K, measured in this work using the Gustafsson probe method.

T (K)	$\lambda_{\text{eff},s}$ (W m⁻¹ K⁻¹)	
	NaYBFK	13XB
298.15	0.240	---
303.15	---	0.260
308.15	---	0.261
318.15	0.251	0.264
333.15	0.258	0.267
358.15	0.270	0.272
368.15	---	0.274
383.15	---	0.282
388.15	0.297	---

A5.3.5.2. Specific heat capacities of zeolites ($C_{p,s}$)

Figs. A5.9 and A5.10 show the values of $C_{p,s}$ as function of temperature reported by L. Qiu [13] for NaY and NaX dehydrated zeolite powders, along with the polynomial equations fitted to the experimental data; the relation between $C_{p,s}$ and T may be represented by the following empirical equation [13]:

$$C_{p,s} = a_0 + a_1T + a_2T^2 + \dots + a_nT^n \quad (\text{A5.19})$$

where, a_0, a_1, a_2 and a_n are model coefficients. The values of $C_{p,s}$ considered in the simulations for zeolites NaYBFK and 13XB were average constant values between the minimum and the maximum temperatures of the bed, and were obtained by extrapolation using the fitted polynomial equations.

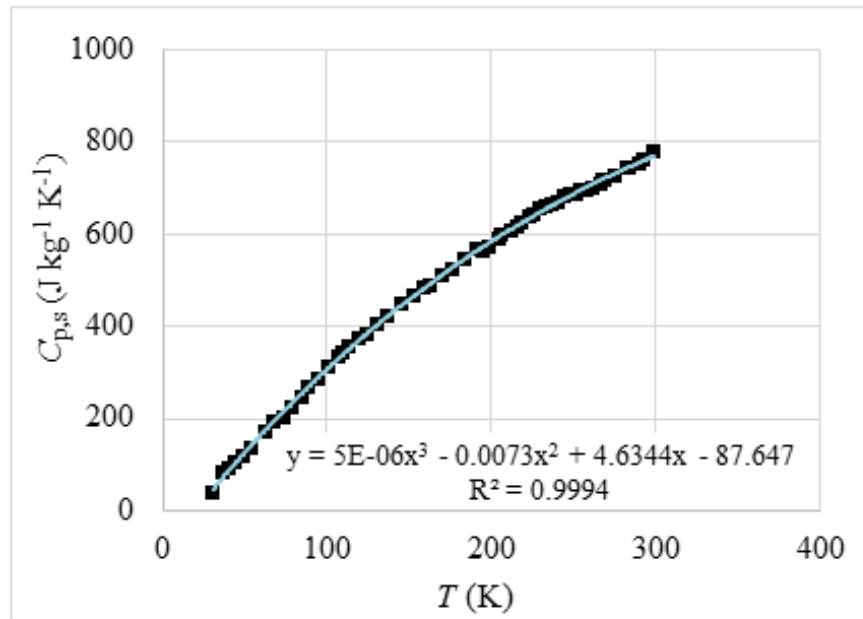


Fig. A5.9 – Specific heat capacity ($C_{p,s}$) of dehydrated zeolite NaY as function of temperature. Experimental data in range 30.8 – 298.5 K from ref. [13] (■) and fitting (—).

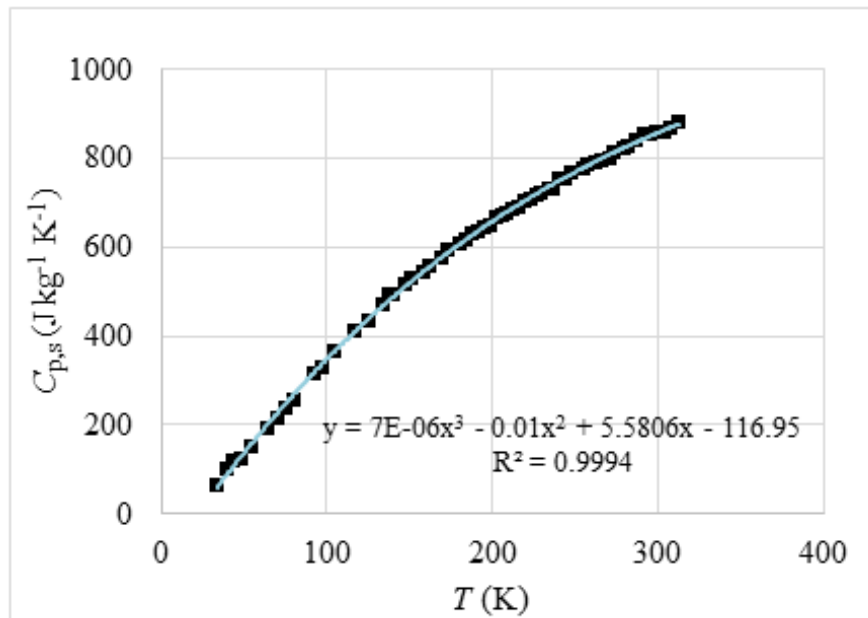


Fig. A5.10 – Specific heat capacity ($C_{p,s}$) of dehydrated zeolite NaX as function of temperature. Experimental data in range 33.7 – 312.3 K from ref. [13] (■) and fitting (—).

A5.4. Simulation results and statistical outcomes from DoE/RSM

A5.4.1. Evolution of $\frac{D_{\text{eff}}}{H}$ along adsorption and desorption stages

Fig. A5.11 shows the variation of $\frac{D_{\text{eff}}}{H}$ with \bar{T} along the isobaric adsorption (Fig. A5.11(a)) and desorption (Fig. A5.11(b)) stages, for the run 25 using NaYBFK.

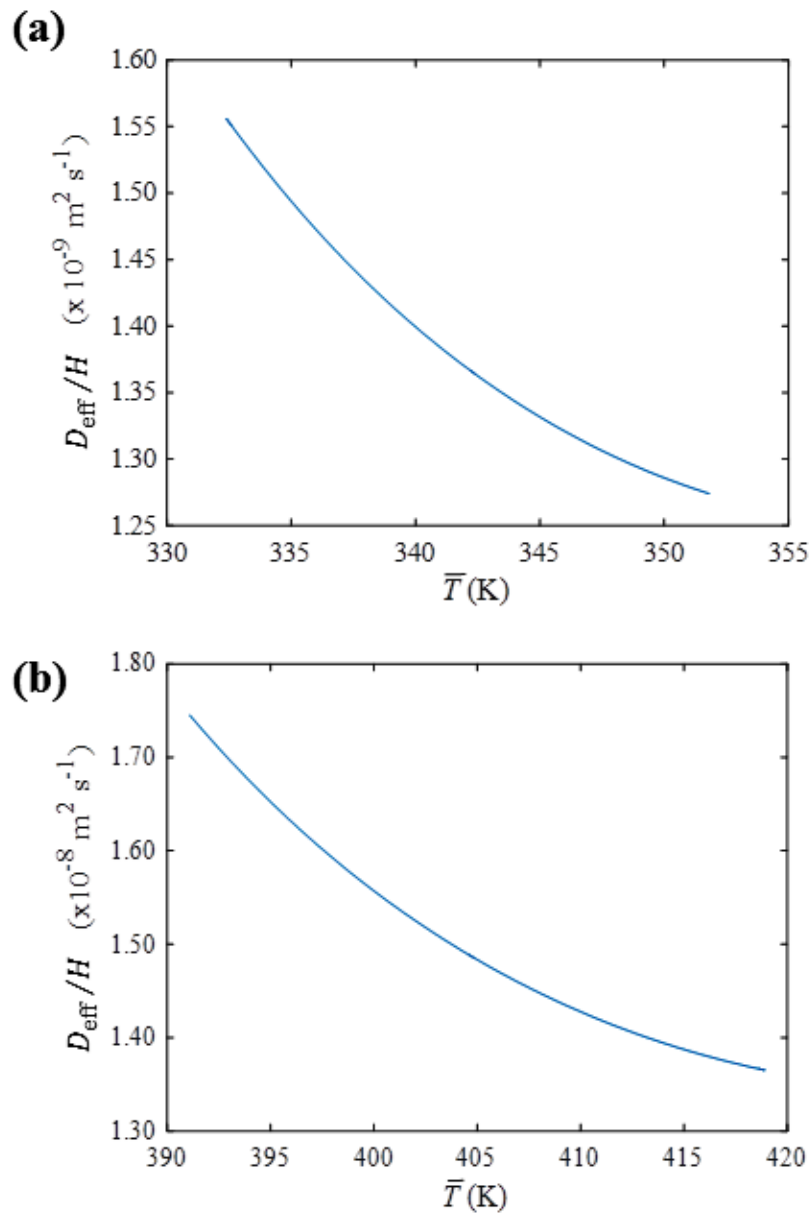


Fig. A5.11 – $\frac{D_{\text{eff}}}{H}$ as function of the average bed temperature along (a) isobaric adsorption and (b) isobaric desorption stages of run 25 using NaYBFK.

A decrease of $\frac{D_{\text{eff}}}{H}$ with \bar{T} can be observed, since that the increase of H in the denominator is more pronounced than that of D_{eff} in the numerator. In the adsorption stage, $\frac{D_{\text{eff}}}{H}$ ranges from *ca.* 1.27×10^{-9} to $1.55 \times 10^{-9} \text{ m}^2 \text{ s}^{-1}$ (\bar{T} decreases with time), while in the desorption it is higher and varies between *ca.* 1.75×10^{-8} and $1.35 \times 10^{-8} \text{ m}^2 \text{ s}^{-1}$ (\bar{T} enhances along time). This trend is different from that of diffusivity in micropores (D_c), which presents an exponential dependence on temperature (Fig. A5.7).

A5.4.2. Pareto charts

Figs. A5.12 and A5.13 show the Pareto charts of COP and SHP for 13XBFK and 13XB considering the Box-Behnken design matrix in Table 5.4, where the main factors affecting the performance are ranked, for an interval of confidence of 95 %.

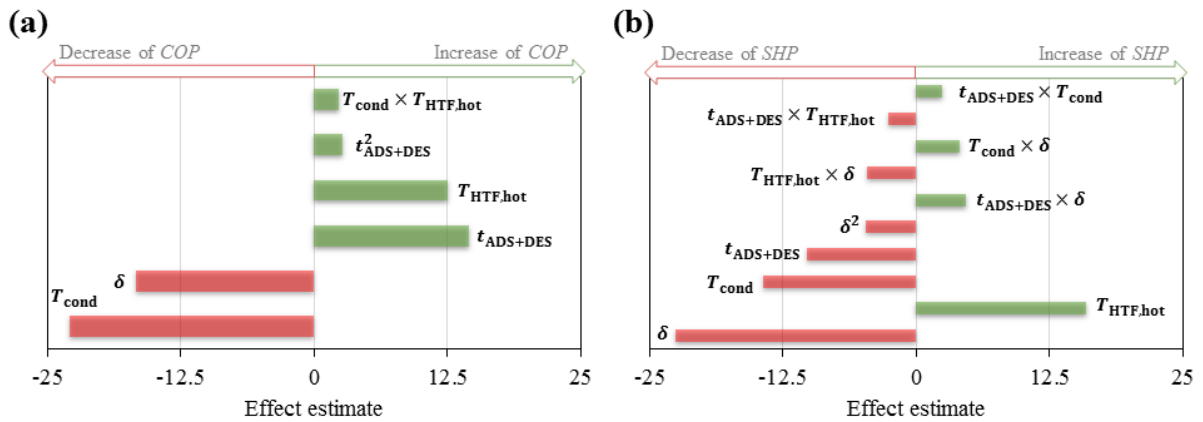


Fig. A5.12 - Pareto charts of (a) COP and (b) SHP obtained for 13XBFK considering the Box-Behnken design of Table 5.4 with confidence interval of 95 %.

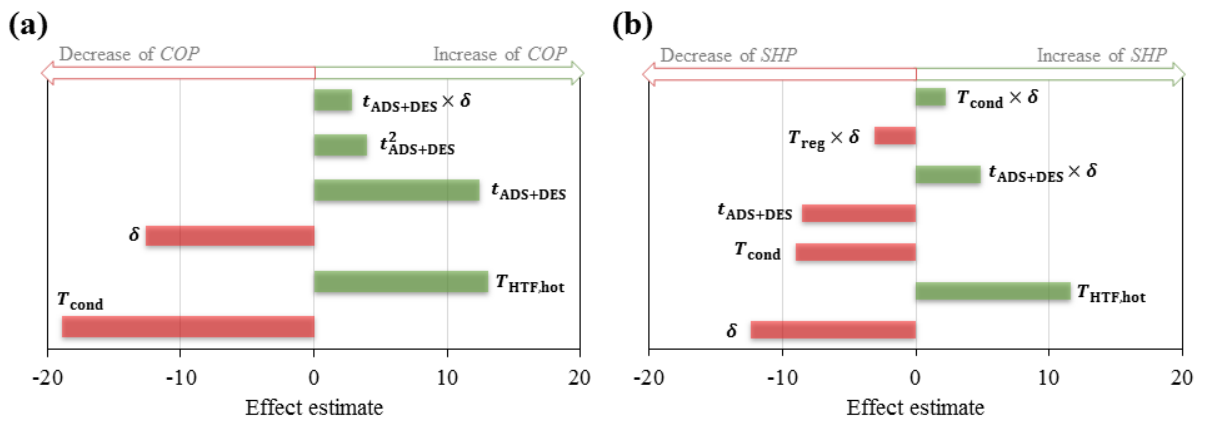


Fig. A5.13 - Pareto charts of (a) *COP* and (b) *SHP* obtained for 13XB considering the Box-Behnken design of Table 5.4 with confidence interval of 95 %.

Nomenclature

a	External surface area of adsorbent per unit bed volume ($\text{m}^2 \text{m}^{-3}$)
a_p	Volumetric external surface area of the grains ($\text{m}^2 \text{m}^{-3}$)
C_p	Specific heat capacity ($\text{J kg}^{-1} \text{K}^{-1}$)
COP	Coefficient of performance
d_p	Adsorbent particle diameter (m)
D_c	Intracrystalline diffusivity ($\text{m}^2 \text{s}^{-1}$)
D_{eff}	Effective diffusivity ($\text{m}^2 \text{s}^{-1}$)
D_K	Knudsen diffusivity ($\text{m}^2 \text{s}^{-1}$)
D_m	Molecular diffusivity ($\text{m}^2 \text{s}^{-1}$)
h_{sv}	Solid/vapor convective heat transfer coefficient ($\text{W m}^{-2} \text{K}^{-1}$)
H	Equilibrium constant
HTF	Heat transfer fluid
k_f	Convective mass transfer coefficient (m s^{-1})
K	Permeability of the adsorbent bed (m^2)
K_{LDF}	LDF global mass transfer coefficient (s^{-1})
m	Mass (kg)
M	Molar mass of adsorbate (kg mol^{-1})
Nu	Nusselt number
P	Pressure (Pa)
P_1	Pressure in the sample chamber after pressurization in the helium pycnometry (psi)
P_2	Pressure in the sample chamber after opening the expansion valve in the helium pycnometry (psi)
Pr	Prandtl number
Q	Heat (J)
Q_{ads}	Isosteric heat of adsorption (J kg^{-1})
r	Spatial coordinate (m)
\bar{r}_{pore}	Average pore radius (cm)
R	Radial position in the adsorbent bed (m)

\mathfrak{R}	Universal gas constant ($\text{J mol}^{-1} \text{K}^{-1}$).
R_c	Adsorbent crystal radius (m)
R_p	Adsorbent particle radius (m)
Re	Reynolds number
SHP	Specific heating power (W kg^{-1})
t	Time (s)
T	Temperature (K)
T^*	Reduced temperature
$T_{HTF,cool}$	Temperature of the cool heat transfer fluid (K)
$T_{HTF,hot}$	Temperature of the hot heat transfer fluid (K)
u	Fluid superficial velocity (m s^{-1})
V_{ec}	Volume of the expansion chamber in the helium pycnometry (cm^3)
V_s	Volume of the adsorbent (excluding intra and inter-particle pores) (cm^3)
V_{sc}	Volume of the sample chamber in the helium pycnometry (cm^3)
$V_{S.T.P.}$	Volume adsorbed at standard temperature and pressure ($\text{cm}^3 \text{g}^{-1}$)
W	Adsorbate loading (kg kg^{-1})

Greek symbols

ΔH_c	Latent heat of condensation (J kg^{-1})
$\Delta \bar{W}_{cycle}$	Cyclic average adsorption loading swing (kg kg^{-1})
η	Dynamic viscosity ($\text{kg m}^{-1} \text{s}^{-1}$)
ε_b	Porosity of the bed
ε_p	Porosity of the particle
λ	Thermal conductivity ($\text{W m}^{-1} \text{K}^{-1}$)
σ	Potential energy parameter (\AA)
Ω	Constant dependent on the particle geometry
$\frac{\xi}{k}$	Potential energy parameter (K)
$\Omega^{(1,1)}$	Collision integral
ρ	Density (kg m^{-3})

ρ_p	Particle density (kg m^{-3})
τ_p	Tortuosity of the particle
φ	Generic notation of T , W and P
$\bar{\varphi}$	Generic notation of \bar{T} , \bar{W} and \bar{P}

Subscripts

a	Adsorbate
ADS	Isobaric adsorption stage
b	Bulk
cond	Condenser
COOL	Isosteric cooling stage
DES	Isobaric desorption stage
eff	Effective
eq	Equilibrium
evap	Evaporator
fin	Final
HEAT	Isosteric heating stage
i	Internal boundary of the bed
ini	Initial
max	Maximum
min	Minimum
o	External boundary of the bed
s	Adsorbent
sat	Saturation
v	Vapor phase

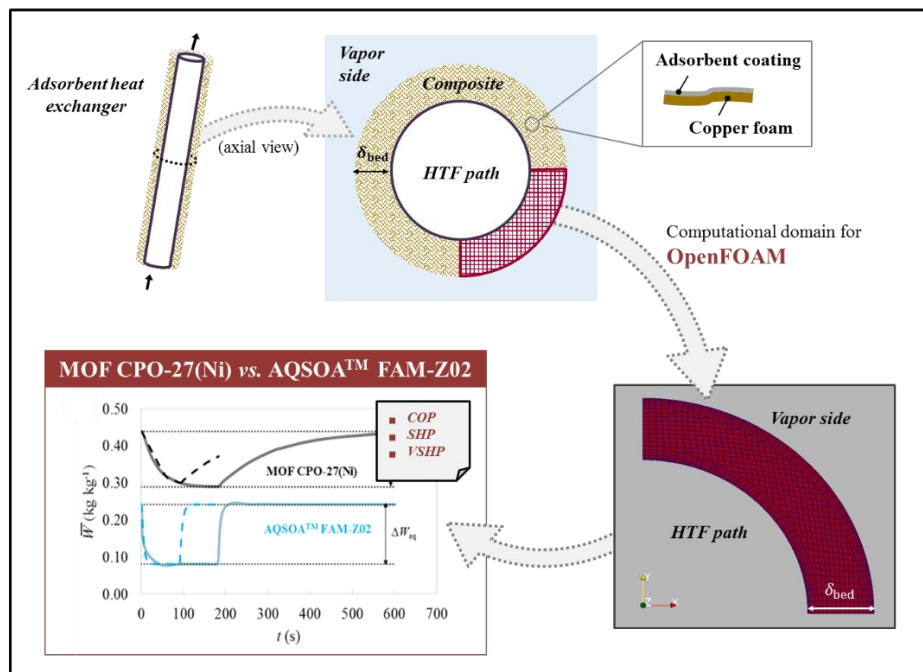
References

- [1] N.D. Nevers, Fluid Mechanics For Chemical Engineers, second ed., McGraw-Hill, Singapore, 1991.
- [2] J.O. Wilkes, S.G. Bike, Fluid Mechanics for Chemical Engineers, second ed., Prentice Hall PTR, New Jersey, 1999.
- [3] A. Bejan, Convection Heat Transfer, first ed., John Wiley & Sons, New York, 1984.
- [4] W.E. Schiesser, The Numerical Method of Lines: Integration of Partial Differential Equations, third ed., Academic Press, San Diego, 1991.
- [5] J.D. Hoffman, S. Frankel, Numerical Methods for Engineers and Scientists, second ed., Taylor & Francis, New York, 2001.
- [6] İ. Solmuş, D.A.S. Rees, C. Yamalı, D. Baker, B. Kaftanoğlu, Numerical investigation of coupled heat and mass transfer inside the adsorbent bed of an adsorption cooling unit, *International Journal of Refrigeration*, 35 (2012) 652-662.
- [7] B. Mette, H. Kerskes, H. Drück, H. Müller-Steinhagen, Experimental and numerical investigations on the water vapor adsorption isotherms and kinetics of binderless zeolite 13X, *International Journal of Heat and Mass Transfer*, 71 (2014) 555-561.
- [8] J.P.S. Aniceto, C.M. Silva, Preparative Chromatography: batch and continuous, in: *Analytical Separation Science*, Vol. 4, Wiley, Germany, 2015.
- [9] J.O. Hirschfelder, C.F. Curtiss, R.B. Bird, *Molecular theory of gases and liquids*, Wiley, New York, 1954.
- [10] P. Demontis, H. Jobic, M.A. Gonzalez, G.B. Suffritti, Diffusion of Water in Zeolites NaX and NaY Studied by Quasi-Elastic Neutron Scattering and Computer Simulation, *The Journal of Physical Chemistry C*, 113 (2009) 12373-12379.
- [11] K. Schumann, B. Unger, A. Brandt, G. Fischer, H. Richter, J. Jänchen, Preparation and Characterization of Compact Binderless Zeolite Shapes with Faujasit and Linde Type A Structure, *Chemie Ingenieur Technik*, 86 (2014) 106-111.
- [12] G. Storch, G. Reichenauer, F. Scheffler, A. Hauer, Hydrothermal stability of pelletized zeolite 13X for energy storage applications, *Adsorption*, 14 (2008) 275-281.
- [13] L. Qiu, *Thermal Properties of Framework Materials: Selected Zeolites, Clathrates and an Organic Diol*, PhD thesis, Dalhousie University, Canada, 2000.

Chapter 6: Computer simulation using OpenFOAM[†]

The performance of the metal-organic framework (MOF) CPO-27(Ni) for adsorption heat pumps using water as adsorbate was investigated through modeling and Computational Fluid Dynamics (CFD) simulations. A customized solver and methodology for simulating adsorption cycles was developed in OpenFOAM and validated using literature data. Due to the potential of adsorbent coatings and metal fibers and foams for improving the performance of such processes, a metal tube of copper, surrounded by a composite of copper foam and CPO-27(Ni) coating, was considered in this study.

For evaporation, condensation and bed regeneration temperatures of 278.15 K, 308.15 K and 368.15 K, respectively, the obtained coefficients of performance and specific heating powers for the composite coating CPO-27(Ni)/copper foam were in the range 1.16-1.39 and 1922-5130 W kg⁻¹. Under similar conditions, the MOF performance was outperformed by the well-known adsorbent AQSOA[™] FAM-Z02, chosen as benchmark material. This was essentially due to the faster intraparticle mass transfer kinetics of the benchmark material. CPO-27(Ni) seems more likely to be applied in systems in which the coefficient of performance is the key factor rather than the power.



[†] Based on:

Joana M. Pinheiro, Sérgio Salústio, Vítor Geraldês, Anabela A. Valente, Carlos M. Silva, Copper foam coated with CPO-27(Ni) metal-organic framework for adsorption heat pump: simulation study using OpenFOAM (submitted).

6.1. Introduction

The demands of a growing global population with rapidly changing consumption patterns for food, mobility and energy are exerting ever-increasing pressure on ecosystems and their life-supporting services [1]. Climate changes are also caused by human activities, primarily greenhouse gas emissions [1]. For mitigating this problem, the European Commission (EU) has defined an energy strategy for the period 2020-2030, which targets: a 40 % cut in greenhouse gas emissions compared to 1990 levels; at least a 27 % share of renewable energy consumption; at least 27 % energy savings compared with the business-as-usual scenario [2]. Buildings are a key element of European energy policies due to the high energy consumption (commercial and residential buildings consume *ca.* 40 % of the primary energy and are responsible for 24 % of greenhouse gas emissions) and the potential for energy savings [3, 4]. The creation of very high energy performance buildings, requiring nearly zero or very low energy consumption, which is essentially covered by renewable sources – the well-known nearly zero energy buildings (NZEBs) –, has been pointed as decisive for sustainable development in this sector [3, 4].

Heat pumps have been considered an excellent choice for NZEBs [5]. Several heat pumping concepts and technologies have been investigated in this scope, including adsorption heat pumps (AHPs) [5, 6]. AHPs are sustainable alternatives to the conventional vapor-compression heat pumps, as they are powered by thermal energy (*e.g.*, waste heat, solar) instead of electricity, and operate with eco-friendly fluids such as water, instead of fluorocarbon type refrigerants [7, 8]. In the case of AHPs for heating applications, heat at a high temperature level is used to transform heat from a low to a medium temperature level, which is the “useful” heat for the customer [9]. Details on the working-principles of AHPs can be found elsewhere [10, 11].

So far the market penetration of AHPs has been small, essentially due to the high costs and significant dimensions of the appliances, along with lower thermal efficiency than, for example, absorption heat pumps, and operation within a narrow window of conditions [12, 13]. Since the AHPs efficiency and cost-effectiveness are governed by the performance of the adsorbents, and by the heat and mass transfer processes within the adsorbent heat exchanger (AHEx), the optimization of the operating conditions and the development of efficient adsorbents are necessary to improve the overall performance of AHPs [12, 14].

Among the identified R&D priorities for AHPs are the development of compact, lightweight, and high surface area AHExs, where the adsorbent is applied in coating configurations to obtain enhanced heating power and compact designs [12]. Recently, Wittstadt *et al.* [15] reported on promising AHExs, such as a flat tube fin heat exchanger with binder-based coating, and an aluminum fiber type heat exchanger with direct adsorbent coating. The use of directly coated metal fibers [15] or foams [16] presents as advantages: high specific surface area available for coating, enhancing the adsorbent mass per unit volume; significant bed porosity that enables good vapor permeability; improved bed thermal conductivity due to the tight contact between the coating and the metal, and the good thermal conductivity of the metal itself.

With respect to the adsorbents, activated carbons, silica gels, silicoaluminophosphates and zeolites are applied nowadays in adsorption heat/cooling, with highlight to AQSOA™ FAM-Z02 (a SAPO-34 developed by Mitsubishi Chemical), which is considered very promising for such applications [12, 14, 17]. Metal-organic frameworks (MOFs) are receiving increasing scientific attention in the field of AHPs, since they may feature potential for energy efficiency and cost improvements [12-14]. MOFs consist of inorganic moieties linked together by organic ligands, forming porous crystalline frameworks. More than 20000 MOFs are currently known, spanning a large variety of topologies and material properties [13]. Their adsorption properties may be tuned, while the water adsorption isotherms remain favorably S-shaped [14]. Some authors have reported theoretical performances (based on equilibrium data) of MOFs for adsorption heating applications: *e.g.*, Lange *et al.* [18] investigated CAU-3/methanol, UiO-67/methanol among other MOF/alcohol working pairs for evaporation at 288 K, condensation at 318 K, and regeneration bellow 395 K, and obtained coefficients of heating performance (*COPs*) up to *ca.* 1.60; Ernst *et al.* [19] reported *COPs* up to 1.50 for H-KUST/methanol, for evaporation at 263 K and 275 K, condensation at 313 K and 323 K, and desorption bellow 413 K; Elsayed *et al.* [20] estimated theoretical *COPs* in the range 1.15-1.80 and 1.10-1.70 for aluminum fumarate/water and CPO-27(Ni)/water pairs, respectively, for evaporation, condensation and regeneration temperatures in the range 278-293 K, 303-318 K and 343-383 K, respectively. CPO-27(Ni) is claimed to be particularly promising for AHPs operating in cold climate (evaporation at 278 K), and regeneration above 363 K [20]. Other advantages pointed out for this MOF are hydrothermal stability and commercial availability, which are major issues for most MOFs

[20, 21]. Lange *et al.* [13] highlighted that MOFs can be coated (without binder) directly on heat exchanger surfaces, which is favorable for practical applications.

In this work, modeling and simulation studies were performed to estimate the heating performance of CPO-27(Ni) MOF for AHPs using water as adsorbate, considering a tubular AHEx composed of a copper foam directly coated with the MOF. The simulations were carried out using a customized solver developed in OpenFOAM, which was previously validated using literature data [10]. The cyclic adsorption process was rigorously simulated, taking into account heat transfer resistances in the bed, and mass transfer resistances inside the adsorbent coating. The overall heating performance of CPO-27(Ni)/water pair was then assessed by means of the coefficient of performance (*COP*), the specific heating power (*SHP*) and the volumetric heating power (*VSHP*). Finally, the performance of the MOF-based AHEx was compared with that of an AQSOA™ FAM-Z02 coated copper foam, for two distinct cycle times (180 or 600 s), in order to gain insights into the potential of MOF CPO-27(Ni) relative to the AQSOA™ FAM-Z02, which is a benchmark for AHPs.

6.2. System description and mathematical modeling

6.2.1. Adsorbent heat exchanger (AHEx) geometry and mesh

The Computational Fluid Dynamics (CFD) simulations were accomplished for a cylindrical AHEx consisting of a central copper tube in which the heat transfer fluid (HTF) circulates for heating/cooling the bed, and the external surface of the tube is covered by a composite (Fig. 6.1). The composite consists of copper foam coated with adsorbent (CPO-27(Ni) or AQSOA™ FAM-Z02). The computational domain and mesh considered in the simulations are indicated in Fig. 6.1.

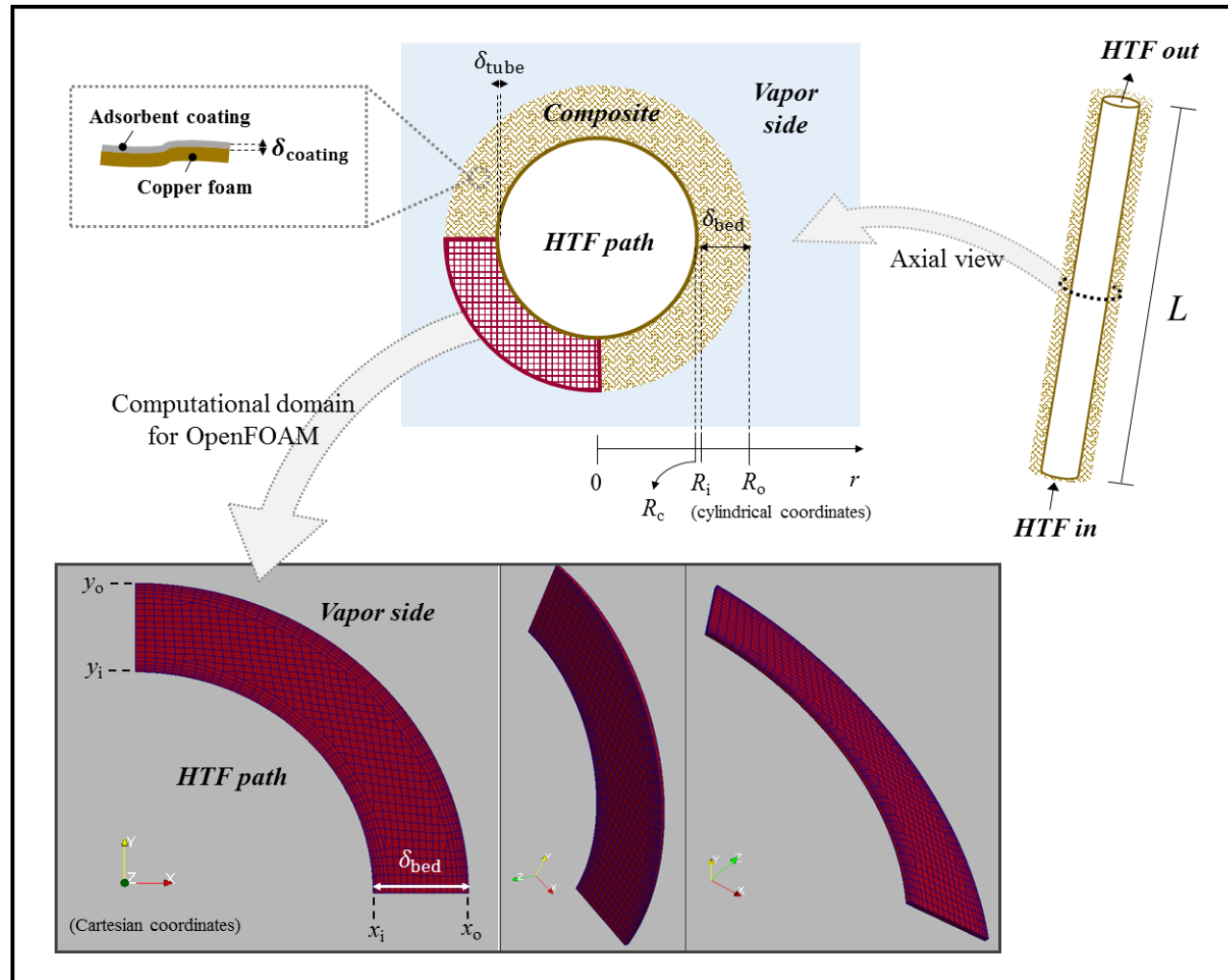


Fig. 6.1 – Schematic representation of the cylindrical AHEx studied in this work, along with the computational domain (2D) and mesh considered in the CFD simulations (HTF – heat transfer fluid; δ - thickness).

6.2.2. Modeling and performance indicators

Since OpenFOAM uses a right-handed Cartesian coordinate system [22], the 2D mathematical model of the unsteady state AHEx unit was written in Cartesian coordinates (Table 6.1): material balance to the composite (copper foam plus adsorbent coating) (Eq. (6.1)); material balance to the adsorbent coating using the Linear Driving Force (LDF) model for a plane sheet geometry (Eq. (6.2)); energy balance to the composite bed (Eq. (6.3)); momentum balance given by Darcy's law (Eq. (6.4)); equilibrium isotherms for CPO-27(Ni)/water and AQSOA™ FAM-Z02/water (Eqs. (6.5) and (6.6), respectively). The boundary conditions (BCs) are given in Table 6.2.

The simulated adsorption cycle is initiated with the isosteric heating stage, considering uniform T , P , and W equal to 308.15 K, 870 Pa, and $W_{eq}(870 \text{ Pa}, 308.15 \text{ K})$, respectively. The values of T , P , and W at the end of the isosteric heating stage are the initial conditions for the desorption step; in turn, the final conditions for the desorption step are the initial conditions for the isosteric cooling stage, etc. Details on the use of *swak4foam* to set non-uniform initial and boundary conditions are given in Annex 6 (Section A6.1.2).

The following simplifications were assumed in the model: (i) the bed porosity is constant; (ii) there is resistance to mass transfer inside the adsorbent coating; (iii) there is no film resistance to heat transfer; (iv) there is no heat transfer resistance between the adsorbent coating and the copper foam; (v) the thermal resistance of the adsorbent coating is negligible, due to its very small thickness (δ_{coat}), and thus the thermal conductivity of the composite bed is considered to be that of copper foam; (vi) the thermal conductivities and specific heat capacities of the composite bed and vapor, and the viscosity of the vapor are constant; (vii) the film thermal resistance between the HTF and the wall of the copper tube is negligible, and there are no heat losses to the environment.

Table 6.1 - Mathematical model of the AHEx unit investigated in this work.

Description	Equation	Eq.
Material balance to the composite	$\varepsilon_b \frac{\partial \rho_v}{\partial t} + (1 - \varepsilon_b)(1 - \zeta)\rho_s \frac{\partial W}{\partial t} + \nabla(\rho_v u) = 0$	(6.1)
Material balance to the adsorbent coating based on the Linear Driving Force (LDF) model ^(a)	$\frac{\partial W}{\partial t} = K_{LDF}(W_{eq} - W), \text{ where } K_{LDF} = \frac{3D_s}{\delta_{coat}^2} \text{ (for plane sheet geometry) and}$ $D_s = D_{s0} \exp\left(\frac{-E_a}{\Re T}\right)$	(6.2)
Energy balance to the composite ^(b)	$\frac{\partial}{\partial t}((\rho C_p)T) + \nabla(\rho_v u C_{p,v}T) = \nabla(\lambda_{eff,bed} \nabla T) + (1 - \varepsilon_b)(1 - \zeta)\rho_s Q_{ads} \frac{\partial W}{\partial t}$ where $\rho C_p = (1 - \varepsilon_b)(1 - \zeta)\rho_s(C_{p,s} + WC_{p,a}) + \varepsilon_b \rho_v C_{p,v} + (1 - \varepsilon_b)\zeta \rho_{copper} C_{p,copper}$, and $\lambda_{eff,bed} = \lambda_{foam} = 0.35[\varepsilon_b \lambda_v + (1 - \varepsilon_b)\lambda_{copper}] + \frac{0.65}{\left(\frac{\varepsilon_b}{\lambda_v} + \frac{1 - \varepsilon_b}{\lambda_{copper}}\right)}$	(6.3)
Momentum balance (Darcy Equation)	$u = -\frac{K}{\eta_v} \nabla P$	(6.4)
Equilibrium isotherms for CPO-27(Ni)/water ^(c)	$W_{eq} = 0.462248 \exp\left[-\left(\frac{A}{10019.2}\right)^4\right], \text{ where } A = \Re T \ln\left(\frac{P_{sat}}{P}\right)$	(6.5)
Equilibrium isotherms for AQSOA™ FAM-Z02/water ^(d)	$W_{eq} = 0.29 \left[\frac{k(P/P_{sat})^{1.01}}{1 + (k-1)(P/P_{sat})^{1.01}} \right], \text{ where } k = 7 \times 10^{-6} \exp\left[1.01(Q_{st} - \Delta H_v)/\left(\frac{\Re T}{M}\right)\right]$	(6.6)

^(a) Equation for K_{LDF} is available from ref. [23]. ^(b) The equation for $\lambda_{eff,bed}$ is available from ref. [16]. ^(c) Isotherm available from ref. [24]. ^(d) Isotherm available from ref. [25]. The $\Delta H_v = f(T)$ was considered.

Table 6.2 - Boundary conditions (BCs) of the 2D model of the adsorption unit investigated in this work (see Fig. 6.1).

Cycle stage	Inner BCs – heat transfer fluid side ^(a)	Outer BCs - water vapor side
Isobaric adsorption (ADS)	$-\lambda_{\text{eff,bed}} \frac{\partial T}{\partial x}(t, x_i) = h_{\text{wall}} [T^{\text{face}}(t, x_i^{\text{face}}) - T_{\text{tube,cool}}]$ $-\lambda_{\text{eff,bed}} \frac{\partial T}{\partial y}(t, y_i) = h_{\text{wall}} [T^{\text{face}}(t, y_i^{\text{face}}) - T_{\text{tube,cool}}]$ $\frac{\partial P}{\partial x}(t, x_i) = \frac{\partial P}{\partial y}(t, y_i) = 0$	$\frac{\partial T}{\partial x}(t, x_o) = \frac{\partial T}{\partial y}(t, y_o) = 0$ $P(t, x_o) = P(t, y_o) = P_{\text{evap}}$
Isosteric heating (HEAT)	$-\lambda_{\text{eff,bed}} \frac{\partial T}{\partial x}(t, x_i) = h_{\text{wall}} [T^{\text{face}}(t, x_i^{\text{face}}) - T_{\text{tube,hot}}]$ $-\lambda_{\text{eff,bed}} \frac{\partial T}{\partial y}(t, y_i) = h_{\text{wall}} [T^{\text{face}}(t, y_i^{\text{face}}) - T_{\text{tube,hot}}]$ $\frac{\partial P}{\partial x}(t, x_i) = \frac{\partial P}{\partial y}(t, y_i) = 0$	$\frac{\partial T}{\partial x}(t, x_o) = \frac{\partial T}{\partial y}(t, y_o) = 0$ $\frac{\partial P}{\partial x}(t, x_o) = \frac{\partial P}{\partial y}(t, y_o) = 0$
Isobaric desorption (DES)	$-\lambda_{\text{eff,bed}} \frac{\partial T}{\partial x}(t, x_i) = h_{\text{wall}} [T^{\text{face}}(t, x_i^{\text{face}}) - T_{\text{tube,hot}}]$ $-\lambda_{\text{eff,bed}} \frac{\partial T}{\partial y}(t, y_i) = h_{\text{wall}} [T^{\text{face}}(t, y_i^{\text{face}}) - T_{\text{tube,hot}}]$ $\frac{\partial P}{\partial x}(t, x_i) = \frac{\partial P}{\partial y}(t, y_i) = 0$	$\frac{\partial T}{\partial x}(t, x_o) = \frac{\partial T}{\partial y}(t, y_o) = 0$ $P(t, x_o) = P(t, y_o) = P_{\text{cond}}$
Isosteric cooling (COOL)	$-\lambda_{\text{eff,bed}} \frac{\partial T}{\partial x}(t, x_i) = h_{\text{wall}} [T^{\text{face}}(t, x_i^{\text{face}}) - T_{\text{tube,cool}}]$ $-\lambda_{\text{eff,bed}} \frac{\partial T}{\partial y}(t, y_i) = h_{\text{wall}} [T^{\text{face}}(t, y_i^{\text{face}}) - T_{\text{tube,cool}}]$ $\frac{\partial P}{\partial x}(t, x_i) = \frac{\partial P}{\partial y}(t, y_i) = 0$	$\frac{\partial T}{\partial x}(t, x_o) = \frac{\partial T}{\partial y}(t, y_o) = 0$ $\frac{\partial P}{\partial x}(t, x_o) = \frac{\partial P}{\partial y}(t, y_o) = 0$

^(a) x_i^{face} and y_i^{face} are the Cartesian positions in the adsorbent bed corresponding to the face of the cells centered in x_i and y_i (Fig. 6.1), and T^{face} is the temperature in the face of the cells centered in positions x_i and y_i .

To assess the overall heating performance of the AHEx unit, the coefficient of performance (*COP*) (which relates the useful heat with the energetic expenses [9]), the specific heating power (*SHP*) and the volumetric heating power (*VSHP*) were calculated as follows:

$$COP = \frac{Q_{ADS} + Q_{cond} + Q_{COOL}}{Q_{DES} + Q_{HEAT}} \quad (6.7)$$

$$SHP = \frac{Q_{ADS} + Q_{cond} + Q_{COOL}}{m_s t_{cycle}} \quad (6.8)$$

$$VSHP = \frac{Q_{ADS} + Q_{cond} + Q_{COOL}}{V_{AHEX} t_{cycle}} \quad (6.9)$$

where Q_{ADS} , Q_{COOL} and Q_{cond} are, respectively, the heats released during isobaric adsorption, isosteric cooling and by the condenser, and Q_{DES} and Q_{HEAT} are the heats supplied to the bed during the isobaric desorption and isosteric heating stages, respectively; m_s is the adsorbent mass (i.e. without the copper foam), V_{AHEX} is the total AHEx volume, and t_{cycle} is the cycle time. Table 6.3 contains the equations to compute the cycle heats (Eqs. (6.10)-(6.14)), and to calculate the masses of adsorbent (m_s), copper foam (m_{foam}) and copper tube (m_{tube}) (Eqs. (6.15)-(6.17)).

Table 6.3 – Equations to compute the heats involved in the four stages of the adsorption heating cycle, and those to calculate the mass of adsorbent (m_s), copper foam (m_{foam}) and copper tube (m_{tube}).

Equation	Eq.
$Q_{\text{ADS}} = \int_{T_{\text{ADS,ini,bed}}}^{T_{\text{ADS,fin,bed}}} [-m_s(C_{p,s} + \bar{W}C_{p,a})] d\bar{T} + \int_{\bar{W}_{\text{ADS,ini}}}^{\bar{W}_{\text{ADS,fin}}} m_s Q_{\text{ads}} d\bar{W} - \int_{T_{\text{ADS,ini,bed}}}^{T_{\text{ADS,fin,bed}}} m_{\text{foam}} C_{p,\text{copper}} d\bar{T} + \int_{\bar{W}_{\text{ADS,ini}}}^{\bar{W}_{\text{ADS,fin}}} m_s C_{p,v}(T_{\text{evap}} - T_{\text{ADS,bed}}) d\bar{W}$	(6.10)
$Q_{\text{HEAT}} = \int_{T_{\text{HEAT,ini,bed}}}^{T_{\text{HEAT,fin,bed}}} [m_s(C_{p,s} + \bar{W}C_{p,a})] d\bar{T} + \int_{T_{\text{HEAT,ini,bed}}}^{T_{\text{HEAT,fin,bed}}} m_{\text{foam}} C_{p,\text{copper}} d\bar{T} + \int_{T_{\text{tube,cool}}}^{T_{\text{tube,hot}}} m_{\text{tube}} C_{p,\text{copper}} dT$	(6.11)
$Q_{\text{DES}} = \int_{T_{\text{DES,ini,bed}}}^{T_{\text{DES,fin,bed}}} [m_s(C_{p,s} + \bar{W}C_{p,a})] d\bar{T} - \int_{\bar{W}_{\text{DES,ini}}}^{\bar{W}_{\text{DES,fin}}} m_s Q_{\text{ads}} d\bar{W} + \int_{T_{\text{DES,ini,bed}}}^{T_{\text{DES,fin,bed}}} m_{\text{foam}} C_{p,\text{copper}} d\bar{T}$	(6.12)
$Q_{\text{COOL}} = \int_{T_{\text{COOL,ini,bed}}}^{T_{\text{COOL,fin,bed}}} [-m_s(C_{p,s} + \bar{W}C_{p,a})] d\bar{T} - \int_{T_{\text{COOL,ini,bed}}}^{T_{\text{COOL,fin,bed}}} m_{\text{foam}} C_{p,\text{copper}} d\bar{T} - \int_{T_{\text{tube,hot}}}^{T_{\text{tube,cool}}} m_{\text{tube}} C_{p,\text{copper}} dT$	(6.13)
$Q_{\text{cond}} = m_s \Delta \bar{W} \Delta H_v + \int_{\bar{W}_{\text{DES,ini}}}^{\bar{W}_{\text{DES,fin}}} m_s C_{p,v}(T_{\text{cond}} - T_{\text{DES,bed}}) d\bar{W}, \text{ where } \Delta \bar{W} = \bar{W}_{\text{DES,ini}} - \bar{W}_{\text{DES,fin}}$	(6.14)
$m_s = \rho_s V_s, \text{ where } V_s = (1 - \zeta)(1 - \varepsilon_b) V_{\text{total,bed}} \text{ and } V_{\text{total,bed}} = \pi L(R_o^2 - R_i^2)$	(6.15)
$m_{\text{foam}} = \rho_{\text{copper}} V_{\text{foam}}, \text{ where } V_{\text{foam}} = \zeta(1 - \varepsilon_b) V_{\text{total,bed}}$	(6.16)
$m_{\text{tube}} = \rho_{\text{copper}} V_{\text{tube}}, \text{ where } V_{\text{tube}} = \pi L(R_i^2 - R_c^2)$	(6.17)

The average temperature (\bar{T}), pressure (\bar{P}) and adsorbate loading (\bar{W}) in the composite bed along time (generically denoted by $\bar{\varphi}$) were computed by:

$$\bar{\varphi}(t) = \frac{\int_{R_i}^{R_o} 2r\varphi(t,r)dr}{(R_o^2 - R_i^2)} \quad (6.18)$$

where t denotes time, r is the radial coordinate, and R_o and R_i are, respectively, the external and internal radius of the adsorbent bed (Fig. 6.1). Before calculating $\bar{\varphi}(t)$, the bed position values were converted from Cartesian to radial coordinates, computing $r = \sqrt{x^2 + y^2}$.

6.3. Computational simulations

6.3.1. OpenFOAM

The open-source OpenFOAM software is foremost a C++ library, used primarily to create application executables, which fall into two categories: solvers and utilities (to perform tasks involving data manipulation and algebraic calculations) [26]. It may be used to solve anything from complex fluid flows involving chemical reactions, turbulence, and heat transfer, to acoustics, solid mechanics, and electromagnetics [27]. Although a wide range of solvers is already included in this software [28], a solver for simulating adsorption processes is not available so far, albeit users have the freedom to create their own or modify the existing ones [26].

6.3.2. Numerical methodology

SimFlow (version 3.1) [29] was used to generate the geometry and the grid (with *ca.* 900 cells) for the simulations. To reduce the numerical effort, only a slice of the adsorbent bed

was considered as the computational domain (Fig. 6.1). The remaining geometry and solution patterns were assumed as mirror symmetry. In order to obtain the P , T and W profiles along the cylindrical adsorbent bed for the four stages of the cycle, a customized solver for adsorption was developed in OpenFOAM (version 4.1) [30]. Fig. 6.2(a) and (b) shows the directory structure for an application in OpenFOAM, generically denoted by *newApp*, and for the *customizedSolver* application developed in this work; Fig. 6.2(c) displays a simplified flowchart of the developed solver. The isobaric stages were simulated considering automatic adjustment of the time step (Δt), while for the isosteric stages a maximum Δt of 10^{-5} s was frequently adopted, to ensure temporal accuracy and numerical stability. Time derivatives, gradient, divergence and Laplacian terms were discretized using, respectively [26]: Euler scheme (backward scheme - second order accurate in time - was tested and produced similar results); standard finite volume discretization of Gaussian integration with linear interpolation; Gaussian integration with total variation diminishing (TVD) interpolation scheme; Gaussian integration with linear interpolation scheme, and explicit non-orthogonal correction as surface normal gradient scheme. The preconditioned conjugate gradient (PCG) with diagonal incomplete-Cholesky preconditioner was used to solve the equations for P and W , and an iterative solver using the Gauss-Seidel smoother for solving the equations for T [26]. The simulations were accomplished in an Intel® Core i7 – 2600K 3.40 GHz, 8GB DDR3/1TB. ParaView application (version 5.0.1) [31] was used for post-processing.

A grid independence test was performed by considering a finer mesh with 3568 cells, and similar results were obtained; hence, the initial grid with *ca.* 900 cells (Fig. 6.1) was considered a good trade-off between accuracy and computational cost (details regarding the considered mesh are given in Annex A6 (Section A6.1.1)).

Fig. 6.3(a) and (b) shows, respectively, the directory structure of a general OpenFOAM case, and that adopted in this work to simulate the four stages of the adsorption cycle: (1) *isostericHeating*, (2) *isobaricDesorption*, (3) *isostericCooling*, and (4) *isobaricAdsorption*. The methodology followed to construct the cases and perform the simulations, and the stopping criteria for each stage are given in Fig. 6.3(b).

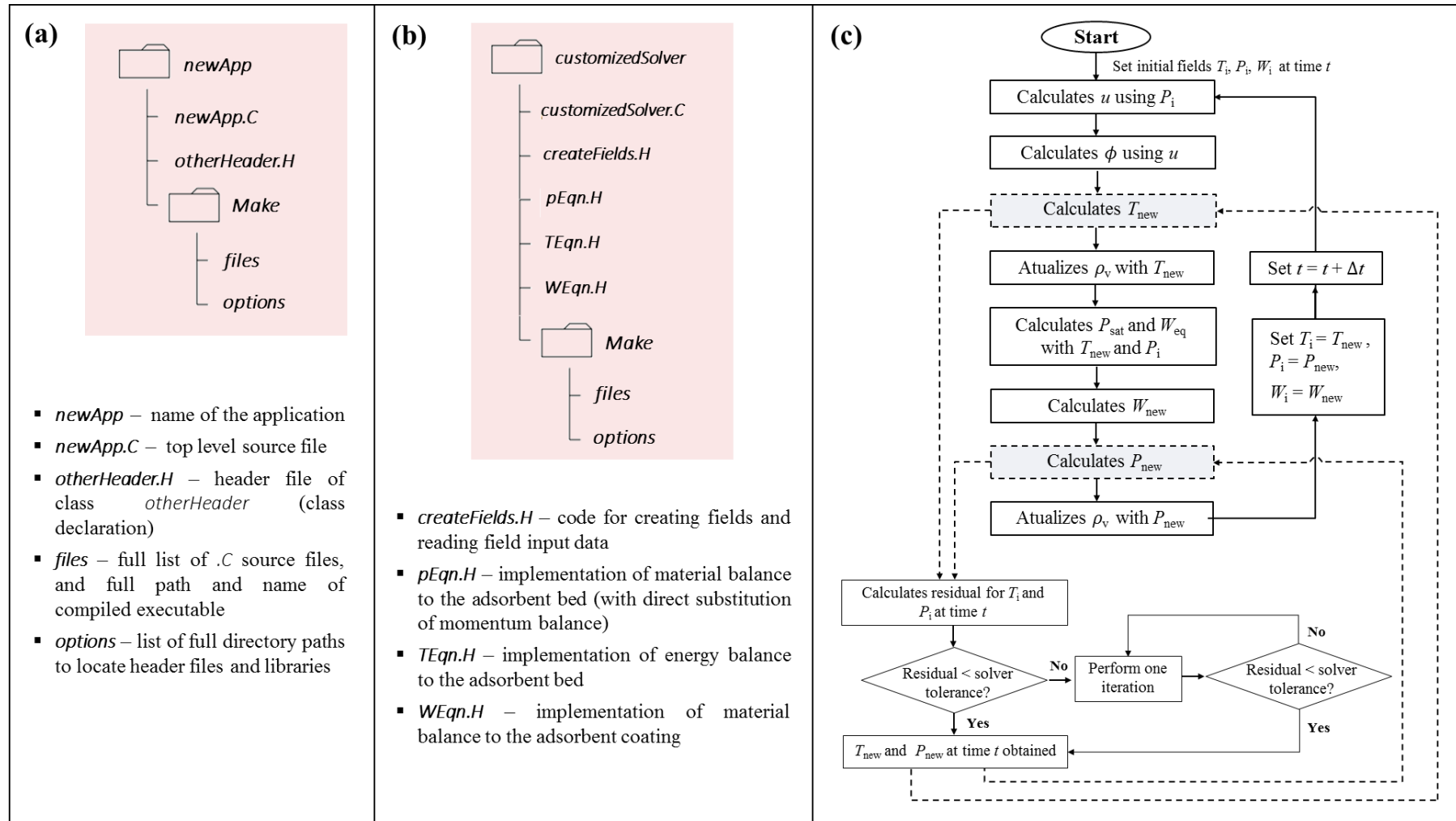


Fig. 6.2 - Directory structure of an OpenFOAM application (a) generically denoted by *newApp* [26], and (b) developed in this work, designated by *customizedSolver*. (c) Simplified flowchart of the *customizedSolver* application.

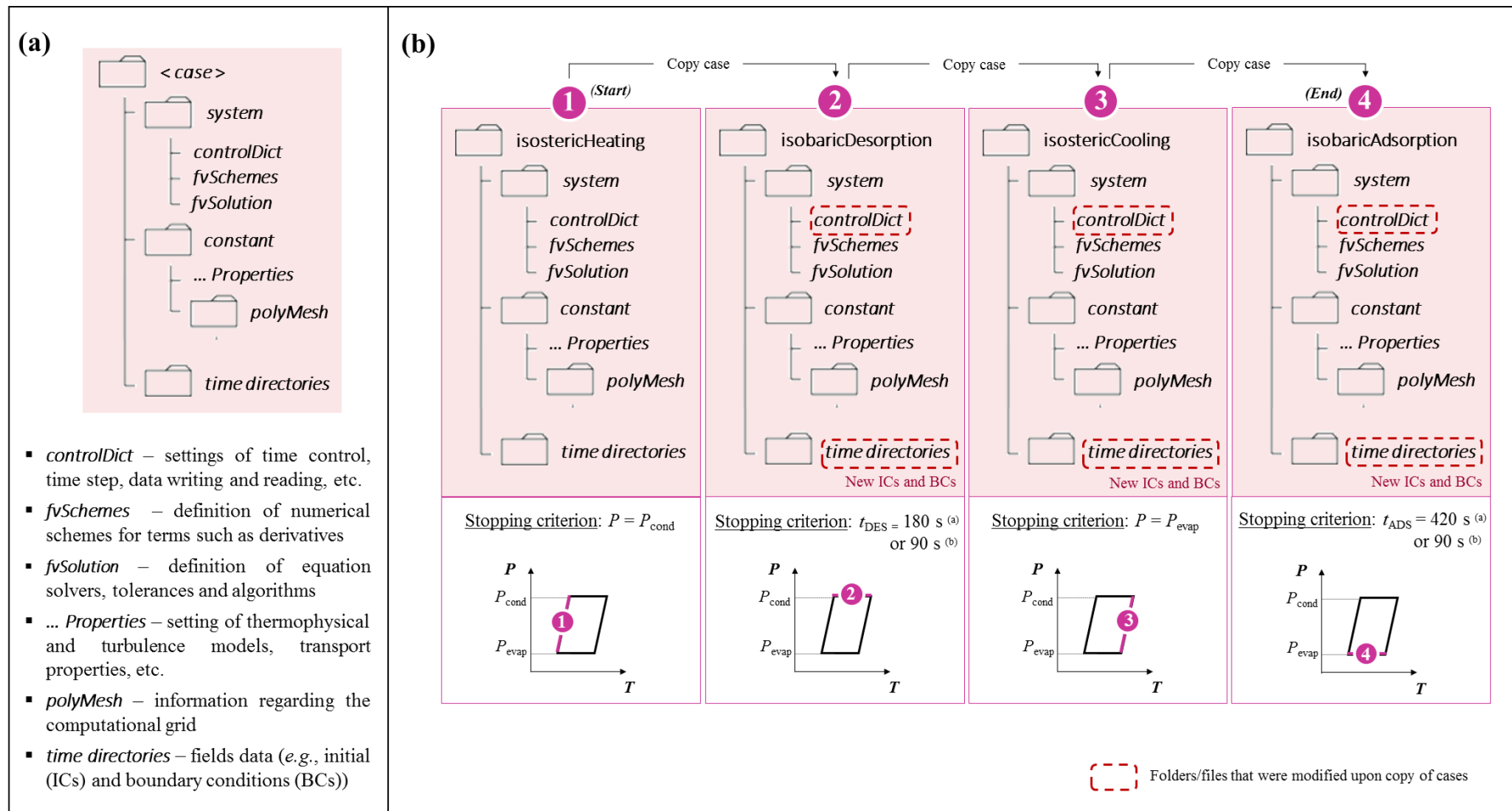


Fig. 6.3 - Directory structure of OpenFOAM cases: (a) general [26]; (b) adopted in this work to simulate the four stages of an adsorption heating cycle. The methodology followed to construct the cases and perform the simulations is outlined, along with the stopping criteria considered for each stage.

6.4. Results and discussion

In the first part of this chapter, the customized solver and methodology adopted in OpenFOAM to simulate an adsorption heating cycle were validated using literature data. In a second part, the AHP simulation results obtained in OpenFOAM for a tubular AHEx composed by CPO-27(Ni) coated copper foam (Fig. 6.1) are presented, along with the estimated heating performances. Finally, to gain insights into the potential of MOFs over benchmark adsorbents for AHPs, the heating performances of CPO-27(Ni) and AQSOA™ FAM-Z02 coated copper foams were compared for two distinct cycle times.

6.4.1. Validation of OpenFOAM solver and methodology using literature data

The solver developed in OpenFOAM was validated using data reported in our previous work of an adsorption heating cycle using ETS-10/water pair and a cylindrical bed geometry [10]. Details on the initial and boundary conditions considered to accomplish these simulations are given in Annex A6 (Section A6.1.3).

Figs. 6.4-6.7 compare the results obtained in this work to those reported by Pinheiro *et al.* [10], showing the time dependency curves of T , P and W during the four cycle stages, and for different bed positions. The results were generally similar, constituting a reasonable validation of the customized solver and methodology developed in OpenFOAM. The major differences appear for $P(t, r)$ during the isosteric heating, where the increase of pressure simulated in OpenFOAM is slower, and during the isobaric desorption, where $P(t, r)$ presents a somewhat irregular behavior. These deviations may be partly related with the stiffness of the equations, leading to numerical instability in some cases.

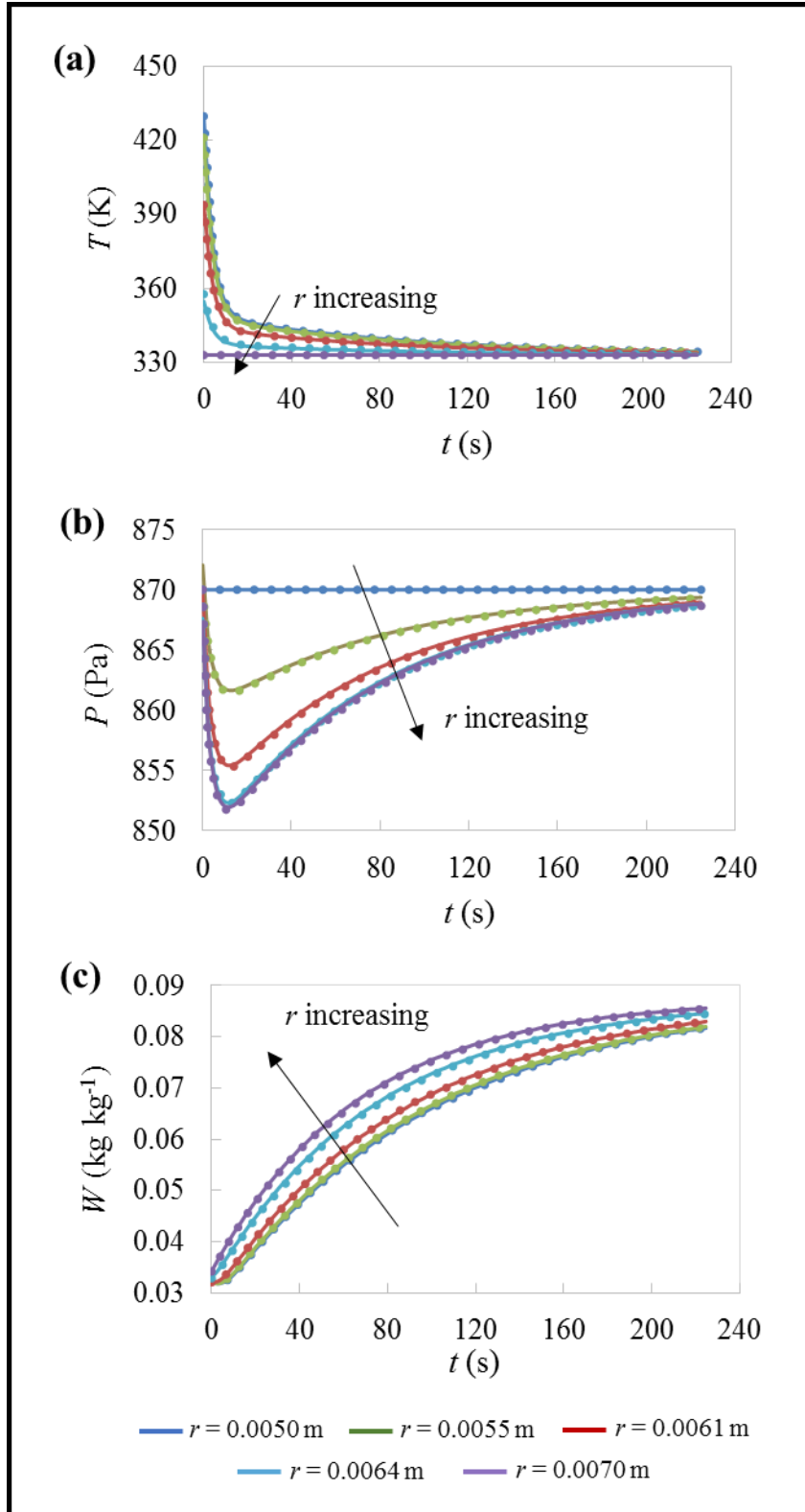


Fig. 6.4 – Evolution of (a) T , (b) P and (c) W along time during the isobaric adsorption stage, for different positions in the cylindrical adsorbent bed reported in ref. [10]. Dotted lines are the results obtained in OpenFOAM, and solid lines are those reported in ref. [10].

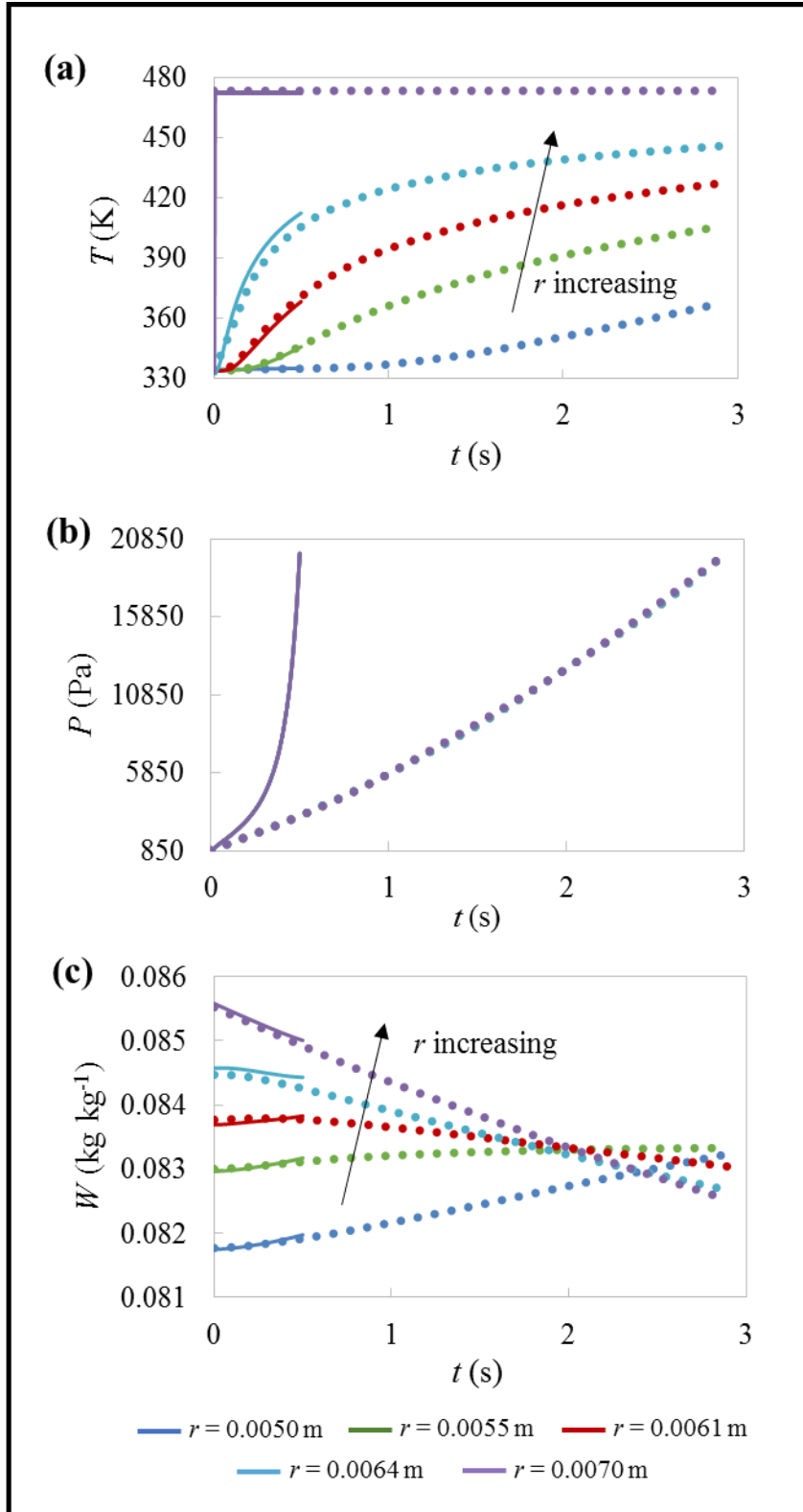


Fig. 6.5 - Evolution of (a) T , (b) P and (c) W along the isosteric heating stage, for different positions in the adsorbent bed reported in ref. [10]. Dotted lines are the results obtained in OpenFOAM, and solid lines are those reported in ref. [10].

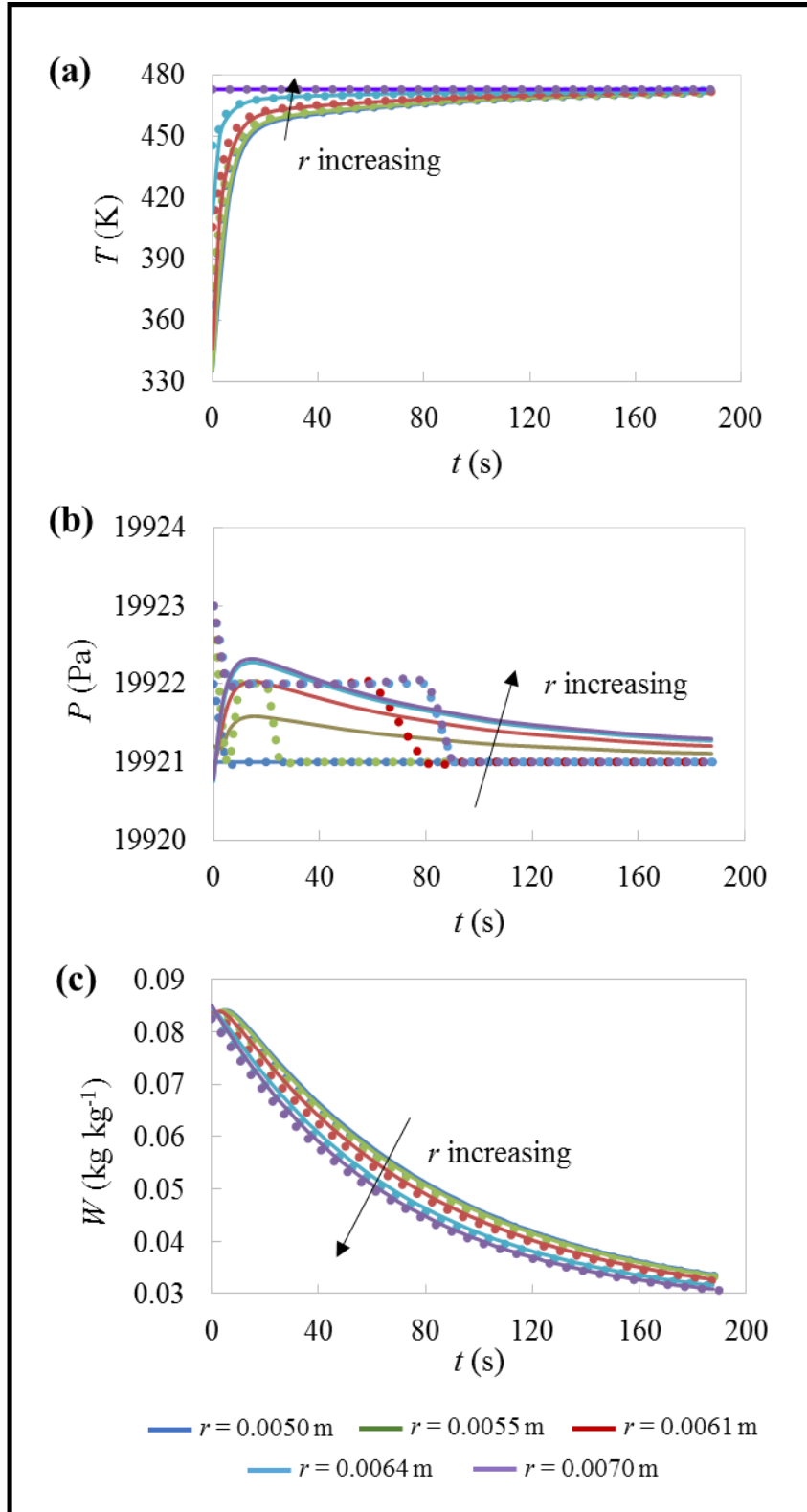


Fig. 6.6 - Evolution of (a) T , (b) P and (c) W along time during the isobaric desorption stage, for different positions of the adsorbent bed reported in ref. [10]. Dotted lines are the results obtained in OpenFOAM, and solid lines are those reported in ref. [10].

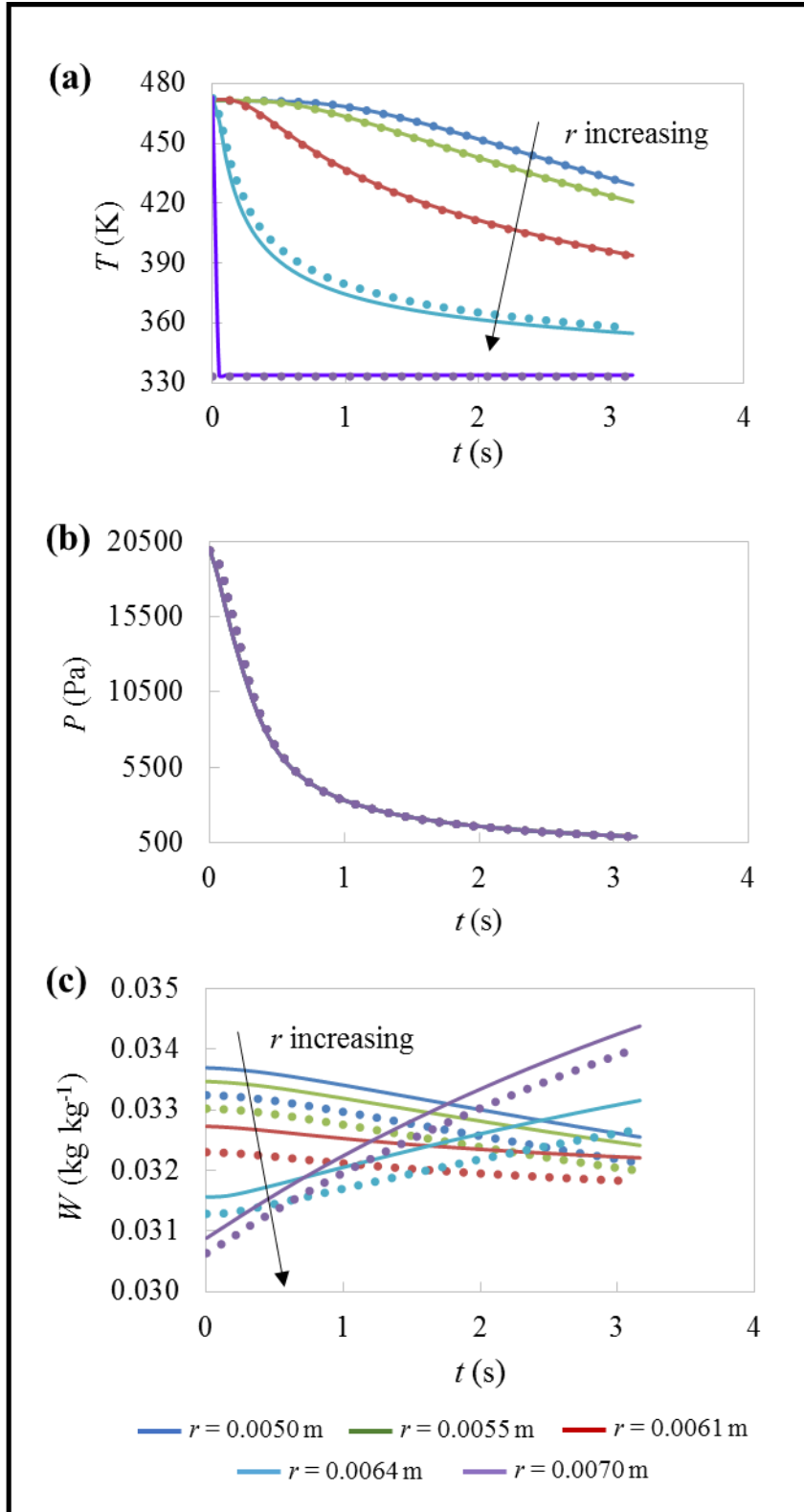


Fig. 6.7 - Evolution of (a) T , (b) P and (c) W along the isosteric cooling stage for different positions in the cylindrical adsorbent bed of ref. [10]. Dotted lines are the results obtained in OpenFOAM, and solid lines are those reported in ref. [10].

6.4.2. Performance of CPO-27(Ni) coated copper foam for AHPs

The operating conditions and main properties used to simulate the water adsorption heating cycle for a tubular AHEx possessing a CPO-27(Ni) coated copper foam (Fig. 6.1) are given in Table 6.4. Several properties regarding the composite foam, such as bed permeability (K) and volumetric fraction of copper foam in the composite bed (ζ), were taken from Freni *et al.* [16]. Data regarding AQSOA™ FAM-Z02 coated copper foam (discussed in Section 6.4.3) are included in Table 6.4.

Table 6.4 – Main properties of CPO-27(Ni) and AQSOA™ FAM-Z02 coated copper foams, and operating parameters considered in the simulations of the adsorption heating cycle.

	CPO-27(Ni)	Ref.	AQSOA™ FAM-Z02	Ref.
$C_{p,s}$ (J kg ⁻¹ K ⁻¹)	1000	[32]	892 ^(a)	[33]
ρ_s (kg m ⁻³)	2600	[34]	2260	[35]
D_{s0} (m ² s ⁻¹)	4.9×10^{-9}	[20]	3.92×10^{-6}	[36]
E_a (J mol ⁻¹)	25125		28035	
Q_{ads} (J kg ⁻¹)	2.881×10^6 ^(b)	This work	3.160×10^6 ^(c)	[25]
Q_{st} (J kg ⁻¹) ^(d)	---	---	4.560×10^6	
<i>Properties of composite foam and copper metal</i>				
δ_{coat} (m) ^(e)	1×10^{-5}			---
K (m ²)	10^{-8}			[16]
ε_b ^(f)	0.8			
ζ	0.52			
h_{wall} (W m ⁻² K ⁻¹)	1500			
ρ_{copper} (kg m ⁻³)	8954			
$C_{p,copper}$ (J kg ⁻¹ K ⁻¹)	390			[37]
λ_{copper} (W m ⁻¹ K ⁻¹)	398			[38]
<i>AHEx dimensions and operating conditions</i>				
L (m)	0.4			---
$R_i ; R_o ; R_c$ (m) ^(g)	0.005; 0.007; 0.0045			---
$P_{evap}; P_{cond}$ (Pa) ^(h)	870; 5624			---
$T_{cond} = T_{min,cycle} = T_{tube,cool}$ (K) ⁽ⁱ⁾	308.15			---
$T_{max,cycle} = T_{tube,hot}$ (K)	368.15			---
t_{cycle} (s)	≈ 600 or 180			---

^(a) Average value between 308 K and 368 K. ^(b) Calculated for half coverage (0.231 kg kg^{-1}) using the Clausius-Clapeyron equation and the isotherm (Eq. (6.5)). ^(c) Based on Fig. 7 of ref. [25], for half coverage of 0.145 kg kg^{-1} . ^(d) Isotherm parameter (Eq. (6.6), Table 6.1). ^(e) The used value is coincident with that reported by Freni *et al.* [16]. ^(f) Foam macro-porosity. ^(g) $\delta_{\text{bed}} = R_o - R_i$; $\delta_{\text{tube}} = R_i - R_c$; y_i and x_i are coincident with R_i , and y_o and x_o are equal to R_o (see Fig. 6.1). ^(h) $P_{\text{evap}} = 870 \text{ Pa}$ corresponds to $T_{\text{evap}} = 278.15 \text{ K}$, which was the reference value considered by Elsayed *et al.* [20] for AHPs operating in cold climate. ⁽ⁱ⁾ The considered $T_{\text{cond}} = T_{\text{min,cycle}}$ and $T_{\text{max,cycle}}$ are within the potential AHP operation range reported for CPO-27(Ni) [20].

Figs. 6.8-6.11 show the evolution of P , T and W fields in the adsorbent bed comprising CPO-27(Ni) coated copper foam, along isosteric heating (stage considered for startup), isobaric desorption, isosteric cooling and isobaric adsorption, for t_{cycle} of *ca.* 600 s.

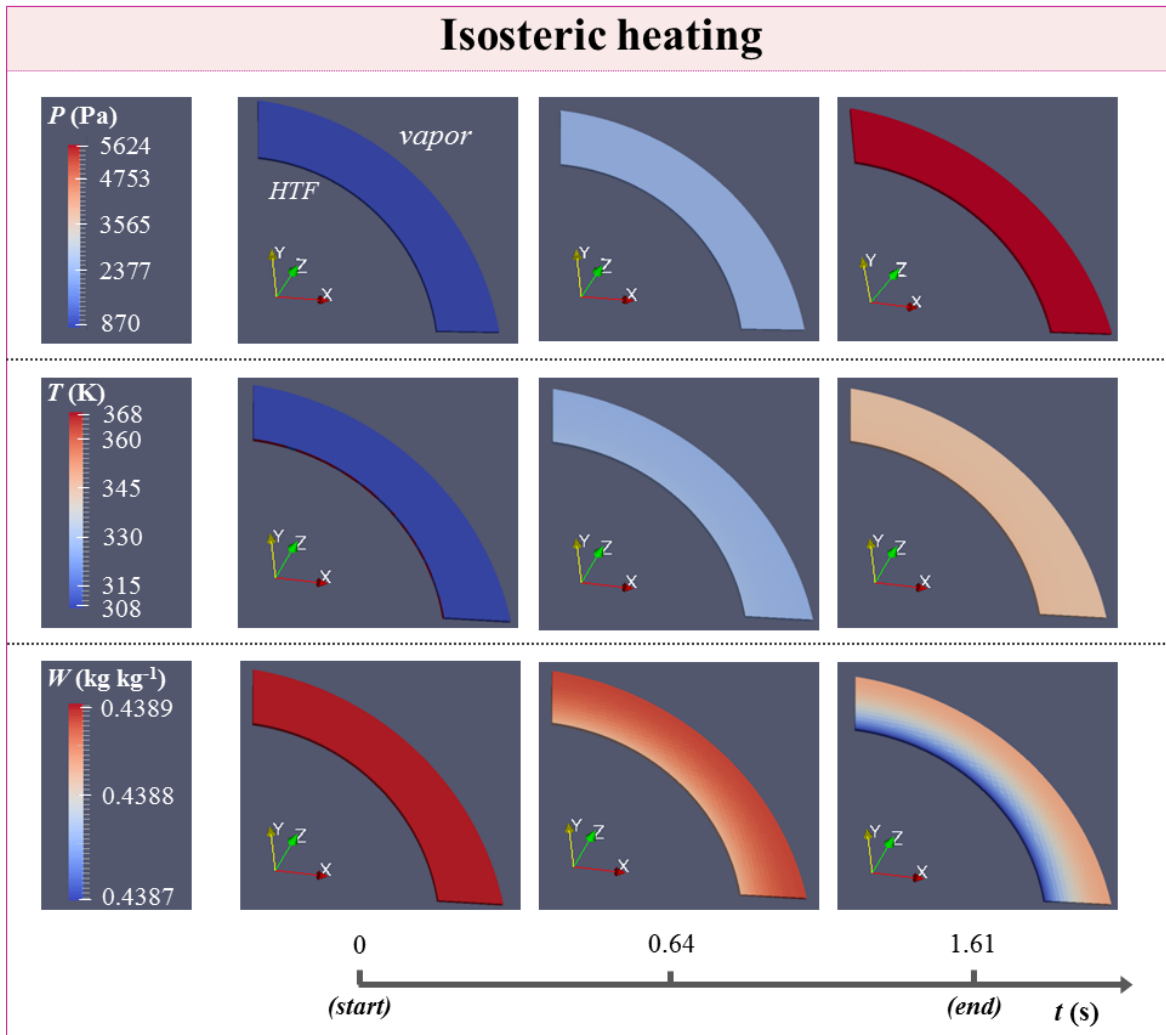


Fig. 6.8 – Evolution of P , T and W along the isosteric heating stage in the CPO-27(Ni) coated copper foam, for t_{cycle} of *ca.* 600 s.

During isosteric heating (Fig. 6.8), the pressure is uniform due to the good vapor permeability of the composite foam, increasing from 870 Pa to 5624 Pa in *ca.* 1.6 s. The temperature increases uniformly along the bed, from 308 to *ca.* 345 K, while W remains approximately constant around 0.439 kg kg^{-1} .

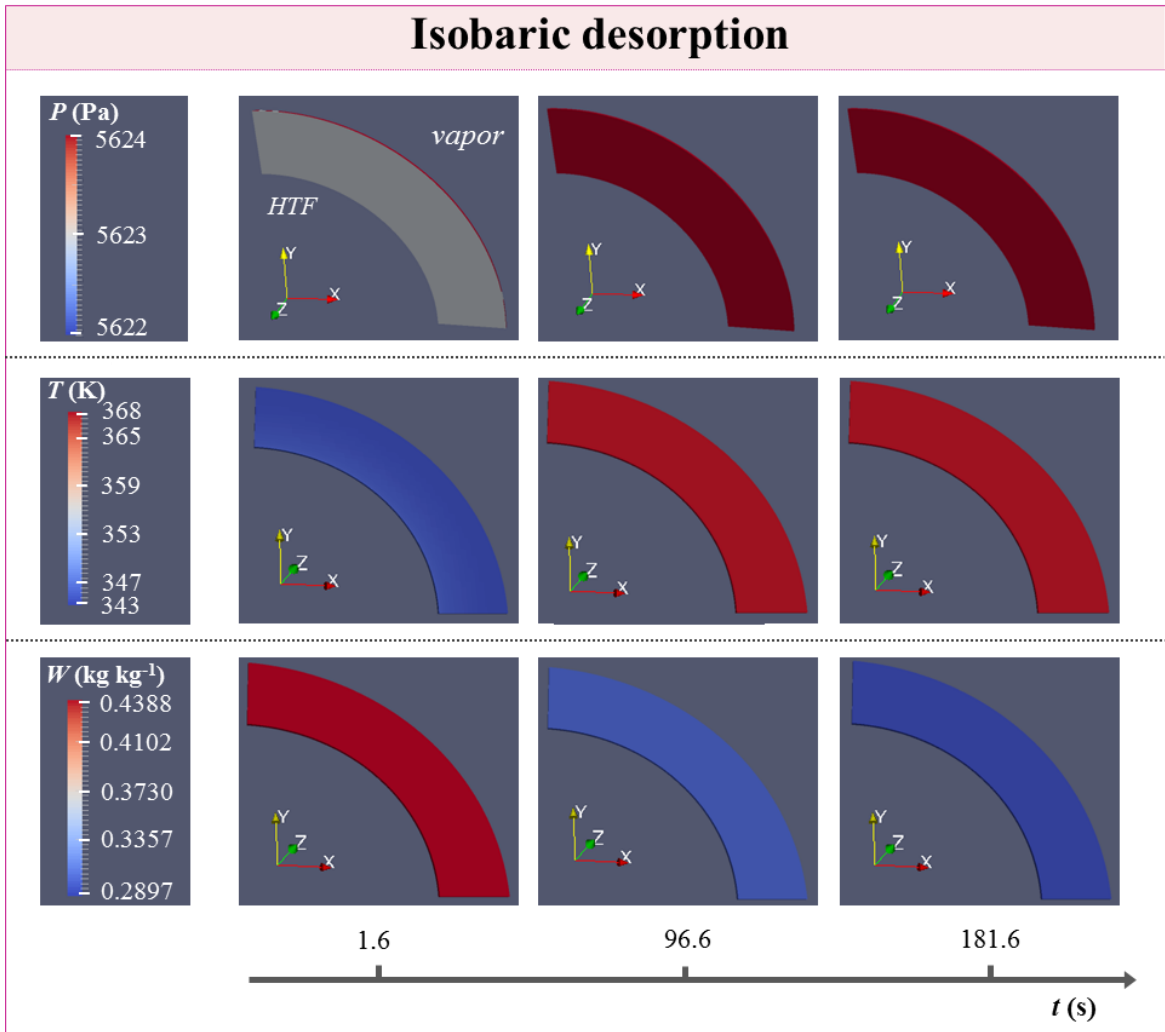


Fig. 6.9 - Evolution of P , T and W fields along the isobaric desorption stage in the composite adsorbent bed of copper foam and CPO-27(Ni) coating, for t_{cycle} around 600 s.

In the isobaric desorption (Fig. 6.9), the pressure is uniform and around 5264 Pa. The temperature increases from *ca.* 343 to 368 K ($T_{\text{max,cycle}}$) in 95 s, due to the significant bed thermal conductivity, small thickness of the adsorbent coating and composite, and good thermal contact between the HTF tube and the foam ($h_{\text{wall}} = 1500 \text{ W m}^{-2} \text{ K}^{-1}$ [16]), which

favor the AHEx overall heat transfer coefficient. On the other hand, it takes *ca.* 180 s for W to achieve $W_{eq} \approx 0.289 \text{ kg kg}^{-1}$ (5624 Pa, 368 K).

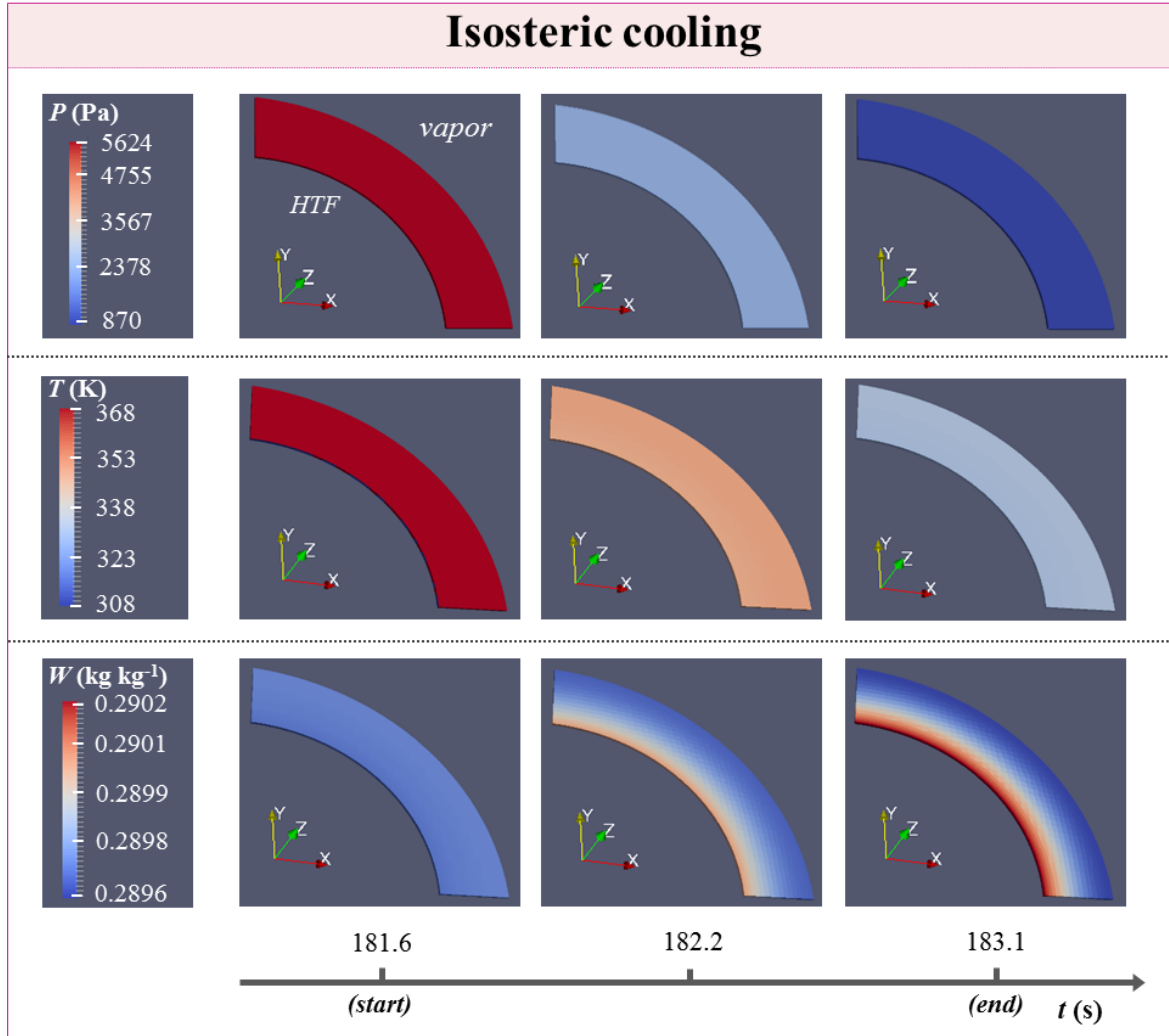


Fig. 6.10 - Evolution of P , T and W in the CPO-27(Ni) coated copper foam along the isosteric cooling stage, for a cycle time of *ca.* 600 s.

The isosteric cooling stage (Fig. 6.10) lasts 1.5 s, in which a pressure decrease from 5624 to 870 Pa occurs while the bed is cooled, and W remains $\approx 0.290 \text{ kg kg}^{-1}$.

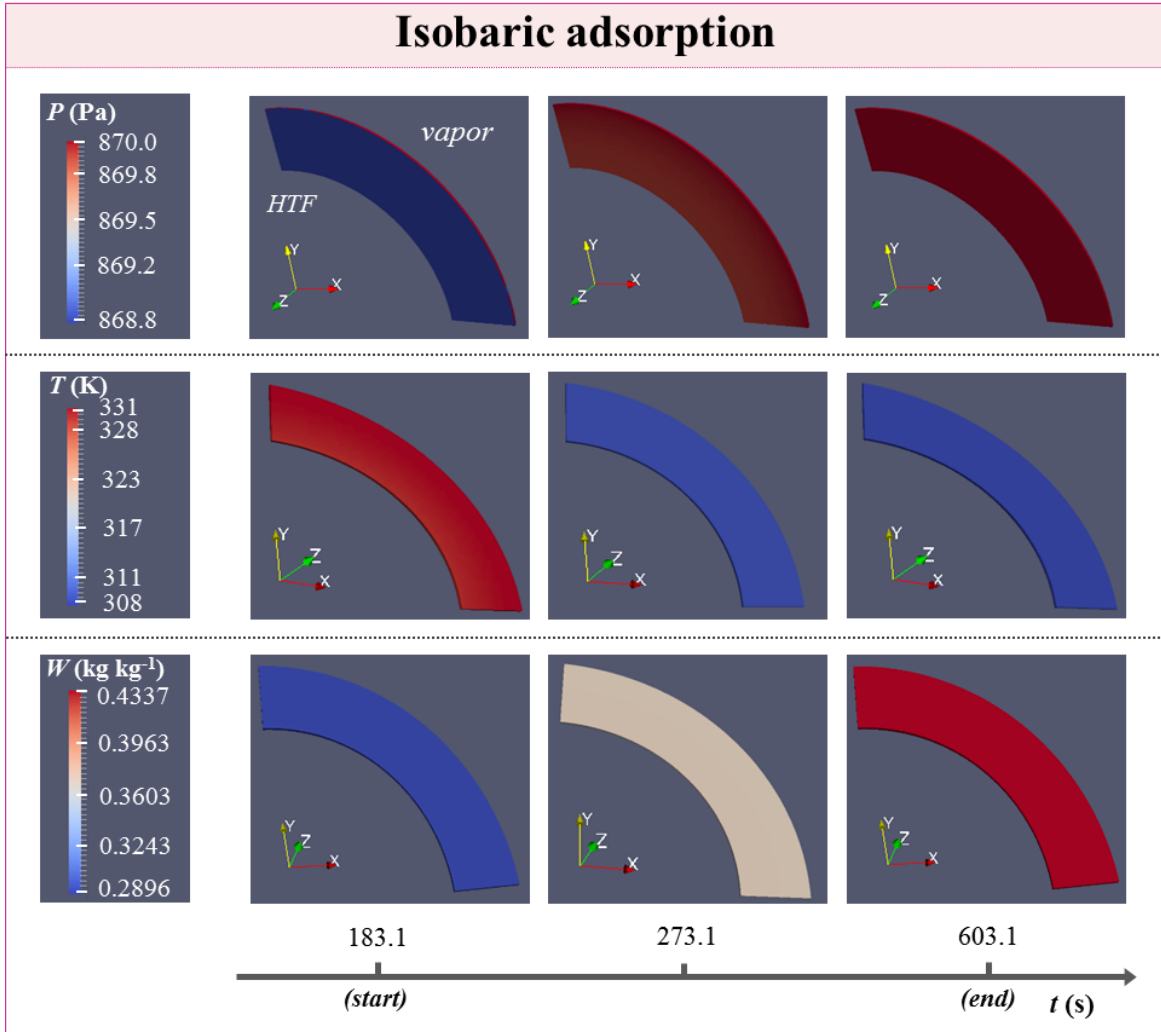


Fig. 6.11 - Evolution of P , T and W along the isobaric adsorption stage in CPO-27(Ni) coated copper foam, for $t_{\text{cycle}} \approx 600$ s.

In the isobaric adsorption stage (Fig. 6.11), the pressure in the composite bed is uniform and around 870 Pa. From $t = 183.1$ s to $t = 273.1$ s, the bed temperature decreases from *ca.* 331 to 308 K ($T_{\text{min,cycle}}$), while W increases from ~ 0.290 to 0.367 kg kg^{-1} . At $t = 603$ s, $W \approx 0.434$ kg kg^{-1} , which is close to the equilibrium value $W_{\text{eq}} = 0.439$ kg kg^{-1} (870 Pa, 308 K). Among the various transport resistances in the composite bed, the intraparticle mass transfer kinetics is clearly the limiting factor of the adsorption process when using CPO-27(Ni) coated copper foam.

Table 6.5 lists t_{cycle} , adsorbent-to-metal mass ratio (m_s/m_{copper} , where m_{copper} is the sum of the mass of copper tube (m_{tube}) and copper foam (m_{foam}) of the AHEx), $\Delta\bar{W}$, ΔW_{eq} ,

Table 6.5 – Values of cycle time (t_{cycle}), adsorbent-to-metal mass ratio (m_s/m_{copper}), $\Delta\bar{W}$, ΔW_{eq} , COP , SHP , $VSHP$, number of necessary AHEx tubes to achieve a power of 2000 W (N_{tubes}) and volume occupied by N_{tubes} ($V_{N_{\text{tubes}}}$), obtained for the copper foam composite bed using CPO-27(Ni) or AQSOA™ FAM-Z02.

Adsorbent	t_{cycle} ($t_{\text{ADS}}, t_{\text{DES}}$) (s)	m_s/m_{copper} (kg kg ⁻¹)	$\Delta\bar{W} \Delta W_{\text{eq}}$ (kg kg ⁻¹)	COP	SHP (W kg ⁻¹)	$VSHP$ (W L ⁻¹)	N_{tubes} ^(a)	$V_{N_{\text{tubes}}}$ (L)
CPO-27(Ni)	≈ 600 (420, 180)	0.092	0.149 0.150	1.39	1922	235	138	8.49
	≈ 180 (90, 90)		0.139 0.150	1.16	5130	627	52	3.19
AQSOA™ FAM-Z02	≈ 600 (420, 180)	0.080	0.161 0.161	1.42	2102	223	145	8.92
	≈ 180 (90, 90)		0.161 0.161	1.40	6877	731	44	2.71

^(a) Considering the AHEx dimensions and the operating conditions in Table 6.4.

COP , SHP , $VSHP$, number of AHEx tubes to ensure a power of 2000 W (N_{tubes}), and volume occupied by N_{tubes} ($V_{N_{\text{tubes}}}$), calculated for the heating cycle using CPO-27(Ni) with t_{cycle} of 600 s (Figs. 6.8-6.11) and 180 s. The simulations were also performed for AQSOA™ FAM-Z02/copper foam, whose discussion is presented in Section 6.4.3.

The m_s/m_{copper} should be as high as possible to favor the COP , although the value of 0.092 kg kg⁻¹ obtained for CPO-27(Ni)/copper foam is smaller than those commonly found in prototypes, which range from 0.29 - 0.67 kg kg⁻¹ [39]. Using foams made of aluminum instead of copper would improve the adsorbent-to-metal ratio, although copper is more malleable, and its thermal conductivity is almost the double of aluminum [40]. For $t_{\text{cycle}} \approx 600$ s, the $\Delta\bar{W}$ of the MOF approaches $\Delta W_{\text{eq}} = 0.150$ kg kg⁻¹, the COP is 1.39, and the SHP approaches 1922 W kg⁻¹; SHP s in the order of thousands are beneficial for practical applications [41, 42]. The obtained $VSHP$ of 235 W L⁻¹ ($t_{\text{cycle}} \approx 600$ s) roughly compares to the literature data: *e.g.*, Wittstadt *et al.* [43] reported $VSHP$ up to 320 W L⁻¹ for an aluminum fiber flat tube heat exchanger using SAPO-34 directly synthesized coating. A relatively high number of AHEx tubes of 138 would be necessary to achieve a targeting power of 2000 W, which occupies at least 8.49 L.

If t_{cycle} is decreased by a factor of *ca.* 3, from 600 s to 180 s, the COP obtained for CPO-27(Ni) significantly decreases from 1.39 to 1.16, due to the drop in $\Delta\bar{W}$, but SHP and $VSHP$ increase by a factor of *ca.* 3, for 5130 W kg⁻¹ and 627 W L⁻¹, respectively, and $V_{N_{\text{tubes}}}$ decreases also by a factor of almost 3.

The theoretical COP (solely based on equilibrium isotherms) reported by Elsayed *et al.* [20] for CPO-27(Ni)/water pair and the same operating conditions to those of this current work ($T_{\text{evap}} = 278.15$ K, $T_{\text{cond}} = T_{\text{min,cycle}} = 308.15$ K and $T_{\text{max,cycle}} = 368.15$ K) was *ca.* 1.55 (see Fig. 5(a) of that work), which means that when going from the purely theoretical scenario to the simulated one, COP dropped roughly 0.2-0.4.

It is noteworthy that using the CPO-27(Ni)/water pair would restrict the AHP operation to relatively low heating temperatures: *e.g.*, for the evaporation and bed regeneration temperatures indicated in Table 6.4, if T_{cond} increases from 308.15 K to 313.15 K, the ΔW_{eq} drops from 0.150 to 0.08 kg kg⁻¹; even if T_{evap} is increased from 278.15 K to 283.15 K, maintaining the bed regeneration temperature of 368.15 K and the T_{cond} of 308.15 K,

$\Delta W_{\text{eq}} = 0.102 \text{ kg kg}^{-1}$, which is half of the value recommended for reasonable operation of AHPs ($\Delta W \geq 0.2 \text{ kg kg}^{-1}$ [44]).

6.4.3. Comparison of copper foams coated with CPO-27(Ni) or AQSOATM FAM-Z02

The zeotype material AQSOATM FAM-Z02 has been considered the most promising adsorbent for adsorption heating/cooling applications [17], and thus it was chosen for benchmarking MOF CPO-27(Ni).

AQSOATM FAM-Z02 surpasses the overall performance of CPO-27(Ni) for cycle times of 180 and 600 s, mainly due to the higher $\Delta \bar{W}$ values of the former, which are always coincident with $\Delta W_{\text{eq}} = 0.161 \text{ kg kg}^{-1}$. Appliances with higher *COPs* and more compact than MOF-based solutions can be build-up using the zeotype: for $t_{\text{cycle}} \approx 180 \text{ s}$, *COP*, *SHP* and $V_{N_{\text{tubes}}}$ of, respectively, 1.40, 6877 W kg^{-1} and 2.71 L were reached for AQSOATM FAM-Z02, in contrast to 1.16, 5130 W kg^{-1} and 3.19 L for CPO-27(Ni). It is noteworthy that for the zeotype, decreasing t_{cycle} from 600 to 180 s, leads to a significant reduction of $V_{N_{\text{tubes}}}$, and the drop in *COP* is less pronounced than that verified for the MOF.

Fig. 6.12 shows the evolution of \bar{P} , \bar{T} and \bar{W} along a complete adsorption heating cycle for AQSOATM FAM-Z02 and CPO-27(Ni) coated copper foams. The evolution of \bar{P} and \bar{T} along time is essentially overlapped for the two adsorbents, partly due to the intrinsic properties of the copper foam, such as high porosity that enables good vapor permeability, and high thermal conductivity. The benchmark adsorbent outperforms CPO-27(Ni) essentially owing to its faster intraparticle mass transfer kinetics (Fig. 6.12(c)): for instance, for the adsorption stage of the cycle lasting 180 s, while AQSOATM FAM-Z02 reaches $\bar{W} = W_{\text{eq}} = 0.242 \text{ kg kg}^{-1}$ (870 Pa, 308.15 K) in *ca.* 45 s ($\frac{1}{2} t_{\text{ADS}}$), the MOF achieves around 75 % of the equilibrium value ($W_{\text{eq}} = 0.439 \text{ kg kg}^{-1}$ (870 Pa, 308.15 K)) during the same period of time ($\bar{W} \approx 0.33 \text{ kg kg}^{-1}$).

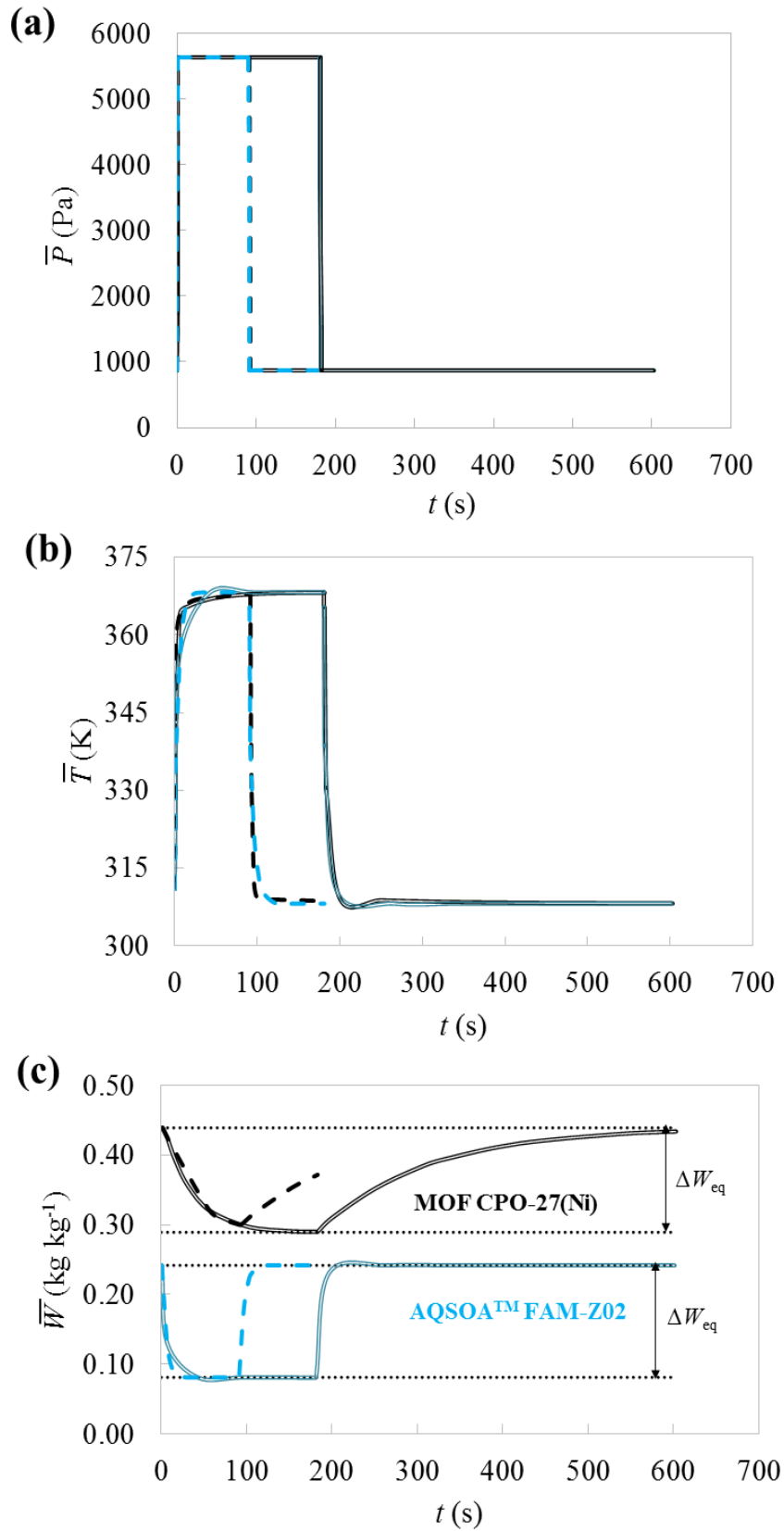


Fig. 6.12 – (a) Average pressure, (b) average temperature and (c) average adsorbate loading along time in a bed of copper foam coated with CPO-27(Ni) (black lines) and AQSOA™ FAM-Z02 (blue lines): t_{cycle} of 600 s (double lines) and 180 s (dashed lines); equilibrium values (ΔW_{eq}) (dotted lines).

Overall, under the investigated operating conditions and bed configuration, the commercial MOF CPO-27(Ni) seems outperformed by the benchmark adsorbent AQSOA™ FAM-Z02. When attempting to enhance the extracted heating power by decreasing the cycle time, the MOF accounts for greater loss of *COP*, essentially due to its higher intraparticle mass transfer resistance compared to AQSOA™ FAM-Z02. It may eventually be considered for applications in which *COP* is the key performance factor, rather than *SHP*. In addition, taking into account the equilibrium features of the pair CPO-27(Ni)/water under the investigated temperatures of evaporation and bed regeneration, the AHP operation would be restricted to relatively low heating temperatures, making the use of this pair unfeasible for applications like domestic hot water production, where high values of T_{cond} around 333 K are desirable.

6.5. Conclusions

The performance of tubular AHEx units possessing adsorbent/copper foam composites were investigated through rigorous modeling and Computational Fluid Dynamics (CFD) simulations. The MOF CPO-27(Ni) was benchmarked against the commercial zeotype adsorbent AQSOA™ FAM-Z02. A customized solver and methodology for simulating adsorption heating cycles was developed in OpenFOAM and validated using literature data.

Taking into account flow and heat transfer resistances within the composite bed, and mass transfer resistances in the adsorbent coating, the cyclic process was simulated, considering typical AHP operating conditions in cold climate ($T_{\text{evap}} = 278.15$ K), with useful heat produced at $T_{\text{cond}} = T_{\text{min,cycle}} = 308.15$ K, and mild adsorbent regeneration ($T_{\text{max,cycle}} = 368.15$ K). The obtained *COPs* and *SHPs* for the composite coating CPO-27(Ni)/copper foam were in the range 1.16-1.39 and 1922-5130 W kg⁻¹, respectively. These performances are inferior to those obtained for the AQSOA™ FAM-Z02 under similar conditions, and are mainly attributed to the lower adsorbate loading swing and higher intraparticle mass transfer resistance of the MOF. The benchmark material also showed to enable more compact AHEx designs.

In the whole, CPO-27(Ni), which is part of a set of very promising claimed materials for which huge scientific investigation is ongoing, seems unable to surpass the performance of a benchmark material for specific AHP applications. Improved performances of MOF-based AHP may be envisaged with the exploitation of the rich chemical variability of MOFs to enhance adsorption capacities and kinetics, while ensuring good hydrothermal stability.

Nomenclature

AHE _x	Adsorbent heat exchanger
BCs	Boundary conditions
C_p	Specific heat capacity ($\text{J kg}^{-1} \text{K}^{-1}$)
COP	Coefficient of performance
D_s	Surface diffusivity ($\text{m}^2 \text{s}^{-1}$)
D_{s0}	Surface diffusivity constant ($\text{m}^2 \text{s}^{-1}$)
E_a	Activation energy (J mol^{-1})
h_{wall}	Heat transfer coefficient between the composite bed (copper foam and adsorbent) and the copper tube ($\text{W m}^{-2} \text{K}^{-1}$)
HTF	Heat transfer fluid
ICs	Initial conditions
K	Bed permeability (m^2)
K_{LDF}	Linear driving force (LDF) global mass transfer coefficient (s^{-1})
L	Length of adsorbent heat exchanger
LDF	Linear driving force
m	Mass (kg)
M	Molar mass of adsorbate (kg mol^{-1})
N_{tubes}	Number of AHEx tubes for a target power of 2000 W
P	Pressure (Pa)
Q	Heat (J)
Q_{ads}	Isosteric heat of adsorption at half coverage (J kg^{-1})
Q_{st}	Isosteric heat of adsorption at zero surface coverage (J kg^{-1})
r	Radial coordinate (m)
R	Radial position in the adsorbent bed (m)
\mathfrak{R}	Universal gas constant ($\text{J mol}^{-1} \text{K}^{-1}$).
SHP	Specific heating power (W kg^{-1})
t	Time (s)
t_{cycle}	Cycle time (s)
T	Temperature (K)

$T_{\text{tube,cool}}$	Temperature of cool tube wall (K)
$T_{\text{tube,hot}}$	Temperature of hot tube wall (K)
u	Fluid superficial velocity (m s^{-1})
V_{AHEx}	Total volume of one AHEx tube (L)
$VSHP$	Volumetric heating power (W L^{-1})
$V_{N_{\text{tubes}}}$	Minimum volume occupied by N_{tubes}
W	Adsorbate loading (kg kg^{-1})
x	Cartesian coordinate (m)
y	Cartesian coordinate (m)

Greek symbols

δ	Adsorbent bed thickness (m)
ΔH_v	Latent heat of vaporization (J kg^{-1})
ε_b	Porosity of the bed
η	Dynamic viscosity ($\text{kg m}^{-1} \text{s}^{-1}$)
λ	Thermal conductivity ($\text{W m}^{-1} \text{K}^{-1}$)
ζ	Volumetric fraction of copper foam in the composite
ρ	Density (kg m^{-3})
φ	Generic notation of T , W and P
$\bar{\varphi}$	Average value of φ (<i>i.e.</i> , \bar{T} , \bar{W} and \bar{P})

Subscripts

a	Adsorbate
ADS	Isobaric adsorption stage
c	Internal boundary of the cooper tube (HTF side)
coating	Refers to the adsorbent coating
cond	Condenser
COOL	Isosteric cooling stage
copper	Refers to the copper tube and copper foam of the AHEx
DES	Isobaric desorption stage
eff	Effective

eq	Equilibrium
evap	Evaporator
fin	Final
foam	Refers to the copper foam of the AHEx
HEAT	Isosteric heating stage
i	Internal boundary of the composite bed (HTF side)
ini	Initial
o	External boundary of the composite bed (vapor side)
s	Adsorbent
sat	Saturation
tube	Refers to the copper tube of the AHEx
v	Vapor

References

- [1] European Environment Agency, The European Environment State and Outlook 2015 - Assessment of global megatrends, 2015.
- [2] European Commission - 2030 Energy Strategy: <https://ec.europa.eu/energy/en/topics/energy-strategy-and-energy-union/2030-energy-strategy>, (accessed in 31.03.2018).
- [3] European Commission - Synthesis Report on the National Plans for Nearly Zero Energy Buildings (NZEBs) (2016): [http://publications.jrc.ec.europa.eu/repository/bitstream/JRC97408/reqno_jrc97408_online%20nzeb%20report\(1\).pdf](http://publications.jrc.ec.europa.eu/repository/bitstream/JRC97408/reqno_jrc97408_online%20nzeb%20report(1).pdf), (accessed in 31.03.2018).
- [4] European Commission - Towards nearly zero-energy buildings (2013): https://ec.europa.eu/energy/sites/ener/files/documents/nzeb_full_report.pdf, (accessed in 31.03.2018).
- [5] Heat Pumping Technologies in near Zero Emission Buildings (nZEB), Heat Pumping Technologies Magazine, 35 (3) (2017).
- [6] HPP Annex 43 - <https://annex43.org/>, (accessed in 31.03.2018).
- [7] D.B. Boman, D.C. Hoysall, D.G. Pahinkar, M.J. Ponkala, S. Garimella, Screening of working pairs for adsorption heat pumps based on thermodynamic and transport characteristics, Applied Thermal Engineering, 123 (2017) 422-434.
- [8] J.M. Pinheiro, S. Salústio, A.A. Valente, C.M. Silva, Adsorption heat pump optimization by experimental design and response surface methodology, Applied Thermal Engineering, 138 (2018) 849-860.
- [9] L. Schnabel, G. Földner, A. Velte, E. Laurenz, P. Bendix, H. Kummer, U. Wittstadt, Innovative Adsorbent Heat Exchangers: Design and Evaluation, in: H.-J. Bart, S. Scholl (eds.) Innovative Heat Exchangers, Springer International Publishing, Cham, 2018, pp. 363-394.
- [10] J.M. Pinheiro, A.A. Valente, S. Salústio, N. Ferreira, J. Rocha, C.M. Silva, Application of the novel ETS-10/water pair in cyclic adsorption heating processes: Measurement of equilibrium and kinetics properties and simulation studies, Applied Thermal Engineering, 87 (2015) 412-423.
- [11] H. Demir, M. Mobedi, S. Ülkü, A review on adsorption heat pump: Problems and solutions, Renewable and Sustainable Energy Reviews, 12 (2008) 2381-2403.
- [12] J.M. Corberan, M. Axell, R.d. Boer, A. Freni, U. Jakob, S. Landolina, P. Lundqvist, M. Monsberger, R. Nordman, T. Nowak, T. Oltersdorf, S. Spoelstra, F. Ziegler, Heat Pumps, in: Strategic Research Priorities for Cross-cutting Technology, Global CCS Institute, European Technology Platform on Renewable Heating and Cooling, Belgium, 2012, pp. 48-75.
- [13] M.F.d. Lange, J. Gascon, F. Kapteijn, T. Vlugt, Adsorption-Based Heating and Cooling – Metal-Organic Frameworks over Zeolites?, AIChE Annual Meeting, San Francisco, 2016.
- [14] S.K. Henninger, S.-J. Ernst, L. Gordeeva, P. Bendix, D. Fröhlich, A.D. Grekova, L. Bonaccorsi, Y. Aristov, J. Jaenchen, New materials for adsorption heat transformation and storage, Renewable Energy, 110 (2017) 59-68.
- [15] U. Wittstadt, G. Földner, S. Vasta, R. Volmer, P. Bendix, L. Schnabel, W. Mittelbach, Adsorption Heat Pumps and Chillers – Recent Developments for Materials and Components, 12th IEA Heat Pump Conference, Rotterdam (2017).

- [16] A. Freni, L. Bonaccorsi, E. Proverbio, G. Maggio, G. Restuccia, Zeolite synthesised on copper foam for adsorption chillers: A mathematical model, *Microporous and Mesoporous Materials*, 120 (2009) 402-409.
- [17] A. Frazzica, A. Freni, Adsorbent working pairs for solar thermal energy storage in buildings, *Renewable Energy*, 110 (2017) 87-94.
- [18] M.F. de Lange, B.L. van Velzen, C.P. Ottevanger, K.J.F.M. Verouden, L.-C. Lin, T.J.H. Vlugt, J. Gascon, F. Kapteijn, Metal–Organic Frameworks in Adsorption-Driven Heat Pumps: The Potential of Alcohols as Working Fluids, *Langmuir*, 31 (2015) 12783-12796.
- [19] S.-J. Ernst, F. Jeremias, H.-J. Bart, S.K. Henninger, Methanol Adsorption on HKUST-1 Coatings Obtained by Thermal Gradient Deposition, *Industrial & Engineering Chemistry Research*, 55 (2016) 13094-13101.
- [20] E. Elsayed, R. Al-Dadah, S. Mahmoud, A. Elsayed, P.A. Anderson, Aluminium fumarate and CPO-27(Ni) MOFs: Characterization and thermodynamic analysis for adsorption heat pump applications, *Applied Thermal Engineering*, 99 (2016) 802-812.
- [21] F. Jeremias, D. Frohlich, C. Janiak, S.K. Henninger, Water and methanol adsorption on MOFs for cycling heat transformation processes, *New Journal of Chemistry*, 38 (2014) 1846-1852.
- [22] OpenFOAM Programmer's Guide, <http://foam.sourceforge.net/docs/Guides-a4/ProgrammersGuide.pdf>, ((accessed in 5.03.2018)).
- [23] A. Patton, B.D. Crittenden, S.P. Perera, Use of the Linear Driving Force Approximation to Guide the Design of Monolithic Adsorbents, *Chemical Engineering Research and Design*, 82 (2004) 999-1009.
- [24] A. Elsayed, E. Elsayed, R. Al-Dadah, S. Mahmoud, A. Elshaer, W. Kaiyaly, Thermal energy storage using metal–organic framework materials, *Applied Energy*, 186 (2017) 509-519.
- [25] H. Wei Benjamin Teo, A. Chakraborty, W. Fan, Improved adsorption characteristics data for AQSOA types zeolites and water systems under static and dynamic conditions, *Microporous and Mesoporous Materials*, 242 (2017) 109-117.
- [26] OpenFOAM User Guide, <http://foam.sourceforge.net/docs/Guides-a4/OpenFOAMUserGuide-A4.pdf>, (accessed in 20.02.2018).
- [27] SimScale, <https://www.simscale.com/blog/2016/10/openfoam-users-should-try-simscale/>, (accessed in 27.02.2018).
- [28] OpenFOAM standard solvers, <https://www.openfoam.com/documentation/user-guide/standard-solvers.php>, (accessed in 27.02.2018).
- [29] simFlow CFD software, <https://sim-flow.com/>, (accessed in 26.02.2018).
- [30] The OpenFOAM Foundation, <https://openfoam.org/>, (accessed in 27.02.2018).
- [31] Paraview application, <https://www.paraview.org/>, (accessed in 5.03.2018).
- [32] M.F. de Lange, K.J.F.M. Verouden, T.J.H. Vlugt, J. Gascon, F. Kapteijn, Adsorption-Driven Heat Pumps: The Potential of Metal–Organic Frameworks, *Chemical Reviews*, 115 (2015) 12205-12250.
- [33] H. Kakiuchi, S. Shimooka, M. Iwade, K. Oshima, M. Yamazaki, S. Terada, H. Watanabe, T. Takewaki, Water vapor adsorbent FAM-Z02 and its applicability to adsorption heat pump, *KAGAKU KOGAKU RONBUNSHU*, 31 (2005) 273-277.
- [34] M. Tagliabue, C. Rizzo, R. Millini, P.D.C. Dietzel, R. Blom, S. Zanardi, Methane storage on CPO-27-Ni pellets, *Journal of Porous Materials*, 18 (2011) 289-296.
- [35] S. Mahzoon, S. Fatemi, Developed Mathematical Model for SAPO-34 Core-Shell Adsorbents in the Adsorption Process of CO₂ from Natural Gas, *Separation Science and Technology*, 49 (2014) 55-67.

- [36] S. Bruckner, T. Demmer, M. Ganswind, D. Bathen, Modeling of Water Adsorption in SAPO-34-Coated Aluminum Foam, *Chemie Ingenieur Technik*, 89 (2017) 757-764.
- [37] G.K. White, S.J. Collocott, Heat Capacity of Reference Materials: Cu and W, *Journal of Physical and Chemical Reference Data*, 13 (1984) 1251-1257.
- [38] W.M. Haynes, *CRC Handbook of Chemistry and Physics*, 97th Edition, CRC Press, 2016.
- [39] I.S. Girnuk, Y.I. Aristov, Dynamics of water vapour adsorption by a monolayer of loose AQSOA™-FAM-Z02 grains: Indication of inseparably coupled heat and mass transfer, *Energy*, 114 (2016) 767-773.
- [40] G. Jiang, L. Diao, K. Kuang, *Advanced Thermal Management Materials*, Springer New York, 2012.
- [41] R.E. Critoph, Performance estimation of convective thermal wave adsorption cycles, *Applied Thermal Engineering*, 16 (1996) 429-437.
- [42] B. Dawoud, On the development of an innovative gas-fired heating appliance based on a zeolite-water adsorption heat pump; system description and seasonal gas utilization efficiency, *Applied Thermal Engineering*, 72 (2014) 323-330.
- [43] U. Wittstadt, G. Fuldner, E. Laurenz, A. Warlo, A. Große, R. Herrmann, L. Schnabel, W. Mittelbach, A novel adsorption module with fiber heat exchangers: Performance analysis based on driving temperature differences, *Renewable Energy*, 110 (2016) 154-161.
- [44] D. Frohlich, E. Pantatosaki, P.D. Kolokathis, K. Markey, H. Reinsch, M. Baumgartner, M.A. van der Veen, D.E. De Vos, N. Stock, G.K. Papadopoulos, S.K. Henninger, C. Janiak, Water adsorption behaviour of CAU-10-H: a thorough investigation of its structure-property relationships, *Journal of Materials Chemistry A*, 4 (2016) 11859-11869.

Annex A6

A6.1. Computational simulations using OpenFOAM

A6.1.1. Grid details

The computational grid was generated in simFlow using an OpenFOAM grid generation utility, has an unstructured topology, 894 cells (859 hexahedra and 35 prisms) and 1880 nodes (grid points). In order to accurately solve the boundary layers near the bed walls (next to the HTF and vapor sides (Fig. 6.1)), a boundary layer mesh with 5 layers and a grid expansion ratio of 1.25 was considered. Since a poor quality grid may lead to inaccurate solutions and/or slow convergence, the mesh quality was confirmed prior to the simulations using the *checkMesh* utility.

A6.1.2. Setting initial (ICs) and boundary (BCs) conditions using *swak4foam*

The main goal of *swak4foam* (Swiss Army Knife for Foam) is avoid the use of C++, enabling non-uniform ICs and BCs to be set without programming [1]. This library combines the functionality of the *funkySetFields* utility that allows setting fields using expressions, and *groovyBC* that enables specifying arbitrary BCs based on expressions [1].

For the simulation of the ETS-10/water case in OpenFOM using literature data by Pinheiro *et al.* [2], non-uniform ICs for T and W in the isobaric adsorption stage were set using the *funkySetFields* utility (see Eq. (A6.1) and (A6.2) in Section A6.1.3). In a second part, in order to simulate the composite beds (MOF CPO-27(Ni) or AQSOA™ FAM-Z02 plus copper foam), Robin type BCs for T were implemented using the *groovyBC* functionality (see inner BCs in Table 6.2, Section 6.2.2).

A6.1.3. Initial (ICs) and boundary (BCs) conditions for the ETS-10/water case

To initialize the simulations for the ETS-10/water pair starting at the beginning of the isobaric adsorption, a uniform pressure (P) of 870 Pa was set, and for T and W the following expressions as function of r were considered:

$$T(0, r) = -1.914 \times 10^7 r^2 + 1.840 \times 10^5 r - 18.513 \quad (A6.1)$$

$$W(0, r) = 1.155 \times 10^6 r^3 - 1.923 \times 10^4 r^2 + 106.162 r - 0.162 \quad (A6.2)$$

Eqs. (A6.1) and (A6.2) were obtained by fitting polynomials to the results obtained for the fourth simulated (steady-state) cycle reported by J. Pinheiro *et al.* [2]. The values of T , P , and W at the end of the isobaric adsorption stage were the initial conditions for the isosteric heating step; in turn, the final conditions for the isosteric heating step were the initial conditions for the isobaric desorption stage, etc. The BCs considered in the simulations are given in Table A6.1. In this case, they were applied in a reverse order of that indicated in Fig. 6.1, *i.e.*, circulation of HTF and vapor in the outer ($r = R_o$) and inner ($r = R_i$) parts of the AHEx, respectively.

Table A6.1 – Boundary conditions (BCs) considered to simulate an adsorption heating cycle using ETS-10/water pair, as reported in ref. [2].

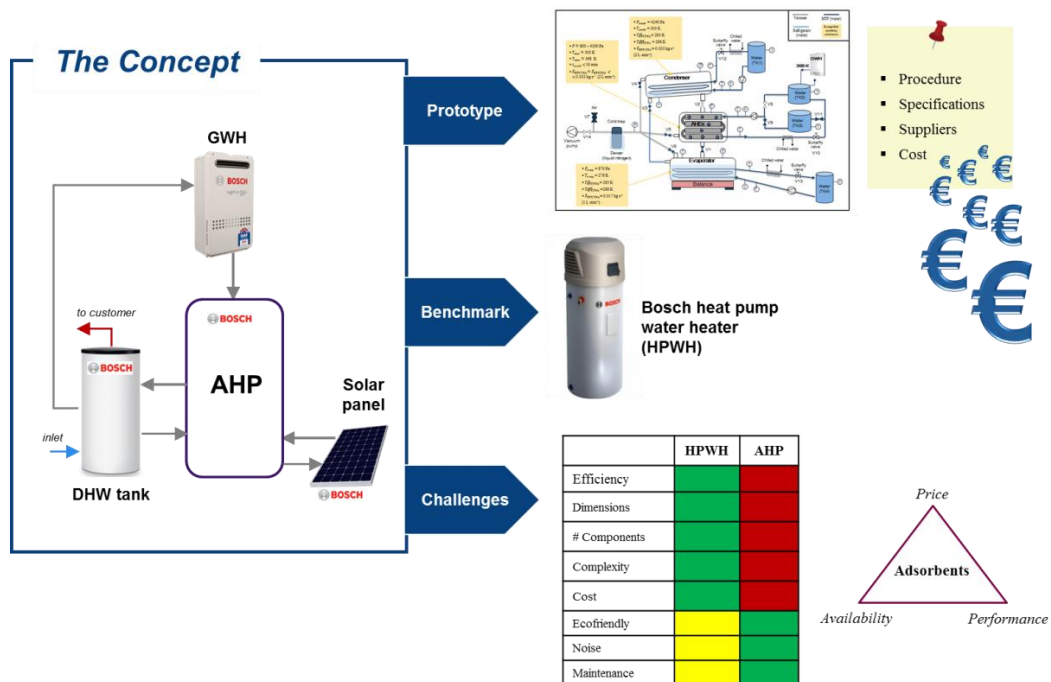
Cycle stage	Inner BCs – water vapor side	Outer BCs - heat transfer fluid side
Isobaric adsorption (ADS)	$\frac{\partial T}{\partial x}(t, x_i) = \frac{\partial T}{\partial y}(t, y_i) = 0$ $P(t, x_i) = P(t, y_i) = P_{\text{evap}} = 870 \text{ Pa}$	$T(t, x_o) = T(t, y_o) = 333.15 \text{ K}$ $\frac{\partial P}{\partial x}(t, x_o) = \frac{\partial P}{\partial y}(t, y_o) = 0$
Isosteric heating (HEAT)	$\frac{\partial T}{\partial x}(t, x_i) = \frac{\partial T}{\partial y}(t, y_i) = 0$ $\frac{\partial P}{\partial x}(t, x_i) = \frac{\partial P}{\partial y}(t, y_i) = 0$	$T(t, x_o) = T(t, y_o) = 473.15 \text{ K}$ $\frac{\partial P}{\partial x}(t, x_o) = \frac{\partial P}{\partial y}(t, y_o) = 0$
Isobaric desorption (DES)	$\frac{\partial T}{\partial x}(t, x_i) = \frac{\partial T}{\partial y}(t, y_i) = 0$ $P(t, x_i) = P(t, y_i) = P_{\text{cond}} = 19921 \text{ Pa}$	$T(t, x_o) = T(t, y_o) = 473.15 \text{ K}$ $\frac{\partial P}{\partial x}(t, x_o) = \frac{\partial P}{\partial y}(t, y_o) = 0$
Isosteric cooling (COOL)	$\frac{\partial T}{\partial x}(t, x_i) = \frac{\partial T}{\partial y}(t, y_i) = 0$ $\frac{\partial P}{\partial x}(t, x_i) = \frac{\partial P}{\partial y}(t, y_i) = 0$	$T(t, x_o) = T(t, y_o) = 333.15 \text{ K}$ $\frac{\partial P}{\partial x}(t, x_o) = \frac{\partial P}{\partial y}(t, y_o) = 0$

References

- [1] Contrib/swak4Foam, <http://openfoamwiki.net/index.php/Contrib/swak4Foam>, (accessed in 5.03.2018).
- [2] J.M. Pinheiro, A.A. Valente, S. Salústio, N. Ferreira, J. Rocha, C.M. Silva, Application of the novel ETS-10/water pair in cyclic adsorption heating processes: Measurement of equilibrium and kinetics properties and simulation studies, *Applied Thermal Engineering*, 87 (2015) 412-423.

Chapter 7: Prototype design

In order to test the studied adsorbent materials and other commercially available adsorbents, an experimental installation of an AHP may be assembled, which requires a heat source. There exists significant know-how on gas water heaters (GWHs) in Bosch Thermotechnology. The use of an AHP coupled with a GWH emerged as a convenient and adequate approach for a prototype. In this chapter, an experimental setup of a hybrid system combining an AHP and a GWH that may be assembled in Bosch Thermotechnology to perform functional tests and measure *COPs* and *SHPs* is presented, along with an experimental procedure. For several components of the setup, technical specifications, supplier's proposals and associated costs are provided, along with a first estimation of the overall cost of the prototype. Finally, a concept for an adsorption appliance for domestic hot water (DHW) production is presented, a brief comparison with the Bosch heat pump water heater (HPWH), and general techno-economic challenges are discussed.



7.1. Prototype

7.1.1. Experimental setup

A scheme of the prototype of the hybrid system combining an adsorption heat pump (AHP) and a gas water heater (GWH) that may be assembled in Bosch Thermotechnology to perform functional tests is shown in Fig. 7.1, along with some exemplified operating conditions. It essentially contemplates:

- (i) a vacuum pump;
- (ii) a cold trap embedded in a dewar containing, for example, alcohol/liquid nitrogen mixture (to avoid condensation of O₂ – dangerous). It is used to solidify or condense water vapor coming from the AHP and prevent it from entering and damaging the vacuum pump, and, on the other hand, avoids the system contamination with oil vapors from the pump. The dimensions of the trap will depend on the amount of water desorbed from the material, which may be determined by thermogravimetric analysis;
- (iii) a condenser composed by several tubes in series with the heat transfer fluid (HTF) (water) circulating inside, and the refrigerant vapor (water) condensing on the outside, within a vacuum stainless steel chamber;
- (iv) an adsorbent heat exchanger (AHEx) inside a vacuum stainless steel chamber, composed of several tubes in series with the HTF (water) circulating inside the tubes, in order to heat or cool the adsorbent, and the adsorbent confined between the tubes with the help of a grid or impregnated on the tubes;
- (v) an evaporator, which consists of a set of tubes in series embedded in a pool of deionized water (refrigerant), where the HTF circulates. It is confined in a vacuum stainless steel chamber;
- (vi) a balance to monitor the variation of the mass of refrigerant inside the evaporator chamber;
- (vii) a set of water tanks with controlled temperature to store the HTFs that circulate in the condenser (TK1), AHEx (TK2 and TK3), and evaporator (TK4);
- (viii) a GWH to heat the HTF (water) necessary for heating and regenerating the adsorbent (connected to TK2);

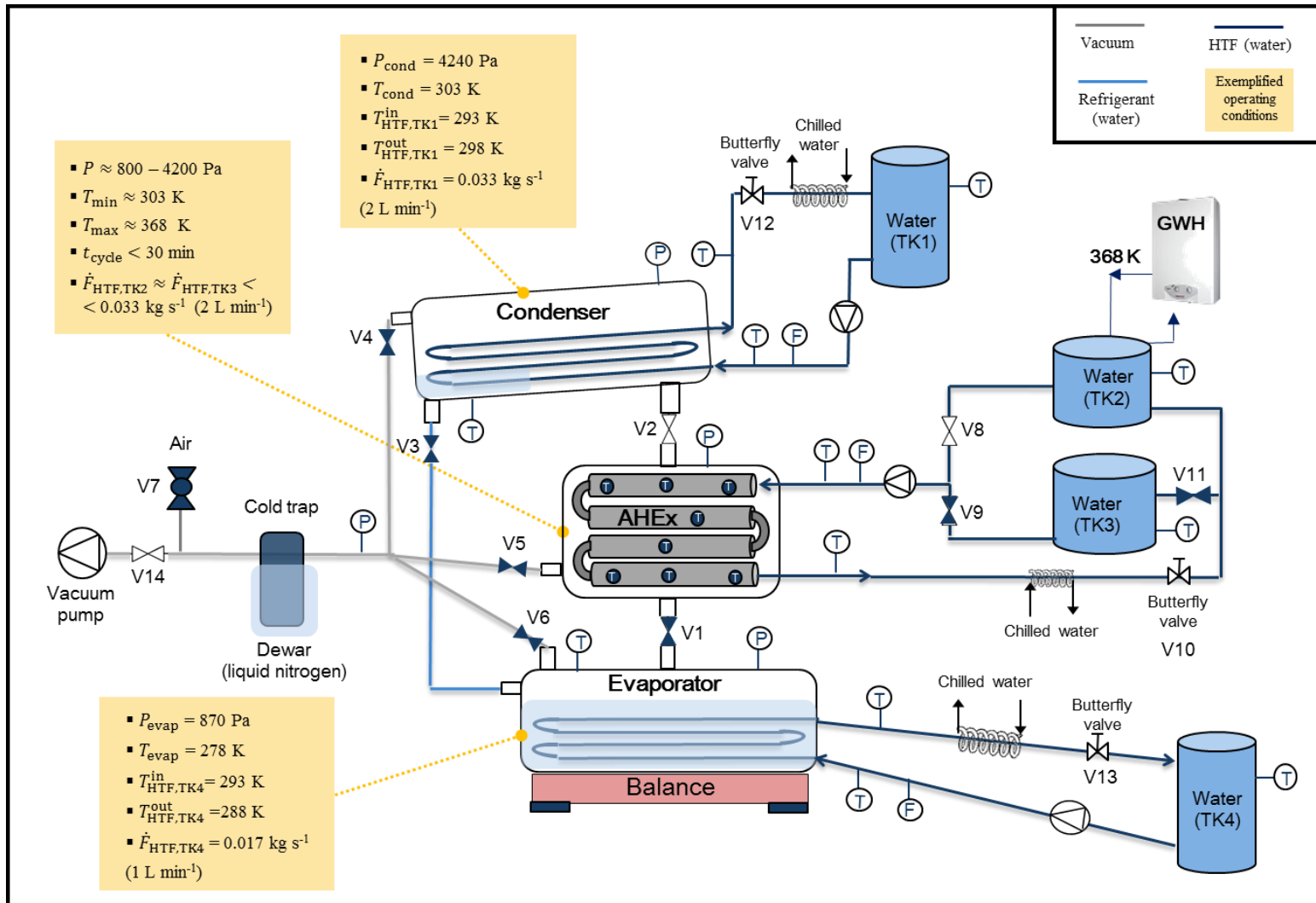


Fig. 7.1 - Experimental setup of a hybrid system combining a heat pump module with a gas water heater (GWH).

- (ix) several instrumentation to monitor pressure (P), temperature (T) and flowrate (F) in several locations along time;
- (x) water pumps and valves in the HTF circuits (butterfly valves for controlling pressure drop, and hence flowrate, if needed), and vacuum valves and a throttling device (V3) (for instance, capillary tube) in the vacuum side of the installation.

7.1.2. Experimental procedure

The experimental procedure to operate the setup in Fig. 7.1 consists of mainly eight steps. The first three concern the evacuation of the adsorbent bed (desorption of water, oxygen, etc.), condenser and evaporator, and the water refrigerant degassing, which have been reported as strictly obligatory tasks prior to the start-up of an AHP [1, 2]. The remaining five stages regard the operation of the AHP during a basic adsorption heating cycle.

1. *Evacuation of the adsorbent bed:* degas the adsorbent during at least 24 h by circulating hot water from TK2 through the AHEx (valve V8 is opened), while simultaneously applying dynamic vacuum (in the vacuum circuit, valves V5 and V14 are opened and the remaining ones are closed). Monitor the pressure inside the AHEx vacuum chamber;

2. *Condenser evacuation:* close valve V5 and open V4 to evacuate the condenser under dynamic vacuum at ambient temperature, while monitoring the pressure inside the chamber (for instance, *ca.* 4 h). At this stage there is no refrigerant liquid inside the condenser;

3. *Evacuation of evaporator and water degassing through freeze-pump-thaw cycling:* with only V14 open in the vacuum circuit, the evaporator (which contains deionized liquid water inside) is immersed in a bath of alcohol/liquid nitrogen (not shown in Fig. 7.1) to freeze the refrigerant (*freeze*). After freezing, V6 is opened to remove the gases in the evaporator chamber (*pump*). Then, valve V6 is closed, and the cooling bath is removed to allow melting the water inside the evaporator (*thaw*), after which gas bubbles will evolve from the liquid to the gas phase. Afterwards, the evaporator is again immersed in the

cooling bath for freezing the water, V6 is opened to remove the gases from the evaporator chamber, and the *freeze-pump-thaw* cycle continues, repeating for another 2-3 times;

4. *Preparation of evaporator prior to isosteric cooling and isobaric adsorption*: valves V1-V6 are closed (static vacuum in the AHP module) and the mass of refrigerant in the evaporator is registered (the mass of the evaporator and chamber are previously measured). The temperature and pressure of the refrigerant liquid in the evaporator are monitored, and the circulation of the HTF from TK4 starts. Depending on the temperature inside the evaporator, a given pressure will be established (vapor-liquid equilibrium conditions);

5. *Isosteric cooling*: with valves V9 and V11 open, the AHEx is cooled with water coming from TK3, and the pressure decrease inside the chamber is monitored (the HTF temperature is higher than that inside the evaporator, to avoid refrigerant condensation in the AHEx in the subsequent stage);

6. *Isobaric adsorption*: as soon as the pressure in the AHEx chamber drops below the evaporator pressure, V1 is opened and adsorption starts. The pressure and temperature in the AHEx and in the evaporator should be monitored meanwhile (*e.g.*, for the latter, P and T may decrease to some extent until the HTF from TK4 supplies enough heat to stabilize the evaporator conditions). When the water ΔT between the AHEx inlet and outlet does not differ significantly (for instance, < 5 K), V1 is closed and the adsorption stage ends. The circulation of the HTFs from TK3 (connected to the AHEx) and TK4 (connected to the evaporator) is now stopped, and the mass of refrigerant remaining in the evaporator is registered to calculate the mass of adsorbed water in the bed;

7. *Isosteric heating*: with vacuum valves V1-V6 closed, the circulation of HTF from TK1 through the condenser and from TK2 through the AHEx starts (for the latter, the water is heated by the GWH), while monitoring P and T inside the chambers. As a result of the adsorbent heating, P inside the AHEx chamber increases;

8. *Isobaric desorption*: as soon as the pressure inside the AHEx chamber exceeds that in the condenser, V2 is opened and the desorption stage starts. The vapor that desorbs due to the bed heating by the hot water coming from TK2 condenses inside the condenser chamber. The condensed refrigerant is then transferred to the evaporator through V3. The P and T inside the chambers are monitored (for instance, T (and P) inside the condenser chamber may increase initially due to the hot vapor coming from the bed and the heat released upon condensation of water, until the HTF from TK1 extracts enough heat to

stabilize the conditions). When the ΔT of the HTF (water) between the condenser inlet and outlet no longer differs significantly (*e.g.*, < 5 K), V2 is closed and the stage ends. The circulation of the HTFs from TK1 and TK2 is stopped, and the mass of refrigerant in the evaporator is registered to calculate the cyclic adsorption loading swing (ΔW_{cycle}).

Finally, with the records of T along time for all the HTFs, the heats involved in each stage of the cycle are calculated as follows:

$$Q_{\text{ADS+COOL}} = \int_{t_{\text{ADS+COOL}}^i}^{t_{\text{ADS+COOL}}^f} \dot{F}_{\text{HTF,TK3}} C_{\text{pHTF,TK3}} (T_{\text{HTF,TK3}}^{\text{out}} - T_{\text{HTF,TK3}}^{\text{in}}) dt \quad (7.1)$$

$$Q_{\text{DES+HEAT}} = \int_{t_{\text{DES+HEAT}}^i}^{t_{\text{DES+HEAT}}^f} \dot{F}_{\text{HTF,TK2}} C_{\text{pHTF,TK2}} (T_{\text{HTF,TK2}}^{\text{in}} - T_{\text{HTF,TK2}}^{\text{out}}) dt \quad (7.2)$$

$$Q_{\text{evap}} = \int_{t_{\text{ADS}}^i}^{t_{\text{ADS}}^f} \dot{F}_{\text{HTF,TK4}} C_{\text{pHTF,TK4}} (T_{\text{HTF,TK4}}^{\text{in}} - T_{\text{HTF,TK4}}^{\text{out}}) dt \approx m_s \Delta W_{\text{cycle}} \Delta H_v \quad (7.3)$$

$$Q_{\text{cond}} = \int_{t_{\text{DES}}^i}^{t_{\text{DES}}^f} \dot{F}_{\text{HTF,TK1}} C_{\text{pHTF,TK1}} (T_{\text{HTF,TK1}}^{\text{out}} - T_{\text{HTF,TK1}}^{\text{in}}) dt \approx m_s \Delta W_{\text{cycle}} \Delta H_v \quad (7.4)$$

where $Q_{\text{ADS+COOL}}$ and Q_{cond} are the heats released from the bed during isobaric adsorption and isosteric cooling, and by the condenser, respectively; $Q_{\text{DES+HEAT}}$ and Q_{evap} are the heats supplied to the bed during isobaric desorption and isosteric heating, and to the evaporator, respectively; $\dot{F}_{\text{HTF,TK1}}$, $\dot{F}_{\text{HTF,TK2}}$, $\dot{F}_{\text{HTF,TK3}}$ and $\dot{F}_{\text{HTF,TK4}}$, and $C_{\text{pHTF,TK1}}$, $C_{\text{pHTF,TK2}}$, $C_{\text{pHTF,TK3}}$ and $C_{\text{pHTF,TK4}}$ are mass flowrates and specific heat capacities of the HTFs in TK1, TK2, TK3 and TK4, respectively; $T_{\text{HTF,TK1}}^{\text{in}}$ and $T_{\text{HTF,TK1}}^{\text{out}}$ are the temperatures of the HTF from TK1 at the inlet and outlet of condenser, respectively; $T_{\text{HTF,TK2}}^{\text{in}}$ and $T_{\text{HTF,TK2}}^{\text{out}}$, and $T_{\text{HTF,TK3}}^{\text{in}}$ and $T_{\text{HTF,TK3}}^{\text{out}}$ are the temperatures of the HTFs coming from TK2 and TK3 at the AHEx inlet and outlet, respectively; $T_{\text{HTF,TK4}}^{\text{in}}$ and $T_{\text{HTF,TK4}}^{\text{out}}$ are the temperatures of the HTF from TK4 at the evaporator inlet and outlet; m_s is the adsorbent mass, and ΔH_v is the enthalpy of vaporization of the refrigerant. The quantification of these heats enables assessing the AHP performance by means of the well-known *COP* and *SHP*.

7.1.3. Specification of components, suppliers proposals and costs

In order to acquire the necessary material to assemble the prototype, several components were specified and suppliers were contacted. The obtained proposals are collected in Annex A7 (Tables A7.1-A7.6). Considering the information gathered so far, the prototype cost exceeds 17000 €, without contemplating the cost of other important components such as heat exchangers and vacuum chambers. Overall, the cost of the AHP prototype is very likely to surpass the budget initially planned by Bosch, which was between 10000 and 20000 €.

7.2. Product concept, comparison with conventional technology, and challenges

7.2.1. Product concept

Fig. 7.2 illustrates a hybrid system for domestic hot water (DHW) production, combining an AHP, a GWH, a solar panel and a water tank. The AHP module is located in the inferior part of the appliance and includes one AHEx, one condenser, and one evaporator powered by solar energy. The GWH is located in the superior part and essentially contemplates a burner and two heat exchangers (primary and secondary). The tank is filled with demineralized water that circulates in the AHP and in the GWH; there is a coil embedded in the tank, where the domestic water circulates to be heated by direct heat transfer, and then delivered to the customer. The system would operate in three distinct modes as follows:

1. *Adsorption heat pumping mode - isosteric cooling and isobaric adsorption:* with the burner off, the solar panel supplies the necessary energy for the evaporation process, and the refrigerant vapor is adsorbed on the adsorbent. Simultaneously, the HTF (cold demineralized water) circulates through the AHEx removing the adsorption heat, and returns hotter to the tank;

2. *Adsorption heat pumping mode - isosteric heating and isobaric desorption:* with the burner on, the HTF (demineralized water) is heated up to 368 K by the GWH, proceeds to the AHEx and supplies the necessary heat for regeneration of the adsorbent.

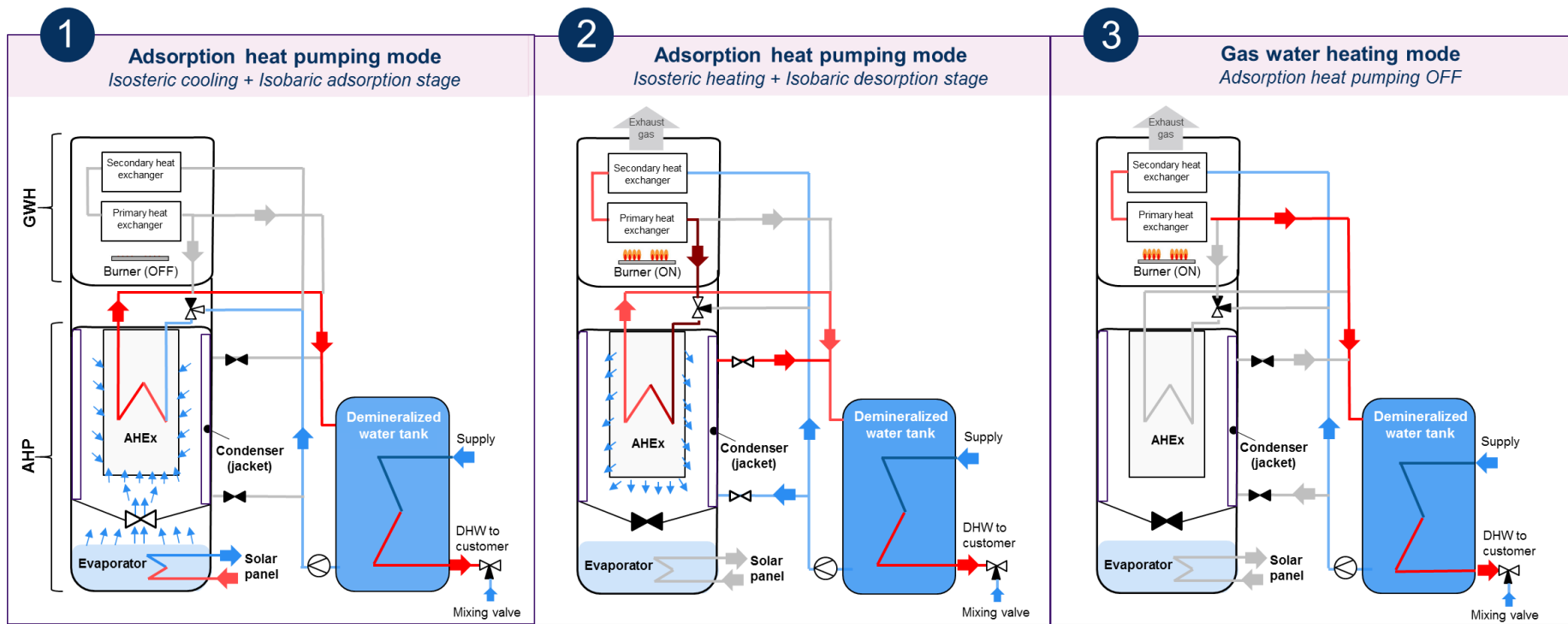


Fig. 7.2 – Hybrid system for DHW production combining an AHP, a GWH, a water tank and a solar panel, and illustration of its three distinct operation modes.

The desorbed vapor condenses on the walls of the AHEx chamber, transferring heat to the demineralized water (HTF) that also circulates inside the condenser jacket. The water exiting the condenser and the AHEx returns to the tank;

3. *Gas water heating mode*: when the AHP is no longer able to satisfy the thermal demand, the GWH works alone to fulfill the customer needs.

Several aspects regarding the product and its operating conditions should be highlighted:

- A tank with demineralized water and an internal coil for the circulation of domestic water is chosen instead of the more conventional DHW storage tanks. In this way, demineralized water is used as HTF in the appliance, minimizing the precipitation and deposition of calcium carbonate on the tube walls. For instance, in GWHs this is the main reason for premature failures;

- It is economically unfeasible if the system operates with water at $T > 373$ K, since special safety measures are necessary (in practice, this means increased complexity and hence increased cost) to avoid leakages of water vapor at pressures above atmospheric to the exterior. This has two evident disadvantages: firstly, the adsorbent regeneration becomes restricted to $T < 373$ K, which impacts negatively on the performance, and limits the T of the DHW produced *via* heat pumping, therefore being necessary a significant contribution of the GWH in the heating process; in second place, it makes the use of commercially available zeolites impracticable;

- The use of thermal oils as HTFs in the appliance would enable operation at $T > 373$ K, but it would increase the solution cost and maintenance efforts (oil oxidation concerns, need for periodical replacement of oil, etc.), and thus this option is not attractive;

- Regarding the energy sources for the evaporator, geothermal sources lead to significant installation costs. The air is the most economic and the dominant energy source, but T_{air} is highly variable. An AHP working with water as refrigerant would not operate when T_{air} is bellow *ca.* 283 K (to avoid freezing of the refrigerant); therefore the GWH would have to cover the demand in this case, which would probably lead to a poor assistance of the heating process by the AHP. A solar panel enables higher T_{evap} than air, and may support the DHW production, so it is considered here, albeit it increases the system costs.

7.2.2. Adsorption system versus Bosch heat pump water heater (HPWH)

Fig. 7.3(a) shows a simplified scheme of the Bosch heat pump water heater (HPWH), based on mechanical vapor compression technology, which includes a heat pump module in the superior part (evaporator, condenser, electrically-driven compressor and fan), and a DHW tank of *ca.* 270 L in the inferior part. It uses air as energy source for the evaporation, and R134A as refrigerant. In Fig 7.3(b) the hybrid system introduced previously in Fig. 7.2 is shown for comparison. Despite its advantages in terms of eco-friendliness (water as refrigerant, minor need of electricity), the adsorption-based system has a higher number of components, is bigger, more complex, and hence more expensive than the HPWH (complexity generally increases the cost). In terms of efficiency, the adsorption-based appliance does not seem competitive with the conventional HPWH, because the AHP performance is highly influenced by the applied adsorbents, and the market does not offer a variety of options to operate under the desirable conditions, i.e., regeneration at $T < 373$ K, high T_{cond} up to around 333 K, and T_{evap} of *ca.* 278-288 K (see discussions in Chapter 2, Section 2.3.2):

- Silica gel is cheap and widely available, but has poor performance for $T_{\text{cond}} > 312$ K;
- MOFs are emerging and claimed as very promising adsorbents, but they still lack techno-economic viability;
- Aluminosilicate zeolites do not work efficiently at such low regeneration temperature;
- AQSOA FAM-Z02, a silicoaluminophosphate specially developed for AHPs and adsorption chillers by Mitsubishi Plastics Inc. (MPI), is the most promising water adsorbent in the market so far for T_{cond} up to *ca.* 323 K, but it is expensive and poorly available. Several unsuccessful contacts were made to acquire this material for characterization and testing. To the best of our knowledge, MPI stopped meanwhile the production of heat exchangers coated with this adsorbent.

From several contacts made with well-established manufacturers of adsorbents like Grace, Oker-Chemie, UOP, CECA, Clariant, BASF and Fuji, the suggested (and affordable) materials for this type of applications are basically conventional zeolites as 13X and 4A,

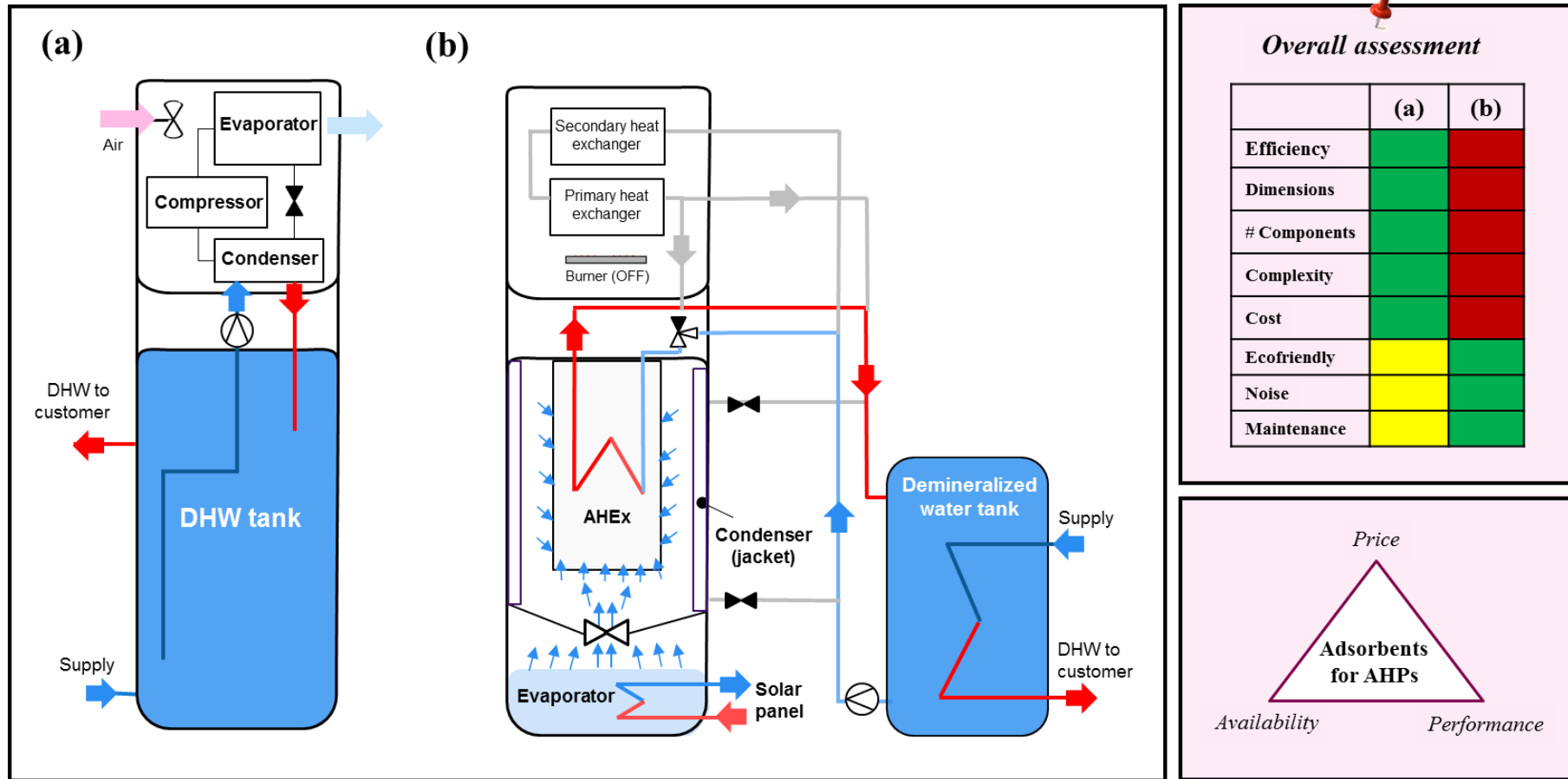


Fig. 7.3 – Scheme of (a) mechanical vapor compression heat pump water heater (HPWH) from Bosch, and (b) adsorption-based system combining a heat pump module, a gas water heater (GWH), a tank for domestic hot water (DHW) production and a solar panel, and overall qualitative assessment of the two systems. Main challenges of the adsorbents for DHW production shown in a triangle: affordable, widely available and high performance adsorbents as key enablers for the development of efficient AHPs.

and silica gel. In general, the majority of the adsorbents in the market were not optimized for these applications; they have been developed for different purposes, like gas separation and catalysis. Overall, this is very likely to be the reason why gas-fired AHPs are most efficient in low temperature heating systems, as reported by the European Heating Industry [3].

In the whole, the future development of efficient AHPs for domestic hot water production is strongly dependent on the commercialization of adsorbents that bring together low price/performance ratio and availability (see triangle in Fig. 7.3). In addition, one should keep in mind that for achieving interesting *SHP* ($> 1000 \text{ W kg}^{-1}$), which strongly impacts on the AHEx dimensions, the conventional configuration of the adsorbents (granules, pellets) should be changed to coatings.

7.3. Final outlook

In order to test the heating performance of several adsorbents in AHPs and evaluate the viability of combining an adsorption system with a GWH for DHW production, a prototype may be assembled and put into operation in the near future at Bosch Thermotechnology. From an initial estimation, the overall cost of the prototype will probably exceed the planned budget, which is in the range 10000 – 20000 €. The endorsement for opportune assembling of the prototype is now in the hands of the company.

Despite the environmental benefits, adsorption-based systems for DHW production present higher dimensions, complexity and cost than the current HPWH solutions commercialized by Bosch, and their efficiency is still constrained by the lack of water adsorbents which are simultaneously affordable, fairly available in the market and possess satisfactory performance under the desired conditions.

Currently, adsorption systems using water as refrigerant for DHW do not seem competitive with conventional mechanical vapor compression technology, and are not viable alternatives to HPWHs in the short-term. This vision is somehow aligned with the information contained in recent governmental reports dedicated to the analysis of low carbon heating technologies, which state that adsorption domestic heat pumps are expected to be significantly more expensive than the electrically powered ones, and that several stakeholders did not see the technology as competitive in the foreseeable future, although it is recognized that there is space for product cost improvements [4]. If improved AHPs are successfully developed to a greater extent, they may win some market share, for instance, in locations where the access to the electricity grid is limited or the electricity supply is uncertain, and where a heat source is abundant. They may also become a next generation of GWHs, allowing to reduce the consumption of gas in the DHW production, due to the introduction of environmental heat into the process.

Nomenclature

AHP	Adsorption heat pump
AHE _x	Adsorbent heat exchanger
<i>COP</i>	Coefficient of performance
C_p	Specific heat capacity ($J\ kg^{-1}\ K^{-1}$)
DHW	Domestic hot water
\dot{F}	Flowrate ($kg\ s^{-1}$)
GWH	Gas water heater
HPWH	Heat pump water heater
HTF	Heat transfer fluid
m_s	Adsorbent mass (kg)
P	Pressure (Pa)
Q	Heat (J)
<i>SHP</i>	Specific heating power ($W\ kg^{-1}$)
t	Time (s)
t_{cycle}	Cycle time (s)
T	Temperature (K)
TK	Storage tank for heat transfer fluid

Greek symbols

ΔH_v	Latent heat of vaporization ($J\ kg^{-1}$)
ΔW_{cycle}	Cyclic adsorption loading swing ($kg\ kg^{-1}$)

Subscripts

ADS	Isobaric adsorption stage
COOL	Isosteric cooling stage
cond	Condenser
DES	Isobaric desorption stage
evap	Evaporator

Chapter 7: Prototype design

HEAT	Isosteric heating stage
max	Maximum
min	Minimum

Superscripts

f	Final
i	Initial
in	Inlet
out	outlet



References

- [1] Y.I. Aristov, Optimal adsorbent for adsorptive heat transformers: Dynamic considerations, *International Journal of Refrigeration*, 32 (2009) 675-686.
- [2] A. Sapienza, S. Santamaria, A. Frazzica, A. Freni, Influence of the management strategy and operating conditions on the performance of an adsorption chiller, *Energy*, 36 (2011) 5532-5538.
- [3] European Heating Industry - Gas heat pumps, <http://www.ehi.eu/heating-technologies/gas-heat-pumps/>, (accessed in 25.06.2018).
- [4] Department for Business, Energy Industrial Strategy - UK, Evidence Gathering - Low Carbon Heating Technologies: Domestic high temperature, hybrid and gas driven heat pumps, London, 2016.

Annex A7







A7.1. Specification of prototype components, proposals from suppliers and costs

Table A7.1 - Identification of components for the vacuum circuit outside the heat pump module (see Fig. 7.1), possible suppliers and costs.

#	Component	Quant.	Supplier	Product designation	Technical information	Dimensions of connections	Cost (€, with VAT)	Drawing
1	Oil sealed rotary vane vacuum pump	1	STV	Trivac D16B 2-stage (Oerlikon) (Part No. LE11265)	Nominal pumping speed: 18.9 m ³ h ⁻¹ ; Ultimate pressure with gas ballast: < 5x10 ⁻³ mbar (0.5 Pa); 230 V, 50 Hz; Maximum operating temperature: 40 °C	25 KF	5850.50	
2	Vacuum pump oil	1 L		Leybold LVO 100 (Part No. L10001)	---	---	24.54	
3	Exhaustion filter for vacuum pump (with lubricant return)	1		AR-16 for TRIVAC D16B (Part No. 18921)	---	---	1601.46	
4	Cartridge for the exhaustion filter of the vacuum pump	1		(Part No. 18972)	---	(to be confirmed)	245.39	
5	Reducing intermediate piece (25KF→16KF) (connect pump to V14)	1		Reducing intermediate piece, s. steel, DN25/16 ISO-KF (Part No. IN211-281)	(see p. C15 of INFICON catalog)	25KF→16KF	23.25	





(Table A7.1 – continued)

Chapter 7: Prototype design – Annex A7

6	Clamping ring for connection of pump (25 KF) to reducing piece #5	1	STV	Clamping ring DN20-25 (Part No. IN211-002)	(see p. C1 of INFICON catalog)	25 KF	7.56	
7	Centering ring for clamping ring #6	1		Centering ring DN 25 ISO-KF, INOX/FPM (Part No. IN 211-068)	(see p. C5 of INFICON catalog)	25 KF	6.03	
8	Clamping ring for connection of reducing piece #5 (16 KF) to V14	1		Clamping ring DN10-16 (Part No. IN211-001)	(see p. C1 of INFICON catalog)	16 KF	6.95	
9	Centering ring for clamping ring #8	1		Centering ring DN 16 ISO-KF, INOX/FPM (Part No. IN 211-066)	(see p. C5 of INFICON catalog)	16 KF	4.98	
10	Valve V14 (different % openings, manual) - membrane valve	1		Bellow Valve 90°, DN16 AL (Part. No. 215375)	Max. operating temperature: 80 °C	16 KF	322.88	
11	Clamping ring to connect valve V14 to a T (16 KF)	1		Clamping ring DN10-16 (Part No. IN211-001)	(see p. C1 of INFICON catalog)	16 KF	6.95	(sames as #8)
12	Centering ring for clamping ring #11	1		Centering ring DN 16 ISO-KF, INOX/FPM (Part No. IN 211-066)	(see p. C5 of INFICON catalog)	16 KF	4.98	(sames as #9)
13	T piece for connection V14-V7	1		T piece DN 16 ISO-KF, s. steel (Part No. 211.292)	(see p. C14 of INFICON catalog)	16 KF	60.27	
14	Clamping ring for connection T - valve V7 (16 KF)	1	Clamping ring DN10-16 (Part No. IN211-001)	(see p. C1 of INFICON catalog)	16 KF	6.95	(sames as #8)	




(Table A7.1 – continued)

Chapter 7: Prototype design – Annex A7

15	Centering ring for clamping ring #14	1	STV	Centering ring DN 16 ISO-KF, INOX/FPM (Part No. IN 211-066)	(see p. C5 of INFICON catalog)	16 KF	4.98	(sames as #9)
16	Valve V7 (on-off, manual) - Safety valve	1		Vent valve (Part. No. 89039)	---	16 KF	368.08	
17	Flexible s. steel tube for connection T- cold trap	1		Flexible metal hose, DN 16KF, 750 mm (Part No. IN211-337)	(see p. C16 of INFICON catalog)	16 KF	111.93	
18	Clamping ring for connection T - flexible tube #17 (16 KF)	1		Clamping ring DN10-16 (Part No. IN211-001)	(see p. C1 of INFICON catalog)	16 KF	6.95	(sames as #8)
19	Centering ring for clamping ring #18	1		Centering ring DN 16 ISO-KF, INOX/FPM (Part No. IN 211-066)	(see p. C5 of INFICON catalog)	16 KF	4.98	(sames as #9)
20	Glass cold trap and supporting ring (to hold the trap in the dewar)	1	KGW- isotherm	Cold Trap KS 80-K16-44XS	Condensate capacity 500 mL with KF NW 10 flanges (Liquid refrigerants: Liquid N ₂ or ice + salt).	10KF	1198.4	
21	Dewar for cold trap	1		Type 44 CAL-S	With viewing stripes (to monitor what is happening inside the trap)	Consistent with trap dimensions		

(Table A7.1 – continued)

Chapter 7: Prototype design – Annex A7

22	Glass-tube connections (trap-s. steel tube)	2	STV	Glass tube connection, Al, FPM DN10KF-10 (Part No. IN211-351)	(see p. C19 of INFICON catalog)	10 KF	182.04	
23	Reducing centering ring for connections glass-tube #22	2		Reducing centering ring DN10-16 ISO-KF, INOX/FPM (Part No. IN211-078)	(see p. C8 of INFICON catalog)	10K <--> 16KF	11.56	
24	Clamping ring for connections of cold trap	2		Clamping ring DN10-16 (Part No. IN211-001)	(see p. C1 of INFICON catalog)	16 KF	13.90	(same as #8)
25	Flexible s. steel tube for connection trap - T of vacuum meter	1		Flexible metal hose, DN 16KF, 750 mm (Part No. IN211-337)	(see p. C16 of INFICON catalog)	16 KF	111.93	(same as #17)
26	T piece for connection of tube #25 to vacuum meter	1		T piece DN 16 ISO-KF, s. steel (Part No. 211.292)	(see p. C14 of INFICON catalog)	16 KF	60.27	(same as #13)
27	Clamping rings for T of vacuum meter	3		Clamping ring DN10-16 (Part No. IN211-001)	(see p. C1 of INFICON catalog)	16 KF	20.85	(same as #8)
28	Centering ring for clamping rings #27	3		Centering ring DN 16 ISO-KF, INOX/FPM (Part No. IN 211-066)	(see p. C5 of INFICON catalog)	16 KF	14.94	(sames as #9)
29	Four-ways s. steel connection	1		Cross piece DN16 ISO-KF, s. steel (Part No. IN211-297)	(see p.C14 of INFICON catalog)	16 KF	81.18	
30	Flexible s. steel tube to connect four-way connection with condenser, evaporator and AHEx	3		Flexible metal hose, DN 16KF, 750 mm (Part No. IN211-337)	(see p. C16 of INFICON catalog)	16 KF	335.79	(same as #17)

(Table A7.1 – continued)

Chapter 7: Prototype design – Annex A7










31	Clamping ring to connect four-way connection with condenser, evaporator, AHEx, and for V4, V5, V6 in between	9	STV	Clamping ring DN10-16 (Part No. IN211-001)	(see p. C1 of INFICON catalog)	16 KF	62.55	(same as #8)
32	Centering rings for clamping rings #31	9		Centering ring DN 16 ISO-KF, INOX/FPM (Part No. IN 211-066)	(see p. C5 of INFICON catalog)	16 KF	44.83	(same as #9)
33	Flanges for welding to condenser, evaporator and AHEx, for connection to the vacuum circuit	3		Flange with tube socket long inox 304 DN16 (Part No. IN211-217)	(see p. C12 of INFICON catalog)	16KF	61.99	
34	Vacuum valves V4, V5, V6 (with different % opening and withstanding T up to 373 K)	3	(to be confirmed with STV)					

Table A7.2 - Identification of components for the vacuum circuit nearby or connected to the condenser (please see Fig. 7.1), possible suppliers and costs.

#	Component	Quant.	Supplier	Product designation	Technical information	Dimensions of connections	Cost (€, with VAT)	Drawing
1	Valve V3 (different % opening; withstand T up to 373 K)	1	(to be confirmed with STV)					
2	Flange for welding to condenser for connection with evaporator	1	STV	Flange with tube socket long inox 304 DN16 (Part No. IN211-217)	(see p. C12 of INFICON catalog)	16KF	20.66	






(Table A7.2 – continued)

Chapter 7: Prototype design – Annex A7

3	Clamping rings for connections V3-flange #2	2		Clamping ring DN10-16 (Part No. IN211-001)	(see p. C1 of INFICON catalog)	16 KF	13.90	
4	Centering rings for connections V3-flange #2	2		Centering ring DN 16 ISO-KF, INOX/FPM (Part No. IN 211-066)	(see p. C5 of INFICON catalog)	16 KF	9.96	
5	Flexible tube for connection condenser-evaporator	1		Flexible metal hose, DN 16KF, 750 mm (Part No. IN211-337)	(see p. C16 of INFICON catalog)	16 KF	111.93	
6	Flange for welding to condenser, for connection to the AHEx	1		Flange with tube socket long inox 304 DN40 (Part No. IN211-219)	(see p. C12 of INFICON catalog)	40 KF (or 25KF)	38.13	
7	Valve V2 (condenser→AHEx) (different % opening; withstand T up to 373 K)	1	(to be confirmed with STV)			40 KF (or 25KF)	---	---
8	Flexible tube for connection condenser-AHEx	1	STV	Flexible metal hose, DN 40KF, 750 mm (Part No. IN211-345)	(see p. C16 of INFICON catalog)	40 KF (or 25KF)	150.06	
9	Clamping rings for connections condenser → AHEx	3		Clamping ring DN32-40 (Part No. IN211-003)	(see p. C1 of INFICON catalog)	40 KF (or 25KF)	23.99	
10	Centering rings for clamping rings #9	3		Centering ring DN 40 ISO-KF, INOX/FPM (Part No. IN 211-070)	(see p. C5 of INFICON catalog)	40 KF (or 25KF)	22.14	

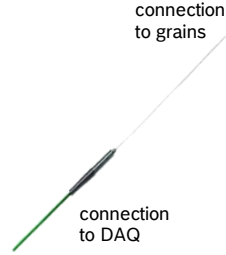

Chapter 7: Prototype design – Annex A7

Table A7.3 - Identification of components for the vacuum circuit nearby or connected to the evaporator (see Fig. 7.1), possible suppliers and costs.

#	Component	Quant.	Supplier	Product designation	Technical information	Dimensions of connections	Cost (€, with VAT)	Drawing
1	Flange for welding to evaporator, for connection to the condenser	1	STV	Flange with tube socket long inox 304 DN16 (Part No. IN211-217)	(see p. C12 of INFICON catalog)	16KF	20.66	
2	Flange for welding to evaporator, for connection to AHEx	1	STV	Flange with tube socket long inox 304 DN40 (Part No. IN211-219)	(see p. C12 of INFICON catalog)	40 KF (or 25KF)	38.13	
3	Valve V1 (evaporator→AHEx) (different % opening, withstanding T up to 373 K)	1	(to be confirmed with STV)			40 KF (or 25KF)	---	---
4	Flexible tube for connection evaporator-AHEx	1	STV	Flexible metal hose, DN 40KF, 750 mm (Part No. IN211-345)	(see p. C16 of INFICON catalog)	40 KF (or 25KF)	150.06	
5	Clamping rings for connections evaporator→AHEx	3	STV	Clamping ring DN32-40 (Part No. IN211-003)	(see p. C1 of INFICON catalog)	40 KF (or 25KF)	23.99	
6	Centering rings for connections evaporator→AHEx	3	STV	Centering ring DN 40 ISO-KF, INOX/FPM (Part No. IN 211-070)	(see p. C5 of INFICON catalog)	40 KF (or 25KF)	22.14	

Chapter 7: Prototype design – Annex A7

Table A7.4 – Identification of necessary temperature, flowrate and pressure sensors for the AHEx circuit (see Fig. 7.1), along with technical requirements, proposals from suppliers and costs.

#. Sensor to measure...	Quant.	Technical requirements				Proposal from supplier				
		Operation range Precision	Monitorization	Geometric/functional constrains	Other info.	Product designation (Supplier)	Operation range Precision or accuracy	Notes	Cost/sensor total (€, with VAT)	Drawing
1. T of adsorbent	16	0 - 100 °C 0.5-1 °C	Monitorization along time; connection to Data Acquisition System (DAQ)	Ensure the lowest thickness possible; Sensor is to be inserted inside the bed (vacuum chamber) → <u>need</u> flexibility. Extension cable is also needed	Pressure: vacuum	Type K probe; KMTSS-IM025G-300 (Omega)	-100-400 °C 1.1 °C or 0.4 %	Sheath diameter: 0.25 mm; Sheath length: 300 mm; metal sheath: s. steel; joint type: grounded + 5 m extension cable. <u>Electrical signal:</u> mV thermocouple output	77.49 1240	
2. T of HTF at AHEx inlet and outlet	2	0 - 100 °C 0.5-1 °C	Monitorization along time; connection to Data Acquisition System (DAQ)	For tube with 6-10 mm of internal diameter; extension cable is needed	Pressure in circuit: atmospheric	Type T probe; T-M-1-3-25-M10-T-5 (Omega)	-100-400 °C 0.5 °C or 0.4 %	M: Close end style; 1: Sensor accuracy class 1 (standard); 3: stem diameter of 3 mm; 25: stem length of 25 mm; M10: process connection M10; T: Lead wire insulation of FEP 250 °C maximum; 5: Lead wire length of 5 m. <u>Electrical signal:</u> mV thermocouple output	78.41 156.82	

(Table A7.4 – continued)

Chapter 7: Prototype design – Annex A7




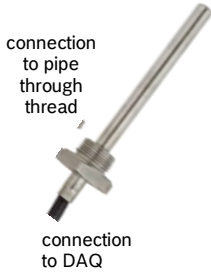

3. T of water in TK2 and TK3	2	0 - 100 °C 0.5-1 °C	No need for monitorization along time	Thermocouples may be immersed in water, or fixed in the tanks. Extension cable is needed.	Pressure: atmospheric	Type T probe; T-M-1-3-50-M10-T-5 (Omega)	(Same as # 2)	Same as # 2, but 50: stem length of 50 mm.	78.41 156.82	(same as #2)
4. Water flowrate at AHEx inlet	1	ca. 0.5 - 3 L min ⁻¹ 0.1 - 0.2 L min ⁻¹	Monitorization along time; connection to Data Acquisition System (DAQ)	Type of connection: ½ or ¾	Pressure in circuit: atmospheric; $T_{max} = 100$ °C	LVB-06-A (STV)	0.5 - 10 L min ⁻¹ Accuracy at ≥ 50 % FS: < 2 % RD; Accuracy at < 50 % FS: < 1 % FS	Working T : < 125 °C; Type of connection: M12 x 1; a feed cable is also required, which is not yet included in the price!; Electrical signal: 4-20 mA	185	
5. P inside AHEx chamber (vacuum)	1	800 - 20000 Pa (8 - 200 mbar)	Monitorization along time; connection to Data Acquisition System (DAQ); Analogic indicator in the chamber	DN 16KF	Continuous exposition to water vapour; $T_{max} \approx 100$ °C; when outgassing the system P may decrease down to ~ 200 Pa (2 mbar)	BourdonVac C (Part No. 16120) (STV)	$10^2 - 10^5$ Pa (1-1000 mbar); Nominal T : 10 - 100 °C	To find vacuum sensors withstanding temperatures up to ~ 100 °C and allowing monitorization of P along time is a big challenge! A thinner scale is needed for readings (Contact alternative suppliers like Iberica Vacuum)	329.33	

Table A7.5 – Identification of necessary temperature, flowrate and pressure sensors for the condenser circuit (see Fig. 7.1), along with technical requirements, proposals from suppliers and costs.

#. Sensor to measure...	Quant.	Technical requirements				Proposal from supplier				
		Operation range Precision	Monitorization	Geometric/function- onal constrains	Other info.	Product designation (Supplier)	Operation range Precision or accuracy	Notes	Cost/sensor total (€, with VAT)	Drawing
1. T of liquid/vapor water refrigerant in condenser	1	0 - 100 °C 0.5-1 °C	Monitorization along time is nice to have	Vacuum need to be ensured in the chamber (no leaks); check how to fix the thermocouple; extension cable is needed.	Continuous exposition to water vapour, vacuum	Type T probe; T-M-1-3-100-G1/4"-T-5 (Omega)	-100-400 °C 0.5 °C or 0.4 %	M: close end style; 1: sensor accuracy class 1 (standard); 3: stem diameter of 3 mm; 50: stem length of 50 mm; M10: process connection M10; T: lead wire insulation of FEP 250 °C maximum; 5: lead wire length of 5 m. <u>Electrical signal</u> : mV thermocouple output	86.10	


(Table A7.5 – continued)

Chapter 7: Prototype design – Annex A7

2. T of HTF at inlet and outlet of condenser	2	0 - 100 °C 0.5-1 °C	Monitorization along time; connection to Data Acquisition System (DAQ)	For tube with 6-10 mm of internal diameter; extension cable is needed.	Pressure in circuit: atmospheric	Type T probe; T-M-1-3-25-M10-T-5 (Omega)	-100-400 °C 0.5 °C or 0.4 %	M: close end style; 1: sensor accuracy class 1 (standard); 3: stem diameter of 3 mm; 25: stem length of 25 mm; M10: process connection M10; T: lead wire insulation of FEP 250 °C maximum; 5: lead wire length of 5 m. <u>Electrical signal</u> : mV thermocouple output	78.41 156.82	
3. T of water in TK1	1	0 - 100 °C 0.5-1 °C	No need for monitorization along time; display	Sensor immersed in water or fixed in the tank. Extension cable is needed.	Pressure: atmospheric	(same as #2)			78.41	(same as #2)
4. Water flowrate at condenser inlet	1	ca. 0.5 - 3 L min ⁻¹ 0.1 - 0.2 L min ⁻¹	Monitorization along time; connection to Data Acquisition System (DAQ)	Type of connection: ½ or ¾	Pressure in circuit: atmospheric; $T_{max} = 100$ °C	LVB-06-A (STV)	0.5 - 10 L min ⁻¹ Accuracy at ≥ 50 % FS: < 2 % RD; Accuracy at < 50 % FS: < 1 % FS	Working temperature: <125°C; Type of connection: M12 x 1; a feed cable is also required, which is not yet included in the price!; Electrical signal: 4-20 mA	185	



(Table A7.5 – continued)

Chapter 7: Prototype design – Annex A7

<p>5. P of refrigerant in the condenser chamber (vacuum)</p>	<p>1</p>	<p>2000 - 20000 Pa (20 - 200 mbar)</p>	<p>Monitorization along time; connection to Data Acquisition System (DAQ) + analogic indicator in the chamber</p>	<p>DN 16KF</p>	<p>Continuous exposition to water vapour; $T_{\max} \approx 100 \text{ }^\circ\text{C}$; when outgassing the system P may decrease down to $\sim 200 \text{ Pa}$ (2 mbar)</p>	<p>BourdonVac C (Part No. 16120) (STV)</p>	<p>$10^2 - 10^5 \text{ Pa}$ (1- 1000 mbar); Nominal T: 10 - 100 $^\circ\text{C}$</p>	<p>To find vacuum sensors withstanding T up to $\sim 100 \text{ }^\circ\text{C}$ and allowing monitorization of P along time is a big challenge. A thinner scale is needed for readings. (Contact alternative suppliers like Iberica Vacuum)</p>	<p>329.33</p>	
---	----------	--	---	----------------	--	--	---	---	---------------	---




Chapter 7: Prototype design – Annex A7

Table A7.6 – Identification of necessary temperature, flowrate and pressure sensors for the evaporator circuit, balance, pressure sensor for the circuit near the cold trap (see Fig. 7.1), data acquisition system (DAQ) components, and some consumables, along with technical requirements, proposals from suppliers and costs.

#. Sensor to measure...	Quant.	Technical requirements				Proposal from supplier				
		Operation range Precision	Monitorization	Geometric/functional constrains	Other info.	Product designation (Supplier)	Operation range Precision	Notes	Cost/sensor total (€ with VAT)	Drawing
1. T of liquid/vapor refrigerant inside evaporator	1	-10 - 80 °C 0.5-1 °C	Monitorization along time is nice to have	Extension cable is needed.	Withstand contact with vapour, liquid and ice (due to degassing procedure), under vacuum.	Type T probe; T-M-1-3-100-G1/4"-T-5 (Omega)	-100-400 °C 0.5 °C or 0.4 %	M: close end style; 1: sensor accuracy class 1 (standard); 3: stem diameter of 3 mm; 50: stem length of 50 mm; M10: process connection M10; T: lead wire insulation of FEP 250 °C maximum; 5: lead wire length of 5 m. <u>Electrical signal:</u> mV thermocouple output	86.10	 <p>connection to condenser through thread</p> <p>connection to DAQ</p>
2. T of HTF at inlet and outlet of evaporator	2	0 - 100 °C 0.5-1 °C	Monitorization along time; connection to Data Acquisition System (DAQ)	For tube with 6-10 mm of internal diameter; extension cable is needed.	Pressure in circuit: atmospheric	Type T probe; T-M-1-3-25-M10-T-5 (Omega)	-100-400 °C 0.5 °C or 0.4 %	M: close end style; 1: sensor accuracy class 1 (standard); 3: stem diameter of 3 mm; 25: stem length of 25 mm; M10: process connection M10; T: lead wire insulation of FEP 250 °C maximum; 5: lead wire length of 5 m. <u>Electrical signal:</u> mV thermocouple output	78.41 156.82	 <p>connection to pipe through thread</p> <p>connection to DAQ</p>




(Table A7.6 – continued)

Chapter 7: Prototype design – Annex A7

3. T of water in TK4	1	0 - 100 °C 0.5-1 °C	No need for monitorization along time; display	Sensor immersed in water or fixed in the tank. Extension cable is needed.	Pressure: atmospheric	Type T probe; T-M-1-3-50-M10-T-5 (Omega)	(same as #2)	(Same as # 2, but 50: stem length of 50 mm)	78.41	(same as #2)
4. Water flowrate at evaporator inlet	1	0.5 - 3 L min ⁻¹ 0.1 - 0.2 L min ⁻¹	Monitorization along time; connection to Data Acquisition System (DAQ)	Type of connection: ½ or ¾	Pressure in circuit: atmospheric; $T_{max} = 50$ °C	LVB-06-A (STV)	0.5 - 10 L min ⁻¹ Accuracy at ≥ 50 % FS: < 2 % RD; Accuracy at < 50 % FS: < 1 % FS	Working T : < 125 °C; Type of connection: M12 x 1; a feed cable is also required, which is not yet included in the price!; Electrical signal: 4-20 mA	185	
5. P of refrigerant in the evaporator chamber(vacuum)	1	ca. 800 - 3000 Pa (8 - 30 mbar)	Monitorization along time; connection to Data Acquisition System (DAQ)+ Analogic indicator in the chamber	DN 16KF	Continuous exposition to water vapour; $T_{max} \sim 40$ °C	BourdonVac C (Part No. 16120) (STV)	$10^2 - 10^5$ Pa (1- 1000 mbar); Nominal T : 10 - 100 °C	To find vacuum sensors withstanding up to ~ 100 °C and allowing monitorization of P along time is a big challenge. A thinner scale is needed for readings. (Contact alternative suppliers like Iberica Vacuum)	329.33	
6. Mass of refrigerant in evaporator	1	3000 g +/- 0.1 g	---	---	Confirm the dimensions of evaporator prior purchasing the balance	Balance model 611-2308 (VWR)	Weighing capacity (g): 6500 g; Readability: 0.1 g	Dimensions: 195 x 175 mm. (Contact other suppliers for further alternatives)	409.84	

(Table A7.6 – continued)

Chapter 7: Prototype design – Annex A7

7. P near the trap (vacuum)	1	100 - 101325 Pa (1 - 1013 mbar)	Analogic or digital indicator in the circuit	Type of connection: 16KF	T in the circuit near trap may be in range ~ 15-95 °C (outgassing of AHEx)	VD81 portable digital vacuum meter (STV)	100 - 1.6×10^5 Pa (1 - 1600 mbar)	$T_{\max} = 50$ °C (!). Contact other suppliers for further alternatives	466.17	
8. Data Acquisition System (DAQ), charts and software	(Contact National Instruments)									
9. Liquid nitrogen	1	---	---	---	---	TR11, 12.2 L flask (Air liquid) + cryogenic gloves	---	Refilling: 2.11 €/L	904.32	

Chapter 8: Final outlook and future work

This chapter provides a final outlook of the PhD dissertation, although each chapter ends with its individual conclusions. Fig. 8.1 summarizes, in a user-friendly way, the information that was discussed along the thesis, regarding the operation and design of adsorption heat pumps (AHPs), performance targets, challenges, useful computational tools for design and optimization, etc.

The worldwide climate changes and the scarcity of natural resources have been driving governmental institutions, as European Commission, to implement measures towards low-carbon society and sustainable development. Particularly, in the building sector, while there is great potential for energy savings, the energy consumption continues high. The construction of nearly zero energy buildings (NZEBs) makes part of the solutions to globally decarbonize the energy system. Heat pumps are versatile and attractive equipments for developing low energy buildings. Certain about the increasing demand for energy efficient and low carbon heating technologies, members of CICECO-Aveiro Institute of Materials (University of Aveiro) and Bosch Thermotechnology (Aveiro) bridged scientific backgrounds to investigate the potential of AHPs for domestic hot water (DHW) production.

Based on a literature review on AHPs, with special focus on water as adsorbate, important achievements, trends and gaps of the R&D in this field were discussed (Chapter 2). In summary: (i) The *COP* of commercial AHPs is essentially in the range 1.30-1.60, which approaches the thermodynamic performance of vapor compression technology. A $COP \geq 1.50 - 1.55$ is considered reasonable for heat pumping, and $SHP > 1000 \text{ W kg}^{-1}$ is required for competitiveness (*e.g.*, for Viessmann technology, $SHP = 1600 \text{ W kg}^{-1}$), for which the use of adsorbent coatings, applied in (compact and lightweight) extended surface heat exchangers, is a must-have. Thus, innovation, novelty and competitiveness in this field requires an improvement of the adsorbent form, increasing the overall complexity and cost of industrialization; (ii) Several adsorbents have been investigated, such as conventional zeolites, silica gel, activated carbons, silicaluminophosphates (SAPOs), and

more recently metal-organic frameworks (MOFs), mainly for water, methanol and ammonia as adsorbates. AQSOA[®] FAM-Z02 (SAPO-34 specially developed by Mitsubishi Plastics for AHPs) has been considered as most promising for adsorption heat transformers. Nonetheless, very few adsorbents reached commercial application due to limited performance, lack of stability (working over 120000 cycles is desirable), poor availability, and/or high price. Under mild regeneration conditions ($T_{\max,\text{cycle}} < 373 \text{ K}$) and T_{evap} in the range 278-288 K, most of the investigated adsorbents are not able to work at T_{cond} of 323-333 K, which is a disadvantage for the domestic hot water (DHW) production. Significant R&D efforts are ongoing to improve the existing materials and develop new ones; (iii) Gas-fired AHPs using water as working fluid for space heating and DHW production have been commercialized by Vaillant and Viessmann, which possess several patents covering aspects of AHP control, components design, and manufacturing. Based on the patent filling dates and the market launch of their appliances, an R&D roadmap for such complex systems comprising around 10 years seems appropriate.

Due to the need for exploring novel adsorbents for AHPs and the recognized potential of ETS-10 for cyclic processes to remove water, this crystalline microporous titanosilicate was investigated for AHPs using water as adsorbate. Several equilibrium and kinetics data were measured for subsequent modeling and simulation of an adsorption unit operating with the ETS-10/water working pair. A simulator was developed in Matlab considering a tubular adsorbent heat exchanger (AHEx) geometry, which was an important tool along the thesis: it facilitated the understanding of the AHP operation and the identification of critical parameters, and allowed the prediction of the performances for different working pairs and distinct geometric/operating conditions. From the numerical simulations, considering $T_{\max,\text{cycle}} = 473 \text{ K}$, $T_{\text{evap}} = 278 \text{ K}$ and $T_{\text{cond}} = T_{\min,\text{cycle}} = 333 \text{ K}$, it was obtained $\Delta\bar{W}_{\text{cycle}} = 0.051 \text{ kg kg}^{-1}$, $COP = 1.36$ and $SHP = 934 \text{ W kg}^{-1}$ for $t_{\text{cycle}} < 600 \text{ s}$ and bed thickness $\delta = 2 \times 10^{-3} \text{ m}$. Higher values of δ led to significant drop of the SHP s to a range that is not competitive (roughly, an increase to $\delta = 4 \times 10^{-3} \text{ m}$ decreased SHP by a factor of two). A comparison of the heating performance of ETS-10 with that of well-known adsorbents like zeolite 13X, zeolite 4A, and silica gel, under the above-mentioned working conditions, showed that zeolite 13X/water was the best pair. The zeolite 13X/water pair outperformed ETS-10/water due to a $\Delta\bar{W}_{\text{cycle}}$ nearly 2.5 times higher than that obtained with the titanosilicate, which led to COP around 1.50 and SHP of

ca. 1200 W kg^{-1} , for $t_{\text{cycle}} < 900 \text{ s}$ and $\delta = 2 \times 10^{-3} \text{ m}$. Hence, zeolite 13X may be an interesting adsorbent for water AHPs if a high temperature heat source is available for bed regeneration, since this material is widely available, is relatively cheap (10-20 € kg^{-1}), and fairly stable. Based on the simulations and sensitivity studies performed for the zeolites and ETS-10, some rules of thumb may be disclosed: (i) for reasonable *COP* and *SHP*, $t_{\text{cycle}} < 900 \text{ s}$, $\delta \leq 2 \times 10^{-3} \text{ m}$ and $\Delta \bar{W}_{\text{cycle}} > 0.12 \text{ kg kg}^{-1}$ are required; (ii) particle size in the range 0.200 – 0.600 mm ensures good compromise between intraparticle mass transfer and bed permeability; (iii) to accomplish the simulations with inferior computational effort, while ensuring similarly accurate results, constant average values of isosteric heat of adsorption (Q_{ads}) (corresponding to half coverage) and overall linear driving force mass transfer coefficient (K_{LDF}) may be used. For the simulated cases, they were typically $3.0 \times 10^6 < Q_{\text{ads}} (\text{J kg}^{-1}) < 3.3 \times 10^6$, and $10^{-2} < K_{\text{LDF}} (\text{s}^{-1}) < 10^{-1}$.

In addition to the need for developing new adsorbents for AHPs, R&D on optimized and efficient AHEx designs and advanced control strategies is crucial. The potential of design of experiments (DoE) and response surface methodology (RSM) for the expeditious optimization of such complex systems was demonstrated using a combined approach of phenomenological and statistical modeling, for the binderless zeolite NaY /water pair. The results showed that DoE/RSM may aid: (i) to identify optimal combinations of geometric and operating parameters (*e.g.*, $(\delta, t_{\text{cycle}})$ pairs), facilitating the development of optimized AHExs; (ii) to develop control strategies that allow an autonomous adaption of the AHP to variable thermal demands, while simultaneously optimizing the overall system performance, which may overall lead to highly efficient “plug & play” AHPs.

Since MOFs are claimed to be very promising adsorbents for AHPs, and the development of improved AHEx designs is a R&D priority, the MOF CPO-27(Ni)/water pair was studied for adsorption heating purposes, considering a tube surrounded by a composite of coating MOF/copper foam. Modeling and simulation studies of the adsorption unit were performed using a customized solver that was developed in OpenFOAM. For $T_{\text{evap}} = 278 \text{ K}$, $T_{\text{cond}} = T_{\text{min,cycle}} = 308 \text{ K}$ and $T_{\text{max,cycle}} = 368 \text{ K}$, the *COP* and *SHP* values were in the intervals 1.16-1.39 and 1922-5130 W kg^{-1} , respectively. Despite the fairly good performance, the considered heating temperature ($T_{\text{cond}} = T_{\text{min,cycle}} = 308 \text{ K}$) is low for DHW production; the MOF does not achieve reasonable $\Delta \bar{W}_{\text{cycle}}$ under more demanding conditions. These results are inferior to those obtained for

the benchmark AQSOATM FAM-Z02, essentially as a result of the lower $\Delta\bar{W}_{\text{cycle}}$ and slower intraparticle mass transfer kinetics of the MOF. Improved performances of MOFs may be envisaged with the exploitation of the rich chemical variability of these materials to enhance adsorption capacity and kinetics properties. Regarding OpenFOAM, it is worth emphasizing that the development of a solver and methodology for simulating adsorption cycles in this software was a first step towards the study of much more complex domains, which is the great advantage of OpenFOAM over dedicated programming software like Matlab.

A prototype for DHW production combining an AHP and gas water heater (GWH) to perform functional tests and measure the performances of several adsorbents was designed, and a protocol for operating the setup was prepared in detail. A cost estimation of the installation was also performed. The prototype can be easily assembled in the near future if promising materials, in terms of techno-economics criteria, can be firstly signaled.

The development of highly efficient AHPs for DHW production is currently constrained by essentially three unfavorable features of the adsorbents: high price, lack of availability, and poor performance at high condensation temperatures. This is likely to be the reason why gas-fired AHPs are reported as most efficient for low heating temperatures. In the whole, water adsorption systems combined with GWHs for DHW production do not seem viable alternatives to heat pump water heaters (HPWHs) in a near future, since they are still too big and significantly more expensive (roughly, they may cost two times more). Several stakeholders from the field of low carbon heating technologies share this vision. Nevertheless, resolving these techno-economic challenges would be highly desirable to replace electrically-driven heat pumps and even GWHs in the medium or long term, as: (i) prices of electricity and natural gas for household consumers tend to increase; (ii) sanitary hot water heat pumps have been the fastest growing heat pump segment in Europe, with double digit growth; (iii) AHPs exclusively intended for DHW production are absent from the market (to the best of our knowledge); (iv) consumers are becoming increasingly aware of the environmental challenges that our World is facing.

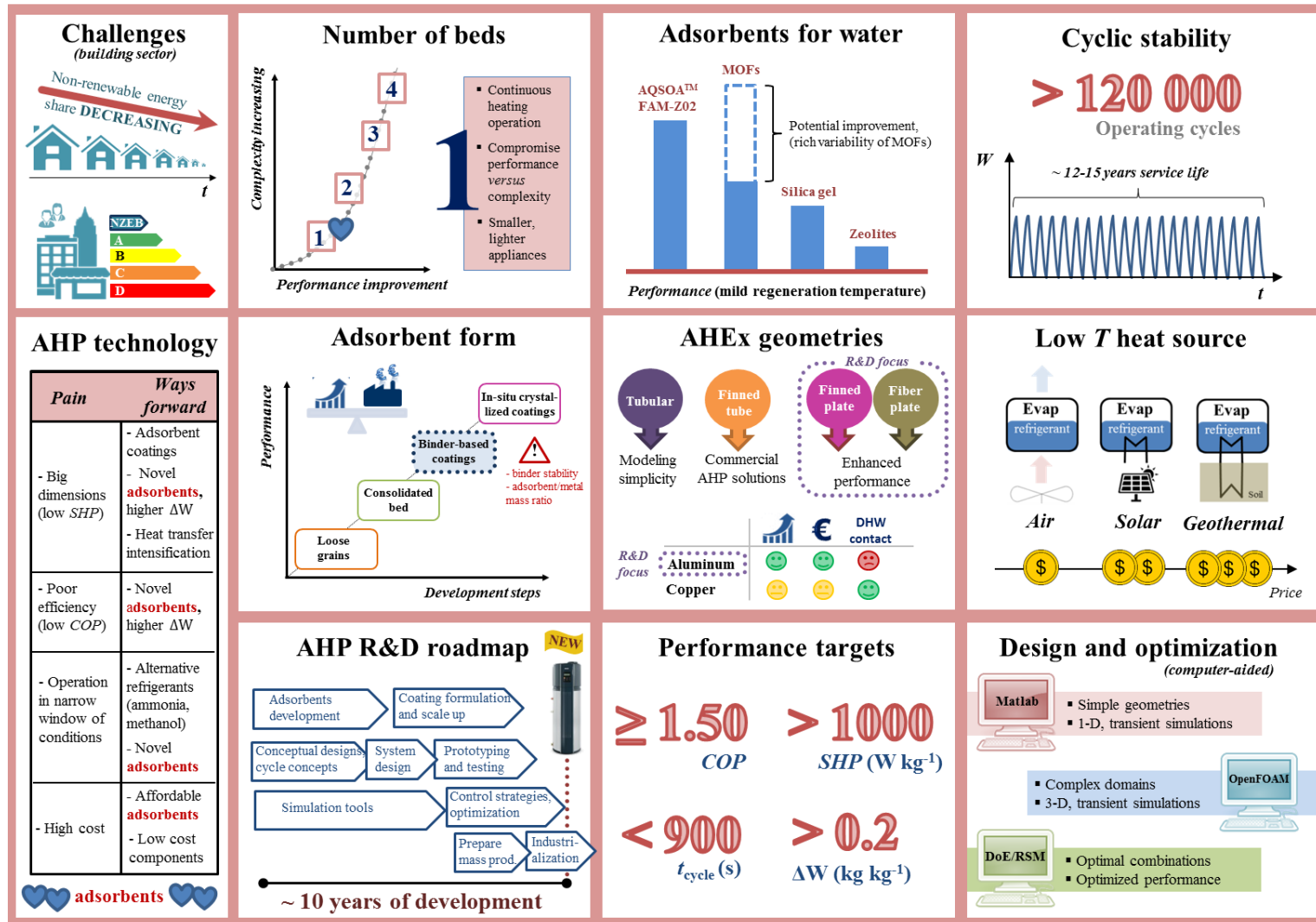


Fig. 8.1 – Infographic with general information regarding AHPs design, performance, optimization and challenges discussed along the thesis.

Suggestions of future work

Based on the work performed along the thesis, some suggestions of future work follow:

- The use of alternative refrigerants, such as methanol and ammonia, or even mixtures of different fluids, may be studied for AHPs, since they enable operation at lower evaporation temperatures compared to water, which makes the use of air as low temperature heat source more viable. Activated carbons are possible adsorbents for ammonia and methanol, are cheap ($< 5 \text{ € kg}^{-1}$) and readily available in the market;
- Since water is undoubtedly the most eco-friendly fluid, novel optimized adsorbents for water may be developed. Taking $T_{\text{evap}} = 278 \text{ K}$, $T_{\text{cond}} = T_{\text{min,cycle}} = 333 \text{ K}$ and $T_{\text{max,cycle}} = 368 \text{ K}$ as reference for DHW production, the isotherms at 333 and 368 K of an ideal adsorbent might resemble those in Fig. 8.2(a), where the values of relative pressure (P/P^σ) of interest are computed. Estimates of *COP* and *SHP* for a promising adsorbent which achieves $\Delta W_{\text{eq}} = 0.2 \text{ kg kg}^{-1}$ under the above-mentioned working conditions are furnished in Fig. 8.2(b);
- Following the principle of parsimony, a simple tubular AHEx was initially considered in the simulations, but one concluded that it is not promising for practical use due to the small area available for heat transfer per unit volume. Given the great potential of OpenFOAM to study complex domains, promising and more complex geometries, like finned-plate and fiber-plate, may be studied in the future;
- Finally, there is a need for reinventing the energy system towards a more sustainable model. In this sense, energy storage solutions may bridge the gap between the supply and demand of thermal energy from renewable sources [1, 2]. For instance, the availability of solar energy depends on the time of the day and the season. It may be captured and stored during the daytime and in the summer months, to be used during the nighttime and the winter months [2]. Thermal energy storage (TES) using adsorption based technologies has been considered the most suitable for residential buildings (see Fig. 8.3(a)) [3]. Closed- and open-cycle adsorption systems for TES are shown in Fig. 8.3(b)-(c). Currently this technology is not economically viable, but the development of novel materials and the

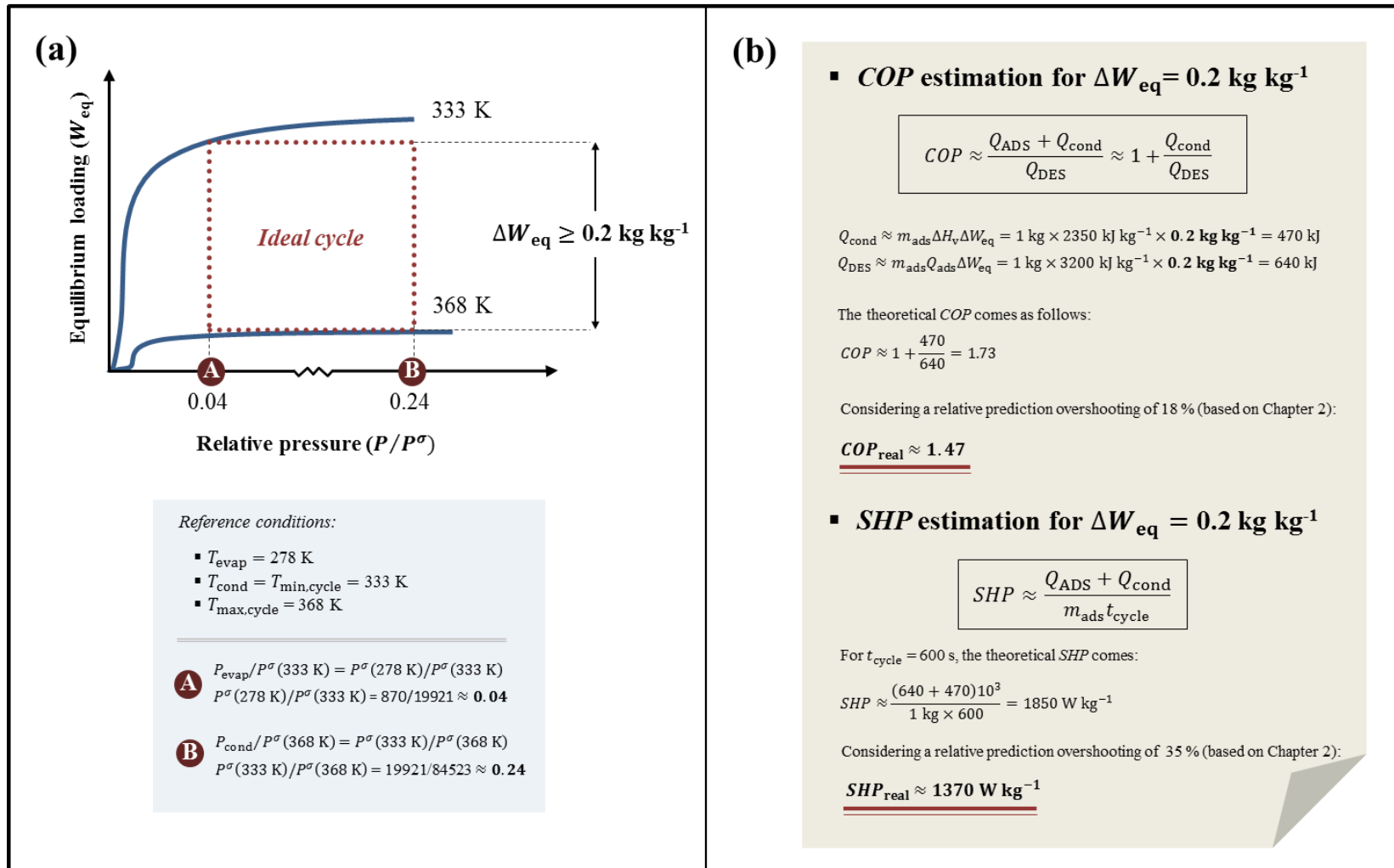


Fig. 8.2 – (a) Draft of water adsorption isotherms at 333 K and 368 K of an adsorbent for AHPs intended to heat domestic water (top), and values of relative pressure (P/P^σ) of interest for the considered application (bottom); (b) Estimates of COP and SHP for $\Delta W_{\text{eq}} = 0.2 \text{ kg kg}^{-1}$ and $t_{\text{cycle}} = 600 \text{ s}$.

system optimization may make it competitive [2]. To conclude, the potential of adsorption TES may be explored in order to create suitable and innovate heat storage solutions for buildings.

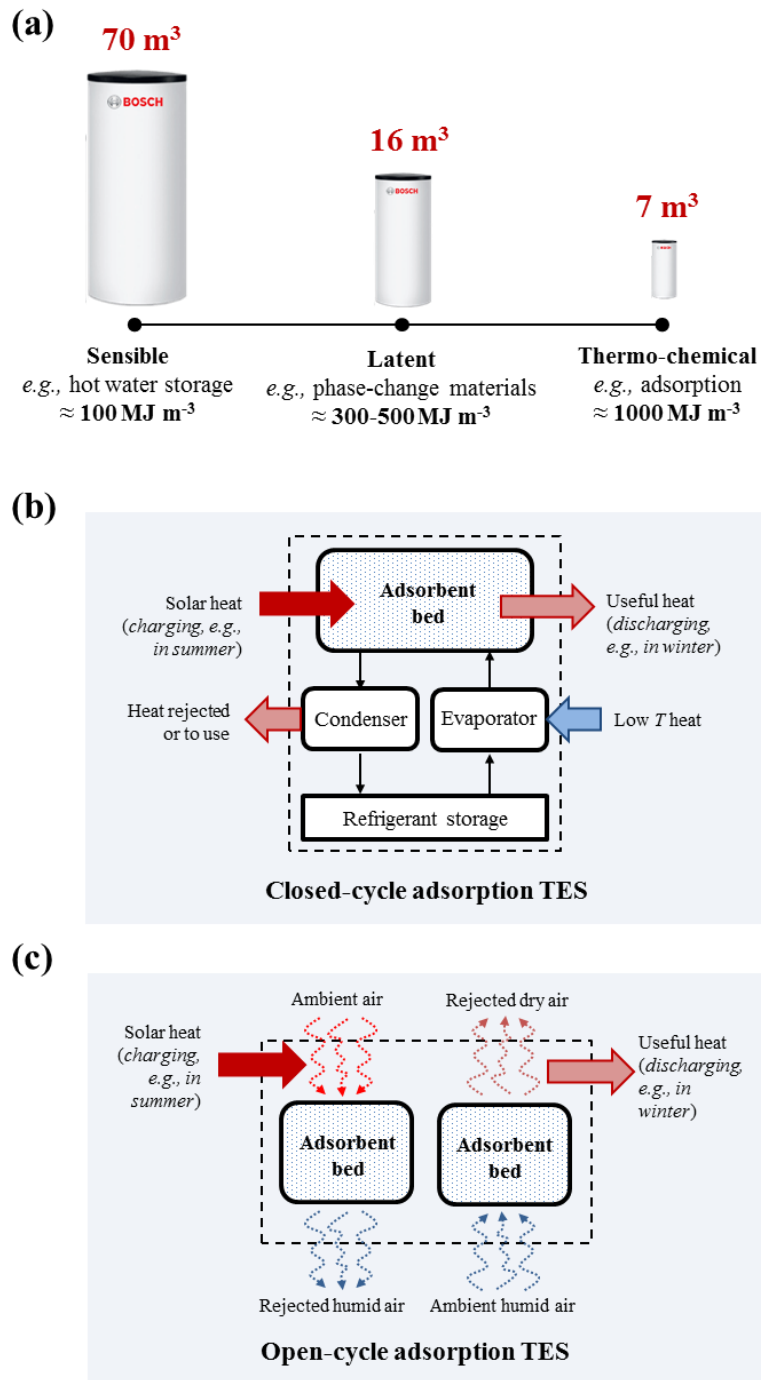


Fig. 8.3 – (a) Volumes required by sensible, latent and thermo-chemical storage systems to store the annual energy for an energy efficient house (6480 MJ) [2]. Adsorption thermal energy storage (TES): (b) closed-cycle, (c) open-cycle [4].

Nomenclature

AHEX	Adsorbent heat exchanger
AHP	Adsorption heat pump
COP	Coefficient of performance
DoE	Design of experiments
K_{LDF}	Intraparticle mass transfer coefficient (s^{-1})
m_{ads}	Mass of adsorbent (kg)
P	Pressure (Pa)
Q	Heat (J)
Q_{ads}	Isosteric heat of adsorption ($J\ kg^{-1}$)
RSM	Response surface methodology
<i>SHP</i>	Specific heating power ($W\ kg^{-1}$)
t	Time (s)
t_{cycle}	Cycle time (s)
T	Temperature (K)
TES	Thermal energy storage
 <i>Greek symbols</i>	
δ	Bed thickness (m)
ΔH_v	Latent heat of evaporation ($J\ kg^{-1}$)
ΔW_{eq}	Equilibrium adsorption loading swing ($kg\ kg^{-1}$)
$\Delta \bar{W}_{cycle}$	Cyclic adsorption loading swing ($kg\ kg^{-1}$)
 <i>Subscripts</i>	
ADS	Isobaric adsorption stage
cond	Condenser
DES	Isobaric desorption stage
evap	Evaporator
max	Maximum
min	Minimum

References

- [1] Re-thinking 2050 - A 100% Renewable Energy Vision for the European Union, EREC – European Renewable Energy Council (2010), https://warwick.ac.uk/fac/soc/pais/research/researchcentres/csgr/green/foresight/energyenvironment/2010_erec_rethinkng_2050.pdf, (accessed in 20.06.2018).
- [2] D. Lefebvre, F.H. Tezel, A review of energy storage technologies with a focus on adsorption thermal energy storage processes for heating applications, *Renewable and Sustainable Energy Reviews*, 67 (2017) 116-125.
- [3] A. Frazzica, A. Freni, Adsorbent working pairs for solar thermal energy storage in buildings, *Renewable Energy*, 110 (2017) 87-94.
- [4] Adsorption Storage Systems - EASE: European Association for Storage of Energy (2016), http://ease-storage.eu/wp-content/uploads/2016/07/EASE_TD_Thermal_Adsorption.pdf, (accessed in 20.06.2018).